Scale-dependent identification and statistical analysis of atmospheric vortex structures in theory, model and observation

Dissertation
zur Erlangung des akademischen Grades eines
Doktors der Naturwissenschaften (Dr. rer. nat.)

am Fachbereich Geowissenschaften
der Freien Universität Berlin

vorgelegt von
Lisa Schielicke

Berlin, Oktober 2016

1. Gutachter:	**Prof. Dr. Uwe Ulbrich** Freie Universität Berlin Fachbereich Geowissenschaften Institut für Meteorologie Carl-Heinrich-Becker-Weg 6-10 12165 Berlin, Deutschland
2. Gutachter:	**PD Dr. Peter Névir** Freie Universität Berlin Fachbereich Geowissenschaften Institut für Meteorologie Carl-Heinrich-Becker-Weg 6-10 12165 Berlin, Deutschland
3. Gutachter:	**Prof. Dr. Rupert Klein** Freie Universität Berlin Fachbereich Mathematik & Informatik Institut für Mathematik Arnimallee 2-6 14195 Berlin, Deutschland
Tag der Disputation:	**17.05.2017**

Abstract

Occurring on various scales vortices are the most prominent feature determining considerably the appearance of the atmospheric flow field. Although, it seems to be subjectively trivial to identify a vortex by the observation of swirling motions, an accepted unified mathematical definition of vortex size and intensity is still missing. In this thesis, the kinematic properties and the dynamic equations of the flow field will be used in order to reveal appropriate size and intensity measures of theoretical models as well as atmospheric vortices.

Well-known methods of vortex identification in atmospheric flows are based on pressure or vorticity fields. We will show that these methods can give inconsistent results in certain flow situations, especially in the vicinity of shear. Therefore, we will introduce a kinematic method called the kinematic vorticity number method (W_k-method) that locally compares the rates of rotation and deformation. A vortex is then defined in regions where the rotation rate prevails over the strain rate. Due to the dimensionless definition as a ratio, the main advantage of the novel method is that it is applicable in different flow situations, different height levels and different grid resolutions giving consistent results. In the thesis, we will show a broad range of successful applications of the W_k-method in multiple different data sets.

Kinematics give considerable insight into the behavior and properties of the flow at one moment in time. However, kinematics do not consider the forces that cause this behavior and how the flow or the vortices will evolve over time. For the complete study of vortex behavior and vortex interactions, we also need to study the dynamic equations. These equations of motion can be used in order to derive theoretical vortex models under idealized conditions. Theoretical vortex models such as the Rankine vortex model reveal that radius and circulation are the most important vortex properties that determine the wind field around a vortex. The W_k-method is able to extract these two properties from the complex flow fields. However, atmospheric vortices differ from theoretical models mainly in the prevailing balance of forces. While theoretical vortex models are derived in an inertial, non-rotating reference frame, we need to investigate atmospheric vortices in a noninertial, rotating reference frame since the effect of Earth's rotation rate becomes non-negligible for larger-scale atmospheric vortices on the mesoscale, synoptic and planetary scale. Therefore, we will introduce two intensity measures on basis of the horizontal equations of motion. The explicit expressions of intensity measures, called energy of displacement and atmospheric moment, depend on the set of forces that balance the pressure gradient force in the radial component of the horizontal equations of motion. We will show that the energy of displacement expressions can be written in terms of different combinations of circulation and vortex size for different atmospheric

vortex types due to the influence of the Coriolis force on larger-scale vortices. While the energy of displacement can be interpreted as the mass-specific work that was necessary to generate the vortex, the atmospheric moment is its mass-related counterpart. Likewise to the seismic moment of earthquakes, the atmospheric moment can be seen as a measure of vortex magnitudes proportional to the total energy released during the vortex life time.

Finally, we will apply our assembled knowledge, measures and methods in the statistical analysis of vortex structures in data of different resolution from reanalysis, models as well as observations. For all data sets and parameters the main findings are the following: The smaller scales usually behave rather power-law (scale-free) distributed while the larger scales of the parameters are rather determined by scales (exponential behavior). With respect to the atmospheric moments, we could identify a power-law distribution that seems to be composed of different vortex types ranging from the convective scale up to the synoptic scale. We found that the power-law exponent is similar to that of earthquakes (Gutenberg-Richter law).

In conclusion, this thesis investigates the relation of vortices on different scales as seen from theory, model and observations. We could introduce and implement a unifying method — the W_k-method — that is able to identify vortices and their properties from differently-resolved flow fields in a consistent manner. To our knowledge, it is probably the first time that such an attempt of interlinking the atmospheric vortices on different scales with help of one single method has been made. The W_k-method not only allows us to compare the different data sets, it furthermore can be applied in various ways as is shown in the present work. Last but not least, the W_k-method allows the presentation of atmospheric vortices in a three-dimensional manner that helps to improve the subjective view we have on vortices.

Zusammenfassung

Wirbel sind wohl die bekanntesten und auffälligsten Phänomene, die das Erscheinungsbild der Atmosphäre maßgeblich prägen. Trotz ihrer auffälligen Rotationsbewegung ist es nicht trivial, einen Wirbel hinsichtlich seiner Stärke und Ausdehnung klar vom dreidimensionalen Strömungsfeld abzugrenzen, da eine einheitlich akzeptierte, mathematische Definition fehlt. In dieser Arbeit werden wir das Problem der Wirbelerkennung einerseits mit Hilfe der Kinematik und andererseits mit Hilfe der Dynamik betrachten. Während die Kinematik bei der Beschreibung der Wirbelgröße hilft, können wir mit Hilfe der dynamischen Gleichungen und daraus abgeleiteten theoretischen Wirbelmodellen Intensitätsmaße finden.

Bekannte Methoden zur Wirbelidentifizierung in atmosphärischen Feldern basieren häufig auf den Parametern Druck bzw. Vorticity. Wir werden im Rahmen dieser Arbeit zeigen, dass diese Methoden in bestimmten Strömungssituationen inkonsistente Ergebnisse liefern; z.B. wenn die Wirbel mit großer Scherung überlagert sind. Kinematische Methoden hingegen erlauben es, Wirbel und insbesondere ihre Größe in vielen Situationen konsistenter zu bestimmen. Ein Beispiel ist die kinematische Vorticity-Zahl, die als Quotient der lokalen Rotationsrate und der Deformationsrate definiert ist. Die kinematische Vorticity-Zahl dient as Grundlage, der in dieser Arbeit eingeführten W_k-Methode. Dabei definieren wir eine Wirbelfläche als ein zusammenhängendes Gebiet, in dem die Rotationsrate gegenüber der Deformationsrate überwiegt. Berücksichtigt man zusätzlich das Vorzeichen der Vorticity, so ist es möglich sowohl Tief- als auch Hochdruckgebiete bzw. zyklonal und antizyklonal rotierende Wirbel zu untersuchen. Aufgrund ihrer dimensionslosen Definition als Quotient hat die W_k-Methode den Vorteil, dass sie in verschiedenen Strömungssituationen, in unterschiedlichen Höhenschichten und in unterschiedlich gut aufgelösten Feldern eingesetzt werden kann, ohne dass subjektive Grenzwerte definiert werden müssen. Wir werden in dieser Arbeit eine breite Palette von Anwendungen der W_k-Methode in verschiedenen Datensätzen präsentieren.

Die Kinematik ermöglicht es zwar den aktuellen Zustand einer Strömung und der in ihr enthaltenen Wirbel zu analysieren, dabei bleiben jedoch die Ursachen sowie die zeitliche Entwicklung der Strömung unberücksichtigt. Möchte man hingegen die zeitliche Entwicklung und die Interaktion von Wirbeln verstehen, so müssen die dynamischen Gleichungen betrachtet werden. Unter stark idealisierten Bedingungen können mit Hilfe der dynamischen Gleichungen theoretische Wirbelmodelle wie das Punktwirbel- oder das Rankinewirbelmodell abgeleitet werden. Diese Modelle zeigen uns, dass das Windfeld, das um einen Wirbel herum induziert wird, durch die Wirbelzirkulation und den Wirbelradius beschrieben werden kann. Mit Hilfe der W_k-Methode können wir diese beiden Parameter für jeden Wirbel bestimmen. Reale atmosphärische Wirbel unter-

scheiden sich von den idealisierten Wirbelmodellen jedoch hinsichtlich der vorherrschenden Kräftegleichgewichte. Während theoretische Wirbelmodelle in einem Inertialsystem hergleitet werden, müssen die atmosphärischen Wirbel in einem rotierenden Nichtinertialsystem betrachtet werden, da der Einfluss der Erddrehung für mesoskalige, synoptischskalige und planetare Wirbel nicht mehr vernachlässigbar ist. Dies führte zur Einführung zweier Intensitätsmaße auf Grundlage der horizontalen Bewegungsgleichungen im rotierenden Bezugssystem. Die expliziten Ausdrücke dieser Intensitätsmaße, genannt Verschiebungsenergie (*energy of displacement*) und atmosphärisches Moment (*atmospheric moment*), hängen vom vorherrschenden Kräftegleichgewicht der radialen Komponente der horizontalen Bewegungsgleichungen ab. Das Kräftegleichgewicht hängt wiederum von der horizontalen Skala der Wirbel ab. Die Verschiebungsenergie lässt sich mit Hilfe der Parameter Wirbelzirkulation und Wirbelradius ausdrücken. Interpretieren ließ sich die Verschiebungsenergie als die massenspezifische Arbeit, die benötigt wurde, um den Wirbel zu erzeugen. Das atmosphärische Moment stellt das massenabhängige Pendant zur Verschiebungsenergie dar, da es zusätzlich das gesamte Volumen berücksichtigt, dass während der Lebenszeit des Wirbels beeinflusst wurde. Analog zum seismischen Moment der Erdbeben, kann das atmosphärische Moment als Magnitude bzw. gesamte freigesetzte Energie der Wirbel interpretiert werden.

Die auf den vorgestellten Überlegungen basierten Maße und Methoden werden anschließend in der statistischen Analyse von Wirbelstrukturen in Datensätzen unterschiedlicher Auflösung angewandt. Dabei beobachten wir, dass sich Wirbel der kleinen Skalen eher potenzverteilt (skaleninvariant) verhalten während die Wirbel der großen Skalen eher exponentialverteilt (skalenbehaftet) sind. Für die atmosphärischen Momenten konnten wir Hinweise auf ein Potenzgesetz finden, dass sich aus den Wirbel der unterschiedlichen Skalen zusammenzusetzen scheint. Der Exponent dieses Potenzgesetze entspricht dem des Gutenberg-Richter Gesetzes der Erdbeben.

Zusammengefasst untersuchen wir in dieser Arbeit Wirbel unterschiedlicher Skalen mit Hilfe theoretischer Überlegungen und Modelle, numerischer Simulationen sowie mit Beobachtungsdaten. Die neu eingeführte W_k-Methode erlaubt es Wirbel und ihre Eigenschaften in unterschiedlich aufgelösten Daten in konsistenter Weise zu bestimmen. Unseres Wissens nach ist das möglicherweise der erste Versuch atmosphärische Wirbel unterschiedlicher Skalen anhand einer einzigen, einheitlichen Methode zu untersuchen. Die W_k-Methode kann darüber hinaus auf unterschiedliche Weise eingesetzt werden, so dass diese Arbeit einen Beitrag leistet, das Wissen um Wirbel und ihre Eigenschaften zu verbessern. Nicht zuletzt erlaubt die W_k-Methode, atmosphärische Wirbel im dreidimensionalen Raum darzustellen und damit das subjektive Bild, das wir von Wirbel haben, zu verbessern.

Publications

Parts of the contents and figures of this thesis are already published in the publications listed below.

- In Chapter 5 material of the following publications presenting intensity measures of atmospheric vortices is used:

  Schielicke, L. and Névir, P. (2009). On the theory of intensity distributions of tornadoes and other low pressure systems. *Atmospheric Research*, 93(1), 11–20, https://doi.org/10.1016/j.atmosres.2008.09.021

  Schielicke, L. and Névir, P. (2011). Introduction of an atmospheric moment combining eulerian and lagrangian aspects of vortices: Application to tornadoes. *Atmospheric Research*, 100(4), 357–365, https://doi.org/10.1016/j.atmosres.2010.08.027

  Schielicke, L. and Névir, P. (2013). Comprehensive analysis of tornado statistics in comparison to earthquakes: intensity and temporal behaviour. *Nonlinear Processes in Geophysics*, 20(1), 47–57, https://doi.org/10.5194/npg-20-47-2013 Published as an Open Access article distributed under the Creative Commons Attribution 3.0 License (https://creativecommons.org/licenses/by/3.0/)

- Parts of chapters 2 and 6 of this thesis present an introduction and first applications of the W_k-method. These are based on/adopted from the following publication:

  Schielicke, L., N évir, P., and Ulbrich, U. (2016). Kinematic vorticity number - a tool for estimating vortex sizes and circulations. *Tellus A*, 68. 29464, http://dx.doi.org/10.3402/tellusa.v68.29464 Published as an Open Access article distributed under the terms of the Creative Commons Attribution 4.0 International License (http://creativecommons.org/licenses/by/4.0/)

Contents

1 Introduction and Motivation

Vortices are one of the most common features of the atmospheric flow field. They occur on various scales ranging from turbulence-scale whirlwinds in the order of centimeters or meters up to the stratospheric polar vortex which spans nearly half of the winter hemisphere with a horizontal scale in the order of about 10^7 m. An overview over different atmospheric vortex types and their characteristic properties is given in Table 1. Lifetime and horizontal scale of vortices seem to be connected via a remarkably simple scaling law introduced by Kolmogorov (1941)[1] (see Figure 1 adopted from Smagorinsky, 1974). This scale-invariant nature of turbulence was captured nicely by Lewis Fry Richardson in his famous poem[2]

> *"Big whirls have little whirls that feed on their velocity,*
> *And little whirls have lesser whirls and so on to viscosity."*

[1] Kolmogorov's law is also called 5/3-scaling law because the energy spectrum scales as $E(k) \sim k^{-5/3}$ where k is the wave number. In spatial space, the energy depending on length l scales as $E(l) \sim l^{2/3}$

[2] Lewis Fry Richardson (1881-1953) was a scientist active in various scientific fields such as computational mathematics, meteorology, fluid mechanics and complex systems (A review of his life and his contributions to the fields of numerics, meteorology and numerical weather prediction is given in Hunt, 1998).

Table 1: *Typical atmospheric vortex types and their characteristic properties (U, W: horizontal/vertical wind speed, L: horizontal scale, H: height, H/L: height-to-length ratio (aspect ratio), T : lifetime, $\Gamma = 2\pi LU$: circulation) Furthermore, the prevailing balance of forces is given where "geostrophic" denotes the balance of the pressure gradient force and the Coriolis force; "gradient wind" denotes the balance of the pressure gradient force and the sum of the Coriolis and centrifugal forces; and "cyclostrophic" denotes the balance of the pressure gradient force and the centrifugal force. Typical values of charateristic properties are taken from classical textbooks (Markowski and Richardson, 2011; Holton, 2004), typical lifetime of tropical cyclones is taken from Camargo and Sobel (2005), who analysed tropical cyclones in the western Pacific. The characteristic lifetime might be slightly different for other basins.*

vortex type:	synoptic low	tropical cyclone	supercell	tornado
U	10 m/s	25 m/s	15 m/s	50 m/s
W	1 cm/s	1 m/s	10 m/s	50 m/s
L	1000 km	300 km	10 km	100 m
H	10 km	10 km	10 km	2 km
H/L	10^{-2}	10^{-1}	10^{0}	$2 \cdot 10^{1}$
T	1-3 days	5-10 days	1-4 hours	10 min
Γ	$6 \cdot 10^7 \mathrm{m}^2/\mathrm{s}$	$2 \cdot 10^7 \mathrm{m}^2/\mathrm{s}$	$2 \cdot 10^6 \mathrm{m}^2/\mathrm{s}$	$3 \cdot 10^4 \mathrm{m}^2/\mathrm{s}$
Hor. balance	geostrophic	gradient wind	cyclostrophic	cyclostrophic

Vortices have a considerable share in reducing imbalances in the climate system. In general, large-scale vortices transport heat and moisture pole- and upwards and therefore reduce the imbalance induced by the global difference in solar influx. Hence, vortices have a large impact on the regional and global climate while large-scale climate conditions on the other hand influence the development of cyclones. Furthermore, vortices have a considerable impact on society. On the one hand, vortices determine the local weather and climate (precipitation amount, temperature, wind). On the other hand, a small number of extreme vortices are able to produce damaging severe weather of different types (gale force winds, extreme precipitation, large hail, tornadoes). Therefore, it is of great importance to understand vortex behavior including their structure, frequency of occurrence, intensity distributions and, in particular, their behavior under different climate conditions.

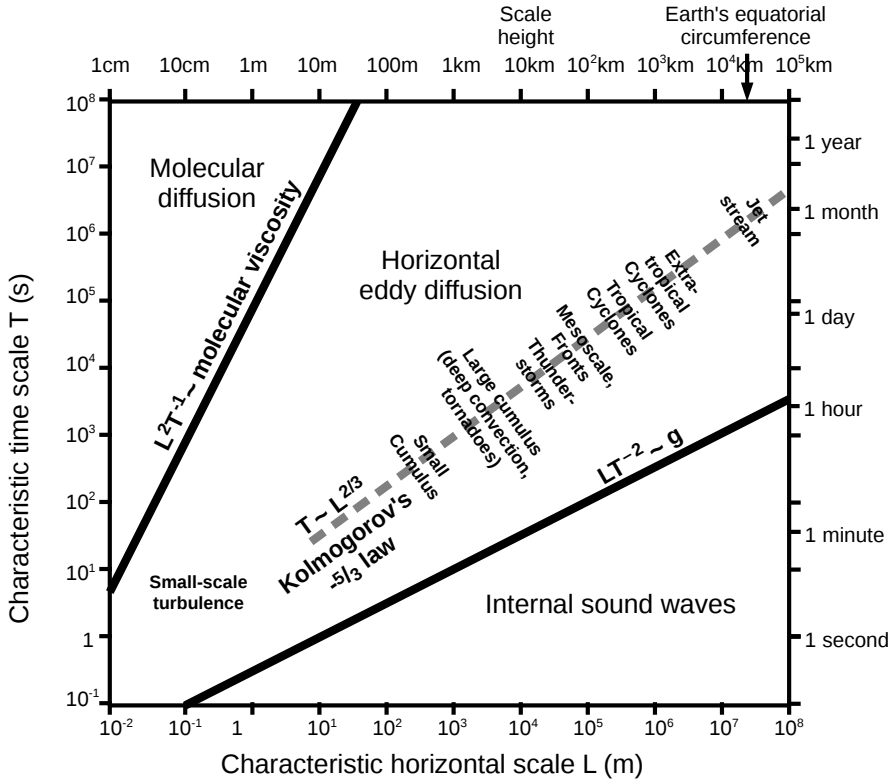

Figure 1: *Scales of atmospheric phenomena, adopted with slight modifications from Smagorinsky (1974), who used Kolmogorov's scaling law of turbulent flows to order the phenomena along a line with slope 2/3 in a double-logarithmic plot of length scale L vs. time scale T. This law comes from the assumption of constant energy dissipation with* $E_{kin}/T = const. \sim L^2/T^3 = const.$. *Molecular diffusion is a slow process and therefore is located at the top left. The unit of the molecular viscosity is* $m^2/s \sim L^2/T$. *Sound waves have high velocities and therefore are located at the bottom right. The group velocity of gravity waves (shallow water equation) is given by* $c_g = \sqrt{gH}$ *where* g *is the gravitational acceleration and* H *is the scale height.*

Surprisingly, despite their importance and impact on daily life, there is neither a clear definition nor a consensus on the intensity or size definition of a vortex (e.g. Neu et al., 2013, who make this statement explicitely for extratropical cyclones). Interestingly, the same is true for other vortices of turbulent flow. Especially in fluid mechanics, the topic of vortex definition and identification is debated since the beginning of hydrodynamics (Jeong and Hussain, 1995) and research in this field is still ongoing (e.g. Chakraborty et al., 2005). Moreover, Jeong and Hussain (1995) state that "*an accepted definition of a vortex is still lacking*". Since the 1990s, numerous fluid dynamical publications addressed this topic. In the following, loads of different (sophisticated) methods were introduced. These methods are often based on the analysis of the kinematics of the flow field. However, only rare applications to the atmospheric flow are found and these applications only dealt with a certain type of vortex (a few studies on tropical cyclones use successfully the so called Okubo-Weiss parameter, that compares kinematic properties in order to identify a vortex, see e.g. Dunkerton et al., 2009; Tory et al., 2013). However, for the study of vortex properties and vortex interactions on different scales likewise to Richardson's poem it is necessary to define a unified method that identifies vortex structures on different scales in a consistent manner. Such a method is still missing, but kinematic methods seem to be the key towards a multiscale identification of vortices.
The main motivations and objectives of this thesis can be summarized as follows

- Vortices can be seen from two perspectives: dynamic (intensity) and kinematic (geometric properties such as size, height, path lengths) perspectives and both sides are important in describing the vortex in its entirety.
- Both topics can be tackled with different approaches: On the one hand, kinematic properties of the flow can be used in order to determine the geometric aspects of the vortex. On the other hand, dynamic equations serve as basis to determine consistent intensity measures.
- Both approaches - kinematic as well as dynamic –will be used in this thesis in order to study vortex structures on different scales with respect to their intensity and their size on basis of a single unified method.

In order to verify the applicability of the method to differently-scaled data sets, we will conduct multiple tests, applications and a statistical analysis of different data sets: simulation, reanalysis and observational data. The statistical analysis of vortex properties of the different vortex types is essential for further and future studies of the behavior of the vortex properties under different climate conditions (e.g. summer vs. winter). Furthermore, it seems that vortices on different scales are in a way connected to each other (cf. Figure 1). If we could proof this connection between different vortex types, we would be able to analyze vortices only on a specific scale and still gain information on

all other scales. For example, in coarse data sets only large-scale extratropical cyclones (and anticyclones) are resolved while vortices on smaller scales are missing. In this case, we might still be able to estimate the behavior for the smaller scales. The last part of this work deals with this topic.
This work is organized as follows: we will refresh the knowledge on the kinematics of the flow field in chapter 2 and will see that the kinematics can serve as a toolbox of vortex identification methods and especially helps in the definition of vortex sizes. The general dynamics as well as vortex dynamics are introduced in chapter 3. These equations allow us to understand vortex interactions and helps in the definition of vortex intensity measures. Theoretical vortex models in chapter 4 reveal under cyclostrophic balance the importance of the vortex properties circulation and radius on the flow field around a vortex. For atmospheric vortices a revision of these properties is necessary since larger-scale atmospheric vortices deviate from a cyclostrophic balance due to the non-negligible influence of Earth's rotation rate on the vortices and new measures of vortex intensity will be derived in chapter 5. Finally, we are able to introduce a unified method of vortex identification: the kinematic vorticity method (W_k-method) in chapter 6. This method allows us to identify all relevant properties of a vortex and will be applied in the statistical analysis of vortices on different scales in chapter 7. We complete the thesis with a conclusion and outlook chapter 8.

2 Kinematics: A toolbox of vortex identification methods

Kinematics is a diagnostic tool. It deals with the motion and deformation of a flow field without considering the forces that cause these motions (Wu et al., 2007). In comparison, dynamics takes into account the causal forces by analysing the prognostic equations of motion. This section only deals with the kinematics and it will be shown how the kinematics can be used to diagnose and visualize the flow field. Moreover, the analysis of the kinematic properties of the flow will be the main tool used in this thesis in order to identify vortex structures and their properties like size and strength in the complex atmospheric flow fields. Since vortices are a typical feature of fluids which do not occur in solids, we will start with an overview over the different properties of fluids and solids.

2.1 On solids, fluids and the occurrence of vortices

We neither observe vortices in solids nor in viscous fluids like honey. Hence, there must be an important difference between solids and fluids in general and between different types of fluids in particular. Thereby, the term fluid designates gases as well as liquids. The main difference between solids and fluids is the way the materials react on forces, more specific on shear forces. Batchelor (2000) distinguishes between simple solids and simple fluids as follows: Assume to apply the same small change in shear forces to either a simple solid and a simple fluid. The *simple* solid will react with only a small amount of change in its shape and in the relative positions of the material elements, while the *simple* fluid reacts with a considerable change of shape and of the relative positions of its elements (see also Shaughnessy et al., 2005). Most common fluids like air and water behave like simple fluids. The term "*simple*" should distinguish simple solids and fluids from more complex materials that behave like fluids in some respects and like solids in other respects such as thixotropic[3] substances (Batchelor, 2000).

The main difference between liquids and gases is their different compressibility. Gases can be compressed easily while liquids can be compressed, however only slightly and with a huge effort: for example the bulk modulus[4] of water is $2{\cdot}10^9$ Pa while that of air near the surface is in the order of 10^5 Pa=1000 hPa (Tipler, 2000). Since the compressibility of liquids is small they are often assumed to be incompressible[5].

The occurrence of vortices – or eddies – in a fluid is closely connected to turbulence in the flow. The distinction between laminar and turbulent flow regimes is measured

[3]Examples of thixotropic substances are paint, jelly or ketchup which behave like elastic solids when being in rest for a time, but behave like liquids when being severely distorted by shaking or stirring.

[4]The bulk modulus describes the resistance of a substance to uniform compression. Its reciprocal value is called compressibility.

[5]Incompressible stands for zero compressibility or a bulk modulus of ∞

in terms of the dimensionless Reynolds number Re which is defined as the ratio of the inertial and viscous forces:

$$Re = \frac{\text{inertial forces}}{\text{viscous forces}} = \frac{\rho U^2 L^2}{\mu U L} = \frac{UL}{\nu} \tag{1}$$

where U and L are the characteristic velocity and length scale in the fluid; μ and ν are the bulk viscosity and kinematic viscosity, respectively with $\nu = \mu/\rho$; and ρ is the density of the fluid. The term $\rho U^2/L$ describes the characteristic magnitude of the inertial forces and $\mu U/L^2$ describes the characteristic order of the viscous forces. It can be interpreted also as the relative importance of advection in comparison to diffusion. For low Reynolds numbers the flow is laminar, for high Reynolds numbers it is turbulent and vortices occur. In general, the Reynolds number of geophysical flows are very large (see Cushman-Roisin and Beckers, 2011) which is in accordance with the observation of vortices over a wide range of scales as a typical feature of geophysical flows. In this work, we concentrate on the analysis of atmospheric vortex structures which can be investigated from different perspectives.

2.2 Eulerian vs. Lagrangian perspective

A fluid can be seen as the sum of a multitude of particles forming a 3-dimensional continuum (Fortak, 1967) where a particle is defined as a group of sufficiently many atoms or molecules such that macroscopic properties (volume, pressure, density and temperature) can be assigned to the particle (American Meteorological Society, 2012).
There are two main perspectives in describing a fluid. One way is to follow the motion of fluid particles over time (e.g. Wu et al., 2007). This description is called *Lagrangian* or *material description*. However, the atmosphere is composed of about $1.1 \cdot 10^{44}$ molecules[6]. Even when following particels with initial volumes of $1\,\text{cm}^3$, we would need to solve the equations of motion for an inconceivable high number of particles on the order of about 10^{24} without knowing exactly the boundary conditions[7]. Therefore, the Lagrangian description is often inconvenient (Wu et al., 2007, p. 15).
On the other hand, a fluid can be described as a spatial field. The physical properties of the fluid and its temporal behavior can then be evaluated at every point in the field. This is called *Eulerian* or *field description*. Since it is not necessary to know which particle

[6] The number of molecules in the atmosphere can be estimated by the following assumptions: Pressure is defined as force per area and the average atmospheric surface pressure is given by $P_s = 1013\,\text{hPa}$. Assuming that on average the only force acting on the Earth's surfaces is the gravitational force, this gives $P_s = mg_0/A_s$ where $g_0 = 9.81\,\text{m/s}^2$ is the gravitational acceleration and A_s denotes the surface area of the spherical, flat Earth $A_s = 4\pi R_0^2$ with radius $R_0 = 6370\,\text{km}$. The total mass of air m is then $m \approx 5.27 \cdot 10^{18}\,\text{kg}$. With help of the Avogadro constant given the number of molecules per mol ($N_A = 6.022 \cdot 10^{23}/\text{mol}$) and with the molar mass of dry air ($M_{air} = 28.9644\,\text{g/mol}$), we can estimate the total number of molecules in the atmosphere as $N = N_A m/M \approx 1.096 \cdot 10^{44}$.

[7] Under the assumption of contant density and a scaling height of 10 km, a volume of $1\,\text{cm}^3$ would contain about $2 \cdot 10^{19}$ molecules. This leads to a particle number of $5.48 \cdot 10^{24}$.

passes a location in the field at a specific time, the Eulerian description contains less information on the fluid than the Lagrangian description.
Both perspectives - Lagrangian and Eulerian - are connected by the material derivative: For an arbitrary field quantity $\phi = \phi(\mathbf{r}, t)$ depending on space $\mathbf{r}$ and time t, the material time derivative D/Dt following the particle (Lagrangian view) is given by the sum of the local time derivative $\partial/\partial t$ of the quantity at a fixed location of the Eulerian field and its advection $\mathbf{u} \cdot \nabla$ with velocity $\mathbf{u}$

$$\frac{D\phi}{Dt} = \frac{\partial \phi}{\partial t} + \mathbf{u} \cdot \nabla \phi \quad . \tag{2}$$

The question arises what the appropriate description of a vortex might be: On the one hand, we can follow the path of a vortex in a fluid likewise to the Lagrangian description of single particles. This Lagrangian-like property of a vortex is for example applied in the study of extratropical cyclone tracks (see e.g. Blender et al., 1997) where the vortex center is followed in time as if it was a Lagrangian particle. However, the vortex is composed of a large number of material particles. Furthermore, the vortex is also part of the spatial field interacting with the physical properties of the surrounding field. There is no clear boundary such that material can flow in and out of a vortex under certain circumstances, e.g. during intensification or weakening. Before we proceed to investigate the large number of particles that a vortex is composed of, we need to find out how we can visualize rotating or swirling motions of single particles.

2.3 Pathlines, streamlines and streaklines

Pathlines, streamlines and streaklines are useful tools for the visualization of flow fields. One way to visualize the flow field is the observation of *streaklines*. At a time t_0, streaklines visualize the spatial position of all particles that have passed a fixed location $\mathbf{x_0}$ prior to that time t_0. An example of a streakline is the trail of smoke of a chimney or the ash plume of a volcano as visualized by satellite images (see Fig. 2 left) or the inserting of dye into a liquid fluid flow. Although, streaklines are not relevant to this work, they are important e.g. in the study of the transport of chemical tracers and their dependence on the large-scale weather pattern.
Another possibility to visualize the flow field is the analysis of *pathlines*. *Pathlines* - also called trajectories - describe the chronological motion of individual particles (an example is given in Fig. 2 right). They are therefore closely connected to the Lagrangian description of fluid motion. A pathline of a particle located at $\mathbf{X} = (X_1, X_2, X_3)$ at initial time $t = 0$ is described by the ordinary differential equations (Wu et al., 2007, p.16)

$$\frac{dx_i}{dt} = u_i(\mathbf{x}, t) \tag{3}$$

with the initial condition $\mathbf{x}(t = 0) = \mathbf{X}$ and u_i denotes the i-th velocity component

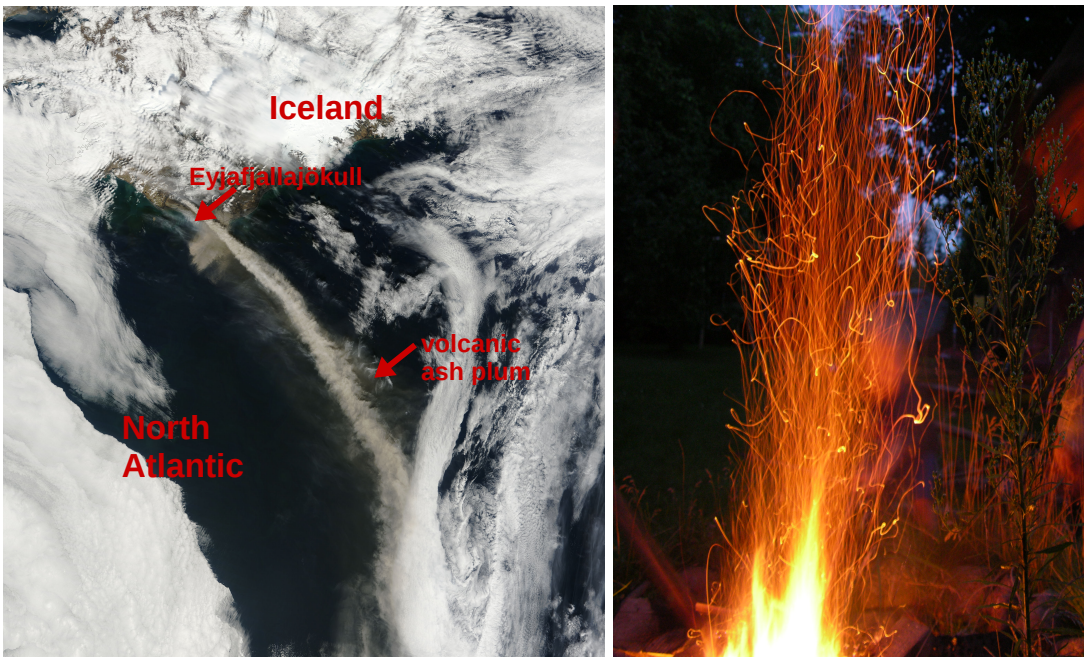

Figure 2: *Examples of streaklines and pathlines in fluid flows: (a) satellite image shows the streakline of Iceland's volcano Eyjafjallajökull emitting ash and steam on 7 May 2010 (NASA image courtesy Jeff Schmaltz, MODIS Rapid Response Team at NASA GSFC; (b) pathlines visualize the laminar and turbulent motions of glut particles from a campfire (image courtesy: Christoph Gatzen).*

($i \in (1,2,3)$). Note, that the pathline is always parallel to the wind field. Single particle trajectories (or pathlines) are a useful tool , in order to identify the origin of particles with the help of backward calculations. With a similar approach Dahl et al. (2014) found that near-ground rotation (vertical vorticity) in a supercell is generated by particles that originate from the outflow of the cell.

On the other hand, *streamlines* give an instantaneous snapshot of the spatial distribution of the flow field (Eulerian description). For fixed time t, a streamline is tangent to the velocity field $\mathbf{u}(\mathbf{x},t)$ described by (Wu et al., 2007, p.16)

$$\frac{dx_1}{u_1(\mathbf{x},t)} = \frac{dx_2}{u_2(\mathbf{x},t)} = \frac{dx_3}{u_3(\mathbf{x},t)} \tag{4}$$

Since both lines are tangential to the velocity, the directions of streamlines and trajectories coincide at every location and every time. However, since the streamline pattern (i.e. the wind field) can change in time, trajectories and streamlines diverge in unsteady flows while they coincide in steady flows where $\mathbf{u}$ is independent of t.

An example of the difference between streamlines and pathlines and their behavior in steady and unsteady flows is given in Figures 3 and 4: Figure 3 shows the geopotential height and horizontal wind fields at the 500 hPa level over Europe and Russia for some time steps between the 9 and 11 July 2010. The summer months of 2010 were

characterized by a stationary blocking weather pattern over Europe and Russia. We picked a quasi-stationary low pressure system located at about 55° N and 80° E in order to visualize the difference between stream- and pathlines. While the flow around the low pressure system is quasi-steady in the beginning (especially at the western bound of the blue box from 9 July 2010 – 00 UTC to 12 UTC), the patterns diverge a fortiori with time (10 July 2010 – 00 UTC to 11 July 2010 00 UTC). This is also mirrored by the corresponding stream- and pathlines in Fig. 4: For the first hours (up to 18 hours for the green trajectory starting in 60° N, 65° E) the stream- and pathlines approximately coincide as long as the wind field stays quasi-stationary in the vicinity of the curves; while the pattern changes, stream- and pathlines diverge (for times along the trajectories larger than 20 hours).
The observation of single particles is helpful in the order to visualize the flow field and detect instantaneous swirling motions with the help of streamlines or identify rotating particles over some timesteps with pathlines. However, since a vortex is composed of many particles that can form material lines, areas or volumes it is necessary to study the change of these shapes over time.

2.4 Change of material lines, areas and volumes over time

We first need to clarify the term *material* line, area and volume: *material* means that the line, area or volume is composed of the same material particles from one time step to another. The rate of change of a straight material line $d\mathbf{x} = \mathbf{x}_1 - \mathbf{x}_0$ is determined by the velocity vectors $\mathbf{u}_1$, $\mathbf{u}_0$ at the ends of the line as can be seen from

$$\frac{D}{Dt}(d\mathbf{x}) = \frac{D\mathbf{x}_1}{Dt} - \frac{D\mathbf{x}_0}{Dt} = \mathbf{u}_1 - \mathbf{u}_0 = d\mathbf{u} \ . \tag{5}$$

For the **rate of change of a material line** $d\mathbf{x}$ of arbitrary shape we can further express eq. (5) as

$$\boxed{\frac{D}{Dt}(d\mathbf{x}) = d\mathbf{u} = d\mathbf{x} \cdot \frac{\partial \mathbf{u}}{\partial \mathbf{x}} = d\mathbf{x} \cdot \nabla \mathbf{u} \ ,} \tag{6}$$

which illustrates that the rate of change of an arbitrary material line is determined by the distribution of the velocity gradient tensor $\nabla \mathbf{u}$ along that line.
The rate of change of a volume element $dv = dxdydz$ follows from the rate of change of

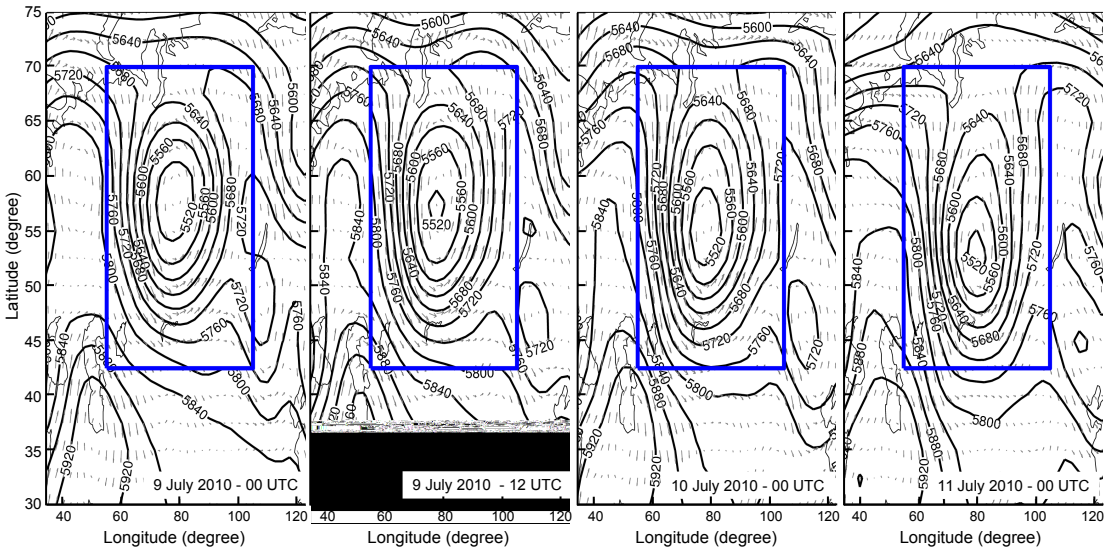

Figure 3: *Geopotential height fields (black contours) and horizontal wind fields (light gray arrows) at the 500 hPa level for some timesteps in the period 9 to 11 July 2010. Data basis is NCEP 2 Reanalysis data. The bold blue box indicates the region that is enlargened in Fig. 4*

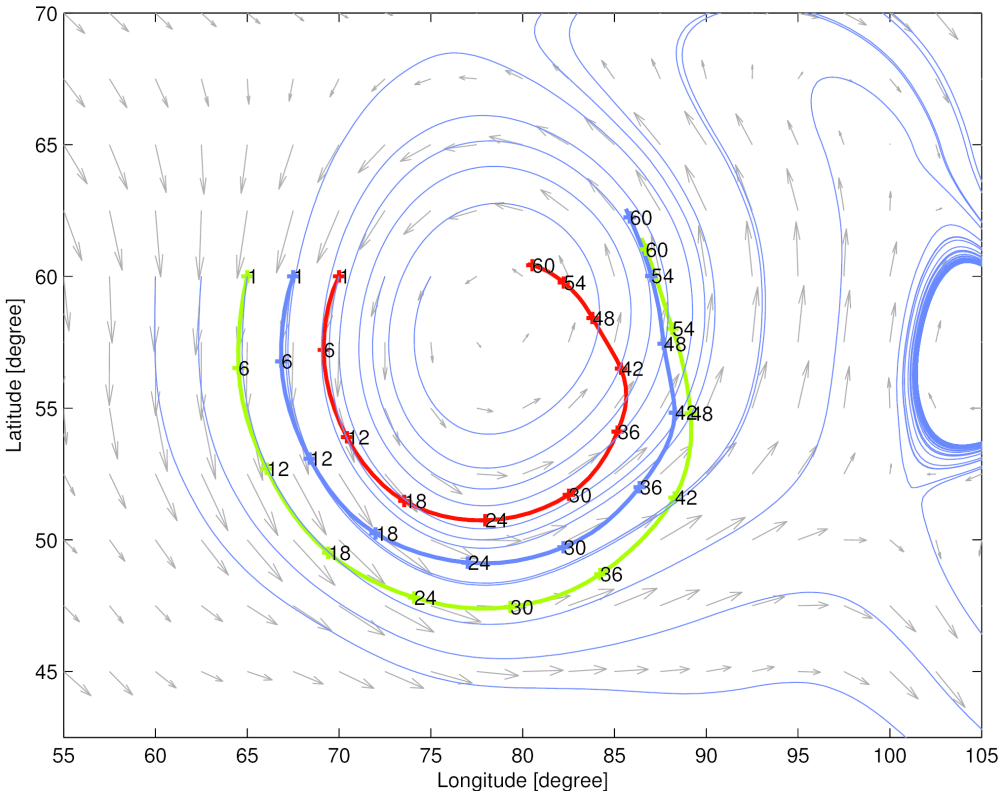

Figure 4: *Wind field (light gray arrows) and corresponding streamlines (thin, blue lines) are calculated from the field on 9 July 2010 – 00 UTC (NCEP 2 Reanalysis data). Three different trajectories are displayed by bold green, red and blue curves. The numbers denote the timesteps in hours of the trajectories.*

line elements (eq. (6)) by applying the product rule

$$\begin{aligned}\frac{D}{Dt}(dv) &= \frac{D}{Dt}(dxdydz)\\ &= dydz\frac{D}{Dt}(dx) + dxdz\frac{D}{Dt}(dy) + dxdy\frac{D}{Dt}(dz)\\ &= dydzdx\frac{\partial u}{\partial x} + dxdzdy\frac{\partial v}{\partial y} + dxdydz\frac{\partial w}{\partial z}\\ &= dxdydz\left(\frac{\partial u}{\partial x} + \frac{\partial v}{\partial y} + \frac{\partial w}{\partial z}\right)\end{aligned}$$

where u, v, w are the components of the velocity vector with $\mathbf{u} = (u, v, w)$ in cartesian coordinates. Finally, we can write for the **rate of change of a material volume element** dv

$$\boxed{\frac{D}{Dt}(dv) = dv\nabla\cdot\mathbf{u}\ .} \tag{7}$$

The rate of change of a volume element is determined by the divergence (dilatation) inside the volume. Positive divergence is connected to an expansion of the volume, while convergence (negative divergence) leads to a shrinking of the volume element. Note, that a volume element might be deformed or rotated as well; however deformation and rotation preserve its size.

To determine the rate of change of a directional material area element $d\mathbf{A} = \mathbf{n}dA$ with vector $\mathbf{n}$ being normal to the surface and $\mathbf{n}\cdot\mathbf{n} = 1$, we can use our knowledge of volume and line elements: Assume a volume element $dv = d\mathbf{x}\cdot d\mathbf{A}$ formed by the directional area element $d\mathbf{A}$ and a directional line element $d\mathbf{x}$ which is not tangent on the area. The the rate of change of the volume element can be written as

$$\frac{D}{Dt}(dv) = \left(\frac{D}{Dt}d\mathbf{x}\right)\cdot d\mathbf{A} + d\mathbf{x}\cdot\left(\frac{D}{Dt}d\mathbf{A}\right)\ . \tag{8}$$

Using equations (6) and (7) gives

$$d\mathbf{x}\cdot d\mathbf{A}\,(\nabla\cdot\mathbf{u}) = d\mathbf{x}\cdot\nabla\mathbf{u}\cdot d\mathbf{A} + d\mathbf{x}\cdot\left(\frac{D}{Dt}d\mathbf{A}\right)\ . \tag{9}$$

Since $d\mathbf{x}$ was chosen arbitrarily, we obtain the **rate of change of an material area element** $d\mathbf{A}$ as

$$\boxed{\frac{D}{Dt}\,(d\mathbf{A}) = [(\nabla\cdot\mathbf{u})\,\mathbf{I} - \nabla\mathbf{u}]\cdot d\mathbf{A}} \tag{10}$$

where $\mathbf{I}$ is the unit tensor. We will see later in chapter 2.6 that $\nabla\mathbf{u}$ can be decomposed into the sum of the symmetric strain-rate tensor and the vorticity tensor and that the rate of change of an areal element is determined by three fundamental processes - deformation, dilatation and rotation - that characterize completely the kinematics of a

flow field. As a further step we might be interested how integral material shapes change over time. For example if we are interested how a certain property that is contained in a vortex volume such as humidity is transported over time or how a frontal boundary changes over time.

2.5 Time-dependent rate of change of material integrals

For calculations of the time-dependent rate of change of a physical quantity F bounded by a material line, area or volume element, we need to take into account both: the rate of change of the material element as well as the rate of change of the physical quantity. Following Wu et al. (2007), we denote F as a physical quantity given by a tensor of arbitrary rank and $\circ$ as a meaningful tensor product. Then the rate of change of a material integral along a line element C using equation (6) is given by (Wu et al., 2007)

$$\frac{d}{dt}\int_C d\mathbf{x}\circ F = \int_C \left(\frac{Dd\mathbf{x}}{Dt}\circ F + d\mathbf{x}\circ\frac{DF}{Dt}\right) \tag{11a}$$

$$= \int_C \left(d\mathbf{x}\cdot\nabla\mathbf{u}\circ F + d\mathbf{x}\circ\frac{DF}{Dt}\right) . \tag{11b}$$

The rate of change of a material integral over a surface A follows similarly with help of equation (10)

$$\frac{d}{dt}\int_A d\mathbf{A}\circ F = \int_A \left(\frac{Dd\mathbf{A}}{Dt}\circ F + d\mathbf{A}\circ\frac{DF}{Dt}\right) \tag{12}$$

$$= \int_A \left(d\mathbf{A}\cdot\left[(\nabla\cdot\mathbf{u})\,\mathbf{I} - (\nabla\mathbf{u})^T\right]\circ F + d\mathbf{A}\circ\frac{DF}{Dt}\right) . \tag{13}$$

Finally, the rate of change of an integral over a material volume using equation (7) can be expressed as

$$\frac{d}{dt}\int_V dvF = \int_V \left(\frac{Ddv}{Dt}F + dv\frac{DF}{Dt}\right) \tag{14}$$

$$= \int_V \left(dvF\nabla\cdot\mathbf{u} + dv\frac{DF}{Dt}\right) \tag{15}$$

This last integral is the basis for the derivation of the fundamental equations that determine the atmospheric flows. These fundamental laws stem from the conservation of mass (continuity equation), from the conservation of momentum (equation of motion) and from the conservation of energy (first law of thermodynamics). The laws are derived from equation (15) for different parameters F: for example, the continuity equation is derived by setting $F = \rho$.

For the temporal changes of material line and area integrals we have seen that the

velocity gradient tensor $\nabla\mathbf{u}$ plays an important role and in case of the temporal changes of a volume integral the divergence of the wind field — which is an invariant of the velocity gradient tensor — is involved. This tensor can be used in order to describe the fluid motion around a point as will be shown in the next section.

2.6 Velocity gradient tensor $\nabla\mathbf{u}$ and its decomposition[8]

Knowledge of the velocity $\mathbf{u}$ and the corresponding velocity gradient tensor $\nabla\mathbf{u}$ at a point gives information about the structure of the flow field surrounding that point. This can be seen by applying a Taylor series expansion to the velocity in the environment of that point: Let $\mathbf{u}(\mathbf{r}_0, t)$ be the velocity at position $\mathbf{r}_0$ and time t. The velocity $\mathbf{u}(\mathbf{r}_0 + \mathbf{r}, t)$ in the environment located at $\mathbf{r}_0 + \mathbf{r}$ can then be approximated by a first-order Taylor series expansion (e.g. Fortak, 1967; Batchelor, 2000):

$$\mathbf{u}(\mathbf{r}_0 + \mathbf{r}, t) = \mathbf{u}(\mathbf{r}_0, t) + \mathbf{r} \cdot \nabla\mathbf{u}(\mathbf{r}_0, t) \ . \tag{16}$$

that results in the sum of a uniform translation ($\mathbf{u}(\mathbf{r}_0, t)$) and a second term that depends on the velocity gradient tensor $\nabla\mathbf{u}$. This velocity gradient tensor $\nabla\mathbf{u}$ can be decomposed into the sum of a symmetric tensor $\mathbf{S}$ and an antisymmetric tensor $\mathbf{\Omega}$

$$\nabla\mathbf{u} = \mathbf{S} + \mathbf{\Omega} \ , \tag{17}$$

with

$$\mathbf{S} = 1/2(\nabla\mathbf{u} + (\nabla\mathbf{u})^T) \quad : \quad \text{rate-of-strain tensor} \tag{18}$$

$$\mathbf{\Omega} = 1/2(\nabla\mathbf{u} - (\nabla\mathbf{u})^T) \quad : \quad \text{vorticity tensor} \tag{19}$$

Here, the superscript T stands for transpose. While the symmetric rate-of-strain tensor $\mathbf{S}$ describes the deformations in the flow field, the antisymmetric vorticity tensor $\mathbf{\Omega}$ is connected to the volume-preserving rotation of the fluid. Both tensors can be used to calculate invariants of the velocity gradient tensor. These invariants have the advantage that they do not change under coordinate transformations such as rotations or translations of the coordinate system.

We know from (6) that the velocity gradient tensor determines the changes of a material line element over time. In order to study the different contributions of the rotation and the strain-rate tensor, equation (6) will be applied to the small line element $\mathbf{r}$ that was introduced to study the velocity in the vicinity of position $\mathbf{r}_0$. Using (17), it becomes

[8] This section 2.6 as well as sections 2.7 and 6.3 are based on/taken from a chapter of a recent publication (Schielicke et al., 2016, chapter 2) which is published as an Open Access article distributed under the terms of the Creative Commons Attribution 4.0 International License (http://creativecommons.org/licenses/by/4.0/. Note, the chapter in this thesis is much more detailed than in the publication even though some text passages are identical.

obvious that the line element can either be deformed or rotated

$$\frac{D}{Dt}(\mathbf{r}) = \mathbf{r} \cdot \nabla \mathbf{u}(\mathbf{r}_0, t) = \underbrace{\mathbf{r} \cdot \boldsymbol{S}}_{Deformation} + \underbrace{\mathbf{r} \cdot \boldsymbol{\Omega}}_{Rotation} \tag{20}$$

Note that this describes the second term on the right-hand side of (16). The contributions and physical interpretations of the rotation tensor and the strain-rate tensor are discussed in more detail in the following two sections.

2.6.1 The vorticity tensor Ω in 3d

In 3d, any antisymmetric tensor has only three independent components. These independent components form a vector. In case of the vorticity tensor $\boldsymbol{\Omega}$, its components are given by the vector components of the vorticity vector $\boldsymbol{\omega} = \nabla \times \mathbf{u}$. The vorticity tensor can be expressed as[9] (Fortak, 1967)

$$\boldsymbol{\Omega} = -\frac{1}{2}\boldsymbol{I} \times \boldsymbol{\omega} \tag{21}$$

where $\boldsymbol{I}$ is the unit tensor. The vorticity vector can be interpreted as one half of the angular velocity vector. This can be clarified by some considerations[10]: The velocity of a rotating rigid body is equal to

$$\mathbf{u} = \mathbf{w} \times \mathbf{r} \tag{22}$$

where $\mathbf{w}$ is the angular velocity which is constant for a rigid body ($\mathbf{w} = const.$) and $\mathbf{r}$ denotes the distance from the rotational axis. Taking the curl of $\mathbf{u}$ leads to[11]

$$\nabla \times \mathbf{u} = \nabla \times (\mathbf{w} \times \mathbf{r}) = 2\mathbf{w} \; . \tag{23}$$

On the other hand, the vorticity vector is defined as the curl of the velocity ($\boldsymbol{\omega} = \nabla \times \mathbf{u}$). Therefore, the angular velocity $\mathbf{w}$ of a rigid body is equal to one half of the vorticity $\boldsymbol{\omega}$

$$\mathbf{w} = \frac{1}{2}\boldsymbol{\omega} \; . \tag{24}$$

In the case of non-rigid motion, the curl is not constant anymore. However, at every single point, the local vorticity can be interpreted as twice the angular momentum of a small element of the continuum surrounding the point (Truesdell, 1954). The element behaves like a rigid body – at least instantaneous and locally – when it is observed from a reference frame with respect to the principal axes of the strain-rate tensor (Wu et al., 2007). More specific, the relative locations of the principal axes of the strain-rate

[9] This can easily be derived by explicitely calculating expression (19) and comparing it to the components of $\boldsymbol{\omega}$.

[10] These considerations follow the way it is presented in Truesdell (1954), who dedicated this interpretation of vorticity to Stokes (cf. Truesdell, 1954, §32).

[11] Explicitely: $\nabla \times \mathbf{u} = \nabla \times (\mathbf{w} \times \mathbf{r}) = \nabla \cdot (\mathbf{r}\mathbf{w} - \mathbf{w}\mathbf{r}) = \underbrace{(\nabla \cdot \mathbf{r})}_{=3}\mathbf{w} + \mathbf{r} \cdot \underbrace{\nabla \mathbf{w}}_{=0} - \underbrace{(\nabla \cdot \mathbf{w})}_{=0}\mathbf{r} - \underbrace{\mathbf{w} \cdot \nabla \mathbf{r}}_{\mathbf{w} \cdot \mathbf{I} = \mathbf{w}} = 2\mathbf{w}$

tensor are instantaneously fixed to each other, i.e. they do not rotate with respect to one another and therefore the motion along these axes is rigid (Truesdell, 1954); we will clarify this in the next section 2.6.2. Therefore, Wu et al. (2007) (cf. chapter 3.1) states that "*it is more precise to interpret the vorticity* $\boldsymbol{\omega}(\mathbf{x})$ *as twice the angular velocity of the instantaneous principal axes of the strain-rate tensor of an fluid element centered at* $\mathbf{x}$". More interpretations of vorticity can be found in Truesdell (1954, §29-§34).
It is now possible to interpret the role of the rotation tensor for the rate of change of a material line element: Plugging expression (21) into (20) gives

$$\frac{D}{Dt}(\mathbf{r}) = \mathbf{r} \cdot \boldsymbol{S} + \frac{1}{2}\boldsymbol{\omega} \times \mathbf{r} \quad . \tag{25}$$

Thus, the second term on the right-hand side only changes the direction of the line element with angular velocity $\boldsymbol{\omega}/2$, but not its length. The rotational share in flow motion does not change the relative locations of particles in the vicinity of point $\mathbf{x}$. These can only be change by the strain-rate tensor $\mathbf{S}$.

2.6.2 The strain-rate tensor S in 3d

Calculation of (25) $\cdot\, \mathbf{r}$ shows that the magnitude of the change of a material line element is determined by the strain-rate tensor alone (Wu et al., 2007):

$$\left(\frac{D}{Dt}\mathbf{r}\right) \cdot \mathbf{r} = \frac{1}{2}\frac{D}{Dt}dl^2 = \mathbf{r} \cdot \mathbf{S} \cdot \mathbf{r} + \underbrace{\frac{1}{2}(\boldsymbol{\omega} \times \mathbf{r}) \cdot \mathbf{r}}_{=0} \tag{26}$$

where $l = \|\mathbf{r}\|$ is the length of the line element. The second term is equal to zero because the scalar triple product of two identical (or parallel) vectors vanishes. For a rigid body, the relative locations of elements along the line does not change and therefore the strain-rate tensor must be zero ($\mathbf{S} = 0$ for rigid bodies). In general, the strain-rate tensor can be decomposed into an isotropic part and a nonisotropic part called the deviator $\mathbf{S}'$ of the strain-rate tensor $\mathbf{S}$ where (Wu et al., 2007)

$$\mathbf{S}' = \mathbf{S} - \underbrace{\frac{1}{3}(\nabla \cdot \mathbf{u})\mathbf{I}}_{\text{isotropic}} \qquad \text{with } tr(\mathbf{S}') = 0 \tag{27}$$

where $\mathbf{I}$ is the unit tensor and the trace of the deviator is zero ($tr(\mathbf{S}') = 0$). The strain-rate tensor is a symmetric tensor. Every symmetric tensor can be brought into a diagonal form, i.e. a form in which all minor elements are zero with exception of the principal diagonal. In order to calculate the eigenvalues $(\lambda_1, \lambda_2, \lambda_3)$, the eigenvalue equation $S_{ij} - \lambda\delta_{ij} = 0$ needs to be solved. This leads to the characteristic third-order equation of the eigenvalues (see e.g. Wu et al., 2007, chapter 2.1.2)

$$\lambda^3 - I\lambda^2 + II\lambda - III = 0 \; . \tag{28}$$

where I, II, III denote the three basic invariants of the strain-rate tensor (Wu et al., 2007). The eigenvalues are real because $\mathbf{S}$ is symmetric. Furthermore, the eigenvalues are associated with three principal directions $(\mathbf{p}_1, \mathbf{p}_2, \mathbf{p}_3)$ that build an orthogonal local Cartesian coordinate system (called principle-axis system by Wu et al., 2007).
Furthermore, for a spherical element of the continuum with radius $\mathbf{r}$ and $|\mathbf{r}| \ll 1$, the term $\mathbf{r} \cdot \mathbf{S} \cdot \mathbf{r}$ in equation (26) represents a quadratic form of variable $\mathbf{r}$ since $\mathbf{S}$ is symmetric. The quadratic form is a way to transform a symmetric tensor to its principle axis. Following Wu et al. (2007), we write

$$2\varphi = \mathbf{r} \cdot \mathbf{S} \cdot \mathbf{r} \tag{29}$$

where φ represents a whole set of quadratic surfaces called the deformation ellipsoids (see Wu et al., 2007, chapter 2.1.2). The gradient of φ is equal to the part of the relative motion around a point that is contributed by the deformation in the flow[12]

$$\nabla\varphi = \mathbf{r} \cdot \mathbf{S} \; . \tag{30}$$

Finally, we can rewrite the local motion at a point $\mathbf{r}_0 + \mathbf{r}$ (see 16) with help of (21) and (30) as

$$\mathbf{u}(\mathbf{r}_0 + \mathbf{r}, t) = \underbrace{\mathbf{u}(\mathbf{r}_0, t)}_{Ttranslation} + \underbrace{\nabla\varphi}_{Deformation} + \underbrace{\frac{1}{2}\boldsymbol{\omega} \times \mathbf{r}}_{Rotation} \; . \tag{31}$$

This is a fundamental decomposition of the flow field around a point which is equal to the superposition of a uniform translational motion, a nonrotational contribution of deformation (which can be written as a potential) and a contribution due to rotation. E.g. Wu et al. (2007, chapter 2.1.2) states: "*The instantaneous state of the fluid motion at every point is the superposition of a uniform translation, an irrotational stretching and shrinking along three orthogonal principal axes, and a rigid rotation around an axis*". Another famous decomposition of the fluid flow is the Helmholtz-Hodge decomposition that is given as the sum of an irrotational part and an divergence-free part (for more details see chapter 3.4.4). In the next section, we will explicitly study this decomposition for two-dimensional flows.

2.7 Kinematics of a 2D flow field[13]

Let u, v be the horizontal components of the horizontal velocity $\mathbf{v}$. In a 2D flow, the velocity gradient tensor in cartesian coordinates is given by :

[12] This can be seen by calculating explicitly (e.g. in components) equation (29) and calculating the gradient of (29) as $\nabla\varphi = \partial\varphi/\partial\mathbf{r}$ under the assumption of constant $\mathbf{S}$ at the location of interest.

[13] This section 2.7 as well as sections 2.6 and 6.3 are based on/taken from a chapter of a recent publication (Schielicke et al., 2016, chapter 2). Note, the chapter in this thesis is much more detailed than in the publication even though some text passages are identical.

$$\nabla \mathbf{v} = \begin{pmatrix} u_x & v_x \\ u_y & v_y \end{pmatrix} . \tag{32}$$

where the subscripts stand for partial differentiation with respect to x, y. The rate-of-strain tensor $\mathbf{S}$ in two dimensions is given by

$$\mathbf{S} = \frac{1}{2} \begin{pmatrix} 2u_x & u_y + v_x \\ u_y + v_x & 2v_y \end{pmatrix} , \tag{33}$$

which can be further decomposed into

$$\mathbf{S} = \frac{1}{2} \begin{pmatrix} \mathrm{D}_h & 0 \\ 0 & \mathrm{D}_h \end{pmatrix} + \frac{1}{2} \begin{pmatrix} \mathrm{Def} & \mathrm{Def}' \\ \mathrm{Def}' & -\mathrm{Def} \end{pmatrix} . \tag{34}$$

with

$$\begin{aligned} \mathrm{D}_h &= u_x + v_y && : \text{horizontal divergence} \\ \mathrm{Def} &= u_x - v_y && : \text{stretching deformation} \\ \mathrm{Def}' &= u_y + v_x && : \text{shearing deformation} \end{aligned} \tag{35}$$

The first tensor on the right-hand-side of equation (34) describes an isotropic expansion[14] (which is zero in case of an incompressible fluid) while the second tensor describes a straining motion without changing the size (area, volume) of a fluid particle although its shape can change (Batchelor, 2000). This second tensor of equation (34) is composed of the shearing and stretching deformation (Fortak, 1967). Local motions due to deformation are summarized in Figure 5. The local strain rate is calculated by the Euclidean tensor norm[15] of the rate-of-strain tensor

$$\|\mathbf{S}\| = \sqrt{\mathbf{S} \cdot \cdot \mathbf{S}^T} = \sqrt{S_{ij} S_{ji}} = \frac{1}{\sqrt{2}} \sqrt{\mathrm{D}_h^2 + \mathrm{Def}^2 + \mathrm{Def}'^2} . \tag{36}$$

Here, the operation $\cdot\cdot$ represents the double inner product of tensors. Note, while the divergence is an invariant of $\nabla \mathbf{v}$, only the sum of the squares of shearing and stretching deformation is invariant. The local strain rate is a measure for the local absolute value of the strain contributed by all deformations including divergence, shearing and stretching deformation.

[14] The isotropic expansion in a 2D flow equals a change of the area in the coordinate directions with a rate of one half of the total divergence.

[15] The Euclidean norm of a tensor A is also written as $\|A\| = \sqrt{Tr(AA^T)}$ (e.g. Kunnen et al., 2010)

The vorticity tensor $\mathbf{\Omega}$ in 2D is given by

$$\mathbf{\Omega} = \frac{1}{2}\begin{pmatrix} 0 & -\zeta \\ \zeta & 0 \end{pmatrix} \text{ with } \zeta = v_x - u_y \, . \tag{37}$$

$\zeta = \mathbf{k} \cdot \nabla \times \mathbf{v}$ is the vertical component of the vorticity vector. $\mathbf{\Omega}$ describes a pure rotation (rigid-body rotation) of a fluid particle around a given point without a change of its area (see Figure 5). The Euclidean tensor norm of the vorticity tensor describes the local rate of rigid-body rotation and is given by

$$\|\mathbf{\Omega}\| = \sqrt{\mathbf{\Omega} \cdot \cdot \mathbf{\Omega}^T} = \sqrt{-\Omega_{ij}\Omega_{ji}} = \frac{1}{\sqrt{2}}\sqrt{\zeta^2} \, . \tag{38}$$

In conclusion, the local motion around a point can be decomposed into symmetric straining and antisymmetric rotational motions as shown in Figure 5. Together with the translational motion $\mathbf{v}(\mathbf{r}_0, t)$ in (16), this gives a complete description of the local flow field, at least up to the first order of the Taylor series expansion in (16).

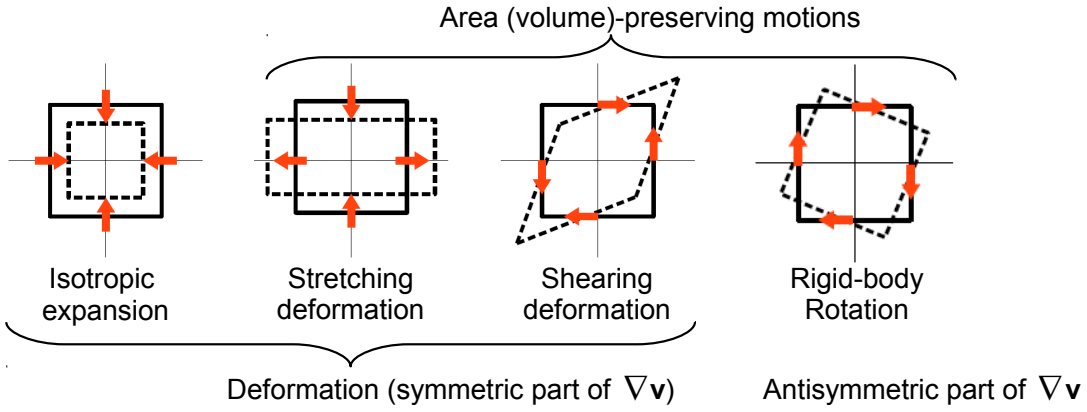

Figure 5: *Decomposition of the local motion in two dimensional flow. Vectors show the direction of the flow field. This decomposition is complete to the linear order of the Taylor series expansion in equation (16). Figure is originally published in Schielicke et al. (2016) (their Figure 1).*

2.8 Final remarks on kinematics

Kinematics give considerable insight into the behavior and characteristics of the flow. A lot of tools that were introduced in this section will serve in the following chapters in order to study the vortex properties. We will see, that methods based on kinematics will be very useful in this respect. However, in order to understand physical mechanisms of the vortex behaviur (e.g. the interactions of vortices or the genesis and lysis of vortices) and the difference between vortices on different scales, we additionally need to take a look at the dynamics of vortices in order to get a complete view on vortices.

3 Dynamics: Scale-dependency, vortex intensity and interactions

A main aim of this thesis is the scale-dependent investigation of vortices. Therefore, it is necessary to study the dynamic equations in order to find similarities and differences over the scales. Moreover, vortex dynamics allows us to study the interactions between vortices and the influence of vortices on their surroundings. Hence, it is an essential topic in the study of vortices.

3.1 Governing equations

Fluid flow can be describe by a set of equations called the primitive equations. They follow from mass conservation (continuity equation), momentum balance (equations of motion or Navier-Stokes equations) and from the conservation of internal energy (first law of thermodynamics). In fact, these equations are derived from calculating the temporal derivatives of the integrals of material volumes introduced in chapter 2.4. Explicitly, the set of primitive equations in a rotating reference frame read

$$\frac{D\rho}{Dt} = -\rho\nabla\cdot\mathbf{u} \qquad \text{Continuity equation} \tag{39a}$$

$$\frac{D\mathbf{u}}{Dt} = -2\boldsymbol{\Omega}_E\times\mathbf{u} - \frac{1}{\rho}\nabla p + \mathbf{g} - \nabla\Phi_z + \mathbf{F}_R \qquad \text{Navier}-\text{Stokes equation} \tag{39b}$$

$$\frac{De}{Dt} = -p\frac{D\alpha}{Dt} + J \qquad \text{First law of thermodynamics} \tag{39c}$$

where the variables are:

ρ:	Density
$\mathbf{u}$:	Velocity vector ($\mathbf{u} = (u, v, w)$)
$\boldsymbol{\Omega}_E$:	Rotation rate of the Earth
p:	Pressure
Φ_z:	Centrifugal potential
$\mathbf{g}$:	Acceleration of gravity
$\mathbf{F}_R$:	Frictional acceleration term
e:	Internal energy
α:	Specific volume ($\alpha = \rho^{-1}$)
J:	Specific heating rate

The mass-specific internal energy e can be described by the caloric equation of state: $e = e(T) = c_v T$ where T is the temperature and c_v is the specific heat at constant volume with $c_v = 717\,\mathrm{J/(kgK)}$ for dry air. This equation states that the internal energy depends only on temperature T.
Furthermore, the equation of state reads

$$p = \rho R T \tag{40}$$

where R is the gas constant ($R = 287$ J/(kgK) for dry air). In a dry, adiabatic and inviscid atmosphere, the primitive equations (39) together with the equation of state (40) constitute a complete closed set of equations. Some comments on the equations will be given in the next sections starting with the continuity equation and the first law of thermodynamics. Furthermore, the equations of motion (Navier-Stokes equations) will be presented and compared for two reference frames – a non-rotating, absolute reference frame and a rotating, noninertial reference frame which is a useful reference frame for studying the motion of the atmosphere on a rotating planet.

3.1.1 Continuity equation

The continuity equation follows from mass conservation (e.g. in Batchelor, 2000, chapter 2.2). For a given mass of fluid, the continuity equation is given by

$$\frac{\partial \rho}{\partial t} + \nabla \cdot (\rho \mathbf{u}) = 0\ . \tag{41}$$

This can also be written as

$$\frac{1}{\rho}\frac{D\rho}{Dt} = -\nabla \cdot \mathbf{u} \tag{42}$$

which can be interpreted as follows: the individual change of density of a fluid particle over time requires non-zero divergence or convergence. For an incompressible fluid, the density is constant. Hence, the continuity equation simplifies to

$$\nabla \cdot \mathbf{u} = 0 \quad \text{for incompressible flow}\ . \tag{43}$$

A scale analysis for horizontal large scale motions in the atmosphere shows, that the individual density changes are one order in magnitude smaller than the three divergence terms ($\nabla \cdot \mathbf{u} = \partial_x u_x + \partial_y u_y + \partial_z u_z$). Therefore, purely horizontal synoptic-scale flow behaves like an incompressible fluid. However, for vertical motions, compressibility due to density changes with height needs to be taken into account (Holton, 2004, chapter 2.5.3).

3.1.2 First law of thermodynamics

The first law of thermodynamics states that the internal energy e changes as the sum of heat added to and the work done by the system. The (mass-specific) internal energy e is related to temperature T as $e = c_v T$ with specific heat at constant volume c_v ($c_v = 717$ J/(kgK) for dry air). The first law of thermodynamics can be written as (e.g. Holton, 2004)

$$c_v \frac{DT}{Dt} = -p\frac{D\alpha}{Dt} + J \tag{44}$$

where $\alpha = \rho^{-1}$ denotes the mass-specific volume and $pD\alpha/Dt$ describes the work done to/by the volume. J is the rate of heating that is given by diabatic sources like e.g. radiation, conduction and latent heat release. Equation (44) represents the *thermodynamic energy equation*. It can also be expressed with help of enthalpy h

$$h = e + p\alpha \quad \text{with } h = c_p T \ . \tag{45}$$

as

$$c_p \frac{DT}{Dt} = \alpha\frac{Dp}{Dt} + J \ . \tag{46}$$

Here, c_p denotes the specific heat at constant pressure ($c_p = R + c_v = 1004$ J/(kgK) with ideal gas constant $R = 287$ J/(kgK) for dry air). Additionally, this equation can be brought into a form with respect to entropy s where entropy changes and specific heating rate are related as $Ds/Dt := J/T$. Then we have (Holton, 2004, chapter 2.7)[16]

$$\frac{Ds}{Dt} := \frac{J}{T} = c_p\frac{D\ln T}{Dt} - R\frac{D\ln p}{Dt} \tag{47}$$

where we used the thermodynamic equation of state (40) in order to substitute the specific volume $\alpha = \rho^{-1}$. This equation can further be expressed in terms of potential temperature. The potential temperature θ is defined as

$$\theta = T\left(\frac{p_s}{p}\right)^{R/c_p} \ . \tag{48}$$

where θ is the temperature a parcel of dry air (characterized by pressure p and temperature T) takes when it is brought adiabatically to a standard pressure p_s (usually p_s =1000 hPa). Thereby, an adiabatic process is a process that occurs without an exchange of heat with the surroundings. Calculating the logarithm of (48) and multiplying c_p leads to

$$c_p \ln\theta - R\ln p_s = c_p \ln T - R\ln p \ , \tag{49}$$

[16] Note, $D\ln T/Dt = T^{-1}DT/Dt$ and $D\ln p/Dt = p^{-1}Dp/Dt$

and its temporal derivative is

$$c_p \frac{D \ln \theta}{Dt} = c_p \frac{D \ln T}{Dt} - R \frac{D \ln p}{Dt} \ . \tag{50}$$

Note, $p_s = const.$ and therefore $Dp_s/Dt = 0$. Comparing (50) with equation (47) gives the first law of thermodynamics with respect to θ:

$$\frac{Ds}{Dt} = \frac{J}{T} = c_p \frac{D \ln \theta}{Dt} \ . \tag{51}$$

If no heat is exchanged with the environment ($J = 0$), i.e. in case of an *adiabatic process*, the first law of thermodynamics simplifies to

$$\frac{D\theta}{Dt} = 0 \ . \tag{52}$$

and θ becomes a conserved quantity. Holton (2004, chapter 2.7.1) states that the adiabatic assumption is a reasonable assumption for synoptic-scale motions in dry regions and θ is a "quasi-conserved quantity for such motions".

3.1.3 Equations of motion in a non-rotating reference frame

The equations of motion describe the relation between the acceleration of a fluid particle and the sum of all forces that act on that fluid particle (Newton's second law of motion). The equations of motion follow from the momentum balance. It is given by (slightly modified after Batchelor, 2000, chapter 3.2)

$$\rho \frac{D_a \mathbf{u}_a}{Dt} = \rho \mathbf{f} + \nabla \cdot \mathbf{T} \tag{53}$$

with

$$\mathbf{T} = -p\mathbf{I} + \mathbf{F}_{N.S.} \ . \tag{54}$$

The index a indicates that the acceleration is observed in an inertial (absolute) reference frame fixed in space. The term $\rho\mathbf{f}$ represents all volume forces (e.g. often $\mathbf{f}$ is only the gravitational acceleration $\mathbf{g}$); $\mathbf{T}$ is the stress tensor, $\mathbf{I}$ is the unit tensor and $\mathbf{F}_{N.S.}$ denotes the Navier-Stokes tensor with $\mathbf{F}_R = \rho^{-1} \nabla \cdot \mathbf{F}_{N.S.}$. The diagonal elements of $\mathbf{T}$ are normal stresses (equal to the pressure), the non-diagonal elements are the shearing stresses. Explicitly, the equation can be written in a more familiar way as

$$\frac{D_a \mathbf{u}_a}{Dt} = \mathbf{g} - \frac{1}{\rho} \nabla p + \mathbf{F}_R \tag{55}$$

where we have set $\mathbf{f} = \mathbf{g}$.

3.1.4 Equations of motion in a rotating reference frame

3.1.4.1 Inertial and noninertial reference frames

In atmospheric dynamics usually a *geocentric* reference frame is used (Holton, 2004). Such a geocentric reference frame is at rest with respect to the rotating earth. After Newton's first law of motion, an object in uniform motion (or at rest) with respect to a fixed coordinate system stays in uniform motion when no forces act on the object. Therefore, this motion is called *inertial motion* and the fixed reference frame is called *inertial* or *absolute reference frame* (Holton, 2004). However for an observer on the rotating earth, an object of uniform motion (or at rest) relative to the rotating reference frame is not in uniform motion with respect to an inertial reference frame. In fact, this motion is accelerated and therefore a geocentric reference frame is referred to as *noninertial reference frame*. The effects of acceleration are included by the introduction of apparent forces. For a reference frame in uniform rotation ($\boldsymbol{\Omega} = const.$) two apparent forces enter the equations: the Coriolis force and the centrifugal force (Holton, 2004). For a reference frame of general motion (translational acceleration as well as nonuniform rotation), additional apparent forces appear (for details see Batchelor, 2000, chapter 3.2).

3.1.4.2 Transformation from a non-rotating, inertial to a rotating, noninertial reference frame

In a rotating[17] reference frame an arbitrary vector $\mathbf{X}$ can be written as

$$\mathbf{X} = X_1\boldsymbol{i} + X_2\boldsymbol{j} + X_3\boldsymbol{k} = X_i\boldsymbol{e}_i \tag{56}$$

where $\mathbf{i}, \mathbf{j}, \mathbf{k}$ denote orthogonal unit vectors fixed to the rotating reference frame (Batchelor, 2000). On the right hand side Einstein's summation convention was used and $\mathbf{e}_i$ stands for the unit vectors. The total time derivative of $\mathbf{X}$ when observed from an inertial, absolute reference frame denoted by index a is then equal to the sum of the total time derivative of $\mathbf{X}$ relative to the rotating reference frame denoted by index r and the rotation of the coordinate axes (see Batchelor, 2000, chapter 3.2)

$$\frac{D_a\mathbf{X}}{Dt} = \mathbf{e}_i\frac{DX_i}{Dt} + X_i\frac{D\boldsymbol{e}_i}{Dt} \tag{57a}$$

$$= \frac{D_r\mathbf{X}}{Dt} + \boldsymbol{\Omega}_E \times \mathbf{X} \tag{57b}$$

where $\boldsymbol{\Omega}_E$ is the angular velocity of the rotating reference frame. In short, the operator to transform a vector from the inertial to the rotating reference frame reads

$$\frac{D_a}{Dt} = \frac{D_r}{Dt} + \boldsymbol{\Omega}_E\times \tag{58}$$

[17] or any type of general moving

Applying this operator (58) to the position vector $\mathbf{r}$ of an air parcel gives

$$\frac{D_a\mathbf{r}}{Dt} = \frac{D_r\mathbf{r}}{Dt} + \mathbf{\Omega}_E \times \mathbf{r} \ . \tag{59}$$

Denoting $D_a\mathbf{r}/Dt = \mathbf{u}_a$ the velocity of the air parcel with respect to the inertial reference frame and $D_r\mathbf{r}/Dt = \mathbf{u}_r$ the velocity in the noninertial reference frame, respectively, the equation can be expressed as

$$\mathbf{u}_a = \mathbf{u}_r + \mathbf{\Omega}_E \times \mathbf{r} \ . \tag{60}$$

The acceleration is obtained by applying operator (58) to (60):

$$\frac{D_a\mathbf{u}_a}{Dt} = \frac{D_r\mathbf{u}_a}{Dt} + \mathbf{\Omega}_E \times \mathbf{u}_a \ . \tag{61}$$

After substituting (60) on the right hand side, we derive

$$\frac{D_a\mathbf{u}_a}{Dt} = \frac{D_r\mathbf{u}_r}{Dt} + \frac{D_r\mathbf{\Omega}_E}{Dt} \times \mathbf{r} + 2\mathbf{\Omega}_E \times \mathbf{u}_r + \underbrace{\mathbf{\Omega}_E \times (\mathbf{\Omega}_E \times \mathbf{r})}_{-\nabla\Phi_z} \ . \tag{62}$$

The term on the left-hand side is the acceleration in the inertial, absolute reference frame and the first term on the right-hand side is the acceleration in the noninertial, relative reference frame. Under the assumption of a constant angular velocity[18] $\mathbf{\Omega}_E = const$, the second term on the right in (62) vanishes ($D_r\mathbf{\Omega}_E/dt = 0$). The third term is the Coriolis acceleration due to relative motion in the nonintertial reference frame and the fourth term is the centrifugal acceleration due to rotation of the coordinates. In the following we will drop the indices "r" and "a".

3.1.4.3 Transforming the equations of motion

Returning to the equation of motion in form of (53), the sum of forces acting on a fluid can be divided in volume and surface forces. In the atmosphere, the volume forces are represented by the pressure gradient force and by Earth's gravitation and the surface forces are caused by friction. Using (62), the equations of motion in the noninertial, rotating reference frame can be written as (following Holton, 2004, chapter 2.2)

$$\frac{D\mathbf{u}}{Dt} = -2\mathbf{\Omega}_E \times \mathbf{u} - \frac{1}{\rho}\nabla p + \mathbf{g} - \nabla\Phi_z + \mathbf{F}_R \quad \text{, noninertial, rotating} \tag{63}$$

These equations are also referred to as *Navier-Stokes equations* and this is the form given as (39b) in the beginning of this chapter 3.1. Here, the index r that previously indicated the relative reference frame has been dropped. Usually, the centrifugal acceleration

[18] The angular velocity of earth indeed changes over time for example due to gravitational interactions with the moon and sun, due to mass redistributions affecting the moment of inertia (see e.g. Schuh et al., 2003, chapter 2.3). However, these changes are quite small: e.g. the length of day varies in the order of 10^{-8} (see e.g. Lambeck, 2005, chapter 5.1.1). For convenience, the angular velocity of earth is assumed to be constant in this thesis.

$\boldsymbol{\Omega}_E \times (\boldsymbol{\Omega}_E \times \mathbf{r}) = -\nabla\Phi_z$ and gravitational acceleration $\mathbf{g} = -\nabla\Phi_g$ are combined to a total geopotential $\Phi = \Phi_g + \Phi_z$ (see Holton, 2004, chapter 1.5.2). $\mathbf{F}_R = \nu\nabla^2\mathbf{u}$ is the frictional force with kinematic viscosity ν. The Navier-Stokes equations can be written in a slightly different way when the material derivative is split into the local time derivative plus the advection according to (2): $D\mathbf{u}/Dt = \partial\mathbf{u}/\partial t + \mathbf{u}\cdot\nabla\mathbf{u}$. The advection can be expressed as

$$\mathbf{u} \times (\nabla \times \mathbf{u}) = \frac{1}{2}\nabla\mathbf{u}^2 - \mathbf{u}\cdot\nabla\mathbf{u} \tag{64}$$

where $\boldsymbol{\omega} = \nabla \times \mathbf{u}$ is the three-dimensional vorticity vector. It can be combined with earth's angular velocity to the absolute vorticity vector: $\boldsymbol{\omega}_a = \boldsymbol{\omega} + 2\boldsymbol{\Omega}_E$. The Navier-Stokes equation (63) then reads

$$\frac{\partial\mathbf{u}}{\partial t} = -(\boldsymbol{\omega} + 2\boldsymbol{\Omega}_E) \times \mathbf{u} - \frac{1}{2}\nabla\mathbf{u}^2 - \frac{1}{\rho}\nabla p + \mathbf{g} + \mathbf{F}_R \tag{65}$$

Finally, the Bernoulli-streamfunction $B = \frac{1}{2}\mathbf{u}^2 + \Phi + h$ is introduced into the equations. B is composed of the sum of kinetic energy ($\mathbf{u}^2/2$), potential energy (geopotential $\Phi = \Phi_g + \Phi_z$) and thermodynamical energy in form of the enthalpy $h = e + p\alpha$. Since the first law of thermodynamics can be written as $\nabla h = T\nabla s + \alpha\nabla p$[19], the Navier-Stokes equations considering the first law of thermodynamics in a noninertial reference frame and – for comparison – in an inertial reference frame, respectively, are given as

$$\frac{\partial\mathbf{u}}{\partial t} = -(\boldsymbol{\omega} + 2\boldsymbol{\Omega}_E) \times \mathbf{u} - \nabla B + T\nabla s + \mathbf{F}_R \qquad \text{noninertial} \tag{66a}$$

$$\frac{\partial\mathbf{u}}{\partial t} = -\boldsymbol{\omega} \times \mathbf{u} - \nabla B^* + T\nabla s + \mathbf{F}_R \qquad \text{inertial, absolute} \tag{66b}$$

The Bernoulli-streamfunction in the inertial, absolute reference frame is given as $B^* = \frac{1}{2}\mathbf{u}^2 + \Phi_g + h$. Note, that the Coriolis force (in form of $-2\boldsymbol{\Omega}_E \times \mathbf{u}$) as well as the centrifugal force ($-\nabla\Phi_z$ that is included in $-\nabla B$) do not appear in the inertial equations. Otherwise, the equations are of similar structure. The inertial equations will be used later when deriving exact vortex solutions of the Navier-Stokes equations.

3.1.5 Horizontal and vertical equations of motion

The equations of motion can be split into a part describing the horizontal motions and another part that describes the vertical acceleration. We will use the Navier-Stokes equations in the form of (63) neglecting friction (these equations are also called Euler equations). Let $\mathbf{u} = \mathbf{v}_h + w\mathbf{k}$ with $\mathbf{u} = (u, v, w)$ be the horizontal and vertical velocity

[19] This can be derived by the following steps: We know that $e = c_v T$ and from equation (44) it follows that $c_v\nabla T = -p\nabla\alpha + J$. We defined the entropy changes as $Ds/Dt = J/T$ and hence it follows that $J = T\nabla s$. Calculating the gradient of enthalpy ($h = e + p\alpha$) leads to $\nabla h = c_v\nabla T + p\nabla\alpha + \alpha\nabla p$. Now we can use the expressions for $c_v\nabla T$ and J and we will obtain: $\nabla h = T\nabla s + \alpha\nabla p$.

components and $\mathbf{i}, \mathbf{j}, \mathbf{k}$ the cartesian unit vectors, then the horizontal and vertical Euler equations read:

$$\frac{D\mathbf{v}_h}{Dt} = -2\mathbf{\Omega}_E \times \mathbf{u} \cdot (\mathbf{ii} + \mathbf{jj}) - \frac{1}{\rho}\nabla_h p \tag{67}$$

$$\frac{Dw}{Dt} = -2\mathbf{\Omega}_E \times \mathbf{u} \cdot \mathbf{k} - \frac{1}{\rho}\frac{\partial p}{\partial z} + g \tag{68}$$

where $g = \|\mathbf{g}\|$ is the magnitude of the gravitational acceleration. The Earth's angular momentum $2\mathbf{\Omega}_E$ has two components:

$$2\mathbf{\Omega}_E = l\mathbf{j} + f\mathbf{k} \quad , \quad \text{with } f = 2\,\|\mathbf{\Omega}_E\| \sin\varphi \;,\; l = 2\,\|\mathbf{\Omega}_E\| \cos\varphi \tag{69}$$

where φ is the latitude and $\|\mathbf{\Omega}_E\| = 2\pi/day \approx 7.27 \cdot 10^{-5} s^{-1}$. There is no component in the west-east direction (pointing in $\mathbf{i}$-direction) because the unit vector $\mathbf{i}$ is at every point perpendicular to the rotation axis of the Earth ($2\mathbf{\Omega}_E$). Explicitly, the Coriolis force components are calculated as

$$2\mathbf{\Omega}_E \times \mathbf{u} = f\mathbf{k} \times \mathbf{v}_h + lw\mathbf{i} - lu\mathbf{k} \;. \tag{70}$$

Finally, an explicit form of the horizontal and vertical Euler equations is derived

$$\frac{D\mathbf{v}_h}{Dt} = -f\mathbf{k} \times \mathbf{v}_h - lw\mathbf{i} - \frac{1}{\rho}\nabla_h p \tag{71a}$$

$$\frac{Dw}{Dt} = lu - \frac{1}{\rho}\frac{\partial p}{\partial z} - g \tag{71b}$$

3.1.6 Horizontal equations of motion in natural coordinates

Before proceeding with the scale analysis, we will transform the horizontal equations of motion (71a) to another coordinate system called natural coordinates (see e.g. Holton, 2004, chapter 3.2.1). Natural coordinates split the flow components into a part tangential to the flow motion (or trajectories) and another part normal to the flow motion. These coordinates are orthonormal, but time- and space-dependent since they follow the trajectories. Their unit vectors are denoted as $\boldsymbol{t}$ (for the tangential component) and $\boldsymbol{n}$ (for the component normal to the motion). Note, that a vertical unit vector is derived by $\boldsymbol{k} = \boldsymbol{t} \times \boldsymbol{n}$. For horizontal motions, the vertical unit vector $\boldsymbol{k}$ is parallel to the vertical unit vector in Cartesian coordinates. The relationship between the horizontal natural coordinates $(\boldsymbol{t}, \boldsymbol{n})$ and the horizontal, Cartesian coordinates $(\mathbf{i}, \mathbf{j})$ is given by

$$\boldsymbol{t} = \mathbf{i}\cos\alpha + \mathbf{j}\sin\alpha \quad , \quad \boldsymbol{n} = -\mathbf{i}\sin\alpha + \mathbf{j}\cos\alpha \tag{72}$$

and

$$\mathbf{i} = \boldsymbol{t}\cos\alpha - \boldsymbol{n}\sin\alpha \quad , \quad \mathbf{j} = \boldsymbol{t}\sin\alpha + \boldsymbol{n}\cos\alpha \tag{73}$$

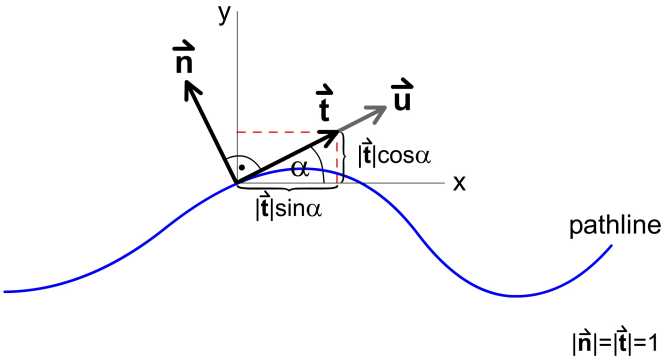

Figure 6: *Relation between natural coordinates following a pathline and cartesian coordinates. The unit vectors* $\boldsymbol{t}, \boldsymbol{n}$ *in natural coordinates have length 1.*

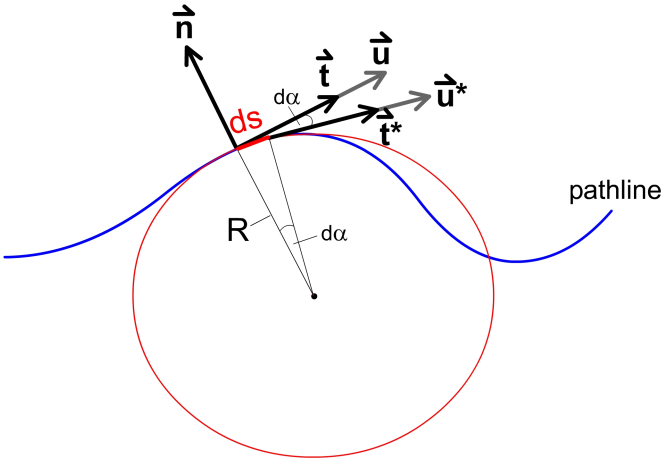

Figure 7: *Relation between the change of angle* $d\alpha$ *and the travelled pathlength* ds *between two locations at the pathlines.* $\mathbf{u}(t = t_1), \mathbf{u}^*(t = t_2)$ *denote the velocities at times* t_1, t_2 *with* $t_1 < t_2$*. Furthermore, the radius of curvature* R *can be understood as the radius of the circle that approximates the travelled pathlength.*

where α is the angle between the unit vectors $\boldsymbol{t}$ and $\boldsymbol{i}$ (see Figure 6). The angle is time-dependent, it changes as $d\alpha = ds/R$ where R is the radius of curvature and ds is the length of the circle with radius R that was travelled in the observed time (see Figure 7)[20]. The temporal evolution $D\alpha/Dt$ is then given as

$$\frac{D\alpha}{Dt} = \frac{v_h}{R} \tag{74}$$

where v_h denotes the magnitude of the horizontal velocity vector $\mathbf{v}_h$ and is given by

$$v_h = \frac{Ds}{Dt} = \sqrt{\mathbf{v}_h \cdot \mathbf{v}_h} \, . \tag{75}$$

The radius of curvature R is positive in cyclonicly curved trajectories and negative in anticyclonicly curved flows. The curvature κ is defined as the reciprocal of the radius of

[20] Note, α is given in radians. Then for a complete revolution of the circle we have $d\alpha = 2\pi$; hence, $ds = 2\pi R$ is the circumference of the circle (see also Bronstein et al., 2005, chapter 3.1.6.2).

curvature: $\kappa = 1/R$. In case of a straight trajectory, the radius becomes infinitely large and the curvature becomes zero.
The horizontal velocity vector $\mathbf{v}_h$ can change its direction ($\boldsymbol{t} = \boldsymbol{t}(t)$) as well as its magnitude ($\|\mathbf{v}_h\| := v_h = v_h(t)$) over time. Therefore, the acceleration is given as

$$\frac{D\mathbf{v}_h}{Dt} = v_h \frac{D\boldsymbol{t}}{Dt} + \boldsymbol{t}\frac{Dv_h}{Dt} \ . \tag{76}$$

The temporal evolution of the tangential unit vector (as given by (72)) is calculated as

$$\frac{D\boldsymbol{t}}{Dt} = (-\mathbf{i}\sin\alpha + \mathbf{j}\cos\alpha)\frac{D\alpha}{Dt} \ . \tag{77}$$

Using expression (74) and (72) then gives

$$\frac{D\mathbf{v}_h}{Dt} = \boldsymbol{n}\frac{v_h^2}{R} + \boldsymbol{t}\frac{Dv_h}{Dt} \ . \tag{78}$$

The nabla-operator in natural coordinates is given as

$$\nabla_h = \mathbf{t}\frac{\partial}{\partial s} + \mathbf{n}\frac{\partial}{\partial n} \tag{79}$$

where s denotes the streamwise direction and n is normal to s. Finally, the horizontal equations of motion (71a) transformed to natural coordinates read

$$\mathbf{n}\frac{v_h^2}{R} + \mathbf{t}\frac{Dv_h}{Dt} = -fv_h\mathbf{n} + lw\mathbf{t}\cos\alpha - lw\mathbf{n}\sin\alpha - \frac{1}{\rho}\left(\mathbf{t}\frac{\partial p}{\partial s} + \mathbf{n}\frac{\partial p}{\partial n}\right) \tag{80}$$

This splits into a streamwise component parallel to the velocity vector describing the temporal change in wind speed Dv_h/Dt (or acceleration) as the sum of a Coriolis force term (denoted as C'' and the streamwise directed pressure gradient (denoted as P_s):

$$\frac{Dv_h}{Dt} = \underbrace{lw\cos\alpha}_{C''} \underbrace{- \frac{1}{\rho}\frac{\partial p}{\partial s}}_{P_s} \qquad \text{parallel to } \mathbf{v}_h \tag{81}$$

and into a component normal to the velocity vector

$$\underbrace{\frac{v_h^2}{R}}_{Z} + \underbrace{fv_h}_{C} + \underbrace{lw\sin\alpha}_{C'} = \underbrace{-\frac{1}{\rho}\frac{\partial p}{\partial n}}_{P} \qquad \text{normal to } \mathbf{v}_h \ . \tag{82}$$

This component displays the balance between the centrifugal force (Z), the Coriolis force terms (C and C') and the pressure gradient force in normal direction (P)[21] The vertical component is the same as in the cartesian coordinate system (see 71b).

[21] More precisely, this equation shows the balance between the *accelerations*.

3.2 Scale analysis of the equations of motion for different vortex types

It is a common method in meteorology to apply a scale analysis to the equations of motion in order to find the dominating balance of forces for different set-ups. Therefore, typical characteristic values of the system of interest (e.g. extratropical cyclones, tornadoes) are used in order to non-dimensionalize the set of equations and in order to identify the terms of dominating order. This method is quite successful even though mathematically it would be better (or mathematically more correct) to derive the prevailing balances by asymptotic limits as is done e.g. in Klein (2008)[22].
For the scale analysis, we need to non-dimensionalize the equations of motion. Therefore, the magnitudes of parameters in the equations needs to be estimated for the different vortex types, we are interested in. In Table 1 in chapter 1 some typical values were already listed. We will add the missing parameters in Table 2.
Characteristic Earth parameters are

$$f = l = 10^{-4} s^{-1}$$
$$g = 10\ m/s^2$$
$$\rho = 1\ kg/m^3$$

Under the assumption that the vortex systems are observed at the moment of their maximum intensity, the tangential component of the equations of motion (equation 81) vanishes because the acceleration is zero at that moment. Therefore, we only need to consider the normal component (82) and the vertical component (71b). Using the characteristic magnitudes[23] in Table 2 and the Earth parameters lead to the following estimate of the magnitudes of the different forces for the different vortex types in case of the normal component (82) of the equation of motion:

[22] Compared to the common scale-analysis method, the asymptotic ansatz has the advantage that for the non-dimensionalization of the equations only typical parameters of the Earth-Atmosphere system are used. Some examples are the Earth's radius, the scale height of the atmosphere, the sound speed in air, the gas constant of (dry) air, etc. These parameters do not depend on the single system (e.g. extratropical cyclones, tropical cyclones, tornadoes, etc.) one is interested in. The explicit values determining a system are introduced by scaling the variables of space (horizontal, vertical spatial coordinates) and time accordingly and separately depending on a single (small) parameter. This can be done for single scale systems separately. The matching of single-scale equations is done by an asymptotic matching procedure in order to derive a multiple-scale system (an example is the study of a tropical cyclone of gradient wind balance embedded in a large-scale quasi-geostrophic environment which was done by Mikusky (2007) (PhD thesis, further work published in Päschke et al., 2012)). This additionally allows to study the interactions of the single-scales with each other. An overview over the method is given in Klein (2008).

[23] The characteristic magnitudes mainly follow from the common literature (e.g. Holton, 2004; Markowski and Richardson, 2011). In some cases the "typical" values show a large variability. In these cases, we decided for typical values within that range such that the magnitudes of the balancing terms are approximately equal – not only in terms of the magnitude, but also in terms of the (exact) calculated numbers.

Equation of motion (normal component)	$\frac{v_h^2}{R}$	+	fv_h	+	$lw\sin\alpha$	=	$-\frac{1}{\rho}\frac{\partial p}{\partial n}$
Abbreviation of forces	Z	+	C	+	C'	=	P
Characteristic scales	U^2/L		fU		lW		$\rho^{-1}\Delta_h P/L$
Extratropical lows	$1.0 \cdot 10^{-4}$		$\mathbf{1.0 \cdot 10^{-3}}$		$1.0 \cdot 10^{-6}$		$\mathbf{1.0 \cdot 10^{-3}}$
Tropical cyclones	$\mathbf{2.1 \cdot 10^{-3}}$		$\mathbf{2.5 \cdot 10^{-3}}$		$1.0 \cdot 10^{-4}$		$\mathbf{5.0 \cdot 10^{-3}}$
Supercells	$\mathbf{2.3 \cdot 10^{-2}}$		$1.5 \cdot 10^{-3}$		$1.0 \cdot 10^{-3}$		$\mathbf{2.5 \cdot 10^{-2}}$
Tornadoes	$\mathbf{2.5 \cdot 10^{+1}}$		$5.0 \cdot 10^{-3}$		$5.0 \cdot 10^{-3}$		$\mathbf{2.5 \cdot 10^{+1}}$

Keeping the dominating terms gives typical horizontal balances of forces that determine the different vortex types. Summarized these balances are given in the following:

Extratropical lows:	C	=	P	*geostrophic balance*
Tropical cyclones:	$Z + C$	=	P	*gradient wind balance*
Supercells:	Z	=	P	*cyclostrophic balance*
Tornadoes:	Z	=	P	*cyclostrophic balance*

It should be noted that these balances are only rough approximations since the typical values of the parameters vary within certain limits. For example, extratropical lows can also be approximated by the gradient wind balance since the centrifugal force is only one order in magnitude smaller than the pressure gradient and the Coriolis force. Especially smaller or more intense systems better fit the gradient wind balance than the geostrophic balance. In fact, extratropical cyclone radii are observed to be subsynoptic i.e. considerably smaller than 1000 km (e.g. Schneidereit et al., 2010). Hence, the gradient wind balance is an appropriate choice for synoptic lows, too.
On the other hand, supercells are also influenced by the Coriolis force (especially the larger or less intense the system is). The Coriolis terms are one order in magnitude smaller than the centrifugal and pressure gradient force. Recent work by Bryan (2015) and Markowski and Richardson (2015) points out that – besides the importance of surface drag – Coriolis force may play an important role in numerical simulations in order to reproduce the observed curved hodographs[24].
Furthermore, it should be noted that these balances of forces have been successfully used as an intensity measure describing the different vortex types (Schielicke and Névir, 2009). More details will be given later in chapters 5.2 and 5.3.

[24] A curved hodograph represents rotational wind shear with height.

Table 2: *Typical atmospheric vortex types and their characteristic properties (U, W: horizontal/vertical wind speed, L: horizontal scale, H: height, H/L: height-to-length ratio (aspect ratio), $\Delta T = C_d \cdot L^{2/3}\, m^{3/2}s$: dissipative time scale with $C_d = 10$ is a factor that gives reasonable results for the time scale, $\Delta_h P$: horizontal pressure anomaly, $\Delta_z P$: vertical pressure anomaly).*

vortex type:	synoptic low	tropical cyclone	supercell	tornado
U	10 m/s	25 m/s	15 m/s	50 m/s
W	1 cm/s	1 m/s	10 m/s	50 m/s
L	1000 km	300 km	10 km	100 m
H	10 km	10 km	10 km	2 km
ΔT	10^5s	10^4s	10^3s	10^2s
$\Delta_h P$	10 hPa	15 hPa	2.5 hPa	25 hPa
$\Delta_z P$	1000 hPa	1000 hPa	1000 hPa	200 hPa
W/U	$\ll 1$	$\ll 1$	≈ 1	≈ 1
H/L	$\ll 1$	$\ll 1$	≈ 1	$\gg 1$

3.2.1 Balanced, horizontal flows of different vortex types

There are some interesting differences between different vortex types that can be attributed to the different balances of forces. Especially, there are differences between high and low pressure systems for vortices on different scales.

3.2.1.1 Geostrophic flow

The geostrophic approximation of the horizontal equation of motion (71a) reads

$$f\mathbf{k} \times \mathbf{v}_h = -\rho^{-1}\nabla_h p \tag{83}$$

With help of equation (83) we can define the geostrophic wind as

$$\mathbf{v}_{h,g} := -\frac{1}{f\rho}\mathbf{k} \times \nabla_h p \tag{84}$$

where the index "g" indicates that the velocity is geostrophic and index "h" indicates that the motion is horizontal. Furthermore in natural coordinates following equation (82), this is expressed as

$$v_{h,g} = -\frac{1}{f\rho}\frac{\partial p}{\partial n}\,. \tag{85}$$

The geostrophic balance does not hold near the equator since the Coriolisparameter $f = 2\boldsymbol{\Omega}_E \sin\phi$ becomes zero at the equator (where latitude $\phi = 0$). The difference between the real, accelerated wind and the geostrophic wind can be expressed by the

Rossby number Ro. The Rossby number is defined as the ratio of the magnitude of acceleration $D\mathbf{u}/Dt \sim U/T$ with $T = L/U$ and the Coriolis force $-2\boldsymbol{\Omega}_E \times \mathbf{u} \sim fU$. Thereby the Rossby number is given as (cf. e.g. Holton, 2004, chapter 2.4):

$$Ro := \frac{U}{fL} \tag{86}$$

Using the typical values for large-scale, synoptic flow from Table 2, the Rossby number is approximately $Ro \approx 0.1$ which means that the deviations between the real and the geostrophic wind is about 10%.
Geostrophic balance describes the balance of the pressure gradient force P and the Coriolis force C. On the northern hemisphere, the low pressure points always to the left of the flow (otherwise $v_{h,g}$ would be negative. This is impossible in case of a purely geostrophic flow – i.e. in absence of other forces – since the real wind coincides with the geostrophic wind) . There is no difference between high and low pressure systems. Both cases are equal. Additionally, this means that highs and lows have the same properties: the same size and the same pressure gradients. However, observations show that there is a difference between extratropical highs and lows concerning their sizes as well as their intensities. This suggests that the gradient wind balance might be a better model for the large-scale synoptic vortices since it better fits the observations.

3.2.1.2 Gradient wind flow

The horizontal equations of motion in natural coordinates (82) under the assumption of gradient wind balance are given as

$$\frac{v_h^2}{R} + f v_h = -\frac{1}{\rho}\frac{\partial p}{\partial n} \, . \tag{87}$$

From this equation, we can derive an expression for the gradient wind speed

$$v_h = -\frac{Rf}{2} \pm \underbrace{\sqrt{\frac{R^2 f^2}{4} - \frac{R}{\rho}\frac{\partial p}{\partial n}}}_{=:\sqrt{D}} \, . \tag{88}$$

In natural coordinates v_h is nonnegative. For all possible cases, we need to discuss equation (88) concerning the signs of the two determining terms: the pressure gradient in normal direction $\partial p/\partial n$ and the radius of curvature R. The first term inside the square root (first term of D) is always positive. The second term of D can be positive or negative. If both terms are either positive or both are negative, we require for physical (nonimaginary) roots:

$$\frac{R^2 f^2}{4} \geq \frac{R}{\rho}\frac{\partial p}{\partial n} \quad \text{for the same signs of } R, \frac{\partial p}{\partial n} \tag{89}$$

Table 3: *Possible cases for the root in the gradient wind equation (88) for the northern hemisphere (after Holton, 2004, chapter 3.2.5).*

	$R > 0$	$R < 0$
$\partial p/\partial n > 0$	$v_h = -f\lvert R\rvert/2 - \sqrt{D} < 0$ unphysical	$v_h = f\lvert R\rvert/2 - \sqrt{D} < 0$ unphysical (cf. (91))
	$v_h = -f\lvert R\rvert/2 + \sqrt{D} < 0$ unphysical (cf. (90))	$v_h = f\lvert R\rvert/2 + \sqrt{D} > 0$ antibaric flow, ***anomalous low***
$\partial p/\partial n < 0$	$v_h = -f\lvert R\rvert/2 - \sqrt{D} < 0$ unphysical	$v_h = f\lvert R\rvert/2 - \sqrt{D} > 0$ anticyclonic flow, ***regular high*** (cf. (90), $v_h < f\lvert R\rvert/2$)
	$v_h = -f\lvert R\rvert/2 + \sqrt{D} > 0$ cyclonic flow, ***regular low*** (cf. (91))	$v_h = f\lvert R\rvert/2 + \sqrt{D} > 0$ anticyclonic flow, ***anomalous high*** (cf. (90), $v_h > f\lvert R\rvert/2$)

In this case, the result of $\sqrt{D}$ is always less than $|R|f/2$:

$$\frac{|R|f}{2} > \sqrt{D} \quad \text{for the same signs of } R, \frac{\partial p}{\partial n} \tag{90}$$

In the case of different signs of the pressure gradient and the radius of curvature, A is always nonnegative ($D \geq 0$) and the square root is always larger (or equal in the trivial case) than $|R|f/2$ (because we always add a positive number to the first term in D):

$$\sqrt{D} > \frac{|R|f}{2} \quad \text{for different signs of } R, \frac{\partial p}{\partial n} \tag{91}$$

All possible cases are summarized in Table 3. Thereby, the term "*regular*" is chosen since it adds the centrifugal force term of small magnitude to the geostrophic balanced vortex which represents the typical balance on the synoptic scale. Note, that the difference between the regular and the anomalous high is only the strength of the centrifugal force compared to the Coriolis force. In a regular high, the influence of the centrifugal force Z on the balance is less than half of the Coriolis force C and in an anomalous high it is larger than $C/2$. This can be seen by the following considerations: From $v_h \gtrless f|R|/2$

follows:

$$\frac{v_h^2}{R} < \frac{f v_h}{2} \quad \text{or} \quad Z < C/2 \qquad \text{for a regular high}$$
$$\frac{v_h^2}{R} > \frac{f v_h}{2} \quad \text{or} \quad Z > C/2 \qquad \text{for an anomalous high}$$

It is possible in the anomalous case that the pressure gradient force approaches zero or vanishes completely. Then the Coriolis force is balanced by the centrifugal force alone which is called inertial flow (cf. Holton, 2004, chapter 3.2.3 for more details). Furthermore, in both high pressure types the pressure gradient normal to the flow and the radius of curvature have the same sign ($R < 0$, $\partial p/\partial n < 0$). Following from (89) this gives a limit for the strength of the pressure gradient (or for the size) of a high pressure system. Rewriting (89) gives

$$|R| \geq \frac{4}{f^2 \rho} \left| \frac{\partial p}{\partial n} \right| \quad \text{or} \quad \left| \frac{\partial p}{\partial n} \right| \leq \frac{\rho f^2 |R|}{4} \tag{92}$$

Hence, for a typical horizontal pressure gradient of 10 hPa/1000 km; $f = 10^{-4} s^{-1}$; $\rho = 1\,\mathrm{kg/m^3}$ the radius of curvature requires to be at least $|R| \geq 400$ km. On the other hand, when the radius of curvature approaches zero $|R| \to 0$, the pressure gradient decreases likewise to zero. Therefore, near the core of a high pressure system the pressure field is weak and flat with low winds (Holton, 2004). Such a limitation is not observed in low pressure systems. We will refer later to this different dynamic behavior in lows and highs when we will introduce the numerical vortex identification procedure in chapter 6.4.

In Figure 8, all four possible cases are summarized. The only cyclonic flow is possible in the regular low. All other possible solutions are characterized by anticyclonic flow. Except of the anomalous low, in all cases the flow is *baric*, i.e. the Coriolis force vector **C** points in the opposite direction of the pressure gradient force **P**. The flow of the anomalous low is called *antibaric* since **P** and **C** point in the same direction (inwards) and their sum is balanced by the centrifugal force (Holton, 2004). Furthermore, this flow is anticyclonic.

Examples of anomalous lows are e.g. anticyclonic rotating mesocyclones in supercells. However, the Coriolis force influences the dynamics only when their size is relatively large. For smaller-scale, more intense systems like tornadoes the influence of the Coriolis force further decreases (nearly vanishes) and the cyclostrophic balance becomes the appropriate model for that vortex type.

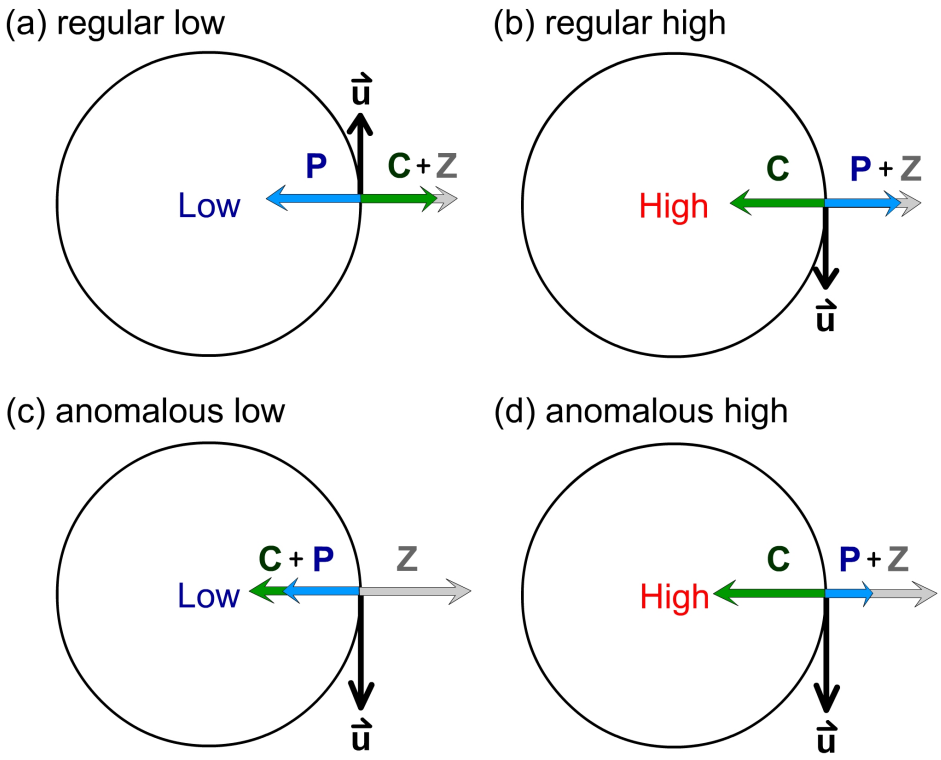

Figure 8: *Force balances for the four possible solutions of the gradient wind equation for the northern hemisphere (see also Table 3).* **P** *denotes the pressure gradient force,* **C** *the Coriolis force, and* **Z** *the centrifugal force. Adopted from Holton (2004), his Fig. 3.5.*

3.2.1.3 Cyclostrophic flow

The cyclostrophic balance describes the balance of centrifugal and pressure gradient force in the horizontal equations of motion (82). In natural coordinates it is given by

$$\frac{v_h^2}{R} = -\frac{1}{\rho}\frac{\partial p}{\partial n} \tag{93}$$

The cyclostrophic wind magnitude v_h is calculated as

$$v_h = \sqrt{-\frac{R}{\rho}\frac{\partial p}{\partial n}} \tag{94}$$

This only holds in two cases[25]:

$$R > 0,\ -\frac{1}{\rho}\frac{\partial p}{\partial n} < 0 \qquad \textit{cyclonic}$$

$$R < 0,\ -\frac{1}{\rho}\frac{\partial p}{\partial n} > 0 \qquad \textit{anticyclonic}$$

[25] In the other non-trivial cases, the square root becomes imaginary and therefore no physical solutions exists.

These cases describe the cyclonic and anticyclonic flow around a low pressure system (see Figure 9). It is not possible to derive cyclonic flow around a high pressure disturbance (imaginary solutions). Since the cyclostrophic balance only holds for small-scale flows where the Coriolis force can be neglected, eddies on these scales are always characterized by low core pressures. Examples of atmospheric vortices of cyclostrophic flow are tornadoes and dust devils. Even though, the majority of the tornadoes (and mesocyclones) rotates cyclonicly. Anticyclonicly rotating small-scale systems are observed, too, even though they occur less frequently.

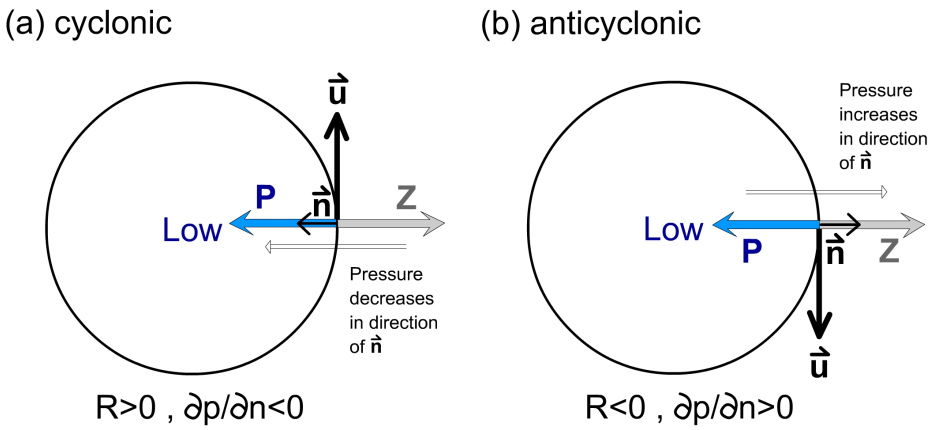

Figure 9: *(a) Cyclonic and (b) anticyclonic flow in cyclostrophic balance.* **P** *denotes the pressure gradient force and* **Z** *the centrifugal force. The unit vector in normal direction is denoted as* $\vec{\mathbf{n}}$*. Adopted from Holton (2004), his Fig. 3.4.*

3.2.2 Vertical balance

The vertical equation of motion was given by (cf. equation 71b):

$$\frac{Dw}{Dt} = \frac{\partial w}{\partial t} + u\frac{\partial w}{\partial x} + v\frac{\partial w}{\partial y} + w\frac{\partial w}{\partial z} = lu - \frac{1}{\rho}\frac{\partial p}{\partial z} - g \tag{95}$$

Scaling these equations with the characteristic parameters given in Table 2 will lead in first order to the *hydrostatic balance* (because the vertical acceleration and the advective terms are relatively small compared to these two terms):

$$\frac{\partial p}{\partial z} = -\rho g \ . \tag{96}$$

The *hydrostatic balance* describes the balance between the vertical pressure gradient and the gravitational acceleration. The hydrostatic balance can be seen as a base state expressed with base state variables $\bar{p}, \bar{\rho}$. In order to derive nonhydrostatic equations, perturbations of the base state need to be considered. Assuming that the total pressure

and total density are given by

$$p = \bar{p}(z) + p'(x, y, z, t) \tag{97}$$

$$\rho = \bar{\rho}(z) + \rho'(x, y, z, t) \tag{98}$$

Here, p' and ρ' denote the deviations from the base states of pressure $\bar{p}$ and density $\bar{\rho}$, respectively. The hydrostatic base state is expressed as

$$\frac{\partial \bar{p}}{\partial z} = -\bar{\rho} g \tag{99}$$

and the perturbations are given by (after Markowski and Richardson, 2011, chapter 1.2.2)

$$\frac{Dw}{Dt} = -\frac{1}{\rho}\frac{\partial p'}{\partial z} - \frac{\rho' g}{\rho} \tag{100}$$

where the Coriolis term lu in equation (95) has been neglected since it is of the order of 10^{-3} and therefore much smaller than the other terms. The first term on the right hand side is the vertical perturbation pressure gradient force and the second term is the buoyancy. It turns out that the influence of this vertical perturbation equation can be estimated by the aspect ratio H/L, i.e. the ratio between the depth H and the horizontal length scale L of the system (cf. Markowski and Richardson, 2011, chapter 1.2.2 for details of the derivation). The vertical acceleration becomes relatively important compared to the vertical perturbation pressure gradient force and buoyancy in case of an aspect ratio of about 1 and larger. This is true for systems with horizontal scales and heights in the same order. In Table 2, we calculated the aspect ratios for the different vortex types and we can see that it is about 1 in the supercell case and much larger than 1 for tornadoes. These vortex types need to be considered nonhydrostatic, while the large scale vortices (extratropical and tropical cyclones) have aspect ratios smaller than one and can be considered hydrostatic.

3.3 Vorticity and Circulation Dynamics

In a fluid, rotation is usually measured by two quantities: vorticity and circulation. While the vorticity vector can be calculated at every point in the field and measures the microscopic rotation at any point, the circulation is an integral, scalar quantity taking into account a finite area. Circulation therefore is a macroscopic description of the rotation involved in this area (Holton, 2004, chapter 4). Both descriptions of rotation are obviously connected to the definition of a vortex. In particular, some authors define a vortex in general as a region of concentrated vorticity (e.g. Wu et al., 2007). Even though this definition is at first not very specific, it shows the importance of these parameters in the study of vortices. Therefore, we will take a closer look on vorticity

and circulation in the following.

3.3.1 Vorticity: Definition and properties

The vorticity vector is defined as the curl of the velocity field. On the rotating earth, the vorticity vector can either be calculated as the curl of the relative velocity $\mathbf{u}_r$ denoted as relative vorticity vector $\boldsymbol{\omega}_r$ or as the curl of the absolute velocity $\mathbf{u}_a$ denoted as absolute vorticity vector $\boldsymbol{\omega}_a$. The latter additionally considers the angular velocity of the earth (cf. eq. 60)

$$\boldsymbol{\omega}_a = \nabla \times \mathbf{u}_a \quad , \quad \boldsymbol{\omega}_r = \nabla \times \mathbf{u}_r \ . \tag{101}$$

In atmospheric sciences, the vertical component of the vorticity vector is of special interest. The vertical components of the absolute and relative vorticity vectors are defined as

$$\zeta_a := \boldsymbol{k} \cdot \nabla \times \mathbf{u}_a \quad , \quad \zeta := \boldsymbol{k} \cdot \nabla \times \mathbf{u}_r \ . \tag{102}$$

where $\zeta_a = \zeta + f$ is the sum of relative vorticity ζ and planetary vorticity $f = 2\|\boldsymbol{\Omega}_E\| \sin\phi$; f depends on latitude ϕ and is called Coriolis parameter. It is convenient to denote ζ as *vorticity* instead of *vertical component of the relative vorticity vector*.
In natural coordinates, the vorticity can be decomposed into shear and curvature vorticity. We have already introduced the natural coordinate system in the context of the derivation of the equations of motion in natural coordinates in chapter 3.1.6. with unit vectors $\boldsymbol{t}, \boldsymbol{n}, \boldsymbol{k}$ following the flow. Summarized for horizontal motion, unit vector $\boldsymbol{t}$ is always parallel to the velocity vector $\mathbf{u}_h$ and therefore parallel to the trajectory and unit vector $\boldsymbol{n}$ is normal to the horizontal velocity such that it points to the left of the flow direction; $\boldsymbol{k}$ is the vertical unit vector. To any point at a trajectory, a circle with a certain radius can be fitted to the trajectory. This radius is called the radius of curvature R and its reciprocal is called curvature $\kappa = 1/R$[26]. In case of a cyclonic motion along the trajectory, R is positive and in case of an anticyclonic trajectory R is negative. In natural coordinates, the vorticity is given as (Holton, 2004, chapter 4.2)

$$\zeta = \underbrace{\frac{v_h}{R}}_{\textit{curvature vorticity}} - \underbrace{\frac{\partial v_h}{\partial n}}_{\textit{shear vorticity}} \tag{103}$$

where v_h denotes the magnitude of the horizontal velocity vector. The first term on the right is the *curvature vorticity* that describes the turning of the wind along the trajectory (Figure 10a). The second term on the right is the *shear vorticity* which describes the change of the wind speed normal to the flow direction (Figure 10b). Note, that the vorticity can be nonzero even for straight trajectories when the speed changes normal to the wind direction as for example in a jet stream depicted in Figure 10b. Furthermore,

[26] Remember, for a straight trajectory the fitted circle and therefore the radius of curvature become infinitely large and the curvature becomes zero.

the vorticity can be zero, even in curved flow as along as shear and curvature vorticity are of the same magnitude but of different sign.

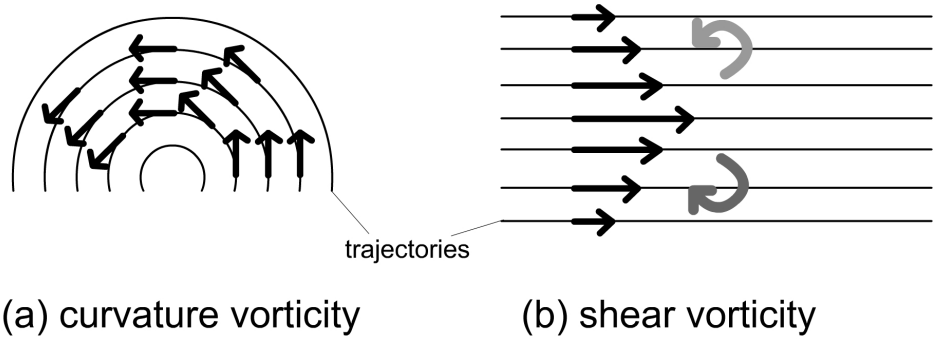

Figure 10: *Vorticity in natural coordinates splits into (a) curvature vorticity and (b) shear vorticity. Note, that both cases are pure, i.e. in (a) the shear vorticity is zero since the velocity does not change normal to the flow and in (b) the curvature vorticity is zero because the trajectories are straight, parallel lines. Black arrows indicate the velocity vectors, thick gray (curved) arrows in (b) indicate the rotation a wooden stick would experience when added to the locations of these arrows in flow (b).*

3.3.2 Vorticity equation

The vorticity equation is derived by taking the curl of the Navier-Stokes equation. We take the curl of the Navier-Stokes equation in the form of equation (65) to derive the *three-dimensional vorticity equation*:

$$\frac{\partial \boldsymbol{\omega}_a}{\partial t} = -\nabla \times (\boldsymbol{\omega}_a \times \mathbf{u}) - \nabla \left(\frac{1}{\rho}\right) \times \nabla p + \nabla \times \mathbf{F}_R \tag{104}$$

where $\partial \Omega_E / \partial t = 0$ was used and $\boldsymbol{\omega}_a = \boldsymbol{\omega} + \boldsymbol{\Omega}_E$. Note, that the rotation of a gradient is always zero. Explicit calculation of $\nabla \times (\boldsymbol{\omega}_a \times \mathbf{u}) = (\nabla \cdot \mathbf{u})\boldsymbol{\omega}_a + \mathbf{u} \cdot \nabla \boldsymbol{\omega}_a - \boldsymbol{\omega}_a \cdot \nabla \mathbf{u}$ leads to the following expression of the 3D vorticity equation

$$\frac{D\boldsymbol{\omega}_a}{Dt} = -\underbrace{(\nabla \cdot \mathbf{u})\boldsymbol{\omega}_a}_{(I)} + \underbrace{\boldsymbol{\omega}_a \cdot \nabla \mathbf{u}}_{(II)} - \underbrace{\nabla \alpha \times \nabla p}_{(III)} + \underbrace{\nabla \times \mathbf{F}_R}_{(IV)} \tag{105}$$

where we used the definition of the material derivative (2). This equation summarizes that the vorticity can be redistributed by either the divergence term (I) or the tilting term (II). Sources of the vorticity are either the solenoidal term (III) or viscous effects (IV).

In the absence of any sources under inviscid, barotropic conditions, i.e. terms (III) and (IV) are zero, vorticity can only be redistributed. The tilting term describes the generation of vorticity by tilting of preexisting vorticity in the direction of interest. An example is the generation of vertical vorticity in the updraft of a thunderstorm where horizontal vorticity is tilted upwards. In this case, the preexisting horizontal vorticity

is caused by low-level shearing winds. With the tilting term (II), the velocity gradient tensor explicitly enters the equation. This means that the vorticity tendency depends on the deformation of the fluid. This can be seen by applying the decomposition of the velocity gradient tensor in the sum of the strain-rate tensor $\mathbf{S}$ and the rotation tensor $\mathbf{\Omega}$ (equation 17) to the relative vorticity part of term (II)

$$\boldsymbol{\omega} \cdot \nabla \mathbf{u} = \boldsymbol{\omega} \cdot \boldsymbol{S} + \underbrace{\boldsymbol{\omega} \cdot \mathbf{\Omega}}_{=0} \tag{106}$$

The second term vanishes because the relative vorticity vector is perpendicular to the rotation tensor $\mathbf{\Omega} = -\mathbf{I} \times \boldsymbol{\omega}/2$. Therefore, deformation plays an important role in the redistribution of vorticity. Vorticity is a field variable that can be calculated at every point in the flow field. It is therefore a local variable. A more global, integral view on the rotation of the flow gives the circulation which is closely related to the vorticity.

3.3.3 Circulation: Definition and tendency equation

The circulation is defined as a closed, material line integral of fluid velocity along that material line C (e.g. Batchelor, 2000, chapter 2.6)

$$\Gamma = \oint_C \mathbf{u} \cdot d\boldsymbol{s} \tag{107}$$

where $d\boldsymbol{s}$ denotes the line element tangent to the circuit C. Note, that we follow a material line C here. This statement is important since it allows us to apply the equations derived in the first fundamentals chapter 2 on the change of material line elements as well as areas and volumes in section 2.4 and the time-dependent rate of change of integrals in section 2.5, respectively. By applying Stokes' theorem ($\oint_C \mathbf{u} \cdot d\boldsymbol{s} = \int_{A'} \nabla \times \mathbf{u} \cdot d\boldsymbol{A}$), the circulation can be related to vorticity as

$$\Gamma = \int_{A'} \boldsymbol{\omega} \cdot d\boldsymbol{A} \tag{108}$$

where A' is the area bounded by the closed curve C in (107). The circulation tendency equation is derived by calculating the material derivative of (107). Thereby, we need to take into account that the material line $d\boldsymbol{s}$ changes in time, too. Therefore, we make use of (11) introduced in section 2.5:

$$\frac{D\Gamma}{Dt} = \oint_C \frac{D\mathbf{u}}{Dt} \cdot d\boldsymbol{s} + \oint_C d\boldsymbol{s} \cdot \nabla \mathbf{u} \cdot \mathbf{u} = \oint_C \frac{D\mathbf{u}}{Dt} \cdot d\boldsymbol{s} + \underbrace{\oint_C d\boldsymbol{s} \cdot \nabla \frac{1}{2}\mathbf{u}^2}_{=0} \tag{109}$$

The second term vanishes because it can be written as the line integral over kinetic energy which is zero for a closed path. In the first term on the right-hand side, $D\mathbf{u}/Dt$

can be replaced by the Navier-Stokes equation (39b):

$$\frac{D\Gamma}{Dt} = -\underbrace{\oint_C 2(\mathbf{\Omega}_E \times \mathbf{u}) \cdot d\boldsymbol{s}}_{Coriolis\ term} - \underbrace{\oint_C \frac{1}{\rho}\nabla p \cdot d\boldsymbol{s}}_{solenoidal\ term} - \underbrace{\oint_C \nabla\Phi \cdot d\boldsymbol{s}}_{=0} + \underbrace{\oint_C \mathbf{F}_R \cdot d\boldsymbol{s}}_{frictional\ term} \tag{110}$$

On the right-hand side, the first term comes from the rotation of the system (Coriolis term), the second and the fourth integral describes the solenoidal (or baroclinic) and frictional effects, respectively. Note, gravitational acceleration $\mathbf{g} = -\nabla\Phi_g$ and centrifugal acceleration $\mathbf{\Omega_E} \times (\mathbf{\Omega_E} \times \mathbf{u}) = -\nabla\Phi_z$ have been combined to the total geopotential $\Phi = \Phi_g + \Phi_z$ (see also the discussion concerning the equation (63)). This integral vanishes, because the closed path integral of the gradient of some arbitrary function is always equal to zero.
The contribution from the Earth's rotation, i.e. the Coriolis term, can be combined with the (relative) circulation Γ on the left to an absolute circulation Γ_a where

$$\Gamma_a = \Gamma + \int_{A'} 2\mathbf{\Omega}_E \cdot d\mathbf{A} \tag{111}$$

where A' denotes the area enclosed in the circuit C[27]. Therefore, we can write the tendency equation of the absolute circulation as

$$\frac{D\Gamma_a}{Dt} = -\oint_C \frac{1}{\rho}\nabla p \cdot d\boldsymbol{s} + \oint_C \mathbf{F}_R \cdot d\boldsymbol{s} \tag{112}$$

Since the frictional force is opposed to the velocity vector ($\mathbf{F}_R \sim -\mathbf{u}$), the second term on the right-hand side is always negative and therefore reduces the absolute circulation. The solenoidal term (first term on the right-hand side) can contribute positively (produce) and negatively (destroy) to the absolute circulation in case of baroclinic conditions, but is zero in case of a barotropic fluid.

3.4 Vortex motions under barotropic, inviscid and incompressible conditions

3.4.1 Kelvin's circulation theorem

Kelvin's circulation theorem states that under barotropic (i.e. density ρ is a function of pressure p only: $\rho = f(p)$) and inviscid ($\mathbf{F}_R = 0$) conditions the absolute circulation Γ_a is conserved

$$\frac{D\Gamma_a}{Dt} = 0\ . \tag{113}$$

[27] That $d/dt(\int_{A'} 2\mathbf{\Omega}_E \cdot d\mathbf{A}) = -\oint_C 2(\mathbf{\Omega}_E \times \mathbf{u}) \cdot d\boldsymbol{s}$ follows directly from equation (13) using $\mathbf{\Omega}_E = const.$; then we have $d/dt(\int_{A'} 2\mathbf{\Omega}_E \cdot d\mathbf{A}) = \int_{A'} d\mathbf{A} \cdot [2\mathbf{\Omega}_E(\nabla \cdot \mathbf{u}) - 2\mathbf{\Omega}_E \cdot \nabla\mathbf{u}] = \int_{A'} d\mathbf{A} \cdot (\nabla \times (2\mathbf{\Omega}_E \times \mathbf{u}))$. Finally, we apply Stokes' theorem that reads: $\oint_C \mathbf{F} \cdot d\boldsymbol{s} = \int_A \nabla \times \mathbf{F} \cdot d\mathbf{A}$ where $\mathbf{F}$ is an arbitrary differentiable vector field and C is the curve that encloses area A. Set $\mathbf{F} = 2\mathbf{\Omega}_E \times \mathbf{u}$ leads to desired equation.

This follows directly from the circulation tendency equation (112) when $\mathbf{F}_R = 0$ (inviscid conditions) and $\rho = f(p)$[28] (barotropic conditions). Holton (2004, chapter 4.1) states that this is analogous to the angular momentum conservation of a solid-body[29].

3.4.2 Vortex lines, surfaces, tubes and filaments

The study of vortex dynamics is closely connected with names like Helmholtz and Kelvin. Their work led to several important theorems that aim to describe the nature of vortices as well as give insight into vortex behavior. First, we need to clarify some concepts concerning vorticity and vortices: The vorticity field is a vector field. Lines tangential to the vorticity vectors are denoted as *vortex lines* and vector surfaces composed of vorticity vectors are called *vortex-surfaces*. Furthermore, vorticity vector tubes are denoted as *vortex-tubes*. The bulk of vortex lines that can be constructed through all points of the circumference of an infinitely small area element build a *vortex filament*. In other words, a vortex filament is a vortex tube with infinitely small cross-section. These concepts go back to Helmholtz (1858).
Under inviscid, barotropic and incompressible conditions, the vorticity tendency equation (105) reduces to

$$\frac{D\boldsymbol{\omega}_a}{Dt} = \boldsymbol{\omega}_a \cdot \nabla \mathbf{u} \tag{114}$$

Since a vortex line is tangential to the vorticity vector this equation can also be seen to represent vortex lines. Comparing (114) with the expression we derived for the change of a material line element $d\mathbf{x}$ over time (see eq. 6):

$$\frac{D}{Dt}(d\mathbf{x}) = d\mathbf{x} \cdot \nabla \mathbf{u} \ ,$$

we observe that both equations are similar in structure and hence we conclude that vortex lines, surfaces, tubes and filaments are material lines, surfaces, and so on. Therefore, we are allowed to use the equations describing the change of material lines, etc. in the derivations of the following Helmholtz' theorems.

3.4.3 Helmholtz' vorticity theorems (1858)

Helmholtz (1858) in his publication called "*Über Integrale der hydrodynamischen Gleichungen, welche den Wirbelbewegungen entsprechen*" ("*On the integrals of the hydrodynamic equations that correspond to vortex motions*") derived three theorems characterizing the dynamics and properties of vortex lines, vortex-surfaces and vortex-tubes of

[28] For $\rho = f(p)$ we can assume $\rho \sim p$ and $\rho^{-1}\nabla p \sim p^{-1}\nabla p = \nabla \ln p$. The closed path integral then reads $\oint \rho^{-1}\nabla p \cdot d\boldsymbol{s} \sim \oint \nabla \ln p \cdot d\boldsymbol{s} = 0$

[29] Note that the circulation of a real (baroclinic, viscid) fluid patch might include non-trivial distributions of vorticity that usually change in time while the mass distribution and hence the moment of inertia tensor of a solid might be spatially non-trivial, but usually does not change in time.

a barotropic, inviscid, incompressible[30] fluid. Forces acting on the fluid are assumed to have a potential. Then the three theorems read (German original from Helmholtz, 1858; translations are given in brackets directly after the quotations): *"Die Untersuchung ergiebt nun, daß wenn für alle Kräfte, welche auf die Flüssigkeit wirken, ein Kräftepotential existirt"* (If all forces that act on the fluid have a potential then the analysis yields that)

(1) *"kein Wassertheilchen in Rotation kommt, welches nicht von Anfang an in Rotation begriffen ist."* (non-rotating water particles do not start to rotate.)

(2) *"Die Wassertheilchen, welche zu irgend einer Zeit derselben Wirbellinie angehören, auch indem sie sich fortbewegen, immer zu derselben Wirbellinie gehörig bleiben."*(Water particles that belong to a vortex filament at a specific time, always belong to that same vortex filament even when the particles are moving.)

(3) *"Daß das Product aus dem Querschnitte und der Rotationsgeschwindigkeit eines unendlich dünnen Wirbelfadens längs der ganzen Länge des Fadens constant ist, und auch bei der Fortbewegung des Fadens denselben Werth behält. Die Wirbelfäden müssen deshalb innerhalb der Flüssigkeit in sich zurücklaufen, oder können nur an ihren Grenzen endigen."* (The product of the cross-section and the rotational velocity of an infinitely thin vortex filament is along its whole length constant and it stays constant even when the vortex filament is moving. Therefore, vortex filaments need to be closed inside the fluid or they end at the boundaries of the fluid.)

For the sake of completeness, we will present the elegant, mathematical proofs of Helmholtz's theorems in the following. Furthermore besides the beautiful, plain and clever way of reasoning, these proofs help to illustrate more explicitly the theoretical concept of vortex tubes and filaments further establishing the understanding of what a vortex is.

3.4.3.1 Proof of Helmholtz's points (1) and (2)

The first point implies that the motion under the assumptions made (inviscid, barotropic, incompressible) is circulation-preserving. This follows directly from Kelvin's circulation theorem (113) under the mentioned conditions. The second theorem can also be formulated as: "*in a circulation-preserving motion the vortex lines are material lines*" (citation is taken from Truesdell, 1954, §46). A proof of the second Helmholtz theorem is presented e.g. in Truesdell (1954) (§93) and goes back to Kelvin (1869): The second theorem is proofed by the following considerations: Assume circulation-preserving motions and let C be a material circuit lying completely on a vortex surface $\boldsymbol{S}$ at time

[30] Helmholtz (1858) does not state explicitly that the fluid must be incompressible. However, he always uses the term "Wassertheilchen", i.e. water particle, which implies incompressible conditions.

$t = 0$ and C is reducible upon $\boldsymbol{S}$. Then the circulation along C is zero (this is proofed under the third point mentioned by Helmholtz, 1858, see later in this chapter) ($\oint_C = 0$ at $t = 0$). At time $t \neq 0$ the particles that initially formed C form another circuit c on a new surface $\boldsymbol{s}$. It is not known if $\boldsymbol{s}$ is also a vortex surface. Since the motion is circulation-preserving the circulation along c is zero, too. Application of Stokes theorem gives $0 = \oint_c d\mathbf{x} \cdot d\mathbf{u} = \int_{A(c)} d\mathbf{A} \cdot \boldsymbol{\omega}$ where $A(c)$ is the area enclosed by c lying entirely on $\boldsymbol{s}$. Since the original circuit C (at $t = 0$) was arbitrarily chosen, this implies $d\mathbf{A} \cdot \boldsymbol{\omega} = 0$ on the surface of $\boldsymbol{s}$. Hence, $\boldsymbol{s}$ is a vortex surface. A vortex surface is a material surface (see also chapter 3.4.2) and the vortex lines forming that vortex surface are therefore material lines (cf. Truesdell, 1954, §93).

3.4.3.2 Proof of Helmholtz's point (3)

In some works the third point is called the *first Helmholtz vorticity theorem* (in e.g. Truesdell, 1954). We will follow this notation here. One part of the the *first vorticity theorem* says that "*the strength of a vortex tube is the same at all cross-sections*" (citation taken from Truesdell, 1954, §43). This part concerns the spatial component of the vortex tubes.

We can show that the circulation of a closed line that lies completely upon a vortex surface and that is reducible on it is zero. This last statement follows from the definition of the circulation as $\Gamma = \int \boldsymbol{\omega} \cdot d\mathbf{A}$: All vorticity vectors of a vortex surface are tangential to that surface ($\boldsymbol{\omega} = \omega\mathbf{t}$) while $d\mathbf{A} = dA\mathbf{n}$ (or the normal $\mathbf{n}$ of the areal patch) is everywhere perpendicular to the vortex surface and therefore the scalar product is zero ($\boldsymbol{\omega} \cdot d\mathbf{A} = 0$) everywhere.

Helmholtz's first vorticity theorem can be proofed by the following considerations: On a vortex tube, two circuits C_1 and C_2 can be connected with each other building a closed path by a line f that is traversed twice (see Figure 11)[31]. The total closed line integral is then given by $C = C_1 + f - C_2 - f$. The minus sign in front of C_2 indicates that the traversed direction of circuit C_2 is taken in the other sense then C_1. By defining the closed path in that way, the total closed circuit C encloses a simply connected (reducible) area of the vortex surface. We have seen, that this integral is zero and we can write

$$0 = \int \boldsymbol{\omega} \cdot d\mathbf{A} = \oint_{C_1} + \int_f - \oint_{C_2} - \int_f . \tag{115}$$

[31] Gauss's integral theorem for an arbitrary vector field $\mathbf{F}$ states that the volume integral over the divergence of $\mathbf{F}$ is equal to the closed surface integral enclosing the volume V' over $\mathbf{F}$ itself: $\iiint_{V'} \nabla \cdot \mathbf{F} dV = \oiint_{S(V')} \mathbf{F} \cdot d\mathbf{S}$. We further know that the divergence of a solenoidal field like the vorticity is always zero $\nabla \cdot \boldsymbol{\omega} = \nabla \cdot (\nabla \times \mathbf{u}) = 0$. Therefore every arbitrarily chosen, closed surface integral over the vorticity field is zero. However, we need to be more specific in case of the proof of two loops lying on the same vortex tube having identical circulation. Note, that we need to take a path as described in the text that lies completely on the vortex tube. It is insufficient to take some arbitrary surface that does not lie wholly on a vortex tube since we than might have contributions to the circulation from the mantel sides forming the tube as well as from both caps.

Hence, the circulations along the two circuits that lie upon the same vortex tube are equal (*spatial constancy of the circulation along a vortex filament or vortex tube*):

$$\oint_{C_1} = \oint_{C_2} \qquad \textit{spatial} \tag{116}$$

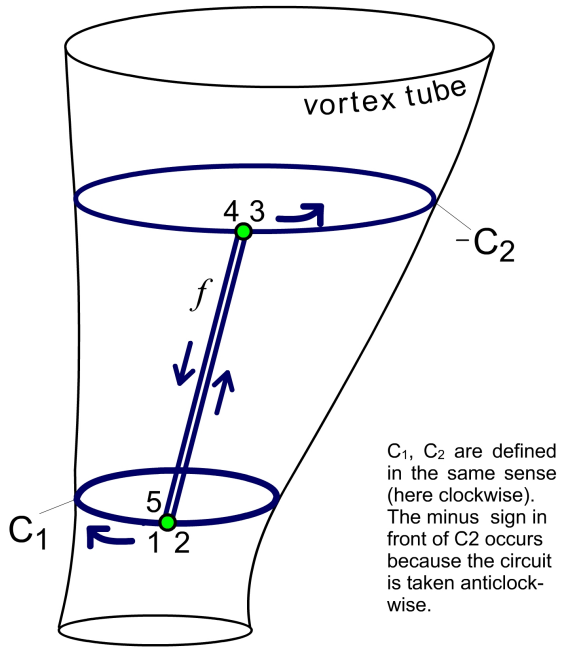

Figure 11: *On the proof of Helmholtz first vorticity theorem: Shown are two circuits C_1, C_2 that lie on a vortex tube. The circuits are connecte by a line f. The total closed path of integration starts at point* 1 *and is given by the following steps in the given order:* $1 \to 2$ *(clockwise),* $2 \to 3$*,* $3 \to 4$ *(anticlockwise),* $4 \to 1$*.*

The second part of Helmholtz's first vorticity theorem treats the constancy of the circulation of a vortex filament in time (*temporal constancy of the circulation of a vortex filament*): the circulation "stays constant even when the vortex filament is moving". The proof of this part follows from Kelvin's circulation theorem (113).

3.4.4 Biot-Savart formula

The Biot-Savart formula is important in the study of vortices and their interaction with each other and with their environment. We will see that it connects the circulation of a vortex with the surrounding velocity distribution. This gives a first hint how important the circulation is in the description of vortices.
Let $\mathbf{u} = (u, v, w)$ be the velocity of an incompressible ($\nabla \cdot \mathbf{u} = 0$), inviscid ($\mathbf{F}_R = 0$) fluid. The vorticity is $\boldsymbol{\omega} = \nabla \times \mathbf{u}$ and its divergence and curl are given as

$$\nabla \cdot \boldsymbol{\omega} = 0 \tag{117}$$

$$\nabla \times \boldsymbol{\omega} = -\nabla^2 \mathbf{u} \tag{118}$$

The second equation is a Poisson equation. It is possible to decompose an arbitrary velocity field $\mathbf{u} = (u, v, w)$ in a part that is described by a velocity potential $\mathbf{u}_\Phi = \nabla\Phi$ which satisfies $\nabla \times \mathbf{u}_\Phi = \nabla \times \nabla\Phi = 0$ and a part that is determined by a solenoidal vector potential $\mathbf{u}_\omega = \nabla \times \boldsymbol{\psi}$:

$$\mathbf{u} = \mathbf{u}_\Phi + \mathbf{u}_\omega = \nabla\Phi + \nabla \times \boldsymbol{\psi} \tag{119}$$

This decomposition is called ***Helmholtz-Hodge decomposition*** and it describes the decomposition of the flow field in an irrotational and a divergence-free part (e.g. Wu et al., 2007). While the velocity potential represents the irrotational part, the solenoidal vector potential gives the divergence-free part. The vorticity, i.e. the curl of the velocity, leads to a Poisson equation:

$$\nabla \times \mathbf{u} = \boldsymbol{\omega} = -\nabla^2\boldsymbol{\psi} \tag{120}$$

that can be solved with help of Green's function[32] in the flow domain V

$$\boldsymbol{\psi} = -\int_V G\boldsymbol{\omega} dV' \tag{121}$$

where G is given for $n = 2, 3$ dimensions as (after Wu et al., 2007, chapter 2.3.2)

$$G(\mathbf{x}, \mathbf{x}') = \frac{1}{2\pi} \log|\mathbf{x} - \mathbf{x}'| \qquad (n = 2) \tag{122}$$

$$G(\mathbf{x}, \mathbf{x}') = -\frac{1}{4\pi|\mathbf{x} - \mathbf{x}'|} \qquad (n = 3) \tag{123}$$

Since $\mathbf{u}_\omega = \nabla \times \boldsymbol{\psi}$ the velocity for incompressible flow is given by the ***Biot-Savart formula*** (after Wu et al., 2007, chapter 3.2.2)

$$\mathbf{u}_\omega(\mathbf{x}) = \frac{1}{2(n-1)\pi} \int_V \frac{\boldsymbol{\omega} \times \mathbf{r}}{r^n} dV \tag{124}$$

where $\mathbf{r}$ is the vector between the vorticity source and location $\mathbf{x}$. Therefore, the Biot-Savart formula describes the relation between a given vorticity field (or distribution) and the velocity induced by that vorticity field.
In case of a vorticity distribution concentrated to a vortex tube C of circulation Γ with a thin diameter (this is also called a vortex filament), the Biot-Savart equation simplifies to (Wu et al., 2007)

$$\mathbf{u}_\omega(\mathbf{x}) = \frac{\Gamma}{2(n-1)\pi} \oint_C \frac{\mathbf{t} \times \mathbf{r}}{r^n} ds \tag{125}$$

where $\mathbf{t}ds$ is a line element of C (see Figure 12) and we used Stokes's theorem in order

[32] The Green's function is mathematically a distribution. This means that it depends on two position variables $\mathbf{x}, \mathbf{x}'$. Integration over the Green's function therefore leads to a new function (or field) that still depends on the position variable. In contrast integrating a function with only one space dependent variable over a specific volume would only lead to a magnitude (e.g. an absolute value of kinetic energy, etc.) of that function inside the volume.

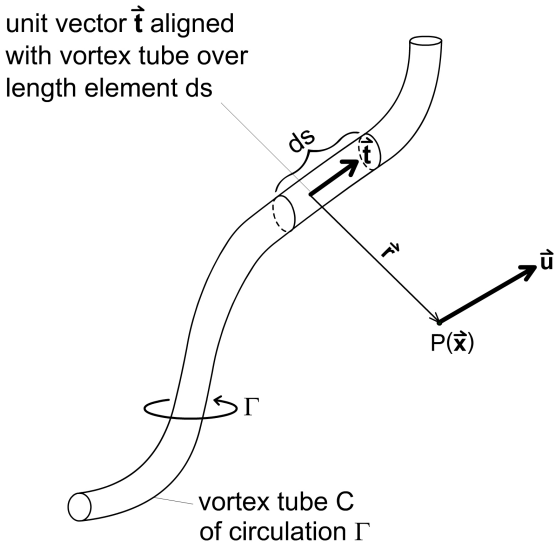

Figure 12: *Vortex filament of circulation* Γ *induces a velocity at point* $P(\mathbf{x}$. *Adopted from Wu et al. (2007), their Figure 3.7*

to introduce the circulation ($\boldsymbol{\omega} dV = (\|\boldsymbol{\omega}\| dA)\mathbf{t} ds = \Gamma \mathbf{t} ds$).

3.4.5 Point vortex dynamics

In this section, we will apply the Biot-Savart formula in order to derive a set of N point vortex equations. A point vortex can be seen as the simplest idealized model of a vortex whose vorticity distribution is concentrated in a point. Using the Biot-Savart formula introduced in the previous section leads to a set of dynamic equations describing the motion of point vortices on a plane.

The equations for a single ($N = 1$) point vortex are derived by the following steps: If the diameter of the vortex filament in equation (125) approaches zero – i.e. in a line vortex – the vorticity becomes singular. For a single straight line vortex the equations further reduce to the two-dimensional equations of a point vortex. In cylindrical coordinates (r, θ, z) with the vortex in the center of the coordinate system, the velocity $\mathbf{u} = (u_r, u_\theta, 0)$ is then given as (Wu et al., 2007, cf.)

$$u_r = \frac{dr}{dt} = 0 \ , \ u_\theta = r\frac{d\theta}{dt} = \frac{\Gamma}{2\pi r} \tag{126}$$

which falls off as $1/r$. Introducing complex variables

$$z = x + iy \ , \ z^* = x - iy \ , \ \frac{dz}{dt} = u + iv \ , \ \frac{dz^*}{dt} = u - iv \tag{127}$$

where the transformation is given as (see Figure 13)

$$x = r\cos\theta \ , \ y = r\sin\theta \ , \ r = \sqrt{x^2 + y^2} \ . \tag{128}$$

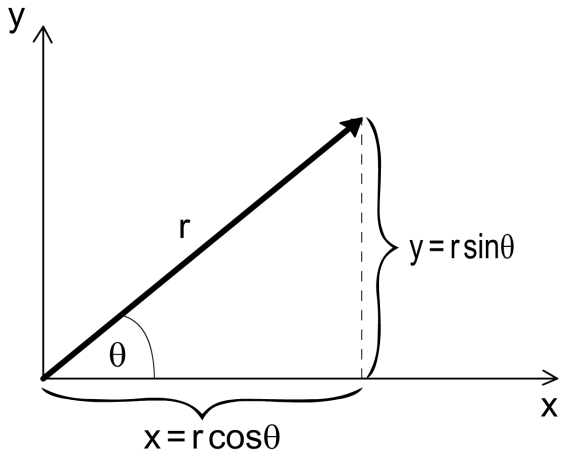

Figure 13: *Relation between complex coordinates and polar coordinates.*

Then the velocity components are calculated as

$$u = \frac{dx}{dt} = -\|\mathbf{u}\| \sin\theta \quad , \quad v = \frac{dy}{dt} = \|\mathbf{u}\| \cos\theta \ .$$

Using (126), the (induced) velocity at location z is given by

$$\frac{dz}{dt} = \frac{i\Gamma}{2\pi r^2} z \ , \quad \frac{dz^*}{dt} = \frac{\Gamma}{2\pi i z} \tag{129}$$

Since $r^2 = zz^*$ equation (129) implies that the motion (at location z) is proportional to one over the distance between the vortex and that point. Hence, having two point vortices at locations z_1 and z_2, one acts on the other as one over their distance

$$\frac{dz_1}{dt} = \frac{i\Gamma_2}{2\pi \|z_1 - z_2\|^2}(z_1 - z_2) \tag{130}$$

$$\frac{dz_2}{dt} = \frac{i\Gamma_1}{2\pi \|z_2 - z_1\|^2}(z_2 - z_1) \tag{131}$$

For N point vortices with circulations Γ_i at locations z_i with $i = 1, .., N$, the motion of the α-th point vortex is then determined by all the other vortices:

$$\frac{dz_\alpha}{dt} = \frac{i}{2\pi} \sum_{\substack{\beta=1 \\ \alpha \neq \beta}}^{N} \frac{\Gamma_\beta}{\ell_{\alpha\beta}^2}(z_\alpha - z_\beta) \tag{132}$$

$$\alpha = 1, .., N \tag{133}$$

where $\ell_{\alpha\beta}^2 = \|z_\alpha - z_\beta\|^2 = (x_\alpha - x_\beta)^2 + (y_\alpha - y_\beta)^2$ is the square of the distance between the two vortices α, β. These point vortex equations can be interpreted as follows (after Aref, 2007): Every vortex α introduces an axisymmetric velocity field around its center that falls off as $\Gamma_\alpha/(2\pi r)$ with distance r from the vortex center (see also Biot-Savart formula in the previous section). Hence, every vortex "feels" the velocity fields of all

other vortices and its motion is determined by the sum of these fields.
Compared to the field perspective where we describe the atmospheric motion with help of a spatial field of vorticity (and with help of the vorticity equation), the point vortex model presents a system with a considerably reduced number of degrees of freedom. Since the vorticity is concentrated at points, we only need to know the initial locations and circulations of the vortices. Assume that about 10-20 vortices determine the large-scale motion of the atmosphere. Then we need to know 30-60 variables (circulations Γ_i and x_i-, y_i-coordinates) to calculate the dynamics. This number is tiny in comparison to a coarsely-resolved data set with a grid resolution of $2.5° \times 2.5°$ longitude×latitude which has about 144×37=5328 data points per hemisphere at a specific height level. Even though the real atmosphere deviates from the inviscid, barotropic, incompressible conditions under which we derived the point vortex equations, the point vortex model might enable the compression of higher-resolved data sets likewise to the compression of video files to the mpeg format. This is an interesting topic for future studies.

3.4.5.1 Scale transformations of the point vortex equations

The dynamics of a system of N point vortices (133) is invariant with respect to scale transformations of the following kind:

$$z \to \lambda \widetilde{z} \quad , \quad t \to \lambda^2 \widetilde{t} \quad , \quad \Gamma \to \widetilde{\Gamma} \tag{134}$$

for any constant λ (e.g. Newton, 2001). This can be seen by directly inserting the transformations into (133)[33]. Note, that the circulations stay invariant. Under these scaling, we derive that the motion of the point vortices scales as follows

$$\frac{dz}{dt} \to \frac{1}{\lambda} \frac{d\widetilde{z}}{dt} \tag{135}$$

In other words, two identical configurations of N point vortices whose distances (or length scales) differ only by a constant factor $\lambda > 1$ move in the same way but the motion is decelerated by a factor of $1/\lambda$. In case of $\lambda < 1$, the motion is accelerated. This is especially important in the case of self-similar vortex collapses that will be investigated in section 3.4.5.4.
In the framework of atmospheric motions, we rather observe that the circulations of

[33] Further (discrete) symmetries are that can be proven by inserting into the equations (133) (after Newton, 2001)

- $t \to -t$, $\Gamma_\beta \to -\Gamma_\beta$: simultaneous time reversal and change of the signs of circulations
- $z \to -z$: rotation about an angle of 180°
- $\Gamma_\beta \to -\Gamma_\beta$, $z \to z^*$: simultaneous change of the signs of circulations and reflection at the horizontal x-axis
- cyclic permutations of the indices of the vortices (all vortices rotated in the same sense of orientation by particular angles)

vortices on different scales (e.g. synoptic scale, mesoscale, convective scale) depend on the length scale L on the synoptic range[34] or even on L^2 on the convective scale[35] or on a combination of both. However, we observe similar vortex arrangements on different scales.

Assume that we have two different sets of N point vortices that differ in horizontal scale and in their circulation by a factor of λ. We want to find out, in which case the point vortex equations remain invariant. Scaling the time by factor of λ

$$z \rightarrow \lambda\widetilde{z} \quad , \quad t \rightarrow \lambda\widetilde{t} \quad , \quad \Gamma \rightarrow \lambda\widetilde{\Gamma} \tag{136a}$$

leads to the invariance of the point vortex equations. Then the motion of the two systems occurs at the same speed

$$\frac{dz}{dt} \rightarrow \frac{d\widetilde{z}}{dt} \tag{137}$$

This might be a hint on the coupling of large- and small-scale motions. More details on the scaling of the circulations of atmospheric motions are discussed in section 6.8.

3.4.5.2 Conserved quantities and general motion of N point vortices

The dynamics of point vortices is characterized by certain conserved quantities. Here, we will introduce two of these conserved quantities due to their relevance to this thesis: the total circulation Γ_{total} and the center of circulation $\mathbf{C}$.

The total circulation is given as the sum over all N circulations

$$\Gamma_{total} := \sum_{\alpha=1}^{N} \Gamma_\alpha = const. \tag{138}$$

That the total circulation is conserved can be seen by the following considerations: We know that under inviscid, barotropic conditions the circulation of each single vortex filament is conserved (see Kelvin's circulation theorem in section 3.4.1) and therefore the total circulation Γ_{total} of all N point vortices is conserved, too.

Furthermore, Kirchhoff (1876) showed that the ***center of circulation***[36] $\mathbf{C}$ of the N point vortices is also a conserved quantity (Kirchhoff, 1876, chapter 20, §2). $\mathbf{C}$ can be derived completely from conserved quantities and is calculated by (see also Müller and

[34] This will be discussed in chapter 6.8; furthermore see Müller et al. (2015).

[35] E.g. the Rankine-vortex model with constant vorticity in the vortex core leads to a linear relationship between circulation and vortex area $A \sim L^2$, see equation 108 and chapter 4.2.1

[36] In the mathematical publications on point vortices the center of circulation is usually called the center of vorticity (cf. e.g. Newton, 2001). However, the term center of circulation seems to be a more appropriate choice since the circulations, i.e. the areal integrals of vorticity, are involved in the calculation rather than the vorticity.

Névir, 2014; Müller et al., 2015, their equation (9))

$$\mathbf{C} = \frac{\sum_{\alpha=1}^{N} \Gamma_\alpha \mathbf{x}_\alpha}{\Gamma_{total}} \tag{139}$$

where $\mathbf{x}_\alpha = (x_\alpha, y_\alpha)$ is the location of the point vortex denoted by α in Cartesian coordinates.

In general, the motion of N point vortices depends on the total circulation. If the sum of all circulations, i.e. the total circulation, is different from zero $\Gamma_{total} \neq 0$ then the N point vortices move around the center of circulation $\mathbf{C}$. If the total circulation approaches zero ($\Gamma_{total} \to 0$), the center of circulation $\mathbf{C} \to \infty$. Hence, in the special case of $\Gamma_{total} = 0$ all vortices translate along parallel paths with the same speed. For systems of $N \leq 3$, the dynamic equations are fully integrable for any values of the circulations (Aref, 2007). For higher-order systems, only certain configurations are integrable (see e.g. Newton, 2001, who remarks that for $\Gamma_{total} = 0$ the $N = 4$ vortex-problem is integrable). The special cases of the motion of $N = 1, 2$ point vortices will be discussed in detail in Appendix A.

3.4.5.3 On the motion of $N = 3$ point vortices in general

The dynamics of $N = 3$ point vortices was solved in a very elegant way by Müller and Névir (2014) who used a geometric representation derived in the framework of Nambu mechanics. The trick is to plot the surfaces of the two conserved quantities[37] in the phase space. The intersection of the two surfaces then yields informations on the motion of the point vortices. Müller and Névir (2014) identified three types of motion: periodic motion, relative equilibria and self-similar collapsing/expanding motions. These motions correspond to an intersection of the surfaces of the two conserved quantities in the phase space of intervortical distances represented by circles (periodic motions), points (relative equilibria) or straight lines (collapsing/expanding motions). The case of $\Gamma_{total} = 0$ is a possible realization of a relative equilibrium state[38] that proved useful in the description of large-scale synoptic motions such as blocking situations (Müller et al., 2015). We will give more details on the motions of $N \leq 3$ point vortices and their application on atmospheric blockings in Appendix A.

3.4.5.4 Self-similar collapsing/expanding motion of N point vortices

Under certain conditions another interesting type of motion occurs: a self-similar collapsing or expanding motion (see appendix A for further explanations). Thereby, the vortices move on logarithmic spirals winding into (or out) the center of circulation while

[37] The two conserved quantities are the Hamiltonian H and a quantity called M that is given as the sum of momentums. We will introduced these quantities later in the appendix A

[38] The relative equilibrium is not limited to the case of $\Gamma_{total} = 0$, it can also occur for $\Gamma_{total} \neq 0$. Then, all vortices move around their center of circulation, but the distances between all vortices remain unchanged.

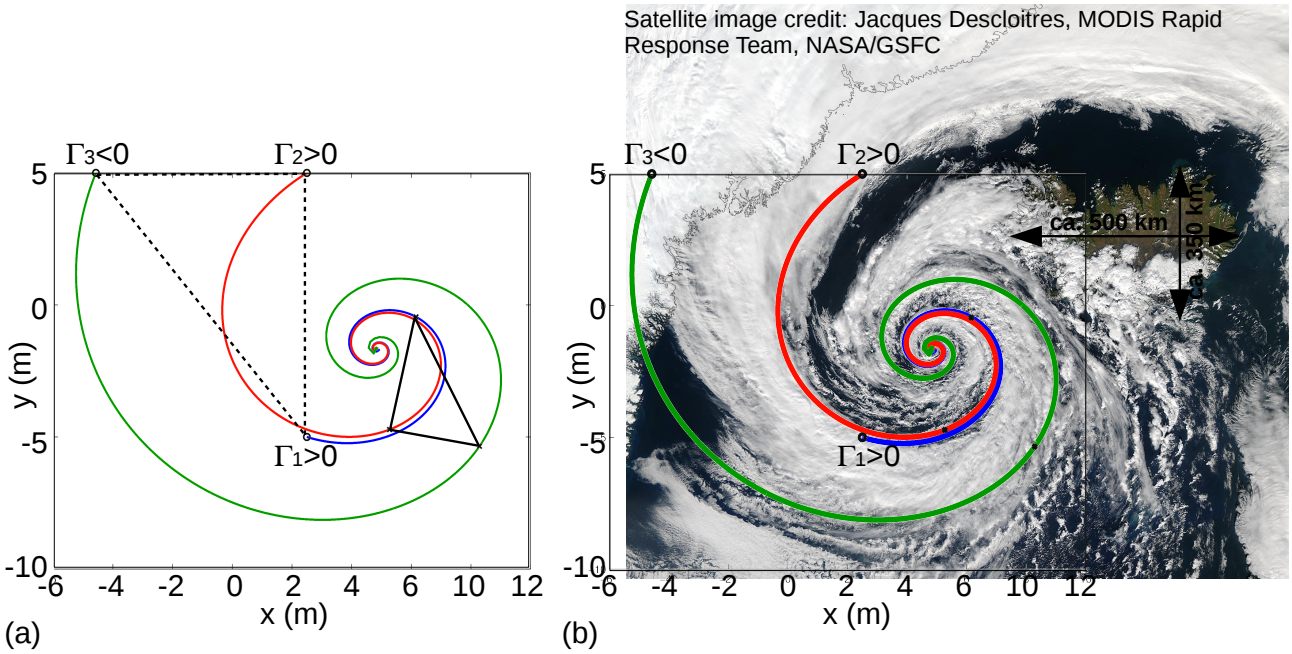

Figure 14: *(a) Trajectories of a collapsing N=3 point vortex system with* $(\Gamma_1, \Gamma_2, \Gamma_3) = (2, 2, -1)\ m^2/s$ *and initial conditions* $(x1, y1) = (2.5, -5)\ m$; $(x2, y2) = (2.5, 5)\ m$; $(x3, y3) = (2.5 - 10/\sqrt{2}, 5)\ m$. *The center of circulation lies at about* $\mathbf{C} = (4.86, -1.67)\ m$. *Dashed triangle corresponds to* $t = 0$ *and solid triangle taken at* $t = 270\ s$ *is similar (same shape, different size) to the dashed one. The initial positions of the three vortices were derived by the method after Aref et al. (1992) shown in Fig. A68. The collapse occurs after about* $t_c \approx 334\ s$ *(b) Same trajectories as in (a) overlaid on a satellite image showing an extratropical low pressure system near Iceland (source: NASA, Aqua MODIS instrument, online available at* `http://visibleearth.nasa.gov/view.php?id=68992`*) The satellite image was taken on 04.09.2003.*

the area spanned by the vortices changes in size but remains constant in shape. In Fig. 14a we plotted an explicit example of the collapsing trajectories of three point vortices with circulations $(\Gamma_1, \Gamma_2, \Gamma_3) = (2, 2, -1)\ \mathrm{m}^2/\mathrm{s}$. Following the example of Kudela (2014)[39], we overlaid the trajectories of the collapsing point vortices with the satellite image of an extratropical cyclone (see Fig. 14b). The similarity of the theoretical solution and the cloud pattern of the real vortex is astonishing. Note, that due to the scale invariance of the point vortex systems, the shape of the collapsing vortex trajectories remains similar (logarithmic spiral) only the time (or circulation as we have discussed earlier in section 3.4.5.1) needs to be scaled accordingly if the horizontal length dimension is scaled by a constant factor (e.g. Newton, 2001; Kudela, 2014). Furthermore, Novikov and Sedov (1979) showed that the collapse of three vortices lead to a resulting vortex whose intensity is larger than the intensity of the three single vortices. Thus, we might interpret the three single vortices as smaller-scale (convective) cells that form a larger-scale vortex. Then, we can assume that the anticyclonicly rotating vortex is a

[39] Kudela (2014) used the same satellite image but overlaid it with the trajectories of N=7 collapsing point vortices.

vortex of cyclostrophic balance (and therefore has a low pressure core likewise to the other cyclonicly rotating vortices as we have shown in chapter 3.2.1.3). In our example given in Fig. 14 the total circulation is equal to $\Gamma_{total} = \Gamma_1 + \Gamma_2 + \Gamma_3 = 3\,\mathrm{m}^2/\mathrm{s}$ which is larger than a single positive vortex. Imagine to have ten sets of this tripole. This will lead to a vortex with a circulation one magnitude larger than the single vortices it is composed of. Such a N=30 point vortex collapse was analysed in Kudela (2014).
Already Novikov and Sedov (1979) presented briefly the solutions of the N=4, N=5 vortex collapses, but also discussed the relevance of the expanding motion with respect to the creation of vortices in e.g. geophysical fluid dynamics. Indeed, a common observation is the split of convective storms. This means that new cells are created from a single cell. Furthermore, collapsing (and expanding) motions might offer a way to understand the interaction of two-dimensional and three-dimension dynamics as well as interactions of the small- and large-scale systems: for example if we interpret the collapsing point as updraft of the larger-scale system or the single point vortices as up- or downdrafts of smaller-scale convective cells embedded in a larger vortex. Hence, the topic of point vortex dynamics is of high relevance to real world fluid dynamics, but further investigations will be necessary to advance a deeper understanding.
Finally, it is worth noting, that the work on point vortices of Müller and Névir (2014) and Müller et al. (2015) and the method of vortex identification that will be introduced in this work later (chapter 6) already inspired several Bachelor's (Sonntag, 2012; Pültz, 2014), Master's (Hirt, 2016) and Diploma thesis (Isernhagen, 2015) at the Institute of Meteorology of the Freie Universität Berlin with emphasis on the application of point vortices to atmospheric blocking situations.

3.5 Concluding remarks

We have introduced and discussed the equations of motion in different reference frames (inertial and noninertial). Thereby, the transformation to a natural coordinate system in a rotating reference frame proved useful in the study of the horizontal flow that occurs around a vortex. We investigated these equations in more detail with help of a scale analysis. The scale analysis revealed the different prevailing balances of forces that occur on different scales. Furthermore, we could show that the properties and the appearance of cyclonic and anticyclonic vortices depend on the scale, too: While the structure of high and low pressure systems is qualitatively similar under geostrophic balance except of the sign of their circulation, the highs are restricted to larger radii and less intense pressure gradients in case of the gradient wind balance. Under cyclostrophic balance, however, cyclonicly as well as anticyclonicly rotating vortices are likewise associated with a low core pressure.
Furthermore, we identified the vorticity as local rotation rate and the circulation as a global measure of rotation. We showed that the circulation is a conserved quantity under

incompressible, barotropic and inviscid conditions. Under these conditions, we derived the important Biot-Savart formula that states that every vorticity distribution induces a velocity field. Moreover, the Biot-Savart formula can be used to estimate the range of influence of a vortex on its environment or on other vortices. This led to the derivation of the point vortex equations which can be seen as a first idealized, simplified model of large-scale atmospheric vortices. However, it is possible to derive other important vortex models from the equations of motion making different assumptions as we will see in the next chapter 4.

4 Theoretical vortex models: Revealing the properties of a vortex

This chapter deals with typical vortex models that can be derived as exact solutions of the Navier-Stokes equations. These models can be useful for improving the physical understanding of vortices and their determining properties. We will show in this chapter that at fixed time the velocity and vorticity profiles of the vortex models are determined completely by two properties: the circulation of the vortex as well as its size (radius). However, only under very idealized assumptions these exact solutions are derived.

4.1 Governing equations in cylindrical coordinates

Since vortices are observed to have a columnar structure, a cylindrical coordinate system seems the appropriate choice in order to determine vortex solutions of the equations of motion. Therefore, some mathematical expressions will be processed explicitly before analysing the equations.

4.1.1 Cylindrical coordinate system

Assume the cylindrical coordinate system with coordinates (r, θ, z) with corresponding unit vectors $\mathbf{e}_r, \mathbf{e}_\theta, \mathbf{e}_z$. The ∇-operator in cylindrical coordinates is given by

$$\nabla = \frac{\partial}{\partial r}\mathbf{e}_r + \frac{1}{r}\frac{\partial}{\partial \theta}\mathbf{e}_\theta + \frac{\partial}{\partial z}\mathbf{e}_z \ . \tag{140}$$

Then, divergence and rotation of an arbitrary vector $\mathbf{A} = (A_r, A_\theta, A_z)$ are given by

$$\nabla \cdot \mathbf{A} = \frac{1}{r}\frac{\partial}{\partial r}(rA_r) + \frac{1}{r}\frac{\partial A_\theta}{\partial \theta} + \frac{\partial A_z}{\partial z} \tag{141}$$

$$\nabla \times \mathbf{A} = \left(\frac{1}{r}\frac{\partial A_z}{\partial \theta} - \frac{\partial A_\theta}{\partial z}\right)\mathbf{e}_r + \left(\frac{\partial A_r}{\partial z} - \frac{\partial A_z}{\partial r}\right)\mathbf{e}_\theta + \frac{1}{r}\left(\frac{\partial}{\partial r}(rA_\theta) - \frac{\partial A_r}{\partial \theta}\right)\mathbf{e}_z \tag{142}$$

and the Laplacian of an arbitrary function f is

$$\Delta f = \frac{1}{r}\frac{\partial}{\partial r}\left(r\frac{\partial f}{\partial r}\right) + \frac{1}{r^2}\frac{\partial^2 f}{\partial \theta^2} + \frac{\partial^2 f}{\partial z^2} \ . \tag{143}$$

Further, we will denote the velocity components by $\mathbf{u} = (u_r, u_\theta, u_z)$ and the vorticity components by $\boldsymbol{\omega} = \nabla \times \mathbf{u} = (\omega_r, \omega_\theta, \zeta)$, respectively. In detail, the vorticity components follow from equation (142)

$$\omega_r = \frac{1}{r}\frac{\partial u_z}{\partial \theta} - \frac{\partial u_\theta}{\partial z} \quad , \quad \omega_\theta = \frac{\partial u_r}{\partial z} - \frac{\partial u_z}{\partial r} \quad , \quad \zeta = \frac{1}{r}\left(\frac{\partial}{\partial r}(ru_\theta) - \frac{\partial u_r}{\partial \theta}\right) \ . \tag{144}$$

4.1.2 Governing equations in the cylindrical coordinate system

For incompressible flow, i.e. constant density ($\rho = const$), the continuity equation $\partial\rho/\partial t + \nabla \cdot (\mathbf{u}\rho)$ reduces to $\nabla \cdot \mathbf{u} = 0$. In component form using (141) the continuity equation is then given by

$$\frac{1}{r}\frac{\partial r u_r}{\partial r} + \frac{1}{r}\frac{\partial u_\theta}{\partial \theta} + \frac{\partial u_z}{\partial z} = 0 \ . \tag{145}$$

In a non-rotating reference frame considering gravity, the Navier-Stokes equations (55) read

$$\frac{\partial \mathbf{u}}{\partial t} = -\mathbf{u} \cdot \nabla \mathbf{u} - \frac{1}{\rho}\nabla p + \mathbf{g} + \nu \nabla^2 \mathbf{u} \ , \tag{146}$$

where we have applied the material derivative (2) and made use of $\mathbf{F}_R = \nu\nabla^2\mathbf{u}$ where ν is the viscosity; $\mathbf{g}$ is the gravitational acceleration and p is the pressure. The advection can be rewritten as $\mathbf{u} \cdot \nabla \mathbf{u} = \frac{1}{2}\nabla \mathbf{u}^2 - \mathbf{u} \times \boldsymbol{\omega}$ such that we obtain equation (66b) under adiabatic conditions ($T\nabla s = 0$). Explicitly, the single components of the equations of motion are written as

$$\frac{\partial u_r}{\partial t} = (u_\theta \zeta - u_z \omega_\theta) - \frac{\partial B^*}{\partial r} + \nu \nabla^2 u_r \quad : \text{ radial component} \tag{147a}$$

$$\frac{\partial u_\theta}{\partial t} = (u_z \omega_r - u_r \zeta) - \frac{1}{r}\frac{\partial B^*}{\partial \theta} + \nu \nabla^2 u_\theta \quad : \text{ azimuthal component} \tag{147b}$$

$$\frac{\partial u_z}{\partial t} = (u_r \omega_\theta - u_\theta \omega_r) - \frac{\partial B^*}{\partial z} + \nu \nabla^2 u_z \quad : \text{ vertical component} \tag{147c}$$

where $B^* = \frac{1}{2}\mathbf{u}^2 + h + \Phi_g$ is the Bernoulli stream function in an inertial, absolute reference frame[40].

4.2 Exact vortex solutions under idealized conditions

Exact vortex solutions follow often from linearization of the vorticity equations that are derived by taking the curl of (147). The vorticity equations become linear when the velocity vector and the vorticity vector are aligned such as in *Beltramian* flow ($\mathbf{u} \times \boldsymbol{\omega} = 0$). Wu et al. (2007) show that the vorticity equations become linear too for *generalized Beltramian* flows where $\nabla \times (\mathbf{u} \times \boldsymbol{\omega}) = 0$. In this section, we will start from highly idealized conditions and work through to more complicated set-ups. In all cases, we will assume axisymmetry, incompressibility and adiabatic conditions.

4.2.1 Inviscid, stretch-free solutions (Point vortex, Rankine vortex)

For axisymmetric columnar vortices, all dependencies in azimuthal direction vanish in (147b), i.e. $\partial/\partial\theta = 0$. Assume the following conditions

[40] Under adiabatic conditions (entropy does not change: $ds = 0$), changes in enthalpy are proportional to pressure changes only: $dh = \rho^{-1}dp + Tds = \rho^{-1}dp$. This can be used in order to derive equations (147) with term $B^* = \frac{1}{2}\mathbf{u}^2 + h + \Phi_g = \frac{1}{2}\mathbf{u}^2 + \frac{1}{\rho}dp + \Phi_g$ with $\int \frac{1}{\rho}dp = \frac{1}{\rho}p$ for $\rho = const$.

(*i*) axisymmetry ($\partial/\partial\theta = 0$);

(*ii*) incompressibility ($\nabla \cdot \mathbf{u} = 0$);

(*iii*) inviscid conditions ($\nu = 0$)

(*iv*) velocity vector is zero except of its azimuthal component $u_\theta = u_\theta(r,t)$.

Then, the vorticity vector has only a non-zero vertical component ζ. Velocity and vorticity components are given by

$$u_r = 0 \quad , \quad u_\theta = u_\theta(r,t) \quad , \quad u_z = 0$$
$$\omega_r = 0 \quad , \quad \omega_\theta = 0 \quad , \quad \zeta = \frac{1}{r}\frac{\partial}{\partial r}(ru_\theta) \; .$$

and the Navier-Stokes equations (147) simplify to

$$\frac{1}{\rho}\frac{\partial p}{\partial r} = \frac{u_\theta^2}{r} \tag{148a}$$
$$\frac{\partial u_\theta}{\partial t} = 0 \tag{148b}$$
$$\frac{1}{\rho}\frac{\partial p}{\partial z} = -g \tag{148c}$$

While the horizontal component of the Navier-Stokes equation (148a) reduces to the well-known cyclostrophic balance that describes the balance between the radial pressure gradient force and the centrifugal force, the vertical component (148c) yields the hydrostatic balance (balance between vertical pressure gradient and gravitation). Note that, even though we call the balance cyclostrophic, the equations are given in an inertial reference frame and the velocity is equal to the absolute velocity. However, the structure of equation (148a) is equal to the cyclostrophic balance in a noninertial, rotating reference frame (cf. equation (93), chapter 3.2.1.3). Nonetheless, we will stick to the term *cyclostrophic*. Wu et al. (2007) call this type of vortex a *pure vortex*. It is characterized by streamlines that are closed circles around the z-axis and by vorticity lines that are aligned to the z-axis.
Further complicating our system by adding a non-zero vertical velocity component to the velocity vector changes condition (*iv*) to

(*iv**) $\mathbf{u} = (0, u_\theta(r,t), u_z(r,t))$.

This gives an additional azimuthal component in the vorticity vector $\boldsymbol{\omega} = (0, \omega_\theta(r,t), \zeta(r,t))$. Then, the components of velocity and vorticity are

$$u_r = 0 \quad , \quad u_\theta = u_\theta(r,t) \quad , \quad u_z = u_z(r,t) \tag{149a}$$

$$\omega_r = 0 \quad , \quad \omega_\theta = -\frac{\partial u_z}{\partial r} \quad , \quad \zeta = \frac{1}{r}\frac{\partial}{\partial r}(r u_\theta) \; . \tag{149b}$$

It should be noted that according to the continuity equation the vertical velocity is independent of height. This means that no axial stretching occurs. In the simpler case of time-independent vertical velocity $u_z = u_z(r)$ the results from above (cyclostrophic/hydrostatic balance) are retained. In the more general case of time-dependent vertical velocity only the vertical component of the Navier-Stokes equations changes to

$$\frac{\partial u_z}{\partial t} = -\frac{1}{\rho}\frac{\partial p}{\partial z} - g \tag{150}$$

while the horizontal equations (cyclostrophic balance) remain. Such a vortex with additional non-zero vertical velocity is called *swirling vortex* (Wu et al., 2007) since the flow is helical with non-zero helicity density $\boldsymbol{\omega} \cdot \mathbf{u} \neq 0$.
The relevant equation of horizontal motion in both cases (148a) give the cyclostrophic balance. Wu et al. (2007) therefore states that a vortex under inviscid, stretch-free conditions *can have arbitrary radial dependence*. Hence, plenty of inviscid vortex models are possible solutions of the Navier-Stokes equations. Some examples are listed below

(1) **Point vortex:**

A point vortex is a vortex of zero dimension. The vorticity is concentrated only in one point in the vortex center. The determining property of a point vortex is its circulation Γ. Velocity and vorticity profiles depend only on the radial component r and can be expressed as (following Newton, 2001)

$$\begin{aligned} u_\theta(r) &= \frac{\Gamma}{2\pi r} \\ \zeta(r) &= \delta(r) \\ u_r &= u_z = 0 \\ \omega_r &= \omega_\theta = 0 \end{aligned}$$

The Dirac delta function is $\delta(r) = \infty$ for $r = 0$ and $\delta(r) = 0$ for $r \neq 0$.

(2) **Rankine vortex:**

The velocity and vorticity profiles are given by (after Newton, 2001)

$$u_\theta(r) = \begin{cases} \left(\frac{\Gamma}{2\pi R^2}\right) r & , \quad r \leq R \\ \frac{\Gamma}{2\pi r} & , \quad r > R \end{cases}$$

$$\zeta(r) = \begin{cases} \frac{\Gamma}{\pi R^2} & , \quad r \leq R \\ \delta(r) & , \quad r > R \end{cases}$$

$$u_r = u_z = 0$$

$$\omega_r = \omega_\theta = 0$$

Here, Γ denotes the circulation calculated at radius R and δ is the Dirac delta function, therefore $\zeta = 0$ for $r > R$. Inside a circle of radius R (inside the vortex core), the flow equals a solid body rotation with constant vorticity. The velocity in the center is zero ($u_\theta(r = 0) = 0$). It constantly increases up to radius R where u_θ is maximal. Outside of R, the velocity declines as $1/r$ similar to the point vortex solution. Velocity and vorticity profiles of the Rankine vortex model and the point vortex model are compared in Figure 15.

Note, that we can rewrite the velocity inside the core with help of the constant vorticity $\zeta = \Gamma/(\pi R^2)$ as

$$u_\theta(r) = \frac{1}{2}\zeta r \quad , \; r \leq R \tag{151}$$

We can also calculate the radial pressure profile by integrating over the radial component of the equations of motion (148a) and assuming incompressible conditions:

$$p(r) \sim \int \frac{1}{\rho} dp = \int \frac{u_\theta^2}{r} dr = \frac{1}{4} \int \frac{\zeta^2 r^2}{r} dr = \frac{1}{8}\zeta^2 r^2 + C \sim r^2 \quad , \; r \leq R \tag{152}$$

C denotes a constant of integration. We conclude that in case of the Rankine vortex model the radial pressure profile follows a parabola inside the vortex core (see also Figure 15b). Analogously, outside the core we obtain an inverted parabola

$$p(r) \sim \int \frac{1}{\rho} dp = \int \frac{u_\theta^2}{r} dr = \frac{\Gamma^2}{4\pi^2} \int \frac{1}{r^3} dr = -\frac{\Gamma^2}{8\pi^2} r^{-2} + C_2 \sim -r^{-2} \; , \; r > R$$

C_2 denotes another constant of integration. Since the pressure is a continuous variable, it is required that both sides of the function $p(r)$ are equal at the radius R. Then it follows that $C_2 = \Gamma^2/(4\pi^2 R^2) + C$ where C is the constant of integration derived in (152). The pressure profile of a Rankine vortex is plotted in Figure 15b.

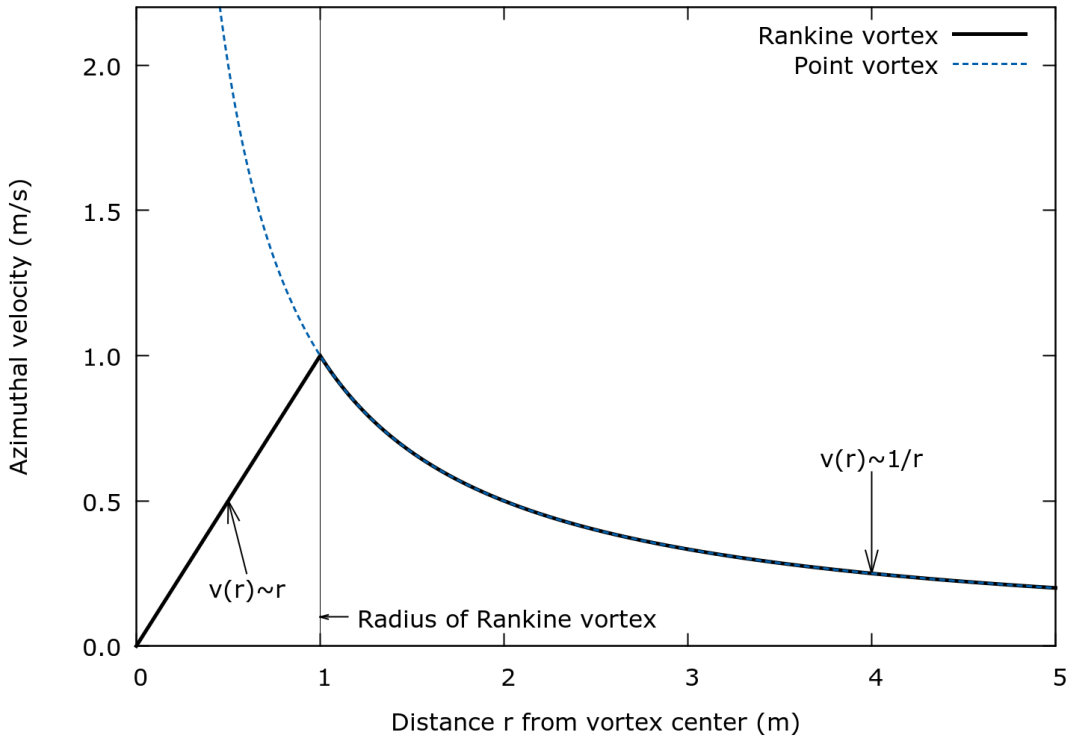

(a) Azimuthal velocity profile

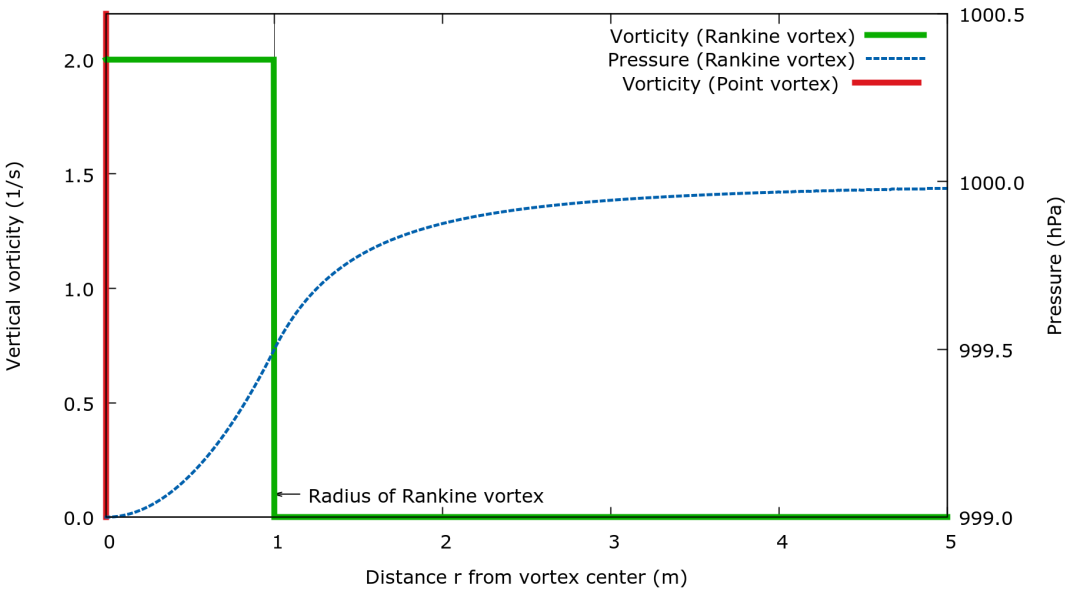

(b) Vertical vorticity and pressure profile

Figure 15: *Comparison of (a) azimuthal velocity and (b) vertical vorticity profiles of a point vortex and a Rankine vortex. Additionally, we plotted the pressure profile of the Rankine vortex in (b). The parameters are plotted in dependence on the distance r from the vortex center. We assumed a circulation of* $\Gamma = 2\pi\, m^2/s$ *for both vortex types and a vortex radius of* $R = 1\, m$ *for the Rankine vortex. Constant of integration C of (152)was set to* $C = 999\, hPa$*;* $\rho = 1\, kg/m^3$.

4.2.2 Viscous, stretch-free solutions (Lamb-Oseen vortex)

We further take into account viscosity. Then the solutions become time-dependent and the conditions change to

(i) axisymmetry $(\partial/\partial\theta = 0)$;

(ii) incompressibility $(\nabla \cdot \mathbf{u} = 0)$;

(iii^*) viscous conditions $(\nu \neq 0)$;

(iv^*) $\mathbf{u} = (0, u_\theta(r,t), u_z(r,t))$.

While the components of the velocity and vorticity vectors still equal the set-up in (149), viscous terms enter the Navier-Stokes equations balancing the accelerations:

$$\frac{1}{\rho}\frac{\partial p}{\partial r} = \frac{u_\theta^2}{r} \tag{153a}$$

$$\frac{\partial u_\theta}{\partial t} = \nu\nabla^2 u_\theta \tag{153b}$$

$$\frac{\partial u_z}{\partial t} = -\frac{1}{\rho}\frac{\partial p}{\partial z} - g + \nu\nabla^2 u_z \tag{153c}$$

The equations of u_θ and u_z are decoupled. If the hydrostatic balance still is assumed, the unsteady terms are compensated only by viscous terms. Setting the vertical velocity to zero $(u_z = 0)$, a simple solution of the Navier-Stokes equations is represented by the

(3) **Lamb-Oseen vortex:**

Velocity and vorticity profiles are time-depending (after Newton, 2001, with slight modifications)

$$u_\theta(r,t) = \frac{\Gamma}{2\pi r}\left(1 - exp\left(-\frac{r^2}{R(t)^2}\right)\right)$$
$$\zeta(r) = \frac{\Gamma}{\pi R(t)^2} exp\left(-\frac{r^2}{R(t)^2}\right)$$
$$u_r = u_z = 0$$
$$\omega_r = \omega_\theta = 0$$

where the time-dependence lies in a time-depending vortex core radius $R(t)$. The Lamb-Oseen vortex represents a decaying vortex that started with the profile $u_\theta(r, t = 0) = \Gamma/(2\pi r)$ of a point vortex at time $t = 0$. The vortex core radius R, initially $R(t = 0) = 0$, increases over time by $R(t) = \sqrt{4\nu t}$. Note, that the vorticity profile is Gaussian. For fixed times t, the velocity profile resembles that of the Rankine vortex for small $r \to 0$ and for large $r \gg R$: for small r, inside the

vortex core the velocity is constantly increasing[41]; for large r, the profile equals that of a point vortex:

$$u_\theta(r,t)|_{r\to 0} \approx \frac{\Gamma}{2\pi R^2} r$$
$$u_\theta(r,t)|_{r\gg R} \approx \frac{\Gamma}{2\pi r}$$

Summarizing, the velocity profile for fixed times is determined completely by circulation Γ and radius R. While the solution resembles the Rankine vortex at the limits of the domain, the profiles of velocity and vorticity are continuously differentiable in contrast to the Rankine vortex. The profiles of the Lamb-Oseen and the Rankine vortex are compared in Figure 16.

4.2.3 Viscous solutions with axial stretching (Burgers vortex)

We allow now the vortex to stretch along the z-axis by a factor γ (can be constant). The conditions change to

- (i) axisymmetry $(\partial/\partial\theta = 0)$;
- (ii) incompressibility $(\nabla \cdot \mathbf{u} = 0)$;
- (iii^*) viscous conditions $(\nu \neq 0)$;
- (iv^{**}) allow vertical stretching $u_z = u_z(r,z,t)$.

A simple linear and uniform z-dependence of the vertical velocity is given by $u_z(z,t) = \gamma(t)z$ where $\gamma(t) > 0$. From the continuity equation (145) then follows that there is a radial inwardly-directed velocity component u. Velocity and vorticity components are given as (after Wu et al., 2007)

$$u_r(r,t) = -\frac{1}{2}\gamma(t)r \quad , \quad u_\theta = u_\theta(r,t) \quad , \quad u_z(z,t) = \gamma(t)z \tag{154a}$$
$$\omega_r = 0 \quad , \quad \omega_\theta = 0 \quad , \quad \zeta = \frac{1}{r}\frac{\partial}{\partial r}(ru_\theta) \; . \tag{154b}$$

Since $u_\theta \neq u_\theta(z)$ and $u_z \neq u_z(r)$, only the vertical vorticity component remains. Wu et al. (2007) point out, that this setting can only be fulfilled locally for $r < \infty$, and $|z| < \infty$. As a further simplification the stretching is assumed to be constant. Instead

[41] This result follows from an Taylor series expansion of the exponential term in terms of r^2: $\exp(-r^2/R^2)|_{r^2\to 0} \approx 1 - r^2/R^2$

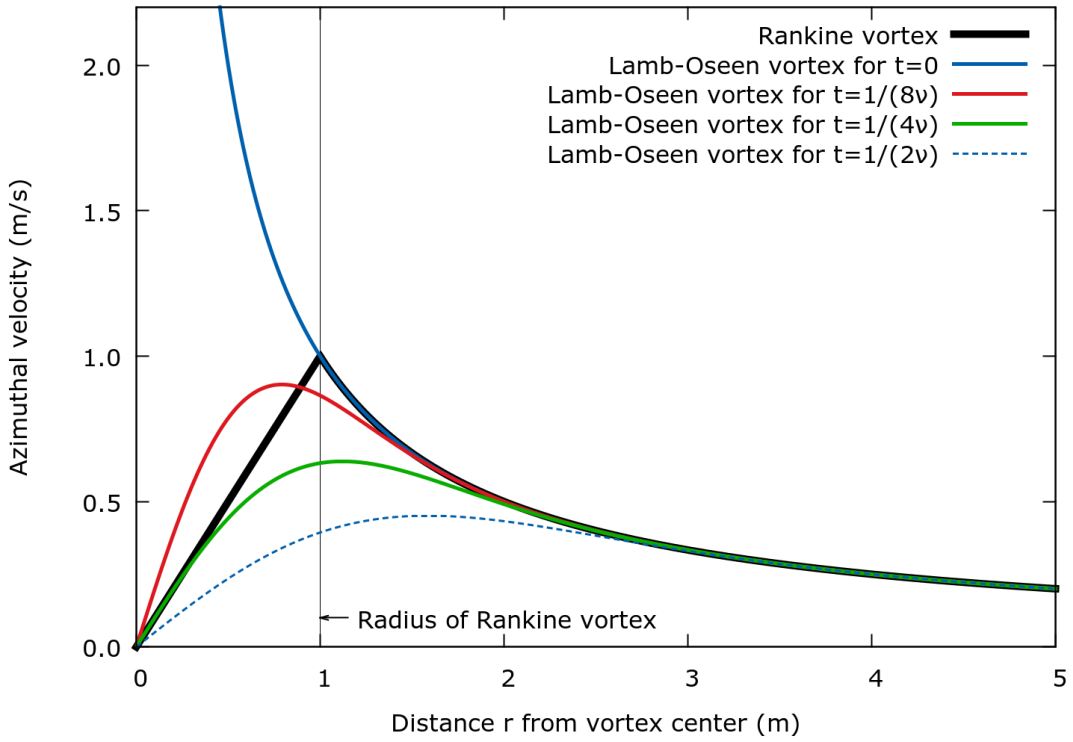

(a) Azimuthal velocity profile

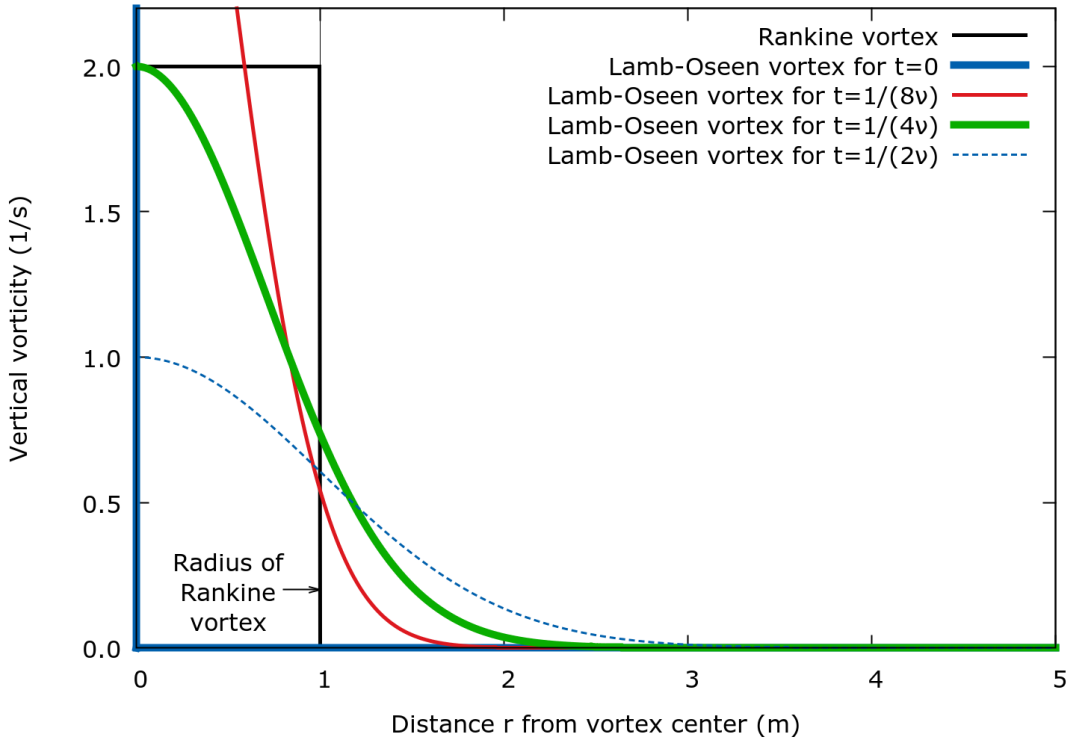

(b) Vertical vorticity profile

Figure 16: *Comparison of azimuthal velocity and vertical vorticity profiles of a Rankine vortex and a Lamb-Oseen vortex for different time steps t. Velocity and vorticity are plotted in dependence on the distance r from the vortex center. We assumed a circulation of* $\Gamma = 2\pi\, m^2/s$ *for both vortex types and a vortex radius of* $R = 1\, m$ *for the Rankine vortex;* $\rho = 1\, kg/m^3$*. Note that for* $t = 0$ *the Lamb-Oseen vortex model is equal to the solution of a point vortex.*

of using the Navier-Stokes equations, it is useful to look at the vorticity transport equations (equation 105 under barotopic conditions for the relative instead of the absolute vorticity). Only the vertical component of the vorticity equations does not vanish

$$\frac{\partial \zeta}{\partial t} = -\mathbf{u} \cdot \nabla \zeta + \boldsymbol{\omega} \cdot \nabla u_z + \nu \nabla^2 \zeta \tag{155}$$

Explicitly after applying the conditions (i)-(iv^{**}), the vorticity equation reads

$$\frac{\partial \zeta}{\partial t} = \underbrace{\frac{1}{2}\gamma r \frac{\partial \zeta}{\partial r}}_{\text{Advection}} + \underbrace{\gamma \zeta}_{\text{Stretching}} + \underbrace{\frac{\nu}{r}\frac{\partial}{\partial r}\left(r \frac{\partial \zeta}{\partial r}\right)}_{\text{viscous}} \tag{156}$$

The advection is in inward radial direction and the stretching is uniform along the z-axis. Under steady conditions ($\partial/\partial t = 0$), a solution is represented by the

(4) **Burgers vortex:**

In the Burgers vortex, the viscous terms are balanced by advective and stretching terms (see (156) for $\partial\zeta/\partial t = 0$). Velocity and vorticity profiles for $\gamma > 0$ are (after Wu et al., 2007, who additionally give a more detailed derivation)

$$\begin{aligned} u_\theta(r) &= \frac{\Gamma}{2\pi r}\left(1 - exp\left(-\frac{r^2}{R_*^2}\right)\right) \\ u_r &= -\frac{1}{2}\gamma r \\ u_z &= \gamma z \\ \zeta(r) &= \frac{\gamma\Gamma}{4\pi\nu} exp\left(-\frac{r^2}{R_*^2}\right) \\ \omega_r &= \omega_\theta = 0 \end{aligned}$$

Here, the core radius R_* is determined by stretching γ and viscosity ν as $R_* = \gamma/(4\nu)$. At fixed time, the azimuthal component of the velocity resembles that of the Lamb-Oseen vortex (cf. Newton, 2001). However, the vortex is stretched along the z-axis and has non-zero u_r- and u_z-components. The vorticity profile is Gaussian.

4.3 Concluding remarks on vortex models

Table 4 gives an overview over the discussed vortex models, the assumptions made and the determining properties. We can conclude, that circulation and radius (together with time) determine the appearance of a vortex. Therefore, these properties should be the first choice when analysing vortex statistics. It should be noted though, that more vortex models of increasing complexity exist (see e.g. Wu et al., 2007). Finally, we want to point out that the highly idealized, theoretical vortex models were derived

Table 4: *Overview over discussed vortex models: assumptions and determining properties. Circulation, radius and time are denoted by* Γ, R, t, *respectively.*

	Stretching	Viscous	Time-dependent	Properties
Point vortex	no	no	no	Γ
Rankine vortex	no	no	no	Γ, R
Lamb-Oseen vortex	no	yes	yes	Γ, R, t
Burgers vortex	yes	yes	no	Γ, R

in an inertial reference frame. In contrast, atmospheric vortices are usually observed in a noninertial reference frame. We will treat this topic in the following chapter 5.

5 Atmospheric vortices: Novel intensity measures based on the horizontal balance of forces[42]

This chapter deals with possible measures of vortex intensity. In order to find appropriate intensity measures, we will use the knowledge summarized in the previous two chapters that treat the dynamics of the flow field. We have seen that the theoretical vortex models were derived under highly idealized conditions in an inertial, non-rotating reference frame. This stands in contrast to the general observation of atmospheric vortices in a noninertial, rotating reference frame considering the rotation of the Earth. Before going into more details on this topic we will first present some commonly used intensity measures of vortices.

5.1 On the intensity of vortices on different scales

It is not trivial to define a unified intensity measure that fits different atmospheric vortex types like tornadoes, tropical and extratropical cyclones. These systems are associated with a low core pressure. They can produce high wind speeds causing severe damage. Therefore, their intensity is often measured by the maximum wind speed (averaged or gust), their minimum core pressure, their maximum vorticity or by classifications based on these local parameters. Pressure — or alternatively geopotential height — and vorticity are common intensity parameters used to classify extratropical and tropical cyclones (e.g. Blender et al., 1997; Hodges et al., 1994). Furthermore, their intensity is measured by the 10-minutes (for tropical cyclones 1-minute) averaged wind speed or by classification schemes based on the wind speed such as the Beaufort-intensity scale for extratropical cyclones (Hanson et al., 2004) or the Saffir-Simpson intensity scale for tropical cyclones (in the North-Atlantic and North-Eastern Pacific). Since there are only few measurements of wind speed and pressure in tornadoes, their intensity is often estimated by the caused damage in terms of the Fujita intensity scale (F-scale, introduced by Fujita, 1971), the Enhanced Fujita-scale (EF-scale WSCE, 2006) or the Torro-scale (introduced by Terence Meaden in 1972 as published in Kirk, 2014). Beaufort-scale (B), Fujita-Scale (F) and Torro-Scale are connected to wind speed via (after Müller, 1979; Fujita, 1971)

$$v(B) = 0.835\, ms^{-1} B^{3/2} \qquad B = [1, .., 12] \tag{157}$$

$$v(F) = 6.300\, ms^{-1} (F+2)^{3/2} \qquad F = [0, .., 5] \tag{158}$$

$$v(T) = 2.365\, ms^{-1} (T+4)^{3/2} \qquad T = [0, .., 10] \tag{159}$$

[42] This chapter is based on three publications: Schielicke and Névir (2009, 2011, 2013). These publications deal with the intensity of vortices on different scales: mass-specific energy of displacement in Schielicke and Névir (2009) and mass-related atmospheric moment in Schielicke and Névir (2011). Further we comprehensively studied the temporal and intensity behavior of tornadoes in Schielicke and Névir (2013). The interested reader is referred to these publications for further details.

Based on these listed local parameters other measures can be deduced such as the kinetic energy (e.g. Kurgansky, 2000; Dotzek et al., 2005), the mass flux or the energy flux density (so called E-scales, introduced by Dotzek, 2009).
The large diversity of intensity measures complicates the search for a unified parameter valid for different vortex types. Which parameter can be used in order to compare vortices on different scales? We treated this topic in our publications Schielicke and Névir (2009, 2011) by defining a mass-specific energy of displacement and a mass-related atmospheric moment based on the horizontal equations of motion. These parameters will be introduced in the next sections.

5.2 Mass-specific energy of displacement (Schielicke and Névir, 2009)

In Schielicke and Névir (2009), we defined a unifying parameter: the mass-specific energy of displacement. Theoretical basis are the horizontal equations of motion in natural coordinates neglecting friction and assuming zero vertical velocity (see chapter 3.1.6, equations (81), (82)). Note, that this approach is similar to the theoretical vortex models (see chapter 4) with the difference that we will work in a noninertial, rotating reference frame taking into account centrifugal as well as Coriolis force terms. While the theoretical vortex model approaches mainly serve the search for an appropriate radial wind profile, we will integrate over the horizontal equations of motion in order to derive an intensity measure. Thereby, we will make use of the theoretically derived wind profiles.
Under the assumption of zero vertical velocity and inviscid conditions we derive two components of the horizontal equations of motion in natural coordinates that read

$$\frac{Dv_h}{Dt} = -\frac{1}{\rho}\frac{\partial p}{\partial s} \quad \text{in streamwise direction, parallel to } \mathbf{v} \tag{160a}$$

$$\frac{v_h^2}{R} + f v_h = -\frac{1}{\rho}\frac{\partial p}{\partial n} \quad \text{in crosswise direction, normal to } \mathbf{v} \tag{160b}$$

where v_h is the magnitude of the horizontal wind vector; p is the pressure; ρ is the density; f is the Coriolis parameter and R is the radius of curvature. At the moment of maximum intensity, the equation in streamwise direction (160a) becomes zero since the motion is not accelerated at this moment. Only the component perpendicular to the flow (160b) remains. Under the further assumption of axisymmetry, the transformation

between the natural $(\boldsymbol{t}, \boldsymbol{n}, \boldsymbol{k})$ and the cylindrical coordinate system $(\boldsymbol{e}_r, \boldsymbol{e}_\theta, \boldsymbol{e}_z)$ is given by

$$\left.\begin{array}{lll} \boldsymbol{n} = -\boldsymbol{e}_r & , \quad \boldsymbol{t} = \boldsymbol{e}_\theta & , \quad \boldsymbol{k} = \boldsymbol{e}_z \\ v_h = u_\theta & , \quad R = r & \\ dn = -dr & , \quad ds = rd\theta & \end{array}\right\} \quad \text{for cyclonic motion } (R > 0)$$

where $u_\theta = v_h$ is the azimuthal component of the wind vector in cylindrical coordinates and the radial and vertical components are zero: $\mathbf{u} = (0, u_\theta(r), 0)$. Using these transformations in equation (80) and neglecting the l-Coriolis terms leads to the following horizontal (azimuthal) equation of motion in cylindrical coordinates

$$\underbrace{\frac{u_\theta^2}{r}}_{Centrifugal\ term\ Z} + \underbrace{fu_\theta}_{Coriolis\ term\ C} = \underbrace{\frac{1}{\rho}\frac{\partial p}{\partial r}}_{Pressure\ gradient\ P} \tag{161}$$

Given in a relative, non-inertial, rotating reference frame, equation (161) represents the counterpart of the azimuthal component of the equation of motion (147b) in an absolute, inertial, non-rotating reference frame that we have used in order to derive solutions for the theoretical vortex models (chapter 4). More details on this transformation can be found in Schielicke and Névir (2009). We obtain (161) in case of anticyclonic motion $(R < 0)$, too. However, the transformations are different:

$$\left.\begin{array}{lll} \boldsymbol{n} = \boldsymbol{e}_r & , \quad \boldsymbol{t} = -\boldsymbol{e}_\theta & , \quad \boldsymbol{k} = \boldsymbol{e}_z \\ v_h = -u_\theta & , \quad R = -r & \\ dn = dr & , \quad ds = -rd\theta & \end{array}\right\} \quad \text{for anticyclonic motion } (R < 0)$$

Moreover, we have already shown in chapter 3.2 that the vortices at their moment of maximum intensity are completely determined by their prevailing horizontal balance of forces. prevailing balances). The accelerations $a(r)$ that balance the pressure gradient force in the horizontal equation of motion are defined as:

$$a(r) := \frac{u_\theta^2}{r} + fu_\theta \tag{162}$$

Finally, we defined the mass-specific energy of displacement e as the radial integral over the accelerations $a(r)$ starting from the vortex center $(r = 0)$ to its radius $r = R$:

$$e := \int_0^R a(r)dr = \int_P^{P_0} \alpha dp \tag{163}$$

where $\alpha = V/m = \rho^{-1}$ is the mass-specific volume. The relationship between the

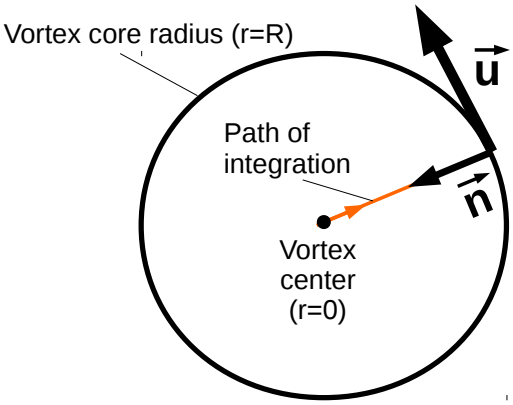

Figure 17: *Path of integration of the energy of displacement.* $\vec{\mathbf{u}}$*: velocity vector,* $\vec{\mathbf{n}}$*: unit vector in normal direction*

natural coordinate system and the path of integration is displayed in Figure 17. At the moment of maximum intensity, the energy of displacement can be interpreted as the work done in order to generate the system[43]. Although the path of integration from the center to the edge of the system is perpendicular to the motion at the moment of maximum intensity, it is exactly the way that the particles were forced to take during the generation and intensification process of the system. These particle paths describe the unbalanced deviations from the prevailing balance of forces, e.g. in case of the cyclones the ageostrophic (asemigeostrophic) components or in case of the tornadoes the acyclostrophic components of the motion.

5.2.1 Tornadoes and cyclostrophic balance

Under cyclostrophic balance, the Coriolis term in (163) vanishes and we approximated the wind field in a tornado by a Rankine vortex profile (see chapter 4.2.1). Inside the radius R of the tornado the velocity increases linearly along the radial component as $u_\theta = \omega_t r$ with angular velocity $\omega_t = const.$; note, that we have defined the angular velocity with help of the vortex radius and its circulation as $\omega_t = \Gamma/2\pi R^2$ in chapter 4.2.1. The velocity is maximal at the vortex core radius $r = R$, hence, $u_{max} = \omega_t R$. The

[43] This can be seen by the following considerations: The first law of thermodynamics is given in terms of internal energy as $c_v DT/Dt = -pD\alpha/Dt + J$ (eq. 44) and in terms of enthalpy as $c_p DT/Dt = \alpha Dp/Dt + J$ (eq. 46). Under adiabatic conditions ($J = 0$) we therefore obtain $\alpha dp = -(c_v/c_p)pd\alpha \sim -pd\alpha$ where the latter describes the work done by volume changes.

energy of displacement expression (equation 163) under these conditions reads

$$e_t = \int_0^R \frac{u_\theta^2}{r} dr = \int_0^R \frac{\omega_t^2 r^2}{r} dr = \frac{1}{2}\omega_t^2 R^2 \tag{164}$$

$$= \frac{1}{2} u_{max}^2 \tag{165}$$

$$= \frac{1}{2}\omega_t u_{max} R \tag{166}$$

Note, that in cylindrical coordinates the vorticity ζ is derived as

$$\zeta = \mathbf{k} \cdot \nabla \times \mathbf{u} = \frac{1}{r}\frac{\partial (r u_\theta)}{\partial r} \tag{167}$$

$$= \frac{1}{r}\frac{\partial (\omega_t r^2)}{\partial r} = \frac{1}{r} 2\omega_t r \tag{168}$$

$$= 2\omega_t \tag{169}$$

Therefore, the energy of displacement in relation to the vertical vorticity ζ reads

$$e_t = \frac{1}{4}\zeta u_{max} R \tag{170}$$

5.2.2 Extratropical cyclones and geostrophic balance

The geostrophic balance is a good approach for extratropical cyclones. In geostrophic balance the velocity is assumed to be constant ($u_\theta = u_g = const.$). Furthermore, in eq. (163) the centrifugal term is neglected. This gives

$$e_{ec} = \int_0^R f u_\theta dr = \int_0^R f u_g dr \tag{171}$$

$$= f u_g R \tag{172}$$

5.2.3 Tropical cyclones and gradient wind balance

In tropical cyclones both terms in eq. (163) are relevant. In Schielicke and Névir (2009), we decided to solve the integral by a semigeostrophic approach. This means that the velocity in the Coriolis term as well as one of the u_θ's in the centrifugal term will be treated to be geostrophic ($u_\theta = u_g = const.$), while the second u_θ in the centrifugal term will vary like the velocity in a Rankine vortex ($u_\theta = \omega_t r$). The integral then reveals

$$e_{tc} = \int_0^R \frac{u_\theta^2}{r} + f u_\theta dr = \int_0^R \frac{u_\theta v_g}{r} + f u_g dr \tag{173}$$

$$= \int_0^R (\omega_t + f) u_g dr \tag{174}$$

$$= (\omega_t + f) u_g R \tag{175}$$

Note, if we apply the Rankine vortex approach to all velocities within (163), the integral will give the same result except of a factor of 1/2 and instead of u_g we have $u_{max} = \omega_t R$.

5.2.4 Results and Summary of Schielicke and Névir (2009)

The prevailing balances of forces and the expressions of the energy of displacement for the different atmospheric vortex types are summarized in Table 5. With help of the mass-specific energy of displacement definition, we were able to analyse the frequency distributions of different vortex types and found a unified behavior with similar decay rates for cyclones and tornadoes (see Figure 18).

Table 5: *Prevailing balances of forces and explicit expression of the energy of displacement for atmospheric vortex types of different scales taken at their moment of maximum intensity; u_θ: azimuthal velocity, f: Coriolis parameter, R: respective radius. Adopted and slightly modified (we adapted the equations to the nomenclature used in this thesis) from Schielicke and Névir (2011) (their Table 1). Z and C stand for the centrifugal and the Coriolis acceleration terms, respectively, that balance the pressure gradient acceleration in the horizontal equation of motion (161).*

Phenomenon	Expression of $a(r)$	Prevailing Balance	Energy of displacement expression
Tornadoes, dust devils	Z	cyclostrophic	$u_\theta^2/2$
Tropical cyclones	$Z + C$	semigeostrophic	$u_\theta^2 + f u_\theta R$
Extratropical cyclones	C	geostrophic	$f u_\theta R$

5.2.5 Improved ansatz for the energy of displacement calculation (modified Rankine vortex)

We will present here an improved ansatz, the ***general modified Rankine vortex***, that allows us to perform the integration on all scales with help of a single wind profile. Especially in case of the gradient wind balance, this is an advantage compared to the somewhat inconsistent semigeostrophic approach where we fixed one of the wind speeds but allowed the other to vary over the vortex core. Observations of radial wind profiles in tornadoes (e.g. Kosiba and Wurman, 2010) and tropical cyclones (e.g. Riehl, 1963; Mallen et al., 2005) document that the radial dependence of the tangential (azimuthal) winds differs from the idealized Rankine vortex model. These authors observe a slower decay of the tangential wind profile than $u_\theta(r) \sim r^{-1}$ for $r \geq R$ (Rankine vortex model). Usually for the inner core a linear dependence $u_\theta(r) \sim r$ is assumed for the modified Rankine vortex model, too. However, observations show that the inner core structure of the radial wind profile deviates from the linear assumption of the Rankine vortex

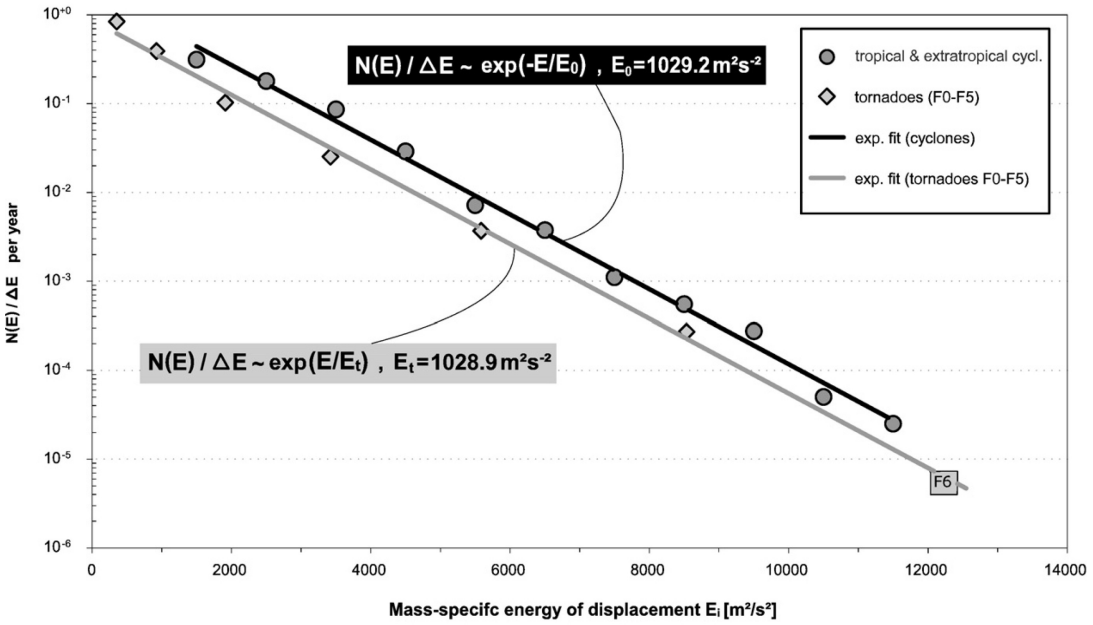

Figure 18: *Summary of density-intensity (energy of displacement) distributions per year of US tornado data (1950-1999) and northern hemispheric cyclone data (1958-1997). The cyclone data is composed of extratropical as well as tropical data. The distributions show the same exponential behavior with a characterisitc, universal energy of displacement scale of about 1000 m^2s^{-2} over the whole range. Figure is adopted from Schielicke and Névir (2009) (their Figure 4). More details on the data and methods as well as discussions and conclusions of the results can be found there.*

model, too (see e.g. Mallen et al., 2005; Kosiba and Wurman, 2010, their Figure 8[44]). Hence, we will slightly modify this generally practiced ansatz here:
In the following, we will assume that the wind field changes radially with an exponent $\alpha > 0$ inside the vortex core radius R, too: e.g. for $\alpha = 1/2$, the azimuthal velocity changes proportional to the square root of the radial component r and we have $u_\theta \sim r^{1/2}$. Outside of R, the velocity should fall off likewise to the Rankine vortex model but with a modified exponent as $1/r^\alpha$. We know from chapter 4.2.1 that an inviscid, stretch-free vortex can have arbitrary radial dependence (see also Wu et al., 2007), hence, we can freely choose α. We will now apply these conditions to our real vortex model at the moment of maximum intensity. The improved ansatz for the azimuthal wind u_θ is given

[44] Kosiba and Wurman (2010) found that the Burgers-Rott vortex (see also chapter 4.2.3) is the best fit to the tornado wind profile. However, the Rankine and the modified Rankine vortex models have the advantage that the calculations can easily be reproduced. Furthermore, we can interpret the (modified) Rankine vortex model as a first rough estimate of the true wind profiles and, additionally, the decay exponents can easily be adopted to true profiles.

by

$$u_\theta(r) = \frac{\Gamma}{2\pi R^{1+\alpha}} r^\alpha \qquad \text{, for } r \leq R \tag{176a}$$

$$u_\theta(r) = \frac{\Gamma}{2\pi R^{1-\alpha}} \frac{1}{r^\alpha} \qquad \text{, for } r > R \tag{176b}$$

Then we can calculate the axisymmetric vorticity distribution inside and outside the vortex core by

$$\zeta(r) = \frac{1}{r}\frac{\partial}{\partial r} r \left(\frac{\Gamma}{2\pi R^{1+\alpha}} r^\alpha \right) = (1+\alpha) \frac{\Gamma}{2\pi R^{1+\alpha}} r^{\alpha-1} \qquad \text{, for } r \leq R$$

$$\zeta(r) = \frac{1}{r}\frac{\partial}{\partial r} r \left(\frac{\Gamma}{2\pi R^{1-\alpha}} r^{-\alpha} \right) = (1-\alpha) \frac{\Gamma}{2\pi R^{1-\alpha}} r^{-\alpha-1} \qquad \text{, for } r > R$$

Note, that the vorticity distribution — similar to the original Rankine vortex model — is not smooth at the vortex core radius. Furthermore, the maximum velocity u_{max} is achieved at the vortex core radius R in agreement with the circulation formula (107). Maximum velocity and the vorticity at the vortex radius $r = R$ are given by

$$u_{max} := u_\theta(r = R) = \frac{\Gamma}{2\pi R} \tag{177a}$$

$$\lim_{\substack{r \to R \\ r \leq R}} \zeta(r) = \frac{1+\alpha}{2} \frac{\Gamma}{\pi R^2} = \frac{1+\alpha}{2} \zeta_{mean} \tag{177b}$$

where

$$\zeta_{mean} = \Gamma / A = \Gamma / (\pi R^2) \tag{178}$$

is the mean vorticity inside the vortex core. Now, we are able to rederive the expressions of the energy of displacement for the vortices of different scales with the new ansatz.

5.2.5.1 Tornadoes/Cyclostrophic balance

The integration of the cyclostrophic balance under assumption of the wind profile (176a) inside the vortex core radius gives:

$$e_t = \int_0^R \frac{u_\theta^2}{r} dr = \int_0^R \left(\frac{\Gamma}{2\pi R^{1+\alpha}} \right)^2 \frac{r^{2\alpha}}{r} dr = \left(\frac{\Gamma}{2\pi R^{1+\alpha}} \right)^2 \int_0^R r^{2\alpha-1} dr$$

$$= \left[\frac{1}{2\alpha} \left(\frac{\Gamma}{2\pi R^{1+\alpha}} \right)^2 r^{2\alpha} \right]_0^R = \frac{1}{2\alpha} \frac{\Gamma^2}{4\pi^2 R^2} = \frac{1}{4\alpha} \underbrace{\frac{\Gamma}{2\pi R}}_{=u_{max}} \underbrace{\frac{\Gamma}{\pi R^2}}_{=\zeta_{mean}} R$$

$$e_t = \frac{1}{4\alpha} \zeta_{mean} u_{max} R \qquad \text{(integration inside the vortex core)} \tag{179}$$

Thereby, we made use of (177a) and (178) in order to derive the last equation.

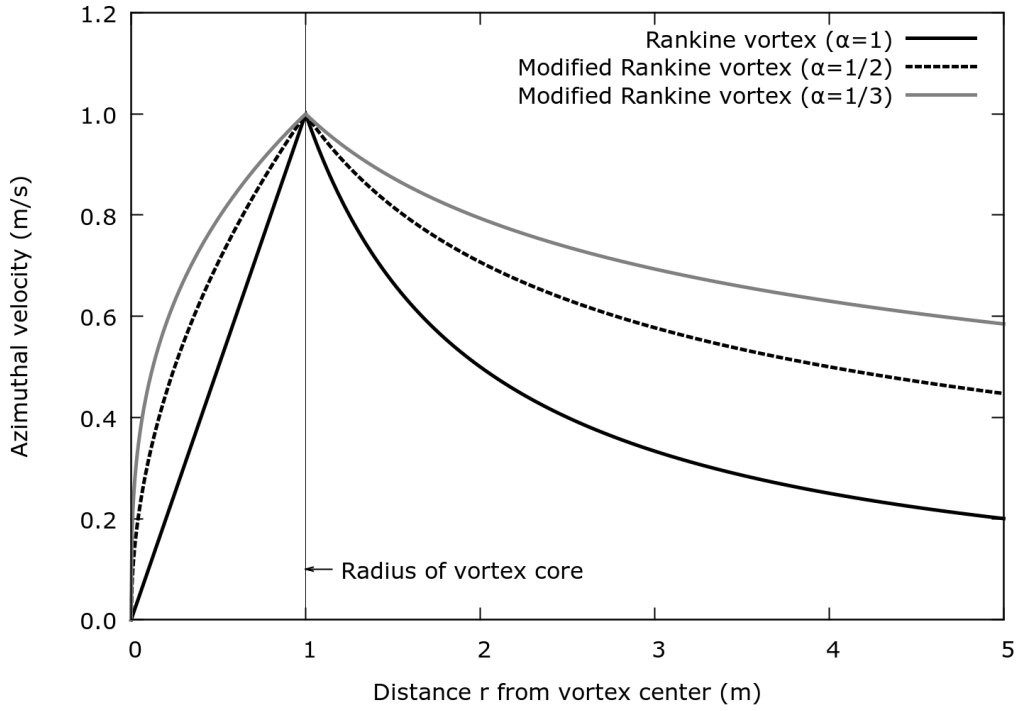

(a) Azimuthal (tangential) velocity profile

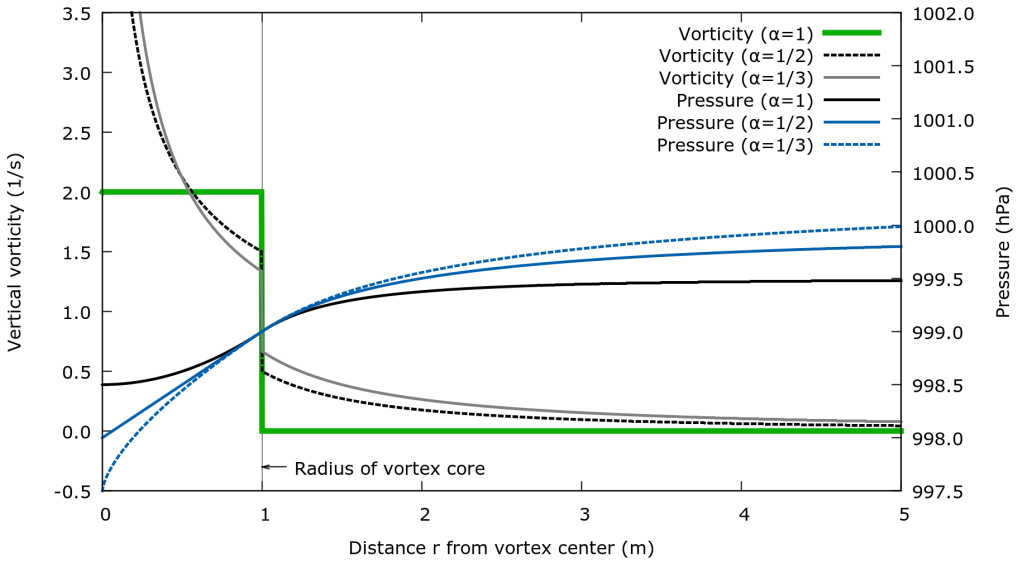

(b) Vertical vorticity and pressure profile

Figure 19: *Comparison of (a) azimuthal (tangential) velocity and (b) vertical vorticity/ pressure profiles of the Rankine vortex ($\alpha = 1$) and of two modified Rankine vortices with $\alpha = 1/2$, $\alpha = 1/3$. We assumed a circulation of $\Gamma = 2\pi\, m^2/s$ and a vortex radius of $R = 1\, m$; $\rho = 1\, kg/m^3$. The pressure profiles were calculated by applying ansatz (176a,b) in (152)assuming cyclostrophic balance only. The constants of integration C of was chosen such that all pressure profiles take $p(r = R) = 999\, hPa$ at the vortex core radius.*

Outside the vortex core, we need to take ansatz (176b) for the wind profile. This leads to

$$e_{t,outside} = \int_R^\infty \frac{u_\theta^2}{r} dr = \int_R^\infty \left(\frac{\Gamma}{2\pi R^{1-\alpha}}\right)^2 r^{-2\alpha-1} dr = \left[\left(\frac{\Gamma}{2\pi R^{1-\alpha}}\right)^2 \left(\frac{1}{-2\alpha}\right) r^{-2\alpha}\right]_R^{r\to\infty}$$

$$= -\frac{1}{2\alpha}\left(\frac{\Gamma^2}{4\pi^2 R^{2-2\alpha}}\right)^2 \left[\underbrace{\lim_{r\to\infty} r^{-2\alpha}}_{\to 0 \text{ for } \alpha>0} - R^{-2\alpha}\right] = \frac{1}{4\alpha} \underbrace{\frac{\Gamma}{2\pi R}}_{=u_{max}} \underbrace{\frac{\Gamma}{\pi R^2}}_{=\zeta_{mean}} R$$

$$e_{t,outside} = \frac{1}{4\alpha}\zeta_{mean} u_{max} R \qquad \text{(integration outside the vortex core)} \tag{180}$$

Hence, under cyclostrophic balance the part of the energy of displacment calculated inside the vortex core and the counterpart calculated outside the vortex core are of equal size:

$$e_t = e_{t,outside} \; ! \tag{181}$$

This means that the total energy of displacement of the vortex is twice the energy of displacement inside the vortex core. As a conclusion we can estimate the total energy of a cyclostrophically-balanced vortex by the knowledge of its maximum wind and mean vorticity. Maximum wind and mean vorticity can furthermore be expressed in terms of the vortex core radius R and the vortex circulation Γ calculated at the core radius.

5.2.5.2 Extratropical cyclones/Geostrophic balance

With the ansatz (176a) and with help of (177a), we derive the geostrophic balanced expression inside the vortex core as

$$e_{ec} = \int_0^R f u_\theta dr = \int_0^R f \frac{\Gamma}{2\pi R^{1+\alpha}} r^\alpha dr = \left[\frac{1}{1+\alpha} f \frac{\Gamma}{2\pi R^{1+\alpha}} r^{1+\alpha}\right]_0^R = \frac{1}{1+\alpha} f \underbrace{\frac{\Gamma}{2\pi R}}_{=u_{max}} R$$

$$e_{ec} = \frac{1}{1+\alpha} f u_{max} R \qquad \text{integration inside the vortex core} \tag{182}$$

Outside the vortex core, we use ansatz (176b) and calculate for $\alpha \neq 1$, $\alpha > 0$:

$$\begin{aligned}
e_{ec,outside} &= \int_R^\infty f u_\theta dr = \int_R^\infty f \frac{\Gamma}{2\pi R^{1-\alpha}} r^{-\alpha} dr = f \frac{\Gamma}{2\pi R^{1-\alpha}} \frac{1}{1-\alpha} \left[r^{1-\alpha} \right]_R^{r\to\infty} \\
&= f \frac{\Gamma}{2\pi R^{1-\alpha}} \frac{1}{1-\alpha} \left[\lim_{r\to\infty} r^{1-\alpha} - R^{1-\alpha} \right] = f \underbrace{\frac{\Gamma}{2\pi R}}_{u_{max}} R \frac{1}{1-\alpha} \left[\lim_{r\to\infty} \frac{r^{1-\alpha}}{R^{1-\alpha}} - 1 \right] \\
&= \frac{1}{1-\alpha} f u_{max} R \left[\lim_{\beta\to\infty} \frac{(\beta R)^{1-\alpha}}{R^{1-\alpha}} - 1 \right] \qquad \text{with } r = \beta R \text{ for } \beta > 1 \\
e_{ec,outside} &= \frac{1}{1-\alpha} f u_{max} R \left[\underbrace{\lim_{\beta\to\infty} \beta^{1-\alpha}}_{(I)} - 1 \right]
\end{aligned} \tag{183}$$

where we have changed the variable r to $r = \beta R$ with $\beta > 1, \beta \in \mathbb{R}$; β denotes (fractional) multiples of the vortex core radius. Term (I) approaches zero only in the case of $\alpha > 1$, for all other cases (including $\alpha = 1$, where we obtain the logarithm in the integration) term (I) grows with increasing radial component. However, we can still assume, that the influence of the vortex on its surrounding decreases with increasing distance to the vortex core. Therefore, we can calculate the energy of displacement magnitudes outside the vortex core for different distances $r = \beta' R$, e.g. for different values of β', and compare them with the magnitude inside the core: We can further write

$$e_{ec,outside} = \frac{1+\alpha}{1-\alpha} \left[\lim_{\beta\to\beta'} \beta^{1-\alpha} - 1 \right] e_{ec} \tag{184}$$

For different values of α and β', we calculated the integrals explicitly (see Table 6). Another approach to derive an explicit β' would be to search for the value when the maximum velocity falls off to a specific value, for example for which β' the velocity will be equal to the half of $u_{max} = \Gamma/(2\pi R)$? We can write the velocity profile outside the vortex core radius as

$$u_\theta(r = \beta' R) = \frac{\Gamma}{2\pi R} \frac{1}{R^{-\alpha}} (\beta' R)^{-\alpha} = u_{max} \beta'^{-\alpha} \tag{185}$$

This value falls off to $u_{max}/2$ for

$$u_\theta(r = \beta' R) = u_{max}/2 \qquad \text{for} \quad \beta' = 2^{1/\alpha} \tag{186}$$

Some values of the energy of displacement for different values of α for this approach are summarized in Table 6. The latter approach however strongly depends on the exponent: the lower the α is, the larger is the distance when the velocity falls off to the half of its maximum due to the shallower decrease of the wind profile. Furthermore, it should be noted that the influence of the Coriolis term on the total energy of displacement magnitude increases with increasing distance from the vortex core.

Table 6: *Ratio of the energy of displacement integrals calculated outside and inside of the vortex core for different values of α and β'. Thereby, α is the exponent of the modified Rankine vortex model and β' is the factor by which we multiply the vortex core radius. The ratios of the last column give the values for the distances when the maximum wind magnitude has fallen off to its half and were calculated with help of equation (186).*

	Ratio of $e_{ec,outside}/e_{ec,inside}$ for different values of α and β':			
	$\beta'=2$ $(r=2R)$	$\beta'=3$ $(r=3R)$	$\beta'=4$ $(r=4R)$	for $u_\theta(r=\beta' R)=u_{max}/2$
$\alpha=\frac{1}{2}$:	1.24	2.20	3.00	3.0 ($\beta'=4$)
$\alpha=\frac{1}{3}$:	0.52	0.88	1.17	6.0 ($\beta'=8$)
$\alpha=\frac{1}{4}$:	0.43	0.74	0.98	11.7 ($\beta'=16$)

5.2.5.3 Tropical cyclones/Gradient wind balance

The energy of displacement expression for the gradient wind balance is given as the sum of the expressions for the cyclostrophic balance and for the geostrophic balance. Hence, we can write

$$e_{tc} = e_t + e_{ec} = \frac{1}{4\alpha}\zeta_{mean} u_{max} R + \frac{1}{1+\alpha} f u_{max} R$$
$$e_{tc} = \left(\frac{1}{4\alpha}\zeta_{mean} + \frac{1}{1+\alpha} f\right) u_{max} R \quad \text{integration inside the vortex core} \tag{187}$$

Note, that the factors in front of the mean vorticity and the Coriolis parameter become equal in case of $\alpha = 1/3$. Then, the factor becomes $3/4$. With help of the derivation of equation (180) for $\beta > 1$ (set $r = \beta R$ in equation 180 and let the limes approach β) we derive an expression outside the vortex core:

$$e_{tc,outside} = e_t + e_{ec} = \frac{1}{4\alpha}\zeta_{mean} u_{max} R + \frac{1}{1-\alpha} f u_{max} R(\beta^{1-\alpha} - 1)$$
$$e_{tc,outside} = \left(\frac{1-\beta^{-2\alpha}}{4\alpha}\zeta_{mean} + \frac{\beta^{1-\alpha}-1}{1-\alpha} f\right) u_{max} R \quad \text{integration outside the vortex core} \tag{188}$$

The total energy of displacement magnitude of the vortex is given by the sum of the two contributions: $e_{tc,total} = e_{tc} + e_{tc,outside}$. Likewise, the total energy of displacement is calculated as such a sum in case of the other balances.

5.2.5.4 Final remark on the improved ansatz

With our improved model (modified Rankine vortex) we generated a consistent model for the radial wind profile in atmospheric vortices. For tropical cyclones the observed average exponent α is equal to 0.5 (e.g. Riehl, 1963; Gray and Shea, 1973, who observed

$\alpha = 0.47 \pm 0.3$). Mallen et al. (2005) fitted the modified Rankine vortex model to the wind profiles of 251 tropical cyclones in the range between the radius of maximum wind RMW and $3RMW$ and observed a mean $\alpha = 0.3\text{-}0.5 \pm 0.1$ depending on the intensity class with small α corresponding to low intensities[45]. Kosiba et al. (2008) observed similar decay exponents in mobile Doppler radar data of a tornado with values between 0.26(low intensity)-0.61(higher intensity) depending on the time in the life cycle of the tornado. Although the range of the observed decay rates α is quite large, we decided to use a value of $\alpha = 0.5$ (the average decay rate) in the following. Based on the gradient wind balance that includes all forces on a rotating planet, we are now able to obtain the expressions of the energy of displacement by comparing the magnitude of the mean vorticity ζ_{mean} with the Coriolis parameter f:

Modified Rankine vortex ansatz for $\alpha = 1/2$:

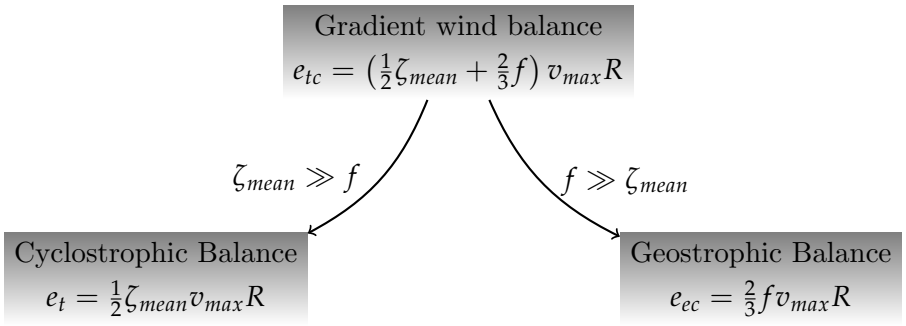

where $\zeta_{mean} = \Gamma/(\pi R^2)$ is the mean vorticity calculated over the vortex area at the moment of maximum intensity.

[45] For prehurricanes ($u_\theta < 30\,\mathrm{m/s}$) and minimal hurricanes ($30\,\mathrm{m/s} \leq u_\theta < 50\,\mathrm{m/s}$) Mallen et al. (2005) observed mean $\alpha \approx 0.3\text{-}0.35$ while $\alpha \approx 0.5$ for major hurricanes ($u_\theta > 50\,\mathrm{m/s}$).

5.3 Mass-related atmospheric moment (Schielicke and Névir, 2011,2013)

So far, we only mentioned mass-specific or local intensity parameters. These parameters only describe the local aspects of the vortices. Since a vortex is additionally characterized by its size, life time and path length, the intensity defined by local parameters alone seems to be incomplete. To overcome this disadvantage, we introduced a mass-related parameter based on the combination of the total mass affected during the vortex lifetime with a local intensity parameter in Schielicke and Névir (2011). As local parameter we chose the mass-specific energy of displacement. The newly-defined parameter – called the *atmospheric moment* – represents the total (mass-related) work done by the vortex. By multiplying (163) with the total mass $M_* := V_*\bar{\rho}$ (V_*: total during lifetime affected volume, $\bar{\rho}$: averaged density of the volume), we defined the atmospheric moment as

$$M_a := M_* e = M_* \int_0^R a(r)dr = \underbrace{V_*\bar{\rho}}_{=M_*} \int_P^{P_0} \alpha dp \tag{189}$$

Further, we can approximate the atmospheric moment as (for the complete derivation see Schielicke and Névir, 2011)

$$M_a \approx \left(\frac{C^{LE}}{C^{HV}}\right) AL_{track}\Delta P \; = \left(\frac{C^{LE}}{C^{HV}}\right) ALe. \tag{190}$$

where e is the expression of the energy of displacement that depends on the scale and on the prevailing balance of forces (see chapter 5.2), $A = \pi R^2$ is the area of the vortex at an instant[46], L_{track} is its path length and ΔP is the pressure difference between the core pressure and the environment (pressure drop or depth) taken at the moment of maximum intensity[47]. C^{LE} and C^{HV} are dimensionless factors. $C^{LE} = \bar{\rho}/\rho_c$ is the ratio of the averaged density inside the lifetime volume and the local density in the center of the vortex at the moment of maximum intensity. It therefore is composed of a Eulerian field variable (ρ_c) as well as Lagrangian aspects of the vortex ($\bar{\rho}$). The dimensionless factor $C^{HV} = L/H$ is the reciprocal of the aspect ratio that relates horizontal (width L) and vertical (height H) dimensions of the vortex. The proportionality of tornado height H and width L with $H/L = const.$ was proposed by Kurgansky (2000). Furthermore, the height and width of extratropical cyclones seem to be qualitatively related, too (Lim and Simmonds, 2007). However, a detailed study showing this proportionality is missing so far. It should be noted, that the constant might have a different value for vortex types on different scales (see also the different values of the estimated aspect ratios of

[46] As area we can also take the over lifetime averaged area.

[47] Instead of using the moment of maximum intensity, it is possible to integrate the mass-related work over the lifetime of a vortex if all informations are available. However, in e.g. the case of tornadoes the intensity is estimated from the most severe damage caused by the tornado even though its intensity over most of the lifetime could have been weaker.

different vortex types presented in Table 2).
The atmospheric moment is defined analogously to the seismic moment of earthquakes. The latter is a measure of the size (or magnitude) of an earthquake. It is further proportional to the energy released during the rupture process. The scalar seismic moment is given by (e.g. Kanamori and Anderson, 1975; Ben-Zion and Ampuero, 2009):

$$M_0 = \widetilde{L} A \Delta\sigma / \widetilde{C} \tag{191}$$

Here, $\widetilde{L}$ is the characteristic length of the fault, A is the rupture surface and $\widetilde{C}$ is a dimensionless shape factor (e.g. for circular faults $\widetilde{C} = 7\pi/16$). $\Delta\sigma = \sigma^0 - \sigma^f$ is the stress drop, i.e. the difference between the initial stress σ^0 before and the final stress σ^f after the earthquake (Ben-Zion, 2003).
The Gutenberg-Richter law is probably the most famous empirical law of geoscience. It describes the relation between the magnitude of earthquakes and the cumulative number of earthquakes $N(> m)$ with magnitudes larger than m. When the magnitude m is expressed in terms of seismic moments M_0 as $m = 2/3 \log_{10} M_0 - 6$, the Gutenberg-Richter law (the cumulative distribution function) becomes a power law (e.g. Pisarenko and Sornette, 2004)

$$N(> M_0) \propto M_0^{-\beta} \tag{192}$$

and the corresponding probability density function reads

$$n(> M_0) = \frac{dN(M_0)}{dM_0} \propto M_0^{-\beta-1} \tag{193}$$

with power law exponent $\beta = 2/3b$ and b-values of approximately 1 (e.g. Ben-Zion, 2003). The b-values depend on the region, e.g. in mid-ocean ridges b is higher than in oceanic subduction zones (Bayrak et al., 2002).
By introducing the atmospheric moment, we were able to compare the famous Gutenberg-Richter law to the probability density distribution of tornadoes and found a power law concerning the atmospheric moment of tornadoes with an exponent slightly smaller (≈ 0.2) than β (see Figure 20). In a follow-up study (Schielicke and Névir, 2013), we found additional evidence for power law behavior partly coextensive with characterisitc scales in the temporal properties of tornado occurrences. Thereby, the characteristic scales reflect the typical diurnal behavior of tornadoes with maximum occurrences in the late afternoon.

5.4 Other integral intensity measures: Circulation and Depth

Of course it is possible to define other integral intensity measures that consider not only local properties of a vortex but also take into account its geometric properties. We already introduced such a measure in chapter 3.3.3: the ***circulation***. The circulation

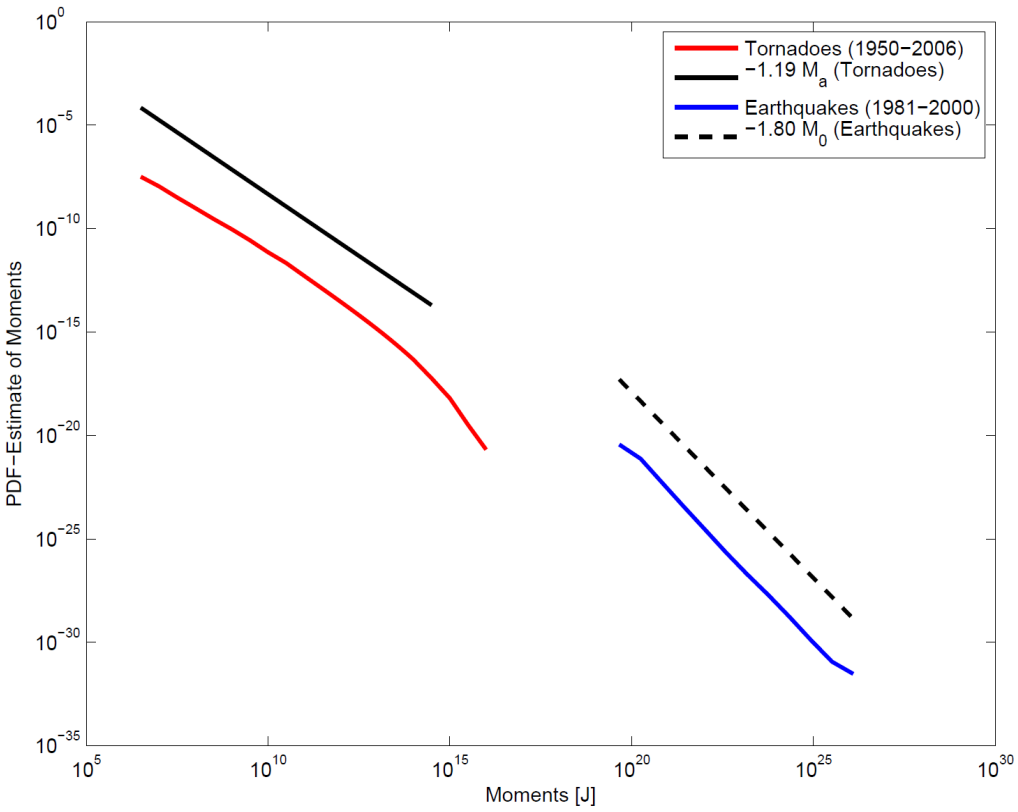

Figure 20: *Gutenberg-Richter law: Comparison of probability density distributions of tornadoes (1950-2006, USA, red curve) and earthquakes (1981-2000 Southern California Seismic Network (SCSN) catalog, blue curve) concerning their moments: atmospheric moment M_a (tornaoes) and seismic moments M_0 (earthquakes) Linear fits have been applied to the double-logarithmic plot of the data with slopes of -1.19 for tornadoes (black solid line) and -1.80 for earthquakes (black dashed line). Figure is adopted from Schielicke and Névir (2013) (their Figure 1). More details on the comparison between earthquake data and tornado data and a discussion of a possible similar underlying structure explaining the similarities can be found there.*

takes into account the vorticity and the area of a vortex and therefore gives a measure of the influence and importance of a system on the global circulation (Sinclair, 1997). It was used by e.g. Sinclair (1994) in order to study extratropical cyclones. Furthermore, we have shown that the circulation plays a crucial role in the wind profile of theoretical vortex models (see chapter 4).

Another integral measure is the depth D of a vortex. Simmonds and Keay (2000) determine the depth of an axisymmetric, paraboloidal low pressure system of radius R as

$$D = \frac{1}{2}\frac{\partial^2 p}{\partial r^2}R^2 = \frac{1}{4}\nabla^2 p R^2 \tag{194}$$

where $D = P - P_0$ and $p(R) = P, p(0) = P_0$ are the pressure values at the radius R, and at the center of the depression ($r = 0$), respectively. Therefore, the depth gives

the difference between the "environmental"[48] and the core pressure. The result for the depth (equation 194) can be derived under the following assumptions: The pressure distribution of a paraboloidal, axisymmetric depression is given by

$$p(r) = \frac{D}{R^2} r^2 + P_0 \qquad \text{with } D = P - P_0$$

Calculating the second partial derivative of $p(r)$ with respect to the radial component gives

$$\frac{\partial^2 p(r)}{\partial r^2} = 2\frac{D}{R^2}$$

Furthermore the Laplacian of the axisymmetric (no angular dependence) pressure distribution $p = p(r)$ in cylindrical coordinates is given by

$$\nabla^2 p = \frac{1}{r}\frac{\partial}{\partial r}\left(r\frac{\partial p}{\partial r}\right) = \frac{1}{r}\frac{\partial}{\partial r}\left(2r^2\frac{D}{R^2}\right) = 4\frac{D}{R^2}$$

.

We have already shown that the assumption of a paraboloidal pressure distribution is identical to the Rankine vortex model with a linearly increasing wind field from the vortex center to its radius (see chapter 4.2.1 for more details).

For the more common case of nonaxisymmetric systems, Simmonds and Keay (2000) proposed to retain the concepts of radius and depth. As a first assumption, the area of a depression can be taken by the area of the positive (negative) Laplacian of pressure surrounding a local maximum (minimum) of $\nabla^2 p$. However, for more than one system inside the same region of positive Laplacian this first assumption fails. Hence, Sinclair (1997) and Lim and Simmonds (2007) searched for the nearest saddle point of the gradients of geostrophic vorticity taken along radial lines that start from the vortex center in order to define the cyclone area. On the northern hemisphere, the positive Laplacian of pressure is proportional to the geostrophic vorticity, i.e. it is proportional to cyclonic motion. The geostrophic vorticity is given by

$$\zeta_g = \frac{1}{\rho f}\nabla^2 p \tag{195}$$

or by using (194), we can write (cf. also Schneidereit et al., 2010, who used the relationship of D, R and ζ_g in terms of the geopotential height field in order to study cyclone intensities and radii):

$$\zeta_g = \frac{4}{\rho f}\frac{D}{R^2} \tag{196}$$

Hence in the geostrophic case, the depth is proportional to the circulation of a synoptic

[48] The pressure taken at radius R.

pressure system

$$D \sim \zeta_g R^2 \sim \Gamma = \int_0^R \zeta dA : \text{ Circulation} \tag{197}$$

However, the proportionality between circulation and depth only holds on the synoptic scale. On other scales, the relation is different and deviates from this linear relation. In order to study atmospheric vortex types on different scales, the energy of displacement and the atmospheric moment seem to be a more appropriate choice since they consider all forces that influence the vortex behavior.

5.5 Relation of energy of displacement, atmospheric moment and circulation for different atmospheric vortices

The circulation is defined over a material closed loop C surrounding the vortex center (see equation (107) in chapter 3.3.3). Assume that we take the loop over the circle corresponding to the radius R of maximum wind $\mathbf{u}_{max}$ of a real vortex and assume this vortex to be perfectly symmetric

$$\Gamma = \oint_C \mathbf{u}_{max} \cdot d\mathbf{S} \tag{198}$$

We assume $\mathbf{u}_{max}$ and $d\mathbf{S}$ to be parallel over the total loop. In case of an axisymmetric system, this leads to

$$\Gamma = 2\pi u_{max} R \tag{199}$$

where $2\pi R$ is the circumference of the vortex. Furthermore, following equation (108) we can also write

$$\Gamma = \zeta_{mean} A \tag{200}$$

where $A = \pi R^2$ is the area of the vortex. This way of integration is different from the integration way leading to the mass-specific energy of displacement expressions which was along the radial component. However, the integrals will be proportional when both carried out along the circle corresponding to R or starting from the center to R where the vortex velocity is u_{max} in both cases. Recall that the explicit expressions of the mass-specific energy of displacement of different vortices can be calculated in two different ways: with different models depending on the scale of the vortex as in Schielicke and Névir (2009)[49] or with help of the modified Rankine vortex ansatz (see section 5.2.5). In comparison, those expressions of the energy of displacement in terms of the variables circulation Γ and area A are summarized in Table 7.

[49] Rankine vortex ansatz for cyclostrophically balanced vortices; semigeostrophic ansatz for vortices in gradient wind balance; constant wind field for geostrophically balanced flows

Table 7: *Different expressions of the energy of displacement in terms of circulation* $\Gamma = 2\pi u_{max} R = \zeta_{mean} A$ *and area* $A = \pi R^2$ *in dependence on the vortex type (*u_{max} *: maximum wind;* R *: vortex core radius;* ζ_{mean} *: mean vorticity inside the vortex core). Derivations can be found in section 5.2. For the modified Rankine ansatz we used a decay exponent of* $\alpha = 1/2$.

Vortex type/balance	**Schielicke and Névir (2009)**	**Modified Rankine ansatz**
tornadoes/ cyclostrophic	$e_t = \left(\frac{1}{2\pi}\right) \cdot \frac{1}{4} \frac{\Gamma^2}{A}$	$\widetilde{e}_t = \left(\frac{1}{2\pi}\right) \cdot \frac{1}{2} \frac{\Gamma^2}{A} = 2e_t$
tropical cyclones/ gradient wind	$e_{tc} = \left(\frac{1}{2\pi}\right) \cdot \left(\frac{1}{2} \frac{\Gamma^2}{A} + f\Gamma\right)$ $= 2e_t + e_{ec}$	$\widetilde{e}_{tc} = \left(\frac{1}{2\pi}\right) \cdot \left(\frac{1}{2} \frac{\Gamma^2}{A} + \frac{2}{3} f\Gamma\right)$ $= 2e_t + \frac{2}{3} e_{ec}$
extratropical cyclones/ geostrophic	$e_{ec} = \left(\frac{1}{2\pi}\right) \cdot f\Gamma$	$\widetilde{e}_{ec} = \left(\frac{1}{2\pi}\right) \cdot \frac{2}{3} f\Gamma = \frac{2}{3} e_{ec}$

As we have already mentioned in chapter 5.4, the energy of displacement expression is only linear in Γ in case of the geostrophic balance but nonlinear in the other cases. However, we see (Table 7) that all expressions can be written as combinations of circulation and area (or radius). By comparing linewise the expressions of the energy of displacement for each vortex type seperately, we observe that the main difference between the expressions derived by different models can be ascribed to different constants. At least in case of the tornadoes (convective scale) and of the extratropical cyclones (synoptic scale), the expressions are only different by a simple constant. Since the gradient wind balance expression of the energy of displacement is composed in a non-trivial manner of the two components — cyclostrophic and geostrophic — the behavior between the original Schielicke and Névir (2009) and the modified Rankine ansatz is more complicated. It should be mentioned that it is not easy to prove the real behavior of the wind field inside a real vortex. There are multiple reasons for that: e.g. the wind field of a real moving vortex is not axisymmetric and often the vortex core is relatively narrow such that the vortex core (or the inner wind field) is not well covered by measurements (e.g. in case of tornadoes). There are attempts to find appropriate models and compare them with measurements for tornadoes (see e.g. Lee et al., 2004) and for tropical cyclones (e.g. Chavas et al., 2015). E.g. Lee et al. (2004) found that the Rankine vortex model as well as the Burgers-Rott model were able to reproduce the pressure field that was observed in one of the rare measurements of the meteorological variables inside a tornado (the tornado moved over one of their probes that was anchored in the tornado's path).
In order to derive the corresponding expressions of the atmospheric moment we can use

the right-hand side of (190):

$$M_a \approx \left(\frac{H}{L}\right) A L_{track} e \tag{201}$$

where we assumed $C^{LE} \approx 1$ and $C^{HV} = L/H$. For the energy of displacement e we can use the appropriate expression listed in Table 7 depending on the vortex type and prevailing balance of forces.

In conclusion, we have shown that the intensity of a vortex can be estimated by integral measures. Integral measures prevail over local ones because they additionally capture the extent of the vortex. Thereby, integral methods provide a complete view on the vortex. Nonetheless, integral intensity measures need a clearly defined size in order to give accurate values of the vortex intensity. We will show in the next section that it is not trivial to define the size of a vortex. This is a current topic and research in this field is still ongoing.

6 Kinematic vorticity number method adopted to atmospheric flows

Although, the concept of vortices is known since the introduction of hydrodynamics, "*an accepted [objective, mathematical] definition of a vortex is still lacking*" (Jeong and Hussain, 1995). The discussion about what defines a vortex is still ongoing (e.g. Thompson et al., 2009). In the first part of this chapter (section 6.1), we will review methods used to identify extra-tropical cyclones in meteorology. We will call these methods *traditional methods* since they are based on well-known meteorological fields like the pressure/geopotential height or the (geostrophic) vorticity fields. In the second part (section 6.2), we will review *kinematic methods* used in fluid mechanics and engineering which are mainly based on the kinematic properties of the fluid. Already Truesdell (1953, 1954) introduced a measure that allows the identification of vortex areas in the flow field: the kinematic vorticity number W_k. This measure proves useful in the analysis of atmospheric vortices that occur not only on multiple scales but are rather often embedded in shear-dominated flow situations, too. We will introduce the kinematic vorticity number in chapter 6.3 and will finally give details on the numerical implementation of the kinematic vorticity number W_k (chapter 6.4). This W_k-method will serve as the basis of vortex size determination in this thesis.

6.1 Traditional methods of extra-tropical cyclone size determination

Extratropical cyclones play an important role in the general atmospheric circulation. They determine not only the local weather on shorter time scales ranging from hours to seasons, but also the long term climate in respect to mean temperatures and mean precipitation amounts. Therefore cyclone activity has been studied by numerous scientists concerning the distributions of their intensities, their genesis and lysis regions and other properties like life times, development speeds, sizes and associated precipitation amounts in Northern and Southern hemispheres (for a recent review on extratropical cyclone studies see Ulbrich et al., 2009). First climatological studies were time-consuming manual analysis limited to selected regions, intensity classes and/or periods: e.g. van Bebber (1891) who defined typical stormtracks including the in Europe well-known Vb storm track that is still of relevance concerning heavy precipitation events and flooding in Mid-Europe; or the study of deep cyclones[50] in the Northern Atlantic region and over Europe from 1930-1991 conducted by Schinke (1993). However, manual analysis is not only time-consuming, it also involves some sort of subjectivity in defining cyclone positions and core pressures depending on the experience of the analyst (see e.g. Haak

[50] Schinke (1993) defined a deep cyclone as a cyclone with a surface core pressure of less or equal to 950 hPa.

and Ulbrich, 1996). The increase of the computer capacity in the last decades allowed to develop numerical methods that identify (and track) extratropical cyclones in digital data (e.g. see Ulbrich et al., 2009; Neu et al., 2013, for an overview over numerical methods). In this chapter, we will concentrate on only a small part of these publications that deal with the determination of cyclone sizes.

In general, meteorological identification methods define extratropical cyclones as local extrema in well-known fields like the pressure/ geopotential height field or the (geostrophic) vorticity field. Therefore, the criteria for estimating cyclone sizes are also based on these fields. Schneidereit et al. (2010) give a detailed review over cyclone size determination methods mainly based on pressure/ geopotential height fields. They summarize the methods into three groups depending on the approach used: (i) based on the derivative of the pressure, (ii) the determination of the enclosed area, or (iii) the application of functional fits.

Nielsen and Dole (1992) were probably the first who determined the sizes of extratropical cyclones. They discussed different possible measures of cyclone sizes, namely the distances between the nearest (1) high, (2) low, or (3) col (saddle point) of sea level pressure; and (4) the horizontal area enclosed by the outermost closed isobar around a low pressure center. Nielsen and Dole (1992) argued that definition (1) and (2) fail in case of cyclone families where the nearest high is missing and in case of lee cyclogenesis, respectively, where the nearest low might be missing. Therefore, they concentrated on definition (3) in their (manual) analysis of surface weather maps. Rudeva and Gulev (2007) and Rudeva (2008) applied definition (3) in a numerical method that searches along 36 radial lines starting from the cyclone center outwards for the pressure at the nearest col. A col is found when the radial pressure gradient falls to zero. In some cases, i.e. in troughs, the radial pressure gradient might not fall to zero within a reasonable distance, then Rudeva and Gulev (2007) and Rudeva (2008) set the pressure value along this search line to the pressure at the distance of 1000 km. In a first step, this leads to a set of 36 pressure values around the cyclone center. Afterwards, the minimum pressure value out of the 36 values was defined as the value of the outermost closed isobar. Wernli and Schwierz (2006) used a numerical contour searching method to determine the outermost closed isobar around single low pressure centers in increments of 2 hPa. The advantage of the method compared to radial search lines is that it allows to detect cylones with a more complex shape. On the other hand, Wernli and Schwierz (2006) discussed caveats of their method, e.g. the method is sensitive to the choice of the contour interval: a reduction/ increase of the contour interval from 2 to 1/4 hPa leads to an increase of 40%/ decrease of 30% of detected cyclones. Furthermore, they observed strong fluctuations in cyclone sizes when low pressure systems are close to each other. To overcome these size variations, Hanley and Caballero (2012) introduce a method

which identifies multicenter cyclones with two or three sea level pressure minima inside the same outermost-closed contour. Although, in some cases the method of Hanley and Caballero (2012) provides more consistent size evolutions compared to the single center method of Wernli and Schwierz (2006) (see Figure 4 of Hanley and Caballero, 2012), in splitting and merging situations, cyclone sizes still seem to vary strongly (see Figures 5 and 6 of Hanley and Caballero, 2012).

Grotjahn et al. (1999) applied a Mexican hat wavelet transform to the sea level pressure in the longitudinal and latitudinal direction around a sea level pressure minimum. They defined the size of the low by the two zero crossings of the Mexican hat. Grotjahn et al. (1999) applied their method to 12 extratropical cyclones, comparing their best wavelet analysis with the sea level pressure field which in most cases - but not all - was successful. Furthermore, in the upper-troposphere the method fails because of the strong ambient flow in which the cyclones are embedded. In order to analyse upper-level features, Grotjahn and Castello (2000) analysed the circular average of the geostrophic kinetic energy around a cyclone center. They applied their method to the geopotential height perturbation field, which was calculated by subtracting a zonal mean from the 300 hPa geopotential height field in a specified sector. The typical geostrophic kinetic energy distribution of a cyclone is near zero at the center, increases up to a maximum, and then decreases again. The scale of the cyclone was defined as the distance where the average geostrophic kinetic energy reached a "cutoff value" outside of the maximum. However, the calculation of anomaly fields is not trivial since the background gradients change in time and space and it is not clear if all systems can be captured by the subtraction of a a large-scale gradient: see e.g. Jeong and Hussain (1995) who discussed the usage of path- and streamlines (see their Fig. 2) or Adrian et al. (2000) who discussed the Galilean decomposition (see their Fig. 2 and 3). Schneidereit et al. (2010) fit one-dimensional Gaussian functions to the geopotential height field surrounding cyclones exceeding a minimum gradient. Therefore, the two-dimensional geopotential height field was maped on a one-dimensional function assuming azimuthal symmetry, that only depends on the distance from the cyclone center. Schneidereit et al. (2010) show the conjunction of the determined radius of a cyclone with the geostrophic wind maximum around the cyclone center. However, in asymmetric cases this method might fail to determine the true extent of the systems as will be shown later in this publication.

The (geostrophic) vorticity field as basis of cyclone size determination was favoured by e.g. Sinclair (1997), Simmonds and Keay (2000), Simmonds (2000), Lim and Simmonds (2007). The advantage of vorticity fields compared to pressure fields is, that it is possible to detect vortex centers even in a strong background flow (see Sinclair, 1994). Furthermore, Sinclair (1994) states that cyclone statistics based on pressure are biased toward the "graveyards" of cyclones favouring slower-moving and deeper systems, since

mobile and developing systems often appear without local pressure minima until they reach a certain intensity. Since the geostrophic vorticity is proportional to the Laplacian of the pressure and geopotential height field, respectively, it represents the curvature and therefore has a smaller spatial scale than pressure (see e.g. Fig. 5 of Murray and Simmonds, 1991; Hodges et al., 2003). This leads to a larger number of systems detected in the vorticity field depending on the spatial resolution of the data (e.g. Ulbrich et al., 2009). Therefore, e.g. Sinclair (1997) uses a radial spatial filter that smoothes the raw data before the analysis. However, by increasing the radius of this filter, smaller systems might disapear; the remaining systems are larger but on average less intense. In order to determine the size of the systems, Sinclair (1997) searches along radial lines starting from the vorticity centers for the distance where either the vorticity falls to zero or the radial vorticity gradient changes its sign (this is equivalent to the search for the nearest col or saddle-point). Sinclair (1997) uses the circulation as an alternative measure for cyclone strength and shows examples, where traditional methods (central pressure and central vorticity) fail to capture the strength properly. However, it is possible that the radial lines from two systems overlap before one of the criteria is met. Hence, Simmonds and Keay (2000) and Simmonds (2000) decided to use a similar definition of cyclone sizes like Sinclair but with a different approach: they search along a number of paths starting from the cyclone center that follow the directions of maximum (negative) gradient. Simmonds and Keay (2000) depict the method to be similar to the definition of a water catchment boundary. Unfortunately, it is not further specified in their work how elongated vorticity streamers that could lead to narrow, elongated systems are handled or if that streamers affect the analysis at all. For example, Sinclair (1997) limits the maximum change in distances between neighboring radial lines to avoid such narrow elongations. Lim and Simmonds (2007) determine the size of a cyclone in a similar way to Sinclair (1997) by searching along radial lines starting from the cyclone center for the distances when the Laplacian of pressure (or geopotential height) falls to zero which was defined as boundary of the cylone. From the determined set of distances the mean radius is calculated. Lim and Simmonds (2007) successfully applied their method to several vertical levels starting from the mean sea level pressure field up to the 500 hPa geopotential height field and found that upper-level systems are on average larger with the largest scale found in the 700-hPa level. Furthermore, they found that well-organized systems on average are larger and more intense than weakly-organized shallow systems.

6.2 Kinematic methods estimating vortex sizes

The traditional methods described in the previous chapter 6.1 which are often applied to atmospheric flows are inadequate in certain flow situations (a detailed discussion on the inadequacy of traditional (or intuitive) methods is given in Jeong and Hussain, 1995). For example, the low pressure definition fails in situations where the local pressure minimum is balanced by viscous forces instead of centrifugal forces. In this case, the motion around the pressure minimum can be nonrotational. Furthermore, the appearance of closed or spiralled streamlines depend on the reference frame. Vortices moving at different speeds need different reference frames: When moving with one vortex speed, another vortex might not appear to have closed or spiralled streamlines. Particle trajectories might not be closed during the lifetime of a vortex or particles might leave the vortex and therefore are inadequate. The definition of a vortex in terms of vorticity thresholds can fail in (high) shear flows. For example, the method might falsely indicate the existence of a vortex in (strong) linear shear flow. The choice of the vorticity threshold is especially complicated in a flow where the vorticity of a purely sheared flow is of the same order as the curvature vorticity of the vortices.

Nonetheless, the vorticity is a measure that is closely connected with vortices. It is associated with the rate of rotation inherit in the flow and, in general, a vortex can be defined as a region where the vorticity is "*high*" (e.g. Thompson et al., 2009). But, how can "*high*" be quantified? In fluid mechanics, vortex identification methods are often based on the analysis of the kinematics of the flow field. Most of the published methods study the relative importance of the rotation inside the velocity gradient tensor (Thompson et al., 2009). The methods only differ in the amount of rotation that is necessary for the identification of a vortex. Thompson et al. (2009) propose the following mental exercise: Starting from a fixed symmetric velocity gradient tensor with zero rotation, the rotation tensor is increased until it reaches a certain threshold that marks the importance of the vorticity compared to the deformation. The difference between different kinematic methods lies in the difference of these thresholds.

Basis of the most common kinematic vortex identification methods is the local examination of the invariants and eigenvalues of the velocity gradient tensor $\nabla \mathbf{u}$. The eigenvalues α are determined by the eigenvalue equation

$$\det(\nabla \mathbf{u} - \alpha \mathbf{I}) = 0 \tag{202}$$

where $\mathbf{I}$ is the unit tensor. This leads to the characteristic equation

$$\alpha^3 - P\alpha^2 + Q\alpha - R = 0 \tag{203}$$

with the invariants P, Q, and R of $\nabla\mathbf{u}$ that are defined as (see e.g. Jeong and Hussain, 1995)

$$P = \nabla \cdot \mathbf{u} \tag{204}$$

$$Q = \frac{1}{2}(\|\mathbf{\Omega}\|^2 - \|\mathbf{S}\|^2) \tag{205}$$

$$R = \det(\nabla\mathbf{u}) \ . \tag{206}$$

Note, that $P = 0$ for incompressible flow.
Some examples of kinematic methods based on the eigenvalues and (combinations of) invariants are the Δ-method, the Q-method (also called Okubo-Weiss parameter), and the λ_2-method (see e.g. Jeong and Hussain, 1995). We will give a short overview over these methods in the following.

6.2.0.5 Q-method (Hunt et al., 1988)

The Q-method investigates the second invariant Q of $\nabla\mathbf{u}$. Q is given by the difference of the tensor norms of the vorticity tensor and the strain rate tensor: $Q = \frac{1}{2}(\|\mathbf{\Omega}\|^2 - \|\mathbf{S}\|^2)$. It is positive if the vorticity tensor prevails over the strain rate tensor, i.e. if the local rotation prevails over the local deformation. Hunt et al. (1988) defined a vortex as a region of $Q > 0$ with the additional requirement that the pressure must be lower in the vortex region. This parameter is also called Okubo-Weiss parameter. It has been used successfully in tropical cyclone studies and in detecting tropical cyclones from gridded data (e.g. Dunkerton et al., 2009; Tory et al., 2013). It is similar to the kinematic vorticity number W_k-method that will be introduced below in chapter 6.3.

6.2.0.6 Δ-method (Chong et al., 1990)

The Δ-method, introduced by Chong et al. (1990), uses the eigenvalues of the velocity gradient tensor $\nabla\mathbf{u}$ in order to classify the local streamline pattern around a point when one is moving with the velocity of that point. Chong et al. (1990) define a vortex core as the region of complex eigenvalues of $\nabla\mathbf{u}$ which imply spiralling motion (see also Haimes and Kenwright, 1999). Complex eigenvalues in incompressible flow ($P = 0$) occur when the discriminant Δ is larger than zero (e.g. Jeong and Hussain, 1995)

$$\Delta = (Q/3)^3 + (R/2)^2 > 0 \tag{207}$$

where Q, R are the invariants of $\nabla\mathbf{v}$ introduced above. Since $R^2 \geq 0$, this method will give a larger vortex area than the Q-method.

6.2.0.7 λ_2-method (Jeong and Hussain, 1995)

Jeong and Hussain (1995) introduced the λ_2-criterion based on the eigenvalues of the symmetric tensor $\mathbf{S}^2 + \mathbf{\Omega}^2 = \mathbf{S} \cdot \mathbf{S} + \mathbf{\Omega} \cdot \mathbf{\Omega}$. For a symmetric tensor, the eigenvalues are real and can be sorted as $\lambda_1 \leq \lambda_2 \leq \lambda_3$. Jeong and Hussain (1995) "*define a vortex core as a connected region of two negative eigenvalues of* $\mathbf{S}^2 + \mathbf{\Omega}^2$", i.e. this is equivalent to the criterion $\lambda_2 < 0$. The λ_2-criterion corresponds to the pressure minimum in a plane when unsteady irrotational straining is discarded in the inviscid, incompressible Navier-Stokes equation. This can be deviated from the following considerations: The incompressible Navier-Stokes equations in an inertial, nonrotating reference frame are given as (see equation (55), and (146), respectively)

$$\frac{D\mathbf{u}}{Dt} = \frac{\partial \mathbf{u}}{\partial t} + \mathbf{u} \cdot \nabla \mathbf{u} = \mathbf{g} - \frac{1}{\rho} \nabla p + \nu \nabla^2 \mathbf{u} \tag{208}$$

where ν is the viscosity. The gradient of this Navier-Stokes equations for incompressible ($\rho = const., \mathbf{g} = const.$) flow read

$$\frac{\partial \nabla \mathbf{u}}{\partial t} + \mathbf{u} \cdot \nabla(\nabla \mathbf{u}) + \nabla \mathbf{u} \cdot \nabla \mathbf{u} = \underbrace{\nabla \mathbf{g}}_{=0} - \frac{1}{\rho} \nabla(\nabla p) + \nu \nabla^2 (\nabla \mathbf{u}) \tag{209}$$

Here, $\nabla(\nabla p)$ is the Hessian of the pressure that contains informations on the local pressure extrema (Jeong and Hussain, 1995). The Hessian of pressure is a symmetric tensor. We have seen in chapter 2.6 that the velocity gradient splits into a symmetric (strain rate tensor) and an antisymmetric (rotation tensor) component ($\nabla \mathbf{u} = \mathbf{S} + \mathbf{\Omega}$, see equation 17). Hence,

$$\frac{D \nabla \mathbf{u}}{Dt} = \underbrace{\frac{D\mathbf{S}}{Dt} + \mathbf{S} \cdot \mathbf{S} + \mathbf{\Omega} \cdot \mathbf{\Omega}}_{\text{symmetric}} + \underbrace{\frac{D\mathbf{\Omega}}{Dt} + \mathbf{S} \cdot \mathbf{\Omega} + \mathbf{\Omega} \cdot \mathbf{S}}_{\text{antisymmetric}} \tag{210}$$

Then the Navier-Stokes equations can be split into a symmetric and an antisymmetric part

$$\frac{D\mathbf{S}}{Dt} + \mathbf{S} \cdot \mathbf{S} + \mathbf{\Omega} \cdot \mathbf{\Omega} = -\frac{1}{\rho} \nabla(\nabla p) + \nu \nabla^2 (\mathbf{S}) \qquad \text{symmetric} \tag{211a}$$

$$\frac{D\mathbf{\Omega}}{Dt} + \mathbf{S} \cdot \mathbf{\Omega} + \mathbf{\Omega} \cdot \mathbf{S} = \nu \nabla^2 (\mathbf{\Omega}) \qquad \text{antisymmetric} \tag{211b}$$

Assuming steady irrotational straining ($D\mathbf{S}/Dt = 0$) and inviscid ($\nu = 0$), incompressible conditions, we see that (211a) reduces to

$$\mathbf{S} \cdot \mathbf{S} + \mathbf{\Omega} \cdot \mathbf{\Omega} = -\frac{1}{\rho} \nabla(\nabla p) \; . \tag{212}$$

A pressure minimum in a plane is characterized by (at least) two positive eigenvalues of the Hessian[51]. However, the minus sign in front of the Hessian of pressure leads to the final requirement of (at least) two negative eigenvalues of the symmetric tensor $\mathbf{S}^2 + \mathbf{\Omega}^2$. Therefore compared to the W_k- and Q-methods, the λ_2 method requires the rotation prevailing over the deformation in only one eigenplane. However for planar flows, the vortex regions defined by the Δ-, Q-, W_k-, and λ_2-methods are equivalent (Jeong and Hussain, 1995).

6.3 Introduction of the kinematic vorticity number method (W_k-method) considering the ratio of rotation and deformation rate[52]

The kinematic vorticity number W_k introduced by Truesdell (1953) is defined as the ratio of the tensor norms of $\mathbf{\Omega}$ and $\mathbf{S}$:

$$W_k = \frac{\|\mathbf{\Omega}\|}{\|\mathbf{S}\|} \tag{213}$$

where both - numerator and denominator - are invariants of $\nabla\mathbf{v}$. In two dimensions, the kinematic vorticity number can be calculated with help of (36) and (38) as

$$W_k = \frac{\|\mathbf{\Omega}\|}{\|\mathbf{S}\|} = \frac{\sqrt{\zeta^2}}{\sqrt{\mathrm{D}_h^2 + \mathrm{Def}^2 + \mathrm{Def}'^2}} \,. \tag{214}$$

We can distinguish between three cases:

$$\begin{aligned} W_k &> 1 \;:\; \text{when } \|\mathbf{\Omega}\| > \|\mathbf{S}\| \;-\; \text{a vortex} \\ W_k &= 1 \;:\; \text{when } \|\mathbf{\Omega}\| = \|\mathbf{S}\| \;-\; \text{pure shear} \\ W_k &< 1 \;:\; \text{when } \|\mathbf{\Omega}\| < \|\mathbf{S}\| \;-\; \text{no vortex} \end{aligned}$$

If the rotation rate prevails over the strain rate W_k is larger than 1 ($W_k > 1$) up to ∞ for the case of pure rigid body rotation with zero deformation. In a pure shear flow the local rate of rotation equals the local strain rate ($W_k = 1$). If the deformation prevails over the rotation the kinematic vorticity number W_k is smaller than 1 ($W_k < 1$). The kinematic vorticity number is a measure for the quality of rotation (Truesdell, 1953): it is possible for two vortices to have the same W_k-value even so one can have small

[51] This becomes apparent when looking at a one-dimensional function of pressure $p(x)$ that has at some location x_0 a local minimum. A local minimum is characterized by a pressure gradient of zero $\partial p/\partial x|_{x=x_0} = 0$ and by a second derivative that is positive $\partial^2 p/\partial x^2|_{x=x_0} > 0$. More general, the Hessian of pressure describes the second derivatives (also mixed derivatives) of pressure in three dimensions.

[52] These sections 2.6, 2.7 and 6.3 are based on/taken from a chapter of a recent publication (Schielicke et al., 2016, chapter 2). Note, the chapter in this thesis is much more detailed than in the publication even though some text passages are identical.

vorticity in a region of small deformation and the other can have large vorticity in a region of large deformation as long as the quality of rotation is the same (e.g. Jeong and Hussain, 1995). Furthermore, W_k can be seen as a measure of how much a vortex resembles a rigid body compared to a deformable fluid where larger values of W_k imply a stronger resemblance to a rotating solid object.
Considering the sign of vorticity will slightly modify the equation with the advantage to study vortices of positive and negative vorticity (or cyclones and anticyclones) likewise. This *extended kinematic vorticity number* W_k^* is given by:

$$W_k^* := \frac{\zeta}{\sqrt{\mathrm{D}_h^2 + \mathrm{Def}^2 + \mathrm{Def}'^2}} \,. \tag{215}$$

The extended kinematic vorticity number is especially useful when one is interested in the study of vortices of a particular circulation, for example the separate analysis of low and high pressure systems in the midlatitudes.

6.3.1 Shear flow

The velocity field of a shear flow has only one component which changes by a constant rate in a direction perpendicular to that component. Without loss of generality, we can assume that the direction of the flow is eastwards ($\mathbf{u} = (u, 0, 0) = u\mathbf{i}$) and that the velocity changes in north-south direction ($\mathbf{u} = \mathbf{u}(y)$)[53]. Note, that this flow is non-divergent, i.e $\nabla \cdot \mathbf{u} = 0$. The velocity gradient tensor is then only determined by one component

$$\nabla\mathbf{u} = \begin{pmatrix} 0 & u_y & 0 \\ 0 & 0 & 0 \\ 0 & 0 & 0 \end{pmatrix} \,. \tag{216}$$

Then, the strain rate $\mathbf{S}$ and the rotation tensors $\mathbf{\Omega}$ are calculated as

$$\mathbf{S} = \frac{1}{2}\begin{pmatrix} 0 & u_y & 0 \\ u_y & 0 & 0 \\ 0 & 0 & 0 \end{pmatrix} \,, \tag{217}$$

and

[53] Under the given conditions, every flow field can be rotated such that the direction of the flow points eastwards and the gradient northwards when moving with a point in the fluid.

$$\mathbf{\Omega} = \frac{1}{2}\begin{pmatrix} 0 & u_y & 0 \\ -u_y & 0 & 0 \\ 0 & 0 & 0 \end{pmatrix} , \tag{218}$$

respectively. The tensor norms of both tensors are identical:

$$\|\mathbf{S}\| = \sqrt{S_{ij}S_{ji}} = \frac{1}{2}\sqrt{u_y^2 + u_y^2} = u_y/\sqrt{2} \tag{219}$$

$$\|\mathbf{\Omega}\| = \sqrt{-\Omega_{ij}\Omega_{ji}} = \frac{1}{2}\sqrt{(-u_y)^2 + (-u_y)^2} = u_y/\sqrt{2} \, . \tag{220}$$

Therefore, the kinematic vorticity number W_k, i.e. the ratio of the tensor norms of rotation and strain rate tensor is equal to 1 in a shear flow

$$W_k = \frac{\|\mathbf{\Omega}\|}{\|\mathbf{S}\|} = 1 \, . \tag{221}$$

6.3.2 On the global balance of deformation and rotation in the flow

There is a global balance between deformations and rotations in an incompressible fluid (i.e. $\nabla \cdot \mathbf{v} = 0$). This can be seen by examination of the Jacobi-determinant $J(u,v)$ of the horizontal velocity components, i.e. the determinant of $\nabla \mathbf{v}$, in 2d:

$$J(u,v) = \det(\nabla \mathbf{v}) = u_x v_y - u_y v_x \tag{222}$$

Equation (222) can be written as divergence[54]:

$$J(u,v) = \nabla \cdot [\nabla v \times u\mathbf{k}] \tag{223}$$

Integrating (223) over the whole 2d domain (area) and application of Stokes' theorem[55] leads to

$$\int_A J(u,v) dA' = 0 \tag{224}$$

On the other hand, the Jacobi determinant is given by[56]

$$4J(u,v) = \mathrm{D}_h^2 - (\mathrm{Def}^2 + \mathrm{Def}'^2) + \zeta^2 \tag{225}$$

[54] This can be evaluated by explicitly calculating the rhs of (223) which leads to the rhs of (222).

[55] Stokes theorem - also called Gauss' theorem - states that the sum of sources and sinks of a property $\mathbf{X}$ inside a region equals the flow of $\mathbf{X}$ through the boundary of that region. In two dimensions, Stokes' theorem can be written as $\int_A dA' \nabla \cdot \mathbf{X} = \oint_S d\mathbf{s} \cdot \mathbf{X}$ where $d\mathbf{s}$ denotes a vector element normal to the boundary S surrounding the area A. This integral is zero for periodic boundary conditions or when $\mathbf{X}$ falls off to zero rapidly enough at the boundary.

[56] This can be evaluated by explicit calculation.

Combining (224) and (225) leads to

$$\int_A \zeta^2 dA' = \int_A (\mathrm{Def}^2 + \mathrm{Def'}^2) dA' - \int_A \mathrm{D}_h^2 dA' \tag{226}$$

Dividing (226) by the integral over the deformations leads to a dimensionless expression relating rotation and divergence to the deformations:

$$\frac{\int_A \zeta^2 dA'}{\int_A (\mathrm{Def}^2 + \mathrm{Def'}^2) dA'} = 1 - \underbrace{\frac{\int_A \mathrm{D}_h^2 dA'}{\int_A (\mathrm{Def}^2 + \mathrm{Def'}^2) dA'}}_{\geq 0} \tag{227}$$

The second term on the right-hand side is always larger to zero since it is composed of positive, quadratic terms only or it is equal to zero in case of zero horizontal divergence ($D_h = 0$). In an incompressible fluid (i.e. for $\mathrm{D}_h = 0$), the global integrals of the deformations and rotations are of the same size

$$\frac{\int_A \zeta^2 dA}{\int_A (\mathrm{Def}^2 + \mathrm{Def'}^2) dA} = 1 \quad \text{for } \mathrm{D}_h = 0 \tag{228}$$

$$\frac{\int_A \zeta^2 dA}{\int_A (\mathrm{Def}^2 + \mathrm{Def'}^2) dA} < 1 \quad \text{for } \mathrm{D}_h \neq 0 \tag{229}$$

Note, that the global integral over vorticity squared is twice the enstrophy ϵ which is a conserved quantity in two-dimensional flow. Therefore, the global integral over the deformations in case of $\mathrm{D}_h = 0$ is also a conserved quantity of the same size as half the enstrophy. Using the mean value theorem[57] leads to the equality between the mean values of the squares of vorticity and deformations in the whole domain: $\overline{\mathrm{Def}^2 + \mathrm{Def'}^2} = \overline{\zeta^2}$ where the line over the variables denotes the areal average. Furthermore, we can define the ratio of the area-averaged square of vorticity and the sum of the area-averaged squares of deformation and divergence as:

$$AW^2 := \frac{\overline{\zeta^2}}{\overline{\mathrm{D_h}^2 + \mathrm{Def}^2 + \mathrm{Def'}^2}} \tag{230}$$

The structure of AW^2 resembles the square of the kinematic vorticity number W_k^2 (see equation 214) where the terms ζ^2 and $(\mathrm{D_h}^2 + \mathrm{Def}^2 + \mathrm{Def'}^2)$ have been exchanged with their area-averages[58]. Due to the equivalence of the squares of deformation and rotation in a flow of zero divergence, AW^2 becomes equal to 1:

$$AW^2\Big|_{D_h=0} = \frac{\overline{\zeta^2}}{\overline{\mathrm{Def}^2 + \mathrm{Def'}^2}} = 1 \tag{231}$$

[57] For any field f in A the area averaged mean value is given by $\overline{f} = \int_A f dA' / \int_A dA'$

[58] However, note that $AW^2 \neq \int W_k^2 dA$.

In case of non-zero divergence, (226) can be rewritten as

$$\int_A (\mathrm{Def}^2 + \mathrm{Def}'^2 - \mathrm{D_h}^2) dA' = \int_A (\mathrm{Def}^2 + \mathrm{Def}'^2 + \mathrm{D_h}^2) dA' - 2\int_A \mathrm{D_h}^2 dA' = \int_A \zeta^2 dA' \tag{232}$$

Hence, we can write $\overline{\mathrm{D_h}^2 + \mathrm{Def}^2 + \mathrm{Def}'^2} - 2\overline{\mathrm{D_h}^2} = \overline{\zeta^2}$. This is equivalent to $AW^2 < 1$ on a global scale:

$$AW^2\Big|_{D_h \neq 0} := \frac{\overline{\zeta^2}}{\overline{\mathrm{D_h}^2 + \mathrm{Def}^2 + \mathrm{Def}'^2}} = 1 - \underbrace{\frac{2\overline{\mathrm{D_h}^2}}{\overline{\mathrm{D_h}^2 + \mathrm{Def}^2 + \mathrm{Def}'^2}}}_{>0} < 1 \tag{233}$$

Note, that in case of irrotational, curl-free flow $AW\big|_{\zeta=0} = 0$, because of the balance of divergence and deformation in (226).

The global balance of deformation and rotation in a two-dimensional flow implies that the knowledge of one part (e.g. the total rotation in the field) is enough to know the magnitude of the other part (e.g. the total deformation). By injecting more rotation (or more vortices) into the fluid, we also add the same amount of deformation to the fluid. The definition of the Jacobian also holds in three-dimensional flow, hence the balance between the three-dimensional deformations and rotations remain. However, only in two-dimensional flow the enstrophy is a conserved quantity while it is not conserved in three dimensions.

In Appendix B we investigated the vertical distribution and seasonal behavior of AW^2 (see Figure B77) in comparison to the area-averaged W_k number (absolute values) in different levels of the atmosphere. While the area-averaged W_k number can be smaller as well as larger than 1, we found that AW^2 is less than 1 at all levels with the smallest values at the lower troposphere ($AW^2 \approx 0.75$ at the 1000 hPa level in the northern hemisphere). However, in the mid- and upper troposphere between about 700 and 300 hPa AW^2 is close to one on both hemispheres independent of the season. This coincides with the assumption that the divergence-free level is located at about 600-500 hPa. Interestingly, the vertical mean of the area-averaged W_k number is relatively stable with values close to 1 although it shows a strong dependence on height and season. More details are given in Appendix B.

6.3.2.1 W_k-method in comparison to other kinematic methods

The kinematic methods that were introduced in the previous chapters are all based on the velocity gradient tensor and its invariants. Therefore, the question arises why we chose the kinematic vorticity number method (W_k-method). Especially since the W_k-method is similar to the Okubo-Weiss parameter (Q-method). We decided in favor of the W_k-method over the other methods since it - as a dimensionless number - allows a comparison of vortex structures relative to the background deformation (or shear).

This further allows to study the application of different dimensionless thresholds of the W_k number used in the vortex identification procedure: A lower threshold of W_k (e.g. W_k slightly smaller than 1) probably detects early circulations that can develop into stronger vortices. On the other hand, a higher threshold of W_k focuses on already developed strong vortices.
We think that this nondimensionality of the kinematic vorticity number is its main advantage in comparison to the other kinematic methods. Furthermore, the $\overline{W}_k$ number averaged in the region of a vortex represents a kinematic circulation and its value gives the resemblance of a vortex with a rotating solid object: The larger this value is the larger is the equivalence to a solid body.

6.4 Numerical Implementation of the kinematic vorticity number method (W_k-method) to identify vortex sizes and circulations

The field of the extended kinematic vorticity number W_k^* (215) will serve as the basic field for the identification of vortex patches. The numerical method will construct a residual vortex patches field by the following two steps:

(i) The field of the kinematic vorticity number W_k^* will be set to 1 at every point where $\left\|W_k^*\right\| > 1$, i.e. where the rotation rate prevails over the strain rate, and it will be set to zero wherever $\left\|W_k^*\right\| \leq 1$;

(ii) The field derived in (i) is multiplied with the relative vorticity field.

This two-step approach leads to a field of distinguishable vortex patches. Figure 21 shows an example how the original relative vorticity and the W_k^*-fields are used in order to derive the field of vortex patches. Note, how nicely the vortices are extracted (see Figure 21(d)) from the continuous vorticity field displayed in Figure 21(c). More details on the method will be given in the following chapters.

6.4.1 Identification of vortex centers

As a first approach in defining the vortex centers, we will use the residual vortex patches field (like that plotted in Figure 21d) and search for relative vorticity extrema. Strictly, local extrema have larger (or smaller) values then the surrounding field. Numerically in grid point space, we compared every grid point in the field (except of the polar caps) to its 8 surrounding grid points. A minimum (maximum) is identified, when the value at that point is smaller (larger) than the 8 surrounding points. However, in order to allow for broad maxima, we relaxed the criterion to values smaller or equal (larger or equal) than the surrounding ones. When an extremum is found, the local position (latitude/longitude; x-,y-position in grid space; height of level) as well as the value of

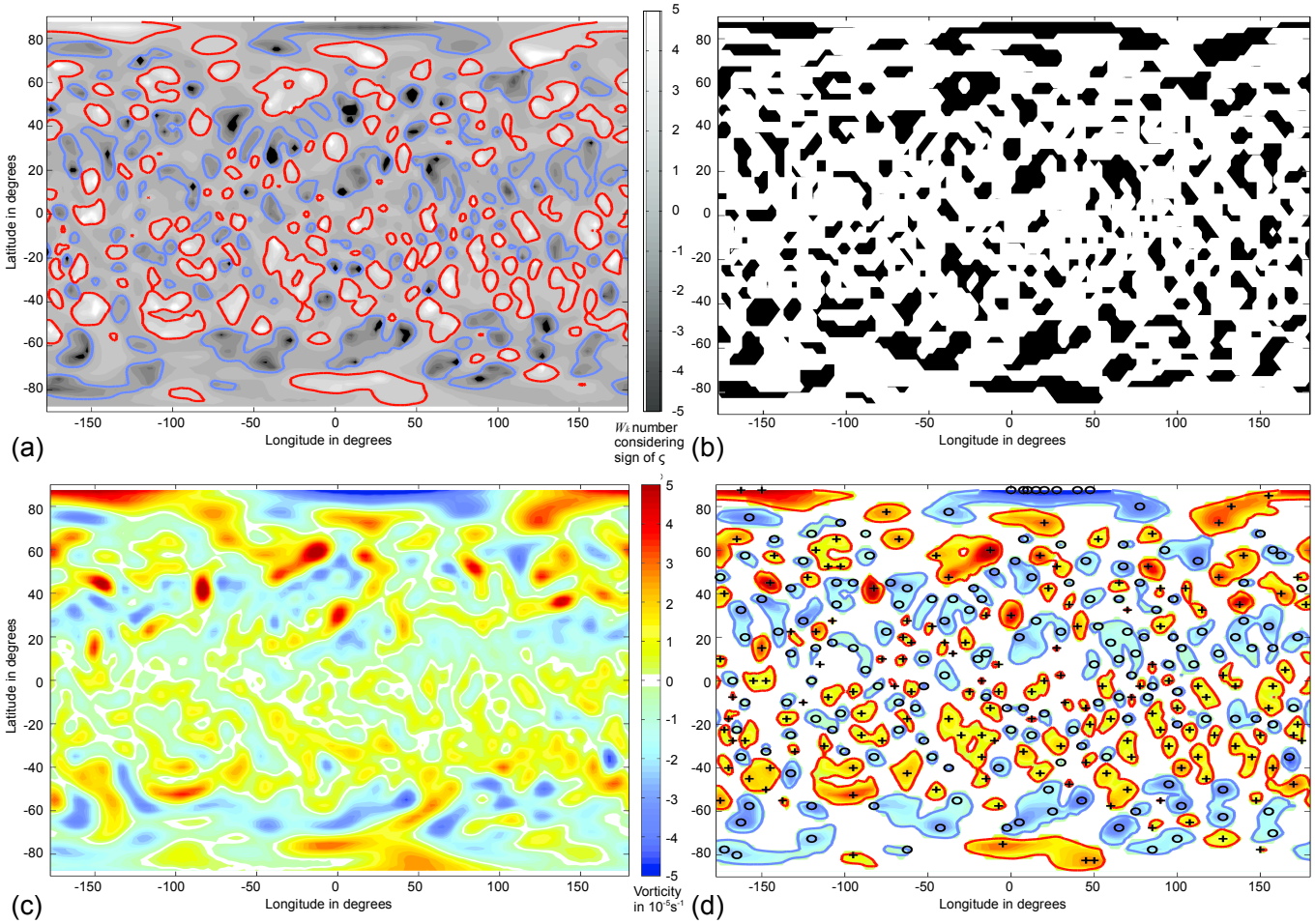

Figure 21: *Steps to derive the residual vortex patches field are plotted for the 15 January 1999 12 UTC: (a) Field of W_k^* considering the sign of the vorticity; (b) mask of vortex patches with value 1 (black) for regions of identified vortices ($\|W_k^*\| > 1$), white areas are dominated by strain - mask sets these regions to 0; (c) Field of relative vorticity, values close to zero are plotted in white; (d) residual field of vortex patches derived by multiplying field (b) with field (c). Red (blue) contours in (a) and (b) correspond to $W_k^* = 1$ ($W_k^* = -1$) contours considering the sign of vorticity, Crosses and circles correspond to identified vorticity maxima and minima in the residual field (d).*

the relative vorticity extremum is registered in a first step. After identification of all maxima and minima, the outermost-closed vorticity contour around each local center is determined. Since it is possible to have more than one maximum (or minimum) inside the same vortex patch area, the search is done for the outermost-closed vorticity contour including 1, 2, 3, etc. maxima (or minima). Numerically, this is implemented by first searching for the zero-vorticity-contour surrounding each vortex patch area completely. In the process, the number N of relative vorticity extrema inside the zero-vorticity-contour is determined. This enables the search method to determine the contour (and its vorticity value) that explicitly include a number from 1 to N vortex centers. Note, that not all possible configurations are fulfilled. See e.g. Figure 22 where for the vortex

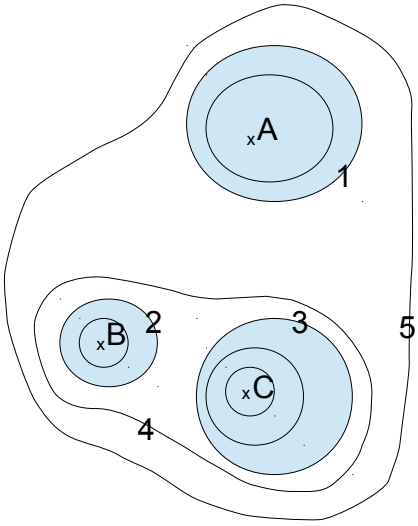

Number of maxima included in contour (labelled 1 to 5)

As seen by vortex centers (labelled A,B,C)

	A	B	C
one	1 (A)	2 (B)	3 (C)
two	---	4 (B,C)	4 (B,C)
three	5 (A,B,C)	5 (A,B,C)	5 (A,B,C)

Figure 22: *Sketch of multiple vorticity centers inside the same contour. The method considers every center separately.*

center labeled A only the configurations of one (A) and three maxima (A,B,C) inside a contour surrounding center A can be determined, while a configuration of two centers inside the same contour is not fulfilled. However, since this search is done for every center separately, all possible configurations will be detected.

6.4.2 Definition of single centers and W_k features

In this thesis we will differentiate between two types of vortex features: ***single centers*** and ***W_k features***.

We will define a ***W_k feature*** as a simply-connected region of $W_k^* > 1$ (for positive circulations on the northern hemisphere) or $W_k^* < 1$ (for negative circulations on the northern hemisphere). Thereby, two points are simply-connected if they are direct neighbors in one of the four directions: north, south, west or east. Note, that a W_k feature can include one or multiple vorticity extrema. Hence, a W_k feature rather represents a large-scale area of likewise circulation such as e.g. a cyclone family.

On the other hand, each ***single center*** includes only a single local vorticity extremum (or a broad extremum, see above in chapter 6.4.1). The size of a single center is determined by finding the outer-most closed contour that surrounds the single vorticity extremum. Single center and W_k feature coincide if only one single vorticity extremum

is located in a vortex patch area. Otherwise, the size of the single centers is smaller than that of the corresponding W_k feature. Hence, single centers rather represent the smaller-scale structures that form the large-scale circulation areas. An example can be found in Figure 21(d) located at about 30°W, 60°N: Here, the W_k feature includes three local vorticity maxima (located at about 50°W, 60°N; 45°W, 50°N) that are arranged such that the W_k feature even possess a gap in the center of its area. This gap occurs because of the relatively strong deformation between the vorticity centers while the vorticity field at this location is still positive (compare with Figure 21c). In this case, the observation of single centers might be better. Especially, when one is interested in the behavior and motion of single storms. Although, the identification of single centers seems to be a more appropriate choice in large-scale data, the computational costs due to the contour-method are large in comparison to the fast numerical identification of W_k features. Hence, the analysis of W_k features is the preferred method when dealing with large data sets in this thesis.

6.4.2.1 Remark on further possible definitions

So far, we have only differentiated between single centers and W_k features. However, it is possible to use a finer differentiation and split W_k features into smaller *single centers* and/or *multiple centers*. After all, it is not trivial to decide if a vortex patch area belongs to a single center system or if it should be split up into multiple smaller vortex areas that include one or more vorticity centers. This decision involves some kind of subjectivity and some things need to be considered. On the one hand, the resolution of the data set should be taken into account. On the other hand, for large-scale flows cyclones and anticyclones should be treated differently. The reason for the last point lies in the different dynamic constraints for cyclones and anticyclones due to the gradient wind balance. We have seen, that anticyclones are constrained to weaker pressure gradients and therefore have in general[59] larger radii than cyclones (see chapter 3.2.1.2). The decision can be implemented in the program with the help of well-considered, well-founded thresholds of gradients or constraints on the distances of two local extrema. There are already program versions of the W_k-method that are capable of identifying multiple vortex centers inside larger W_k features. Still, these versions need to be well tested which should be a focus of future work.

6.4.3 Determination of vortex sizes

Knowledge of the position of the surrounding contour permits the calculation of the area as well as the circulation of the vortex. The area can be determined in two ways. On the one hand, the vortex area can be calculated as the sum of all grid boxes that lie inside the determined contour. In grid space, every grid point can be associated

[59] when the same pressure disturbance is assumed

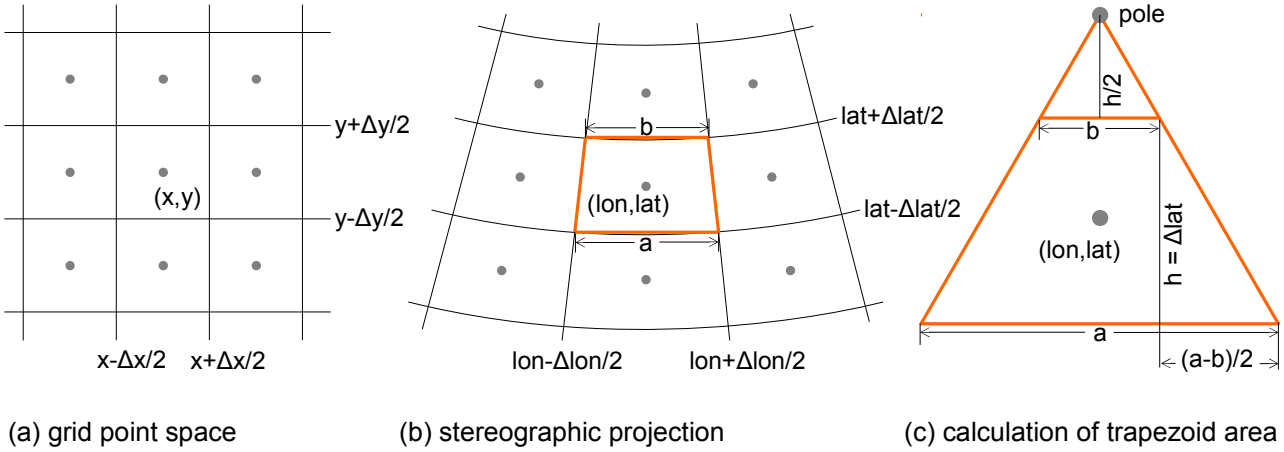

Figure 23: *Appearance of grid boxes (a) as regular squares in grid point space and (b) approximately as trapezoids (orange) in stereographic projection; (c) Calculation of trapezoid area around a grid point (and triangle at the poles, respectively). Gray dots represent grid points.*

as the center point of a box surrounding the point (see Figure 23a,b). In a standard lat/lon projection the grid boxes appear regularly. However, this is not an equal-area projection. While the latitudes are equally-spaced with 1° latitude being equal to about 111 km, the distance between two meridians depends on the latitude with zero distance at the poles and about 111 km at the equator[60]. The length of a distance Δx in km is given by

$$\Delta x = \frac{2\pi R \cos\theta}{360\circ} \Delta lon \tag{234}$$

where $R = 6370$ km is the Earth's radius, θ the latitude and Δlon the distance in degree longitudes to be converted. Due to the difference between the upper and lower length of a grid box, the shape of the grid box can be approximated as isosceles trapezoid - except at the poles where the shape is a triangle with base b and height $h/2$ (cf. Figure 23c). The area of a grid box with the parallel sides a and b (w.l.o.g. $a > b$), and height $h = \Delta lat$, i.e. an isosceles trapezoid, is calculated by (see Figure 23c):

$$A_{Trapezoid} = \left(a - \frac{(a-b)}{2}\right) h \qquad \text{for } |lat| < 90° \tag{235}$$

$$A_{Triangle} = \frac{bh}{4} \qquad \text{for } |lat| = 90° \tag{236}$$

An example of the grid box method is given in Figure 24a. Here, the thick blue line encloses the area determined by the grid box method while the greenish yellow contour stands for the true vortex area.

[60] When assuming a radius of the Earth to be 6370 km, the circumference is given by $U = 2\pi R \approx 40000$ km, then 1° longitude corresponds to 111 km.

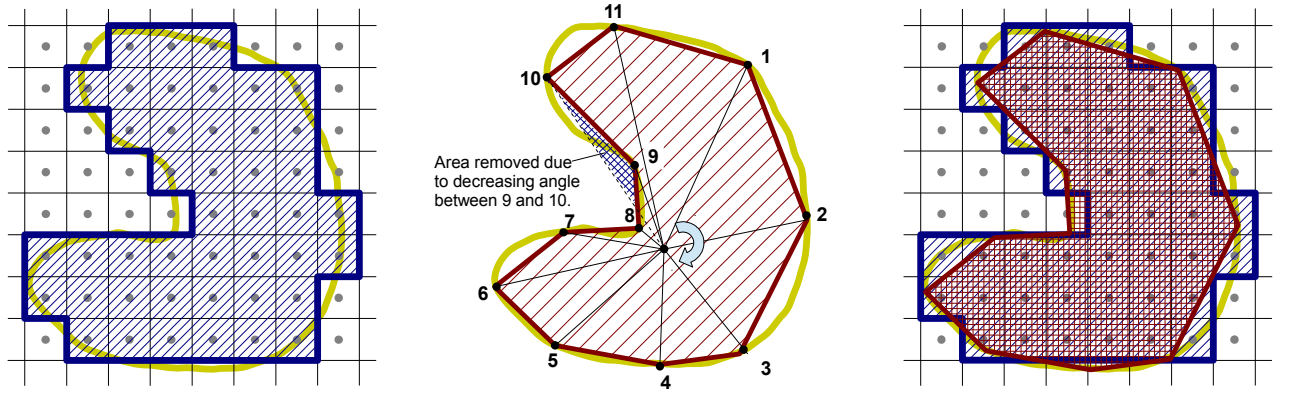

(a) Grid box method (b) Contour method (c) Comparison between both methods

Figure 24: *Calculation of vortex area by (a) grid box method (sum over all grid box areas inside a closed contour), all boxes inside the thick blue line count to the total area, and (b) contour method (sum over triangles formed by two neighboring points on the contour and the vortex center). Vortex center indicated by dot inside the greenish yellow contour; (c) comparison between both methods. Greenish yellow contour in all sketches represents the true vortex contour*

Another way to calculate the size of a vortex can be done by taking into account the (outermost) closed contour directly. The contour around the vortex center is split in smaller parts forming triangles considering the vortex centroid and two neighboring contour points. The total area is then represented by the sum over all triangles. Since the side lengths are know, the triangle areas A are calculated by Heron's formula (see e.g. chapter 3.2.1.2 in Bronstein et al., 2005, pages 145–147):

$$A = \sqrt{s(s-a)(s-b)(s-c)} \qquad \text{with} \quad s = \frac{a+b+c}{2} \tag{237}$$

where s is half of the circumference of the triangle. Numerically, we sum up over all areas considering the direction of the contour (clockwise/counterclockwise). If the direction grows or decreases monotonically, the total area equals the sum of the single triangles. However, it is possible, that the contour changes the direction as in the example in Figure 24b between the contour points labeled 9 and 10. The contour points are monotonously ordered in clockwise direction starting from points 1 to 9. From point 9 to 10, the direction changes (counterclockwise), and is afterwards clockwise again until the contour is closed from point 11 to 1 (cf. Figure 24b). In Figure 24c, grid box and contour method are compared. In conclusion, both methods seem to capture well the true size of the vortex (indicated by the greenish yellow contour) and give comparable results[61].

[61] A few subjective tests for single dates have been conducted. Those tests conferred that the sizes determined by both methods are of comparable order.

6.4.4 Determination of circulations

With help of the methods of size determination described in the previous section the circulation of a vortex can easily be calculated using equation (108) (see chapter 3.3.3). With help of the grid box method the circulation is estimated by

$$\Gamma = \int \zeta dA \approx \sum_{i=1}^{N} \zeta_i A_i \tag{238}$$

where ζ_i is the relative vorticity at the ith grid point and A_i the area associated with that grid point. The summation is done over all N grid boxes that belong to the identified vortex area.

The circulation of a vortex can also be estimated with help of the contour method: With the help of equation (107), see chapter 3.3.3, we can write the circulation of two-dimensional data as

$$\Gamma = \oint \mathbf{u} \cdot d\mathbf{s} \approx \sum_{j=1}^{M} \left(u_j ds_{xj} + v_j ds_{yj} \right) \tag{239}$$

where u_j, v_j are the horizontal wind components in west-east, and north-south direction, respectively. Index j stands for the jth point on the closed contour with a total of M points[62]. ds_{xj}, ds_{yj} are the x, y-components of the jth line element along the closed contour. A line element between two neighboring points on the contour displays a vector that connects these two points. This second method needs an interpolation step of the wind field onto the contour and is therefore computationally more time-consuming. Anyway, both methods yield circulations of comparable magnitude.

6.4.4.1 Remarks on the size determination method

Both methods are in use throughout the computer program. Although, the grid box method should be preferred because of reduced computation time, the contour searching method is especially important in relatively coarse data. In coarsely-resolved data, often multiple vorticity extrema lie inside the same vortex patch area. Only the contour method is able to separate these extrema. The knowledge gained by the contour method can be used in the decision-making whether the vortex patch areas are associated with single or multiple centers (see chapters 6.4.1 and 6.4.2).

6.4.5 Determination of individual circulation centers

After the decision was met how many vorticity centers should lie inside the same vortex patch area, we can determine the center of circulation as an alternative location of the vortex center. We have already introduced the center of circulation in the context of

[62] On a closed contour, the first and the last point are identical.

point vortices (see chapter 3.4.5.2, equation 139). However, instead of calculating the circulation center of a number point vortices, we want to derive the center of circulation of an extended vortex patch area. Thereby, the contribution of each grid point needs to be considered. Assume, that the vortex (or the vortex patch area) is composed of N grid points. We can then calculate the ***individual center of circulation*** as the sum of the circulation in every grid box times its coordinates divided by the total circulation $\sum_{i=1}^{N} \Gamma_i$ of the vortex patch area:

$$\mathbf{C} = \frac{\sum_{i=1}^{N} \Gamma_i \mathbf{x}_i}{\sum_{i=1}^{N} \Gamma_i} \tag{240}$$

where $\mathbf{x}_i$ denotes the grid box location and Γ_i the associated circulation of the i-th grid point that belongs to the total vortex patch area. Hence, the center of circulation represents the central point of a vortex weighted by its circulation magnitude.

6.5 Vortex tracking

Tracking denotes the chronological connection of vortex centers of successive time steps assuming that the individual systems represent the same physical feature (Neu et al., 2013). There are maybe as many variations of tracking schemes as there are identification methods. Tracking methods vary in their degree of sophistication from simpler nearest-neighbor search methods to more complicated methods that take into account various parameters in order to find the most appropriate track. Furthermore, the tracking methods depend on the basic field that is used for the identification of the cyclones (pressure (geopotential height)/vorticity), on the spatiotemporal resolution of the data (via different thresholds), on the preprocessing of the data (filtered/unfiltered) and on the investigated feature type (fast-moving/slow-moving, small-scale/large-scale). An overview over 15 identification and tracking methods of extratropical cyclones is given in Neu et al. (2013, and in their supplementary material which can be found online at http://dx.doi.org/10.1175/BAMS-D-11-00154.2). In the following, we will present some approaches of commonly used tracking methods.

6.5.1 General approaches of extratropical cyclone tracking

Basically, all extratropical cyclone tracking methods involve the search of the nearest neighbor that best fits. While some authors define ”nearest” literally with respect to the distance between centers, others additionally include e.g. differences in core pressure or vorticity magnitudes between identified and predicted values in their interpretation of the ”nearest” neighbor.

Most methods search for the nearest neighbors in consecutive time steps in certain predefined search ranges that can be arranged symmetric or asymmetric around the

cyclone center to account for the general motion of the cyclones[63] (e.g. Blender et al., 1997; Trigo, 2006). The explicit thresholds of the maximum searching ranges depend on the spatiotemporal resolution of the data. Furthermore, some authors consider the former motion of the cyclone in order to extend the searching range in the direction of the former motion (Lionello et al., 2002) or in order to use the predicted position as a starting point for the search of the nearest neighbor (e.g. Wernli and Schwierz, 2006; Hanley and Caballero, 2012).

Additionally to the prediction of the cyclone position based on steering winds and prior motion, Sinclair (1994) estimates core pressure and vorticity from prior trends. Subsequently, two matching systems are found by minimizing a cost function of the weighted sum of the deviations of the three parameters from the predicted values. In a similar manner, Murray and Simmonds (1991) and Simmonds et al. (1999) calculate the probabilities of each cyclone surrounding the predicted position based on weighted parameters such as distance and core pressure and match the cyclone with the highest probability. While Murray and Simmonds (1991) and Simmonds et al. (1999) developed their method based on thresholds and weights appropriate for the southern hemisphere that is characterized by rather long-living, large-scale cyclones, Pinto et al. (2005) adopted the method, thresholds and weights to the northern hemispheric circulation which is characterized by a larger spectrum of extratropical cyclones ranging from small-scale, fast-moving to large-scale, quasi-stationary systems.

We would like to close this section with two interesting approaches which influenced the tracking method based on the W_k number that will be introduced in the following section: Hewson and Titley (2010) perform a half-time tracking method. This means that systems identified at time step t are moved forward about a half time step to $t+1/2$. Thereby, the forward motion is based on the steering wind and on the previous motion of the cyclone. Systems detected at time step $t+1$ are moved backward in time about a half time step to $t+1/2$ by using the steering winds. Together with other parameters such as consideration of feature type and changes of the layer thickness the best match is searched. Another interesting approach is used by Kew et al. (2010) who identified not only the location of the system's center as an extremum of the investigated field, but the area around that center. Thereby, the area has a predefined (mesoscale) size and is identified by searching for the enclosing contour (isolines of the field) that best fits the predefined size. The shape of the area is not necessarily circular. After identification of the points that form the system's area, these points are advected by the wind field for half a time step and for the second half of that time step with the temporally interpolated wind field at the new location. Two systems match and a track is formed, if the systems of consecutive time steps overlap by more than 10% of the area. Originally introduced for the identification of potential vorticity anomalies at the lower stratosphere, Kew adopted the method to the 850 hPa level geopotential height

[63] In general, the extratropical cyclones move faster to the east than to the west.

fields in order to identify low-level cyclones in the framework of the IMILAST project (Neu et al., 2013).
In the following section, we will introduce a method based on the W_k-method that uses similar approaches such as the half-time tracking of Hewson and Titley (2010) and the advection of the points forming the system of Kew et al. (2010). The reasons why we will introduce another tracking method are primarily based on the fact that we want to use the information on vortex size and circulation that we already obtained during the identification procedure.

6.5.2 Introduction of a tracking method based on the W_k-method

For our needs, two requirements on the tracking method are most important: First, the method should be based on the knowledge gained by the identification procedure (W_k method) and should mainly use the information on the vortex size. Second, the method should be relatively simple in order to enable reproducibility by other scientists. Simplicity further allows to more easily detect the causes of problems and change the settings if problems occur. A schematic overview over our tracking method approach is plotted in Figure 25. The tracking method can be structured into the following steps:

(1) At time step $t = t_0$ and at the consecutive time step $t = t_0 + \Delta t$ all vortex structures and their properties are identified. Especially, the outermost-closed contour is identified (Fig. 25 1a/1b).

(2) The deformation of the outermost-closed contour is calculated with help of equation (6). At time step $t = t_0 + \Delta t$, the backward deformation is derived by calculating the deformation multiplied with minus one (Fig. 25 2a/2b).

(3) Inside the contours — deformed as well as undeformed — the mean wind is calculated by averaging over the velocities at all points that are enclosed by the contours.

(4) The deformed/undeformed contours are forward advected in case of time step $t = t_0$ and backward advected in case of time step $t = t_0 + \Delta t$, respectively. Both advections are calculated to the half time step that lies between both time steps at $t = t_0 + \Delta t/2$. We derive two fields for the forward and backward advected contours.

(5) In the following, we will denote N the number of systems detected at time step $t = t_0$ and N_2 the number of systems detected at the consecutive time step $t = t_0 + \Delta t$. For each system i with $i = [1, .., N]$ we search for overlapping systems separately. The overlap is determined by the multiplication of two masks: mask A is set to one at every point that is enclosed by the deformed/undeformed and forward advected contour of system i and zero elsewhere. In a second loop over the systems j with

$j = [1, .., N_2]$ that occurred at the consecutive time step, we determine a mask B that is set to one at every point enclosed by the deformed/undeformed and backward advected contour of system j and is set to zero elsewhere. A match of two systems is found if the total sum over all grid points of the product of mask A and mask B is different from zero (Fig. 25, step 3). Note, that more than two systems can match.

(6) We need to differentiate five possibilities of matches:

- ***Genesis:*** Systems at the consecutive time step that have no match are seen as the genesis of a new system and are defined as the starting point of a new track.

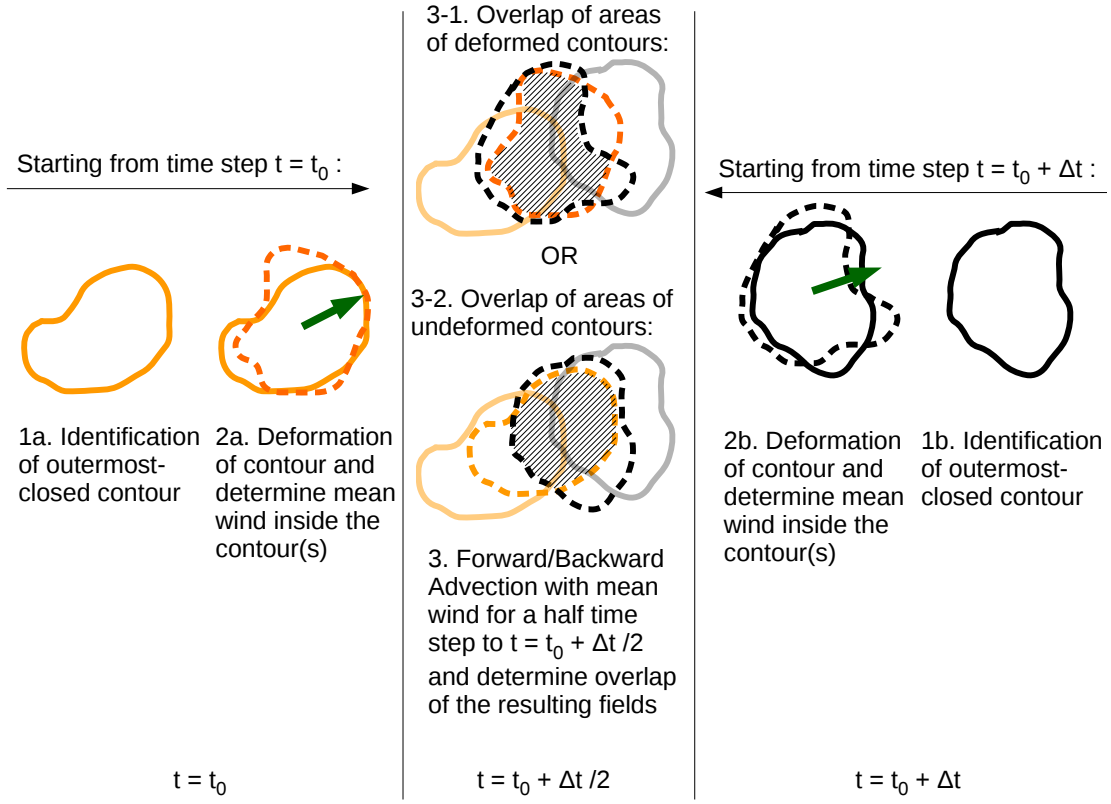

Figure 25: *Scheme of tracking method: After identification of the vortices and their outermost-closed contours for two consecutive time steps $t = t_0$ and $t = t_0 + \Delta t$ (1a/1b), the deformations of the contours are determined with help of equation (6) and the mean winds inside the contours are calculated (2a/2b). In case of the subsequent time step, the deformation is multiplied with minus 1 to account for the backward transformation. Finally, the deformed/undeformed contours are forward (in case of time step $t = t_0$)/ backward (in case of time step $t = t_0 + \Delta t$) advected with the mean wind to the half time step ($t = t_0 + \Delta t/2$) between the two initial time steps (3-1/3-2) and the overlap of the resulting fields is determined (3). Solid/dashed lines correspond to originally identified/modified (deformed and/or advected) contours; orange (black) lines correspond to time step t_0 ($t_0 + \Delta t$). Hatched area denotes overlap; green thick arrow represents the mean wind inside the contours.*

- ***Continuation of track:*** Systems at the consecutive time step that have exactly one match are used to form (or continue) a track by connecting the centers of circulation of the two systems.
- ***Merge:*** Two or more systems at time step $t = t_0$ match with a system at the consecutive time step $t = t_0 + \Delta t$. Only one of the systems will continue the track while the others will end. More details will be given below.
- ***Split:*** One system at time step $t = t_0$ matches with two or more systems at the consecutive time step $t = t_0 + \Delta t$. Only one of the systems will continue the track while the others will be defined as genesis points of new tracks. More details will be given below.
- ***Lysis:*** For a system at time step $t = t_0$ no match is found at the consecutive time step. The circulation center of the system at time step $t = t_0$ is defined as the last position of the track.

Note that a system can be short-lived with a track that contains only one point equal to the genesis and lysis point at the same time.

(7) Steps 1-6 are repeated over all time steps.

The merging/splitting decision is met based on three parameters: (1) the distance between the centers of circulation; (2) the ratio of the areas of the systems at time step $t = t_0 + \Delta t$ compared to the areas of the systems at time step $t = t_0$; (3) the number of overlapping grid points. Systems with the minimum distance, the ratio closest to 1 and with the highest number of overlapping points continue the track. If the three parameters yield no unique result, the decision is met in the following order: the distance prevails over the ratio, the ratio prevails over the sum of the overlapping grid points. If the identification number (ID) of the system with the best ratio and the highest number of overlapping grid points is different from the ID of the system with the smallest distance, then the first ID prevails over the latter and gives the system that continues the track.
It should be noted, that the tracking procedure — as it is presented here — is work in progress and yet still needs to be tested properly. Although both versions of using either the deformed or the undeformed contours are implemented, we will use the second version (advection of undeformed contours) throughout this thesis. The main reason for this decision is that — although the material contours are deformed and advected over time — the material is not bounded to the pressure levels which will serve as the basic levels used in our investigations. Moreover, the advection is not bounded to the mean wind advection on pressure levels as we have assumed so far. However while material can leave or traverse pressure levels, it is frozen to isentropic levels[64] under adiabatic,

[64]Isentropic levels are levels of constant entropy which are characterized by constant potential temperature θ. This is in a way similar to isobaric levels which are characterized by the same pressure.

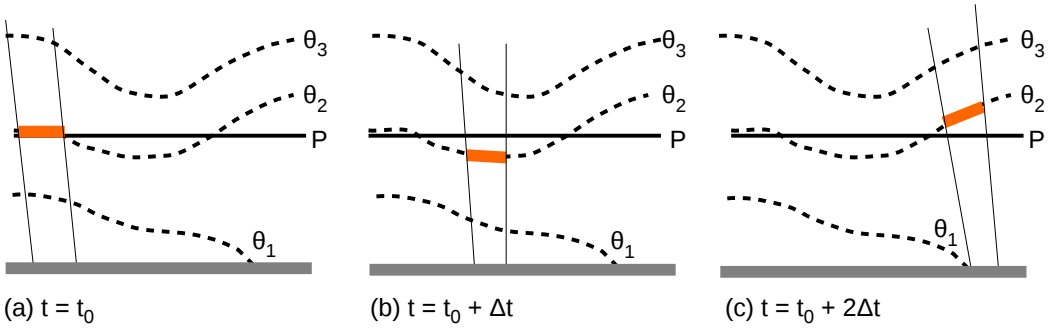

Figure 26: *Motion of a material surface (orange) under adiabatic conditions along an isentropic surface (dashed black lines, denoted as θ_i) for different time steps (a)-(c). Thick gray line represents the surface, thick black solid line represents a pressure surface P and thin black lines correspond to the vortex tube which encloses the material surface (orange). Adopted and slightly modified from Lackmann (2011, his Fig. 3.1).*

inviscid conditions which means that material can only be redistributed, advected or deformed on these levels. This difference between pressure levels and isentropic levels is depicted in Figure 26. However, due to the assumption that the vortex structures are not strictly flat but have a vertical extent, we can still advect the "material" areas and approximately still capture a part of the vortex tube (see Fig. 26, the vortex tubes are indicated by the thin solid black vertically aligned lines).

In conclusion, the tracking procedure can be seen as a first guess approach in order to identify the new locations of the systems. The procedure probably works best in the case of large-scale rather two-dimensional flow but might fail in the case of very small systems embedded in large background gradients and under diabatic conditions. Note that the genesis and lysis of systems on the pressure levels can also be attributed to the fact that the material leaves the pressure surface. The tracking scheme could further be improved by using the three-dimensional dynamic equations in order to follow smaller parcels of air in time or by dynamical interpolation of the three-dimensional fields. Since these approaches are computationally time-consuming so far the improvement of the tracking scheme should be seen as a topic of future work and the presented procedure should be seen as a first simple approach with development potential.

However, in comparison to pressure levels under adiabatic, inviscid conditions isentropic levels are material surfaces. This means that material can only be deformed and redistributed under these conditions.

6.6 Test of W_k-method in idealized set-ups (Schielicke et al., 2016)

In this section, we will compare different size determination methods — traditional as well as kinematic ones — in idealized two-dimensional set-ups. We will specify the methods used for comparison reasons in the idealized cases in section 6.6.1. The experimental set-ups are described in section 6.6.2, followed by a presentation of the results (section 6.6.3) and a discussion (section 6.6.4). Note, that this chapter 6.6 (with slight modifications) is part of a publication that was recently published (Schielicke et al., 2016, their chapter 3). Major modifications will be notified explicitly.

6.6.1 Description of the tested size estimation methods

In a first step, local maxima (minima) in the two-dimensional vorticity (pressure) field are identified. A local maximum (minimum) is found when the 8 surrounding points have lower (higher) values than the central point. In a second step, the following four size estimation methods are applied:

(1) *p-method*: the outermost-closed isobar around a local pressure minimum in 1 hPa increments;

(2) *Gaussfit-method*: a Gaussian fit applied to the surrounding pressure distribution of a low pressure center adopted from Schneidereit et al. (2010);

(3) *ζ-method*: the outermost-closed (positive) vorticity contour around a local vorticity maximum determined by increments of 10^{-8} s^{-1}; and

(4) *W_k-method*: the kinematic vorticity number criterion $W_k = 1$ around a local vorticity maximum introduced in section 6.3.

For a synoptic-scale system with typical values of radius $R = 1000$ km, wind speed $v = 10$ m/s and a pressure drop of $\Delta p = 10$ hPa (which is equal to a core pressure in the order of 1000 hPa at the ground) the vorticity is in the order of $10^{-5}\,s^{-1}$. The increments of the p- and ζ-method were chosen such that they represent about 0.1 % of these typical magnitudes.
For methods (1), (3) and (4), contour lines are calculated by a standard contouring function. The area A is calculated by the sum over all triangle areas formed by two neighboring contour points and the vortex center. By assuming that the area A is circularly distributed around the center, the system's radius R is calculated as $R = \sqrt{A/\pi}$. In method (2), the 2D pressure field surrounding the low pressure center is mapped to a 1D radial distribution: In a first step, the surrounding pressure distribution is interpolated on 36 radial lines (every 10°) starting from the vortex center up to 1000 km (every 50 km). In a second step, the mean of the 36 pressure values for each distance r is determined. Finally, a Gaussian fit is applied to the resulting pressure distribution

with a gnuplot fitting procedure, that fits the following function to the 1D distribution: $p_{Gauss}(r) = a \cdot \exp(-(r - r_0)^2/2b^2)$, where a gives the pressure drop and b represents the radius which is equal to the standard deviation of the Gaussian distribution. The vortex center is located at r_0.

6.6.2 Experimental set-up

The four size estimation methods are tested and compared in different idealized set-ups. The aim of these tests is to find out, how well the different methods perform in re-extracting the predefined vortex sizes from various flow fields.
In the idealized test cases, the pressure field p will be predefined. Geostrophic wind $\mathbf{v}_g$ and geostrophic vorticity fields ζ_g are calculated from the pressure field by

$$\mathbf{v}_g = \frac{1}{\rho f}\mathbf{k} \times \nabla p \quad , \quad \zeta_g = \frac{1}{\rho f}\nabla^2 p \; . \tag{241}$$

For simplification, density ρ and Coriolis parameter f are assumed to be constant ($\rho = 1$ kg/m^3, $f = 10^{-4}$ s^{-4}); $\nabla^2 p$ is the Laplacian of the pressure; $\mathbf{k}$ is the vertical unit vector.

6.6.2.1 Reference case - idealized low pressure system

A low pressure disturbance defined by a 2D Gaussian distribution with intensity $\Delta p = 2.5$ hPa[65] and radius $R = 250$ km:

$$p^\star = \Delta p \exp\left(-\frac{(x - x_0)^2 + (y - y_0)^2}{2R^2}\right) \tag{242}$$

is superposed to a flat pressure field of 1000 hPa, so that the total pressure field p in hPa is given by $p = 1000 - p^\star$; (x_0, y_0) give the location of the center of the disturbance, here $x_0 = y_0 = 0$.

6.6.2.2 Idealized test case 1 - superposition of two low pressure systems

The superposition of two low pressure systems on a flat pressure field of 1000 hPa is investigated for varied distances between the two centers. The pressure disturbances of the lows ($p_1^\star$, $p_2^\star$) are given by two 2D Gaussian distributions of different intensities ($\Delta p_1 = 10$ hPa, $\Delta p_2 = 2.5$ hPa) and different sizes ($R_1 = 250$ km, $R_2 = 160$ km) calculated by equation (242). The total pressure field is given by $p = 1000 - p_1^\star - p_2^\star$. The first low indicated by index 1 is fixed at the location $(x_0, y_0) = (0, 0)$. Low 2 changes its position stepwise in southwesterly direction starting at the location of low 1 (or a distance of 0 km) up to a distance of about 1400 km in 70.7 km steps (50 km to

[65] In (Schielicke et al., 2016), we wrote $\Delta p = 5$ hPa. This is wrong. Here, we changed Δp to its correct value of 2.5 hPa. Hence, it fits to our results (see Fig. 29).

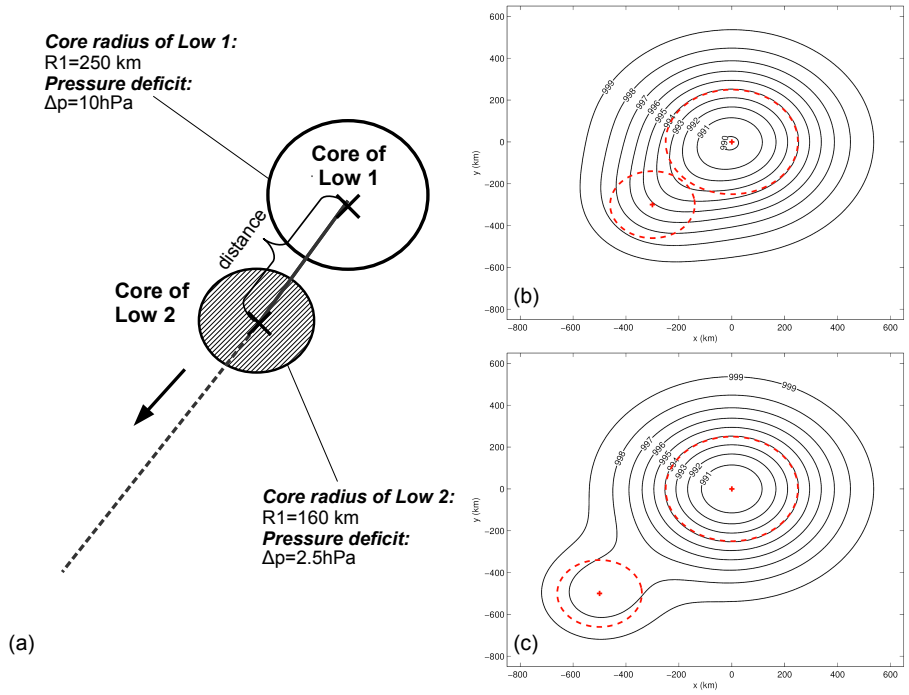

Figure 27: *Experimental set-up of ideal test case 1: the superposition of two low pressure disturbances with different intensities and sizes on a flat pressure field. The smaller low 2 is moved stepwise along the dashed line following the thick black arrow. (a) Sketch of experimental set-up, (b) pressure field for a distance of 353.6 km, (c) pressure field for a distance of 707.1 km. Red crosses indicate the low centers, red dashed circles correspond to their radii. Adopted from Schielicke et al. (2016), their figure 2.*

the south/50 km to the west; see Fig. 27 for set-up and two examples). The resolution of the calculated fields is 10 km.

6.6.2.3 Idealized test case 2 - superposition of a low pressure system and a jet

In this test case, a low pressure disturbance $p^\star$ with $\Delta p = 5$ hPa and $R = 250$ km (see eq. 242) is superposed by a jet streak pressure-gradient p_{jet} on a flat pressure field of 1000 hPa. For changing distances between the low center and the jet axis, the size of the low pressure disturbance is determined by the different methods and compared to the original R. The jet streak's pressure gradient is calculated by a Gaussian error function (abbreviated by erf). The jet axis is oriented in west-east direction. The (south to north) pressure profile is given by $p_{jet} = \Delta p_{jet} \cdot \mathrm{erf}((y - y_{Gauss})/(\sqrt{2}\sigma))$ where y_{Gauss} is the position of the jet axis and $\Delta p_{jet} = 7.5$ hPa gives the pressure difference between the edges of the jet and the jet axis. Since the geostrophic wind is proportional to the pressure gradient, the wind field associated with the jet is Gaussian distributed with a standard deviation of $\sigma = 350$ km. The total pressure field in hPa is given by $p = 1000 - p^\star - p_{jet}$. The low is fixed at the location $(x_0, y_0) = (0, 0)$. The position of the jet axis moves stepwise (50 km steps) from 1400 km south to 1400 km north of the low center (see Fig. 28 for set-up and examples).

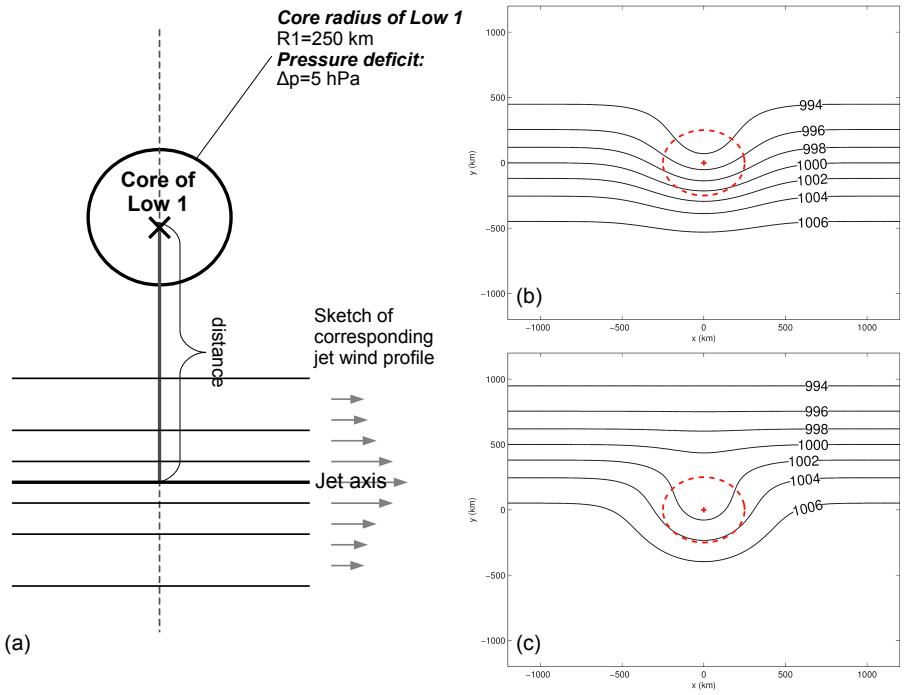

Figure 28: *Experimental set-up of ideal test case 2: the superposition of a low pressure disturbance and a non-trivial jet streak gradient on a flat pressure field. The jet axis is moved stepwise from south to north as indicated by the dashed lines. (a) Sketch of experimental set-up, (b) pressure field for a distance of 0 km between jet axis and vortex center, (c) like in (b) for a distance of 500 km (jet axis north of vortex). Red cross/red dashed circles indicate the vortex center/radius. Adopted from Schielicke et al. (2016), their figure 3.*

6.6.3 Results

Note, subscripts of the radii R correspond to the method, e.g. G for Gaussfit method, W for the W_k-method, and so on. Multiple letters are used when radii coincide.

6.6.3.1 Reference case - idealized low pressure system

The vortex core radius identified by the W_k-method and by the Gaussian fit (not shown) coincide with the wind maximum at a radius of $R_{W,G} = 250\,\mathrm{km}$ (blue(wind), black(W_k) curves in Fig. 29) which is equal to the predefined radius. W_k equals 1 when rotation and deformation are of the same size: Vorticity and deformation distributions cross at $R_{WG} = 250\,\mathrm{km}$ and converge far away from the vortex center (red(ζ), yellow(deformation) curves in Fig. 29). The deformation peaks outside of the vortex area identified by the W_k- and Gaussfit-method with a lower, broader peak than the vorticity. Vorticity-dominated and deformation-dominated areas are adjacent regions in the vortex. The p-method identifies the largest radius (about 350 km, green line in Fig. 29)[66] when the outermost-closed isobar is determined by increments of 1 hPa. A finer

[66] In Schielicke et al. (2016), we erroneously wrote 450 km. However, as can be seen from Fig. 29 $\approx$ 350 km is correct.

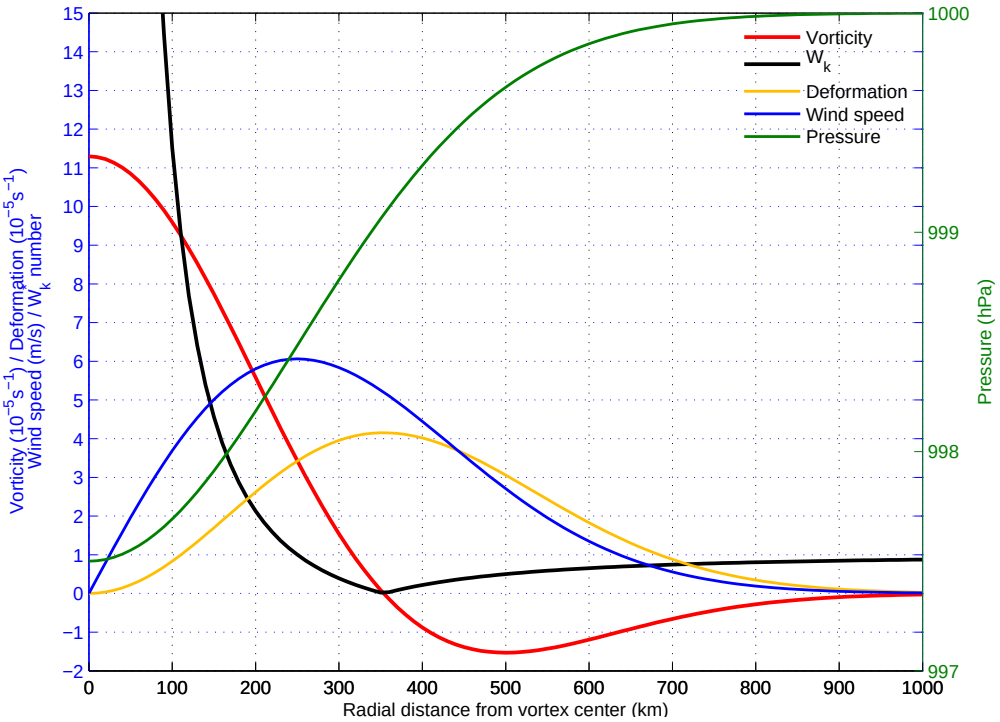

Figure 29: *Undisturbed, axisymmetric reference case: Vorticity $\zeta(r)$ in 10^{-5} s^{-1}, kinematic vorticity number $W_k(r)$, deformation (local strain-rate) in 10^{-5} s^{-1}, wind speed $v(r)$ in m/s (left axis), and pressure $p(r)$ in hPa (right axis) as function of the distance from the vortex center. $W_k = 1$ at a distance of 250 km and $\zeta = 0$ at a distance of 320 km. Adopted from Schielicke et al. (2016), their figure 4.*

increment of 0.1 hPa determines a larger radius of about 700 km.

6.6.3.2 Idealized test case 1 - superposition of two low pressure systems

The splitting of the two systems, i.e. the identification of two single instead of one system, occurs at a smaller distance in the vorticity field (for ζ-/W_k-method see red/blue curve in Fig. 30) at around 420 km which coincides approximately with the sum of the undisturbed radii $R_1 = 250$ km, $R_2 = 160$ km) compared to the pressure field (for p-/ Gaussfit-method around 770 km; green/yellow curve in Fig. 30). With growing distances the radii of both systems increase until the values stabilize (around 900 km for the p-, Gaussfit-method and 700 km for the ζ-, W_k-method). The stepwise increase of R_p can be attributed to the coarse increment of 1 hPa for the contour lines since this behavior is not observed for finer increments (not shown). While the p- and ζ-methods show strong variations in the vicinity of the splitting point, the W_k- and the Gaussfit-method show only slight variations and otherwise coincide with the predefined radii.

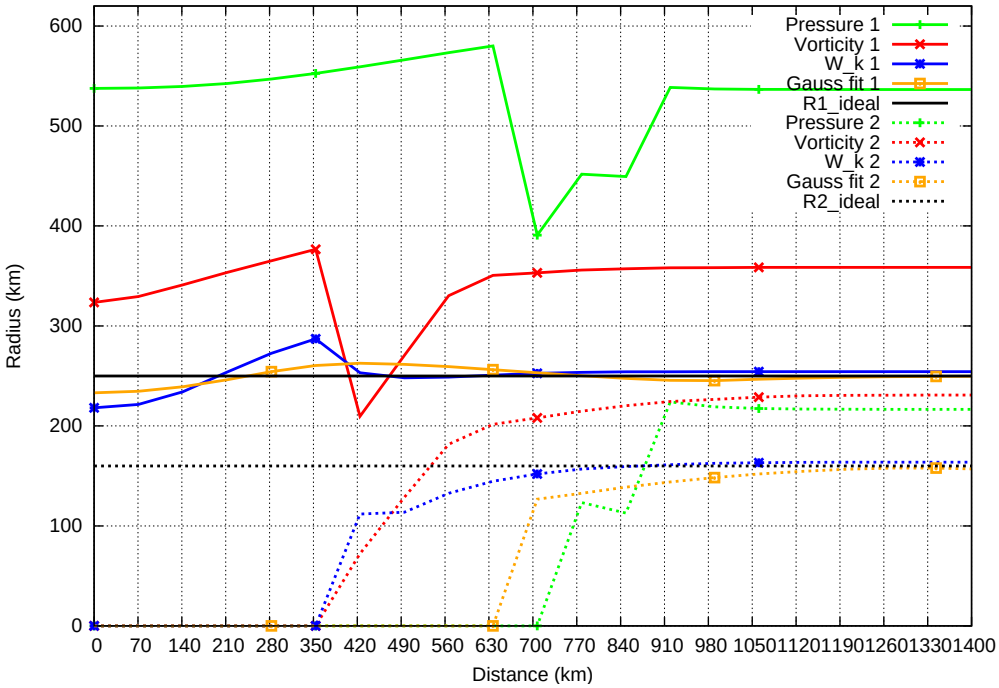

Figure 30: *Identified radii by the four methods in ideal test 1 (superposition of two low pressure systems 1 and 2). Plotted are the identified radii as a function of the distance between the two centers. Symbols plotted every 5th data point. Adopted from Schielicke et al. (2016), their figure 5.*

6.6.3.3 Idealized test case 2 - superposition of a low pressure system and a jet

When the jet axis is in the vicinity of the low center, the methods based on pressure (p-method/Gaussian fit: green/yellow curve in Fig. 31) show strong variations and a lack of identification for distances between 0 and 500 km; while the W_k- and ζ-method are not strongly affected (blue/red curve in Fig. 31). For the application of the Gaussfit-method a local pressure minimum is needed[67]. When the Gaussfit-method is modified such that the fit is applied to the pressure field surrounding the local vorticity maximum, radii can be identified over all distances (yellow, dashed line in Fig. 31). However, the variations are strong when the jet axis is close to the vortex. The W_k-method reproduces the predefined radius of the low with slight variations. The radius identified by the ζ-method is proportional to that identified by the W_k-method, although the outermost-closed vorticity contour is not zero when the jet axis is south and near the vortex center (not shown).

6.6.4 Discussion of results

We have seen in the previous section that some methods are not capable in identifying the cyclone radii in particular flow situations. E.g. near the splitting point of two lows,

[67] That is slightly different from the method of Schneidereit et al. (2010) which only needs the average gradient of geopotential height to exceed a certain threshold.

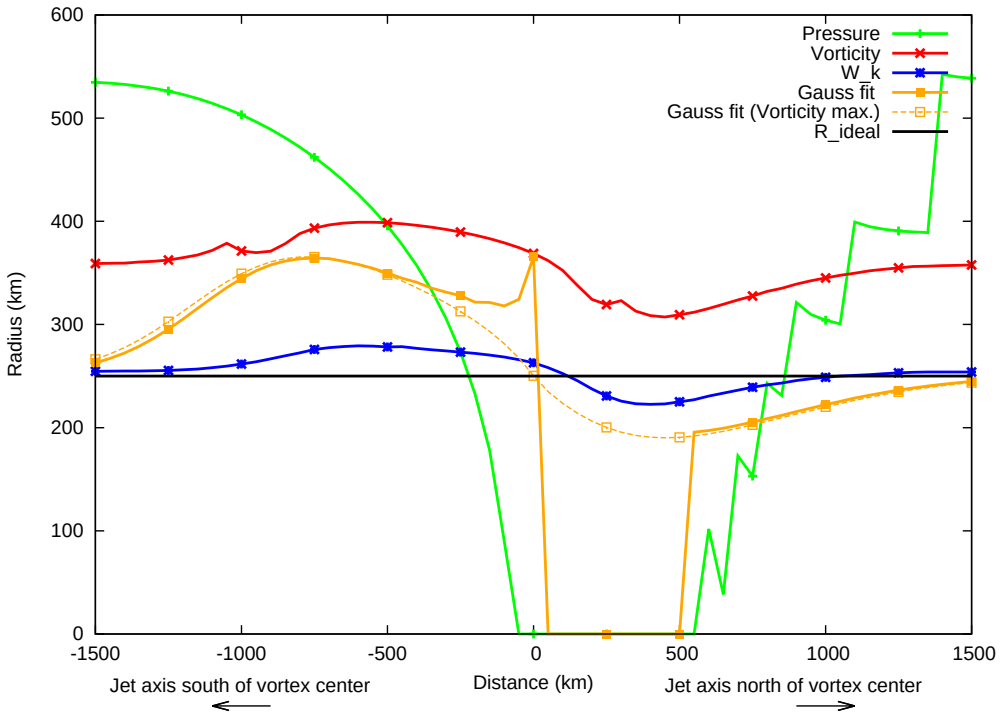

Figure 31: *Radius determination by the four methods of the low pressure disturbance which was superposed by a jet streak (ideal test 2). Plotted are the identified radii as a function of the distance between the jet axis and the center of the low (for negative/positive distances the jet axis is south/north of the vortex center). Symbols plotted every 5th data point. Dashed yellow line: Gaussfit-method applied to the pressure field surrounding the local vorticity maximum instead of the local pressure minimum (solid yellow line). Adopted from Schielicke et al. (2016), their figure 6.*

the ζ- and the p-method showed strong variations. In some asymmetric fields caused by the superposition of a low and a jet, the Gaussfit-method is strongly affected and the p-method partially fails to identify the cyclone. We will now discuss the reasons for the failure and what part of the vortex is seen by the different methods.

6.6.4.1 p-method

The part of the vortex that is identified by the outermost-closed isobar strongly depends on the flow situation and on the contour value/increment. This is in accordance with Wernli and Schwierz (2006) who observed an increase of 40% (decrease of 30%) of detected cyclones by a reduction (increase) of the contour increment from 2 to 1 hPa (4 hPa). Likewise to streamlines, the p-method only represents a snapshot of the flow at a certain time step. This can be very different in various flow situations and from one time step to another. As a result, the area of a cyclone is only poorly represented by pressure/ geopotential height contours. This is especially important when investigating mobile and developing systems, respectively (Sinclair, 1994).

6.6.4.2 Gaussfit-method

In the undisturbed case, the Gaussfit-method coincides with the wind maximum and the maximum of the radial pressure gradient, respectively (see also Schneidereit et al., 2010). Even in case of the superposition of two lows, the Gaussfit-method nicely reproduces the predefined radii. This result was expected since the predefined low pressure disturbances were already Gaussian distributed and the asymmetry of the pressure field surrounding a pressure minimum is only minor. On the other hand, the superposition of a jet and a low involves much more asymmetry (ideal test case 2 in section 6.6.3.3). In this case, the Gaussfit-method fails in re-extracting the radius when all surrounding points are considered even though the predefined low pressure disturbance was originally Gaussian distributed.

6.6.4.3 ζ-method

The vorticity can be split up into shear and curvature vorticity. In the undisturbed case, cyclonic curvature exist in the whole domain. At the wind maximum the shear vorticity changes its sign resembling the flow situation at a jet axis (Fig. 32), but curvature vorticity is still positive. Vorticity becomes zero not until both parts are balanced. In the disturbed ideal test cases 1 and 2 the observed outermost-closed vorticity contour is partly different from zero. Hence, a fixed threshold would fail: either it would only identify strong vortices whose intensity might not be comparably strong since the background shear is misleading or it would only identify undisturbed systems, neglecting vortices embedded in shear. If no restriction to a fixed vorticity threshold is made, R_ζ changes approximately proportional to the W_k-method and it seems to be an alternative to that method. On the other hand, it is not easy to interpret which part

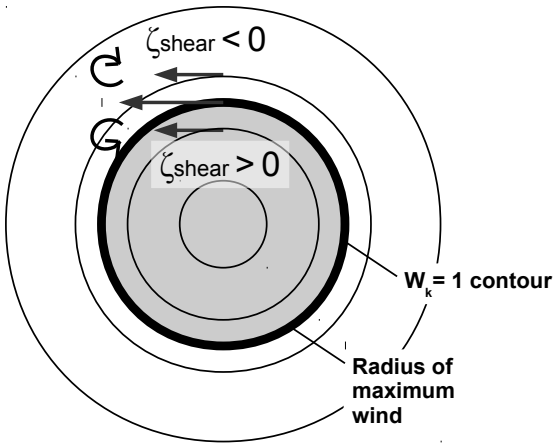

Figure 32: *Scheme of the wind field and shear vorticity of an idealized cyclone on the northern hemisphere (NH). $W_k = 1$ contour and radius of maximum wind coincide. Shaded area marks the area of positive shear vorticity ($\zeta_{\text{shear}} > 0$). Adopted from Schielicke et al. (2016), their figure 7.*

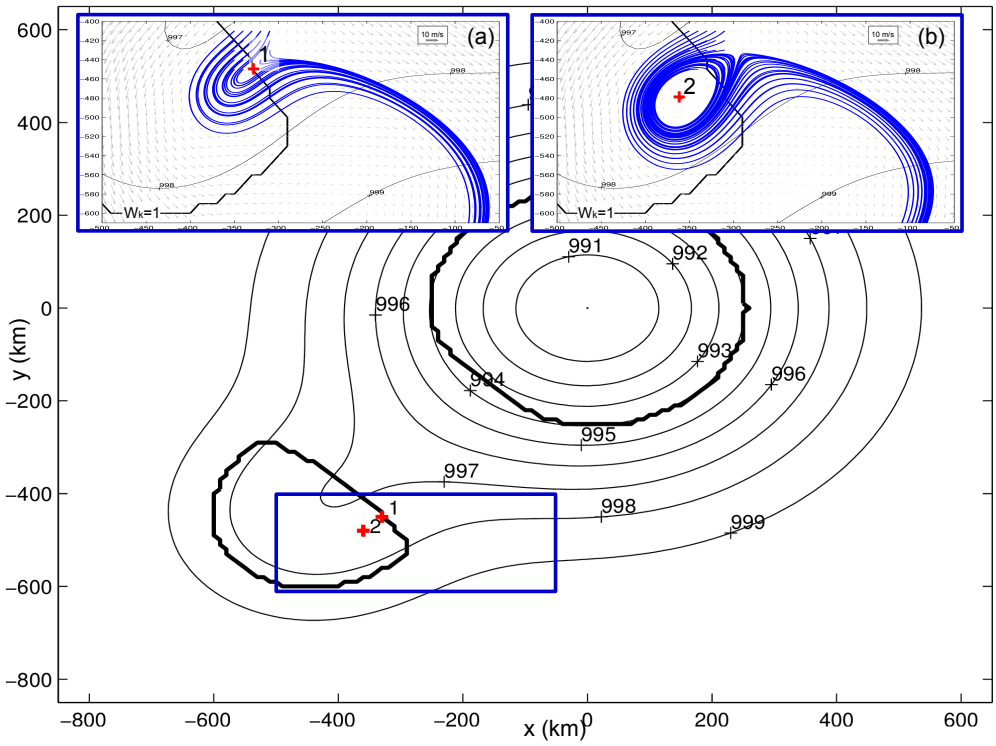

Figure 33: *Streamlines at the vortex core boundary and inside the vortex core: Superposition of two lows with a distance of 636 km between the two centers. Black thin lines are the isobars, black bold lines are the identified $W_k = 1$ contour line. The blue box displays the area of the two insets labelled (a) and (b) in the top of the figure. In the insets the streamline patterns (blue thin lines) around two different points are added: (a) Point 1 is located on the $W_k = 1$ contour; (b) Point 2 is located inside the $W_k = 1$ contour (inside the identified vortex). Gray arrows indicate the velocity vectors around the points 1 and 2, respectively. Adopted from Schielicke et al. (2016), their figure 8.*

of the vortex is then extracted. Here, an interpretation in terms of shear and curvature vorticity is difficult. It is even more complicated when the (contour) threshold changes along certain directions as is done in Sinclair (1997) and Lim and Simmonds (2007) who determined the boundary of a vortex when either the vorticity is zero or the radial gradient of vorticity changes its sign along a set of radial lines. That definition can lead to a zero contour in one direction and a different nonzero value in another direction for the same system.

6.6.4.4 W_k-method

The kinematic vorticity number is larger than one ($W_k > 1$) when the rotation prevails over the deformation at a point and it is exactly one in case of a pure shearing motion. In case of an idealized cyclone, it can be seen that for a point located at the radius of maximum wind its neighboring wind field resembles a pure shearing motion and therefore the $W_k = 1$ contour coincides with the radius of maximum wind (Fig. 32). In order to display the meaning of $W_k > 1$ and $W_k = 1$ in a more nontrivial case, we plotted

the local flow field around a point (blue streamlines in Fig 33) at the boundary (defined by $W_k = 1$, thick black contours in Fig. 33) of a vortex and inside the vortex (defined as $W_k > 1$) in case of the superposition of two lows (see Fig. 33). The local point at the boundary (point 1, Fig. 33a) is embedded in a shearing environment. Particles that first are near to that point separate rapidly following the streamlines. In contrast, the local point inside the contour (point 2, Fig. 33b) is surrounded by particles that stay in the vicinity of that point moving in spirals or closed circles around that point.
Summarized, particles inside the $W_k = 1$ contour stay close to each other, i.e. mass is accumulated inside the vortex. Therefore, the part of the vortex identified by the W_k-method can be interpreted as a vortex core. This statement is also supported by a calculation of the positive vorticity concentrated inside the $W_k = 1$ contour relative to the total positive vorticity. In the undisturbed reference case about 84 % of the positive vorticity is concentrated inside the vortex core (inside the $W_k = 1$ contour). However, it should be noted that the area influenced by the vortex can be much larger than the area of its core.

6.7 First applications of the W_k-method to reanalysis data (Schielicke et al., 2016)

In this chapter, we will apply the W_k-method to reanalysis data in comparison to commonly used methods such as vorticity contours. We will apply the method in a real storm case example and will give first statistics for the midlatitudes of the northern hemisphere in the second part of this section. This chapter is part of a publication that was recently published (Schielicke et al., 2016, chapter 4). The text is only slightly modified to better fit into the context of this thesis.

6.7.1 Reanalysis data

The data used for the analysis are the geopotential height and the horizontal wind fields of the NCEP/NCAR Reanalysis provided by the Research Data Archive of the National Centers for Environmental Prediction National Weather Service NOAA US Department of Commerce (1994). The data is available 4 times per day on a regular $2.5° \times 2.5°$ grid (Kalnay et al., 1996). We analyzed the geopotential height data on 12 pressure levels from 1000 hPa to 100 hPa (100, 150, 200, 250, 300, 400, 500, 600, 700, 850, 925, 1000 hPa) for the northern hemisphere winter months (December, January, February) of the years 1999/2000 (abbreviated by DJF 1999/2000).

6.7.2 Methods

6.7.2.1 Calculation of W_k^*-fields

For every 6-hourly time step in the period DJF 1999/2000, geostrophic W_k^*-fields were computed from the derivations of the geostrophic wind fields on each pressure level with help of (215). The derivations were calculated as central differences omitting the poles. We further restricted the analysis to the northern hemisphere and a latitudinal band between 30°N and 80°N (including these latitudes). No terrain filtering was used in the lower levels. The geostrophic wind fields $\mathbf{v}_g$ were derived from the geopotential height fields Φ by $\mathbf{v}_g = f^{-1}\mathbf{k} \times \nabla\Phi$ with Coriolisparameter $f = 2\Omega \sin\phi$ where $\Omega = 2\pi/\text{day} = 7.2921 \cdot 10^{-5}\,\text{s}^{-1}$ is the rotation rate of Earth and ϕ is the latitude. Every grid point that yield $|W_k^*| > 1$ was set to 1, every point with $|W_k^*| \leq 1$ was set to zero. In this way, we derive a vortex patch field which cuts out the vortex structures.

6.7.2.2 Properties of W_k features and single vortex centers

After calculating the W_k^* fields as described above, simply connected regions[68] of $W_k^* > 1$ (positive circulations/lows) and of $W_k^* < 1$ (negative circulations/highs) were separately identified in each field. As we have introduced in chapter 6.4.2, we will call a single simply connected region of $W_k > 1$ a ***W_k feature***. Note, that a W_k feature can include multiple vorticity centers and therefore rather represents a large-scale circulation area (or cyclone family) in such cases. Therefore, we additionally analyzed ***single vortex centers*** including single vorticity extrema. Such single centers were determined by the outermost-closed vorticity contour enclosing only one vorticity center (see also chapter 6.4.2). Note, that the area/circulations of the single centers are smaller or equal in total than that calculated for the W_k feature. In order to account for broad extrema we further restricted the minimum distance between isolated vorticity extrema inside the same $W_k > 1$ region: if two systems are closer than 600 km ($\approx 5°$latitude = twice the resolution), they were considered as a single broad center. Then the outermost-closed vorticity contour around both centers was calculated by a standard contouring method. W_k features/single centers are composed of a set of grid points. Each grid point is associated with a grid box area of $2.5° \times 2.5°$. Note, that this area depends on the latitude. The sizes of the W_k features/single centers were determined by the sum of all grid box areas associated with the feature/center and corresponding circulations Γ_{total} were calculated by (238). The radius of a system was determined as $R = \sqrt{A/\pi}$ under the assumption that the area belongs to circular system (likewise to the effective radius definition in Rudeva and Gulev, 2007). Furthermore, we calculated the center of circulation of each feature/center by $\mathbf{C} = \sum_i \Gamma_i \mathbf{x}_i / \Gamma_{total}$ where the summation is done over each grid box included in the simply connected region/outermost-closed contour (cf.

[68] Two points are simply connected if they are neighbors in either N,S,E or W direction.

Müller et al., 2015, additionally see also equation (240)). Γ_i is the circulation associated with the ith grid point and $\mathbf{x}_i$ is the coordinate vector of this grid point.

6.7.2.3 Temporal and vertical tracking of Anatol storm

Only in the real storm case example (section 6.7.3), we additionally did a temporal and vertical tracking for the explicit storm Anatol. Anatol was traced over its life time by manually connecting the appropriate storm centers of successive time steps on the 1000 hPa level. The vertical tracking of the storm was done following the work of Lim and Simmonds (2007) by a numerical method that searches for the nearest vortex center in superposed vertical levels starting from the 1000 hPa level. A vertical connection between two centers in neighboring pressure levels was confirmed when the distance between those centers was less than about 340 km. This distance accounts for a diagonal vertical tilt (north-west/-east, south-west/-east) from about 50° latitude polewards (the diagonal distance between grid points in 50° latitude is about 330 km which further decreases polewards).

6.7.2.4 Cyclone statistics of the winter season DJF 1999/2000

For the statistics, all identified W_k features/single centers of positive circulation per time step are taken into account irrespective of their temporal evolution. We will analyze the frequency distributions concerning the radius with a box width of 50 km for systems with radii larger than 200 km. This allows a comparison to the existing literature like Golitsyn et al. (2007); Schneidereit et al. (2010). However, the identified absolute circulations cover several orders in magnitude complicating the definition of linear box widths. Therefore, we will compute complementary cumulative distributions for the analysis of the circulations of lows and highs. These distributions are statistically more stable and were already successfully used in the analysis of cyclone/anticyclone kinetic energies in Golitsyn et al. (2007).

6.7.3 Application of the W_k-method in real winter storm Anatol: Description and Results

The capability of the W_k-method to identify cyclones even in the upper troposphere and in high-shearing situations is tested exemplarily in a real winter storm case. The investigated example storm - known as storm *Anatol* in Germany - occurred between $2-4$ December 1999 (see Fig. 34 for Anatol's track). The lowest observed pressure was 953 hPa recorded at 3 December 1999 18 UTC near the north east coast of Denmark (Jutland, see Ulbrich et al., 2001). Anatol hit Denmark and northern Germany at the afternoon and evening of 3 December 1999 with gusts up to 50 m/s. It was one of three extreme storm events affecting Europe in December 1999 (Ulbrich et al., 2001), and it was among the costliest European winter storms between 1980 and 2013 (NatCatSER-

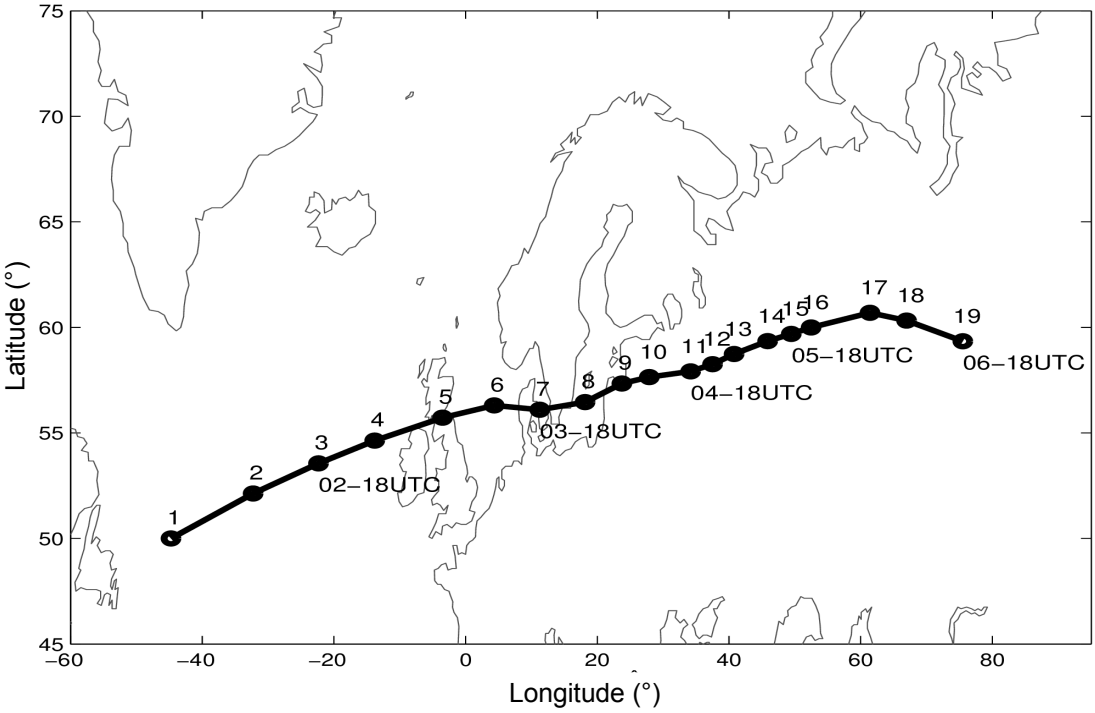

Figure 34: *Track of Anatol's circulation center at the 1000 hPa level: starting at 2 December 1999 06 UTC. Every circle and number represents a six hourly step, some selected dates are additionally plotted below the corresponding circles. Adopted from Schielicke et al. (2016), their figure 9.*

VICE of Munich Re, 2014). It caused a record storm surge at the Danish and German North Sea coast (Ulbrich et al., 2001). Furthermore, the storm was associated with a strong jet in the middle and upper troposphere and is therefore a challenging situation for size estimation methods.

The temporal development of Anatol reveals its rapid intensification from a wave like structure over the North Atlantic to a mature cyclone in less than 24 hours (Fig. 35). Note, how the contours of the geopotential in 1000 and 500 hPa show a rather wave-like pattern and the low-level (850 hPa) vorticity is rather weak in the beginning (2 December 1999 12 UTC, see Fig. 35a). In addition, the vorticity center is embedded in a large-scale cyclonic (positive) vorticity field. The black arrow and the white cross in Figure 35 indicate the positions of the vortex centers near the surface and in the upper troposphere, respectively. During the intensification period, the system is strongly baroclinic (see Fig. 35b,c). Lower- and upper-level centers become aligned during maturity (see Fig. 35d at 4 December 1999 00 UTC). In comparison, the extended W_k-field considering the sign of vorticity isolates nicely the cyclonic and anticyclonic vortices from the continuous (vorticity) fields (Fig. 36). The storm center can easily be detected (see black arrows). The intensification of Anatol is also mirrored in the maximum W_k-value inside the storm which is 2 in the beginning (2 December 1999 12 UTC, Fig. 36a), 12 hours later $W_k \approx 10$ and 24 hours later $W_k \approx 15$ implying that the rotation is 15 times larger than

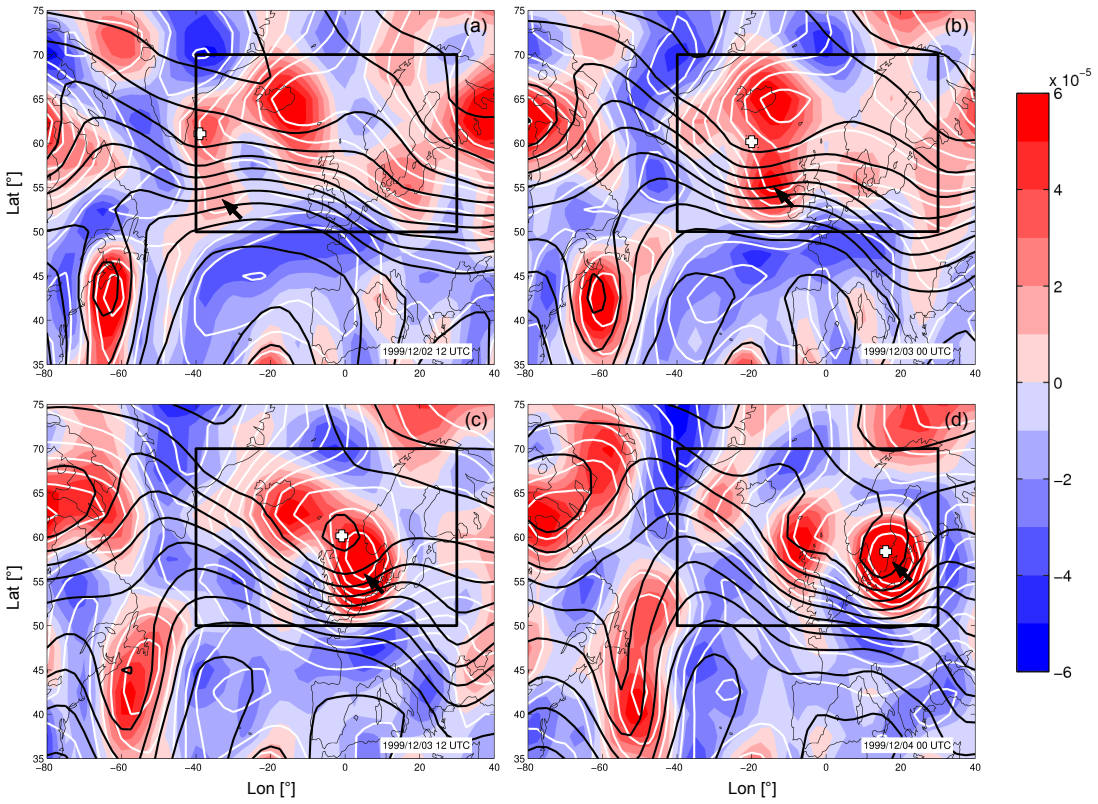

Figure 35: *Development of storm Anatol (2.-4.12.1999, 12 hourly steps) in traditional fields: Geopotential height (in gpdm at 1000 hPa (white)/ 500 hPa (black) contours) and low-level (850 hPa) relative vorticity (color shaded) fields. Black arrow/white cross indicate the position of the storm center in 1000 hPa/500 hPa. Contours of the geopotential are given every 4 gpdm in 1000 hPa (white) and every 8 gpdm in 500 hPa (black). Black box corresponds to the section plotted in Figure 37). Adopted from Schielicke et al. (2016), their figure 10.*

the deformation inside the storm. Note however, that the maximum of the W_k-value does not always coincide with the vorticity maximum or minimum.

The vertical structure and development of storm Anatol as seen from the W_k-method's perspective (Fig. 37a-d, top row) supports that the system is only shallow in the beginning (black arrow, Fig 37a), but rapidly intensifies due to the interaction with an upper-level vortex (white cross, Fig 37) that leads to strong stretching of the vortex (Fig. 37b,c). The strongest baroclinic tilt is observed at 3 December 1999 00 and 12 UTC (Fig. 37b,c). In addition, horizontal interactions between vortex centers are observed: e.g. see the interaction of the icelandic low (center located at about $-20°$W, $65°$N) with storm Anatol at the 1000 hPa level. The area of the icelandic low is deformed over time, so that it appears to rotate around storm Anatol (Fig. 37 b,c); later it follows Anatol (Fig. 37d).

The evolution of Anatol's circulation over its lifetime shows a rapid intensification over the first 6 timesteps (36 hours) by one order in magnitude from about 10^7 to 10^8 (Fig. 38a). Compared to that rapid intensification at the beginning, the circulation dissipated

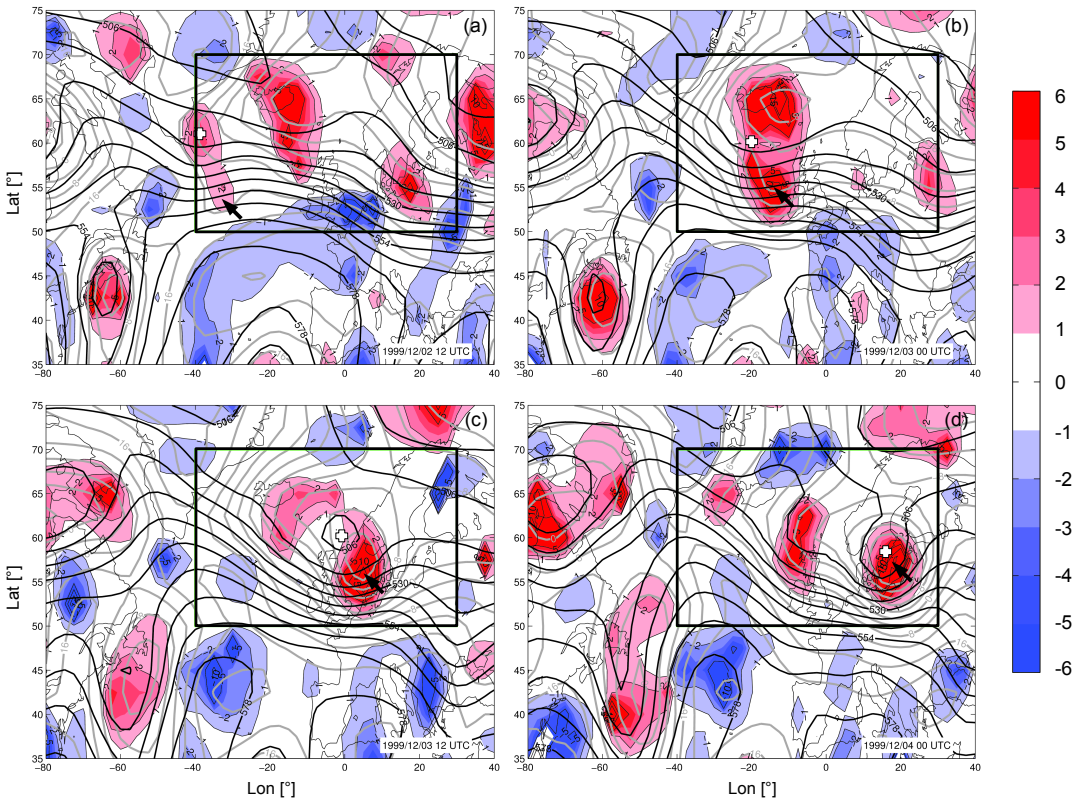

Figure 36: *Development of storm Anatol (2.-4.12.1999, 12 hourly steps) in kinematic fields: Low-level (850 hPa) extended kinematic vorticity number (color shaded) field considering the sign of vorticity. Positive (negative) values of W_k correspond to cyclones (anticyclones). Isolines of $|W_k| = 1, 2, 5, 10, 15$ are added (labelled thin gray contours) Other fields/tokens similar to that in Figure 35. Adopted from Schielicke et al. (2016), their figure 11.*

much slower by a nearly constant gradient of about 264 m^2/s^2 after reaching its maximum at 3 Dec 1999 18 UTC/4 Dec 1999 00 UTC (Fig. 38a). Simultaneously, the area on the 1000 hPa level broadens over Anatol's life time nearly constantly (see Fig. 38b). After about 13 time steps at 5 Dec 1999 18 UTC (78 hours after initiation), the vertical connection between lower- and upper-level vortex becomes less organized as can be seen by the drop of the vertical means relative to the vortex characteristics identified in 1000 hPa. At the end of Anatol's life time the connection between the vertical levels is less pronounced.

6.7.3.1 Discussion of W_k-method in comparison with traditional methods

In order to compare the W_k-method's view on Anatol with the ζ-method's perspective, vorticity isosurfaces of 1, 3, $5 \cdot 10^{-5} s^{-1}$ of the geostrophic vorticity field are plotted in Figure 37e-h (bottom row). The main difference between the fields is obvious at upper-levels: due to the stronger shear in the upper levels, the vorticity centers are rather embedded in regions of positive vorticity than clearly separated. This complicates a

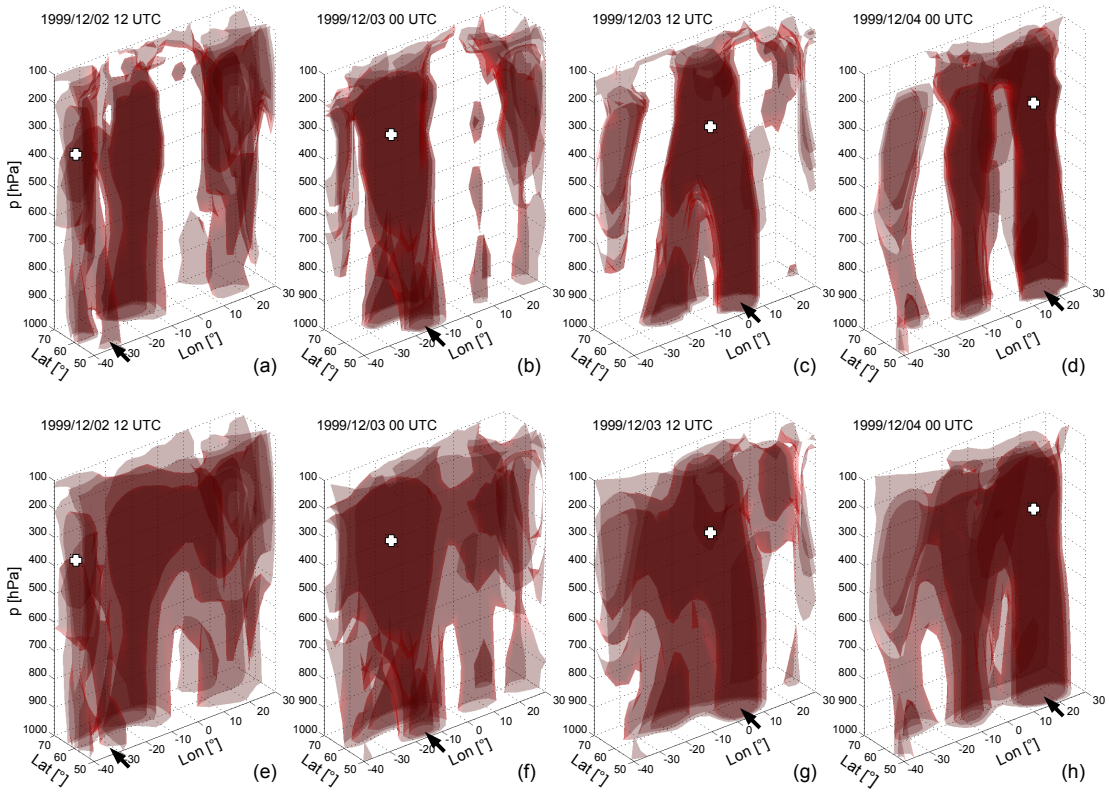

Figure 37: *Vertical development of storm Anatol (2.-4.12.1999, 12 hourly steps): in W_k (a)-(d) and ζ_g (e)-(h) fields. Plotted are isosurfaces of the cyclonic (positive) geostrophic vorticity [$(1,3,5) \cdot 10^{-5}\mathrm{s}^{-1}$]: (a)-(d) Vorticity is plotted in the field of $W_k > 1$, (e)-(h) Field of positive geostrophic vorticity. Values of $W_k < 1$ as well as negative vorticity values are blank. Lighter colors correspond to lower values of vorticity. Black arrow and white cross indicate the position of the storm center in 1000 hPa and in the upper levels, respectively. Adopted and modified from Schielicke et al. (2016), their figure 12. Note, that in Schielicke et al. (2016) subfigures (a) and (e) are erroneously similar. This misprint is corrected here.*

study of upper- and lower-level vortices by means of fixed threshold values of vorticity alone. By fixing the threshold to a value (e.g. $3 \cdot 10^{-5}s^{-1}$), lower-level features - especially during formation - would not be detected since the vorticity is to small as in Fig. 37a,e. Flaounas et al. (2014) use a fixed threshold of $\zeta = 3 \cdot 10^{-5}s^{-1}$ applied to the 850 hPa level vorticity fields of the ERA-Interim data set which has a higher horizontal resolution of $1.5° \times 1.5°$ than NCEP. Flaounas et al. (2014) reasoned, that this value is adequate even in the initial stage of the cyclone development at this specific level. However, in the coarsly-resolved NCEP data set used in our analysis, the formation of Anatol would have been missed especially near the ground. A fixed vorticity threshold needs to be carefully chosen for each height level because vorticity magnitudes generally increase with height due to an increase in shear with height. Still, it is not clear if this mixture of thresholds give a consistent measure of the extent of a cyclone and if different thresholds in different levels lead to comparable sizes. However, an adjustment

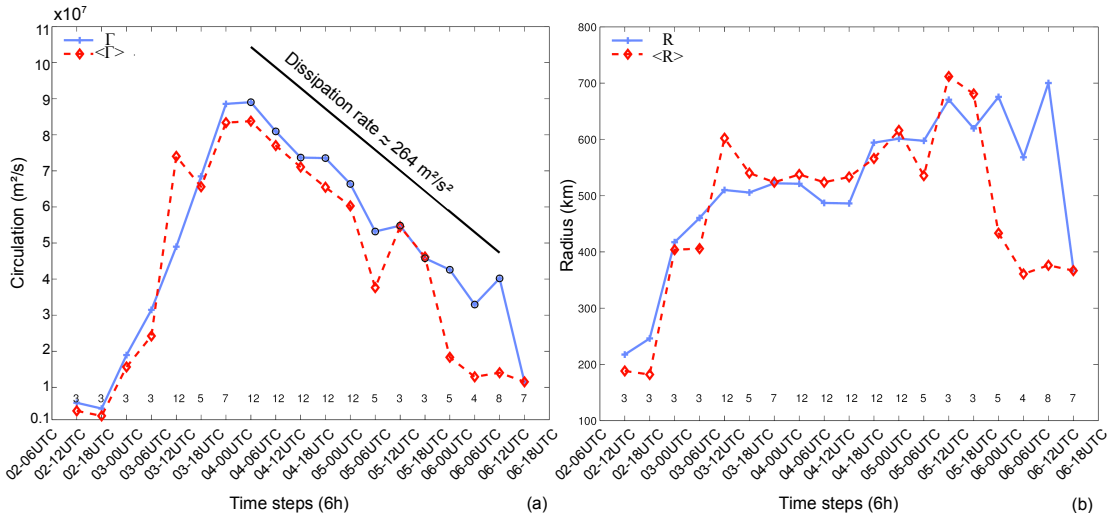

Figure 38: *Properties of storm Anatol over its lifetime: (a) Circulation* Γ *and (b) Area* A *in 6-hourly time steps starting from 1999/12/02-06 UTC to 1999/12/06-18 UTC; corresponding radius* ($R = \sqrt{A/\pi}$) *was added to the right axis in (b). Red, dashed lines correspond to the vertical averaged values of* Γ *and* A *(small numbers near the bottom indicate the number of vertical levels used for the vertical average), blue, solid lines correspond to the value at 1000 hPa. For the calculation of the circulation, geostrophic wind has been used. Adopted from Schielicke et al. (2016), their figure 13.*

of thresholds is not necessary when the W_k-method is used since it relates the rotation to the background deformation (and shear) and therefore separates the relevant parts of the vortices (i.e. the vortex cores) from the rest of the flow field.

Campa and Wernli (2012) used a different approach in order to study the vertical distribution (and interaction) of potential vorticity (maxima) in cyclones. They used a fixed radius of 200 km around a surface cyclone center (SLP field) and analyzed the vertical column of air limited by this area. They restricted their analysis to surface cyclone centers at the moment of maximum intensity (lowest core pressure during life time) and up to 24 hours before that maximum was reached. Campa and Wernli (2012) found the radius of 200 km to fit best their needs as a compromise between a radius that is too small and possibly misses upper-level features (100 km) and a radius that leads to too much averaging (300 km). Especially during the development of a cyclone, the system is usually (strongly) tilted and a fixed radius might miss the upper-level features (more on the relationship between tilt, forcing and cyclogenesis as well as a classification of cyclones concerning those parameters can be found in Gray and Dacre, 2006). An advantage of the W_k-method in such an analysis is that it allows to account for the vertical tilt when the area would be limited to the vortex tube surrounding the cyclone axis. Compared to the method of Campa and Wernli (2012) who use a more Eulerian perspective connected to the Lagrangian tracing of surface centers, the W_k-method would describe a rather Lagrangian perspective following the whole vortex tube. A vortex tube is defined as a surface composed of vortex lines that has a constant circulation for every cross section at an instant of time. However, the circulation can change over time due

to e.g. baroclinic production. That the W_k-method detects approximately a vortex tube can be seen in Fig. 38a where the circulation at the 1000 hPa level is compared to the vertical mean circulation over the identified vortex height. The identified circulations are approximately similar like in a vortex tube.
Furthermore, we have seen that the W_k-method can visualize horizontal vortex interactions (e.g. the interaction of icelandic low and storm Anatol). Although we did not focus on them in this work, we have studied successfully the horizontal interaction of low and high pressure systems at the 500 hPa level in Müller et al. (2015) where we introduced a pattern recognition technique based on the W_k-method in order to determine the circulations and locations of vortices in Omega-blocking situations using point vortex equilibria.

6.7.4 Cyclone size and circulation statistics of the winter season DJF 1999/2000

We have seen, that the W_k-method is able to extract vortex structures even in upper levels of the atmosphere in a real winter storm case in the previous section. In order to gain even more confidence in the results obtained by the W_k-method, we will compare the results of the identified cyclones with existing statistics.

6.7.4.1 Results and discussion

On average about 41±6 W_k features occur at the 1000 hPa level and a smaller number of about 30±5 W_k features at the 600 hPa level (see Fig. 39). The number of single centers is only a bit larger (≈46±7 in 1000 hPa vs. ≈39±7 in 600 hPa). The number in lower and upper levels seem to be correlated over long time periods (Fig. 39). That more systems are detected at the 1000 hPa level might be related to the fact that near the surface more disturbances of the geopotential height field are initiated due to topography and friction. Interestingly, the occurrence of Anatol at the beginning of December is connected with a rather low number of cyclones compared to the rest of the plotted period (Fig. 39). Likewise a rather low number of W_k features is observed at the end of December where two intensive storms hit Europe (storms Lothar and Martin, see Ulbrich et al., 2001, for more details on the storms). With this low number of events it can not be clarified, if this connection between intense storms and low total numbers of cyclones is only random. Future work is necessary.
For the relative frequency distributions concerning the radii two general observations can be given (see Fig. 40): (1) The majority of the systems is subsynoptic with radii smaller than 1000 km in both levels and (2) systems in the upper level tend to be larger than at the lowest level. At the 1000 hPa level a broad peak occurs at radii around 300–500 km for W_k features as well as for single centers (solid lines in Fig. 40). This peak is shifted and sharpened to larger radii at the upper levels (sharper peak around 400–700 km, dashed lines in Fig. 40). Especially, the W_k features can be very large at the upper level

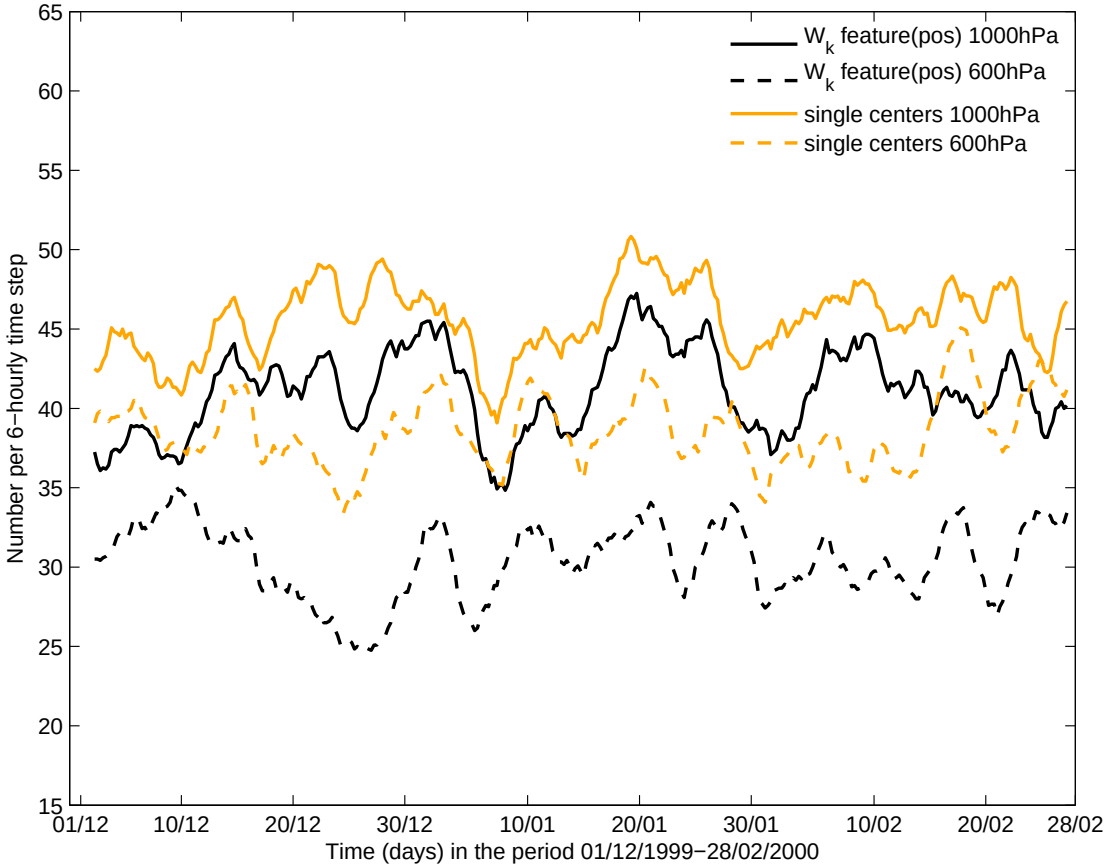

Figure 39: *3-days running mean of the number of identified lows: cyclonic W_k features (black)/single centers (orange) in 1000 hPa (solid) and 600 hPa (dashed) for DJF 1999/2000 in 30°−80° N. Mean numbers/*total numbers *over the whole period are in 1000 hPa: 41.1/*14.339 *(W_k features), 45.6/*15.905 *(single centers), and in 600 hPa: 30.4/*10.607 *(W_k features), 38.6/*13.469 *(single centers), respectively. Adopted from Schielicke et al. (2016), their figure 14.*

reaching synoptic scale, while only a small number of single centers reach radii larger than 1000 km at the 600 hPa level. The observation that the majority of the radii are sub-synoptic is in accordance with the literature, i.e. Schneidereit et al. (2010) observed the highest frequency between 300–500 km at the 1000 hPa level (Gaussfit-method). While methods based on pressure usually show higher radii and less systems per time step (e.g. Rudeva and Gulev, 2007, observe around 14-20 cyclones with an effective radius of about 600 km). However, it should be noted, that the W_k-method identifies vortex cores. Therefore, the total area influenced by the vortex can be considerably larger as was seen in the idealized cases in section 6.6

W_k features that are on general larger than single centers also have higher circulation magnitudes than single centers (Fig. 41). Furthermore, W_k features in the upper level are more intense reaching higher values of circulations. However, the circulation distributions of single centers in both levels are nearly equal (yellow lines in Fig. 41). Note that the curves decrease nearly exponentially indicating the existence of a characteristic

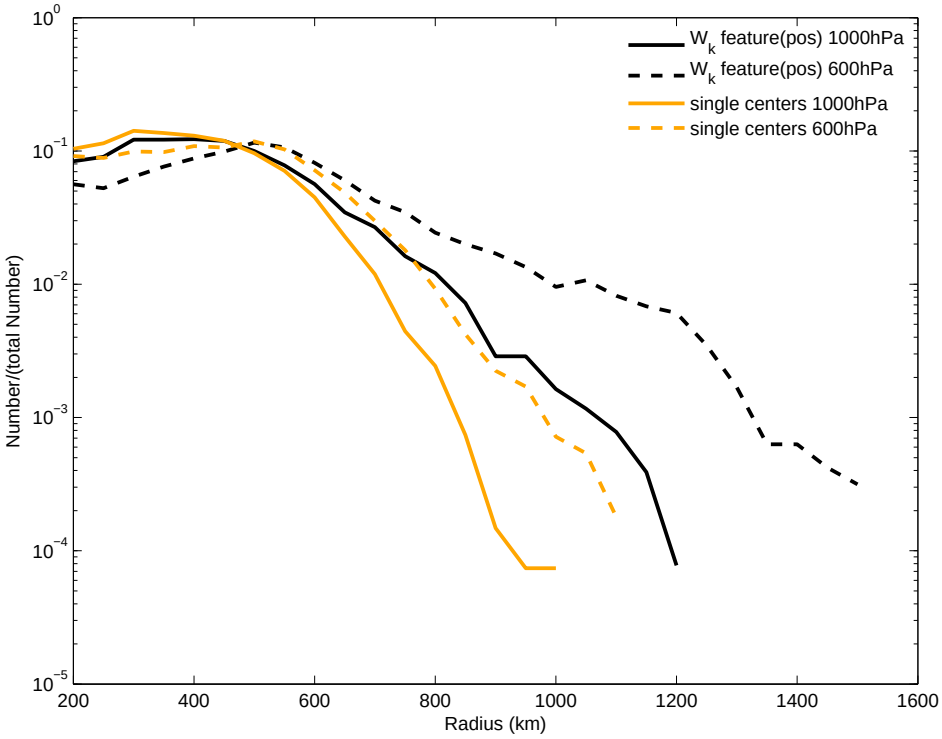

Figure 40: *Relative frequency distributions concerning the radii: cyclonic W_k features (black)/single centers (orange) in two different pressure levels (1000 hPa solid, 600 hPa dashed). DJF 1999/2000, 30°−80° N. Only systems with radii* $\geq$ 200 *km were included. Total number of systems in 1000 hPa: 12.862 (W_k features), 13.530 (single centers), and in 600 hPa: 9.521 (W_k features), 11.148 (single centers), respectively. Note the logarithmic scaling of the ordinate axis. Adopted from Schielicke et al. (2016), their figure 15.*

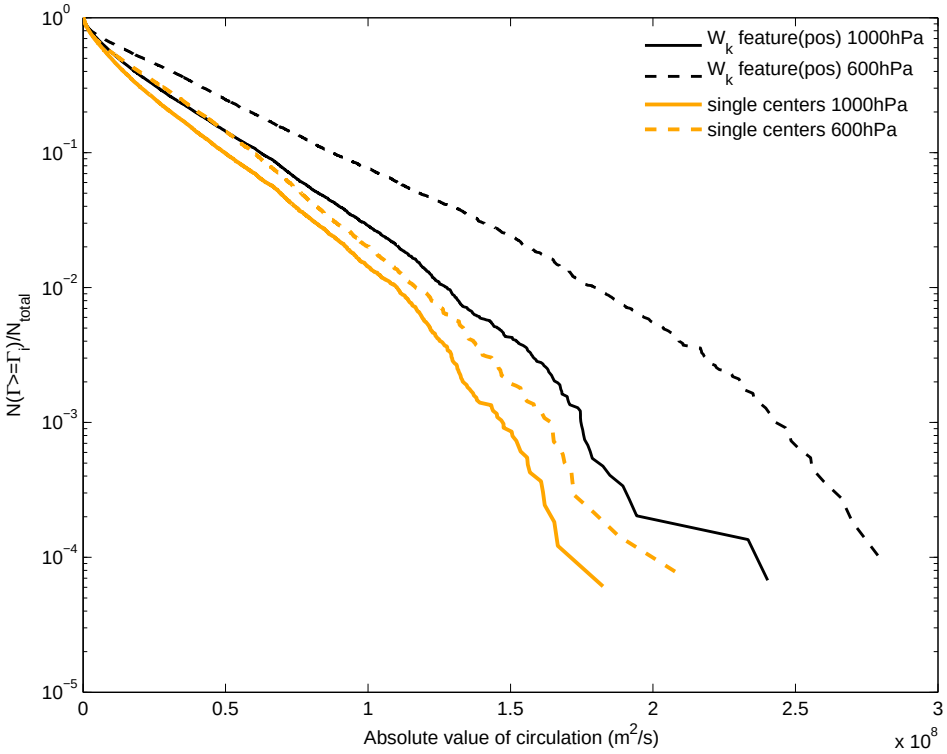

Figure 41: *Complementary cumulative distribution of the circulations: cyclonic W_k features (black)/single centers (orange) in two different pressure levels (1000 hPa solid, 600 hPa dashed). DJF 1999/2000, 30°−80° N. Note the logarithmic scaling of the ordinate axis. Adopted from Schielicke et al. (2016), their figure 16.*

scale of circulation of the vortices. The majority of the systems has circulations in the order of $10^7\,\mathrm{m}^2/\mathrm{s}$ which is in accordance with the results in Sinclair (1997). Only about 1% of the single centers at the 1000 hPa level reach circulations of more than $1 \cdot 10^8 \mathrm{m}^2/\mathrm{s}$. At its maximum intensity, Anatol reached a circulation of about $0.9 \cdot 10^8 \mathrm{m}^2/\mathrm{s}$. An estimate from synoptic-scale characteristic values of velocity ($U = 10\,\mathrm{m/s}$) and radius ($R = 1000\,\mathrm{km}$) leads to a circulation of approximately $\Gamma \approx 2\pi RU = 6 \cdot 10^7 \mathrm{m}^2/\mathrm{s}$ which is in accordance with our observations, too.

6.7.5 Conclusion and Summary of results

We have tested the W_k-method in real (reanalysis) data. The W_k-method could be applied successfully to the data. The W_k-method rather identifies vortex cores, hence the identified systems are smaller than that identified with the help of traditional methods based on the (surface) pressure fields. The main findings concerning the reanalysis data are:

- The W_k-method applied to 3d fields visualizes the interactions between vortex centers: in the real case example of storm Anatol the horizontal interaction of vortex centers (icelandic low, Anatol) and the vertical interaction of upper- and lower-level vortex which led to the rapid intensification could be visualized with help of the W_k-method.
- In general, vortices (single centers as well as W_k features) at the 1000 hPa level are smaller and less intense than at the 600 hPa level. The majority of the vortices on both levels have radii smaller than 1000 km which is in agreement with the published literature (e.g. Schneidereit et al., 2010).

Summarized, the W_k-method seems to be a promising tool for the determination of vortex properties and the study of vortex interactions. So far, we applied successfully the 2d definition of the W_k number in different vertical atmospheric layers which is sufficient for (quasigeostrophic) synoptic-scale systems.

In the following chapter, we would like to test the sensitivity of the W_k-method with respect to a reduced or increased W_k threshold. We hope that this allows the study of either early circulations in the genesis state or very intense ones compared to the background deformation.

6.8 Systematic testing of the influence of the W_k threshold in the identification of vortices

In this part, we concentrate on the identification of vortices and their properties with the W_k-method and its dependence on the specific W_k threshold. So far, we defined vortices as simply-connected regions of $W_k > 1$. Here, we will investigate different thresholds.

6.8.1 Data

Again, we used the NCEP-DOE AMIP II reanalysis data (resolution of 2.5°, 6 hourly). We concentrated on one year, 1999, of the data set and on three pressure levels: 1000, 600, and 300 hPa (lower boundary, divergence-free level, and near-tropopause level). We focused on the northern hemisphere, but also applied the original $W_k = 1$ threshold to the southern hemisphere for purpose of comparison. The main reason for this restriction is the large computing time that is necessary to conduct the results, especially for smaller thresholds.

6.8.2 Methods

As in chapter 6.4.2 introduced, we differentiate between single centers (SC) and W_k-features (Wkf). The latter can include one or more vorticity extrema. W_k-features are defined as simply-connected regions with W_k values larger than a certain threshold. In order to determine simply-connected regions, only the four direct neighbors around a point above (or below) the threshold are considered.
Single centers are defined as the region around a single vorticity extremum inside an area of W_k values larger than a certain threshold. For the identification of the vorticity extrema all 8 neighbors are considered. The outermost-closed (vorticity) contours around single centers are determined by a standard contouring method. In case of *isolated* W_k-features that only include a single vorticity extremum, single centers and W_k-features coincide.
We will use the extended W_k^*-method in order to analyze cyclonic and anticyclonic circulations. The extended W_k^*-method additionally considers the sign of the vorticity in the identified vortex areas. The identification of the vortex structures is analogous to the method described in chapter 6.4 with different thresholds for W_k^*. We decided to use the following thresholds for the $W_k = \|W_k^*\|$ value on the northern hemisphere:

$W_k = 0.8$: below the original 1 value, can be used to detect early circulations

$W_k = 1.0$: the original value for the purpose of comparison

$W_k = 1.2$, $W_k = 1.5$, $W_k = 2.0$: above 1, can be used to identify stronger circulations

On the southern hemisphere, we will use the $W_k = 1$ threshold in order to compare the results to the northern hemisphere.
Vortex structures (single centers/W_k-features) are analyzed for every timestep and at each height level separately regarding their numbers, radii and circulations. The result-

ing time series is smoothed by a 3-days running mean (12 time steps, temporal resolution of 6 hours) and will be compared with respect to the means/standard deviations (numbers, radii), and median/quartiles (absolute values of circulation), respectively.

6.8.3 Results

6.8.3.1 Number

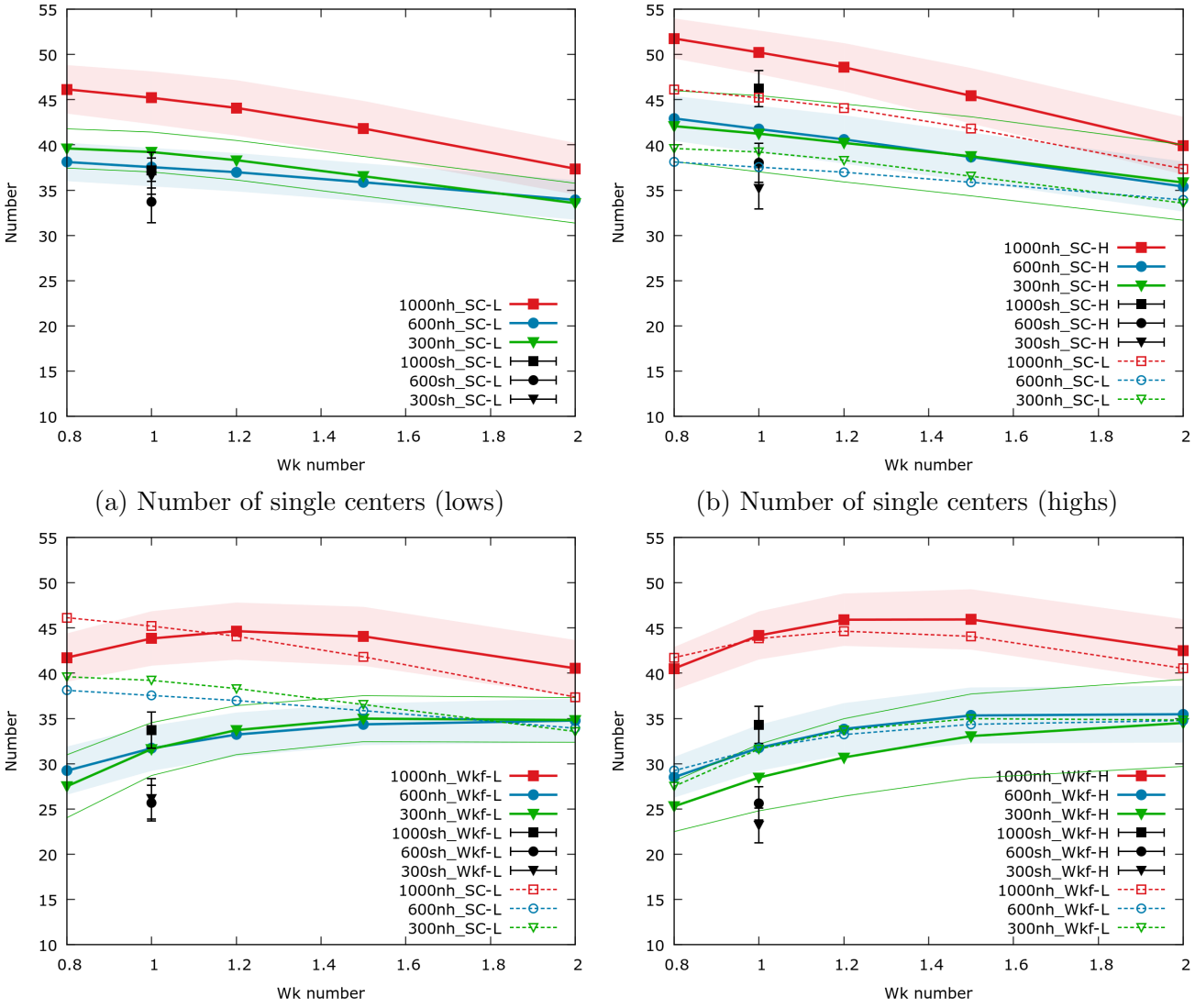

(a) Number of single centers (lows)

(b) Number of single centers (highs)

(c) Number of W_k features (lows)

(d) Number of W_k features (highs)

Figure 42: *Mean number of identified systems per time step (3-days running mean) and standard deviations (red/blue colored areas, thin green lines) as a function of the W_k-thresholds at different pressure levels (300, 600, 1000 hPa): (a) Single centers (lows), (b) single centers (highs), (c) W_k-features (lows), (d) W_k-features (highs). For comparison reasons, the means of SC (lows) are added to (b),(c) and Wkf (lows) to (d) (Abbreviations in legend/text:* nh/sh*: northern/southern hemisphere,* SC*: single centers,* Wkf*: W_k-features,* L*: lows,* H*: highs)*

In general, we observe a nearly linear decrease of the single centers (SC) numbers with

increasing W_k thresholds (see Fig. 42). The numbers of the W_k features (Wkf) first increase up to a W_k threshold of 1.2-1.5 and then decrease or remain constant with further increasing the W_k threshold. In the following, we will structure the results in more detail:

- ***Dependence on height level:*** In all cases, the numbers at the 1000 hPa level is significantly larger than at the upper levels.
- ***Comparison of SC/Wkf numbers:*** The SC numbers are higher than that of the Wkf for low W_k thresholds, but lower or equal for higher W_k thresholds ($W_k \geq 1.5$).
- ***Comparison of lows/highs:*** SC highs are more numerous than SC lows while the number of Wkf highs and lows is approximately equal (except of the Wkf highs at the 300 hPa level which have smaller numbers).
- ***Comparison of southern/northern hemisphere:*** In general, the numbers at all levels are smaller on the southern hemisphere compared to the northern hemisphere (about 3-7 less SC, about 5-10 less Wkf).
- ***Variability:*** The standard deviations are in the order of about ± 4 and therefore are relatively small in all cases.

6.8.3.2 Vortex radii

In general, most of the identified radii of both single centers and W_k-features, highs and lows are subsynoptic, i.e. they have radii smaller than 1000 km and the mean radii are in the range of 200-600 km depending on the height level and W_k thresholds (see Fig. 43). Thereby, the mean radii decrease with increasing W_k thresholds.

- ***Dependence on height level:*** The smallest mean radii of all systems (SC, Wkf, lows and highs) are observed at the 1000 hPa level. Systems at the upper levels tend to be slightly larger ($\approx$100 km larger) than systems identified near the ground. For high W_k thresholds ($W_k \geq 1.5$) all mean radii detected at the particular levels coincide.
- ***Comparison of SC/Wkf radii:*** Up to a threshold of $W_k = 1.2$, the SC are in general smaller than the Wkf. However, the means approach each other with a further increase of the W_k threshold.
- ***Comparison of lows/highs:*** The means and standard deviations of the SC/Wkf highs and SC/Wkf lows are almost equal (although there is a difference between SC and Wkf). An exception constitutes the SC lows at the 600 hPa level which are larger than the other SC.

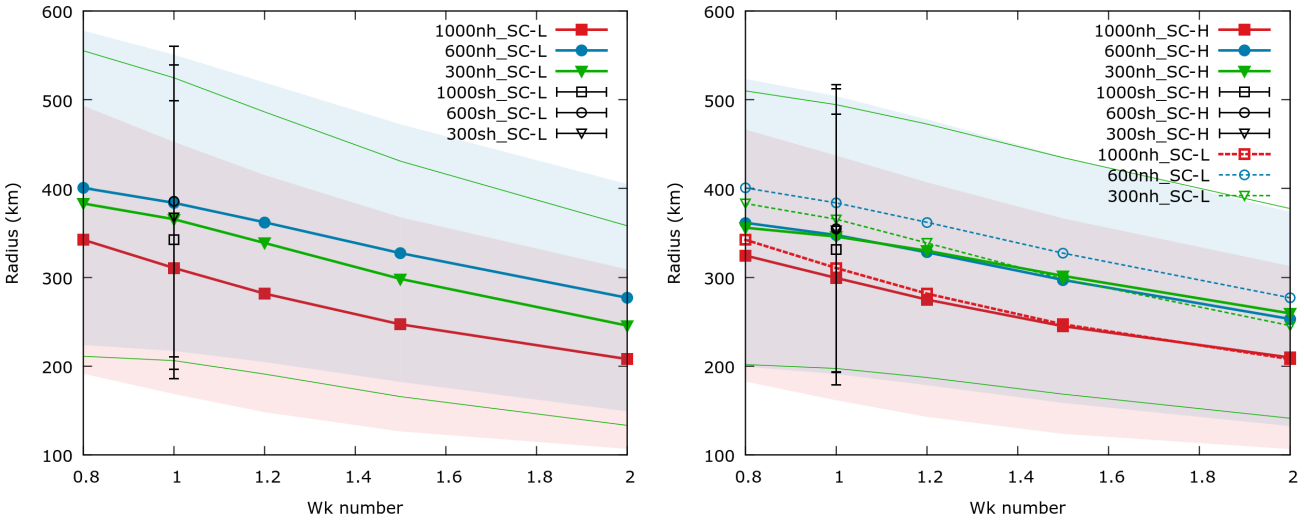

(a) Radius of single centers (lows)

(b) Radius of single centers (highs)

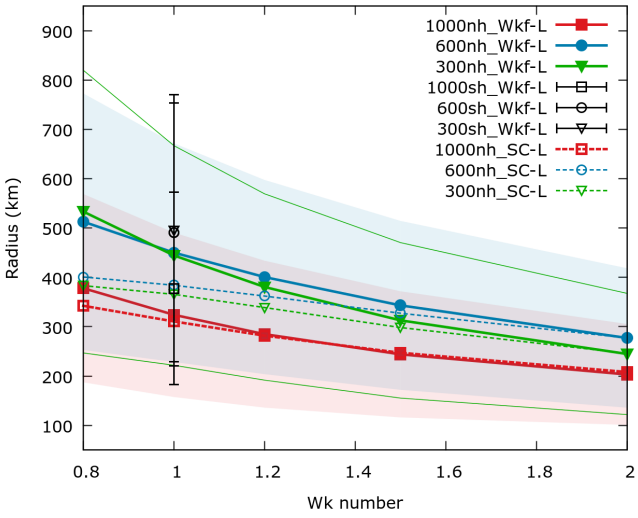

(c) Radius of W_k features (lows)

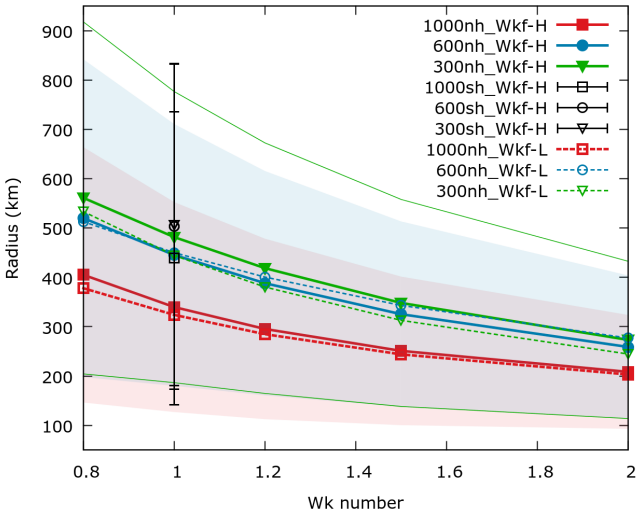

(d) Radius of W_k features (highs)

Figure 43: *Mean radii and standard deviations (red/blue colored area, thin green curves) of identified systems as a function of the W_k-thresholds at different pressure levels (300, 600, 1000 hPa): (a) Single centers (lows), (b) single centers (highs), (c) W_k-features (lows), (d) W_k-features (highs). Note the different ranges (y-axis) for SC and Wkf. For comparison reasons, the means of SC (lows) are added to (b),(c) and Wkf (lows) to (d). (Abbreviations in legend/text:* nh/sh*: northern/southern hemisphere,* SC*: single centers,* Wkf*: W_k-features,* L*: lows,* H*: highs)*

- ***Comparison of southern/northern hemisphere:*** At the upper levels, southern hemispheric systems are almost equal only little larger than the northern hemispheric ones. At the 1000 hPa level, the southern hemispheric systems are considerably larger than the northern hemispheric systems.

- ***Variability:*** The ranges covered by one standard deviation around the means are relatively broad with values of about 200 to 300 km. Therefore, all means lie within one standard deviation of the other distributions.

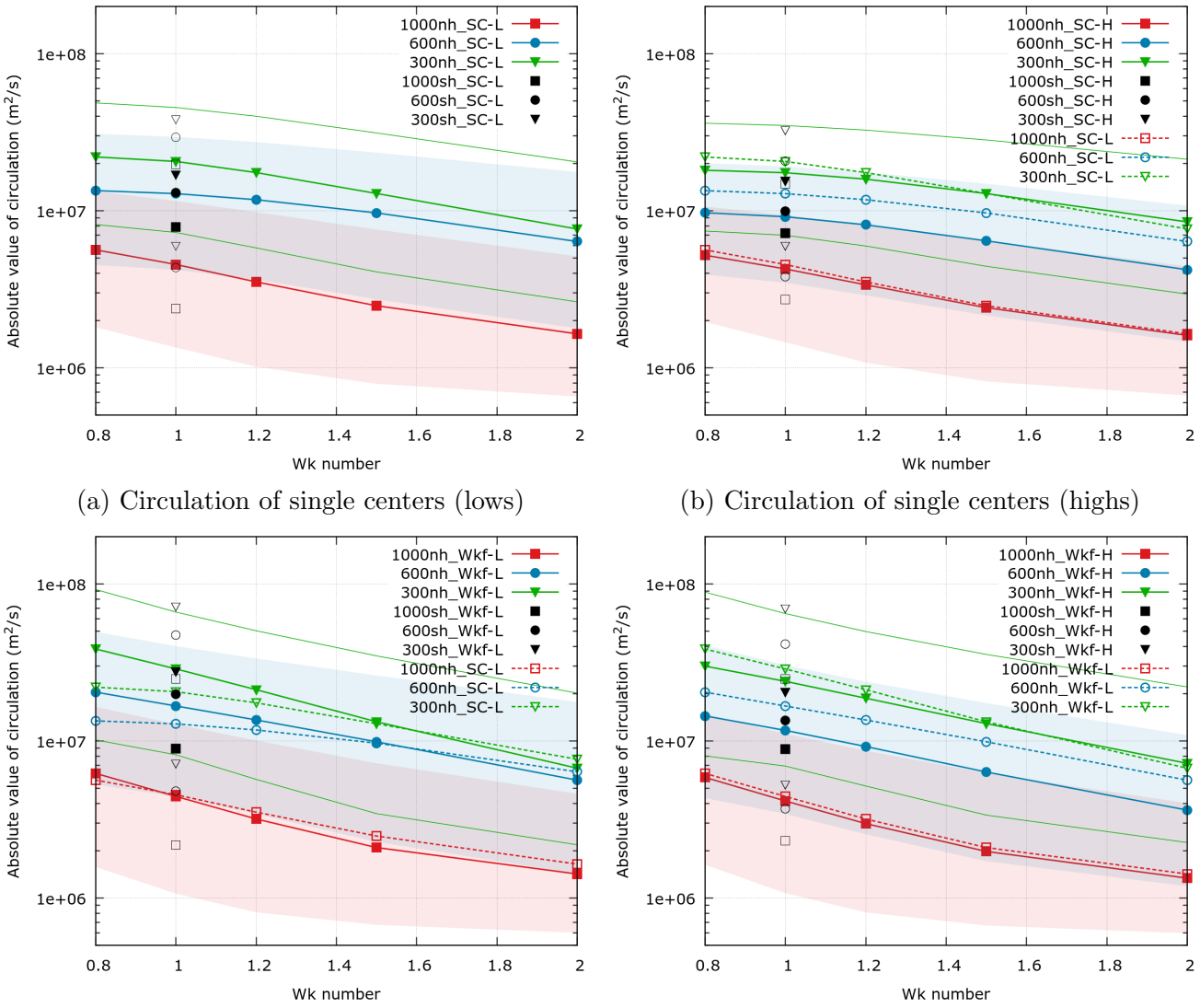

(a) Circulation of single centers (lows)

(b) Circulation of single centers (highs)

(c) Circulation of W_k features (lows)

(d) Circulation of W_k features (highs)

Figure 44: *Log-normal plot of circulations of identified systems as a function of W_k-thresholds: (a) Single centers (lows), (b) single centers (highs), (c) W_k-features (lows), (d) W_k-features (highs). Filled symbols are the medians of the distributions. Red, blue colored area, thin green curves indicate the lower (0.25) and upper (0.75) quartiles. Black open symbols correspond to the 0.25 and 0.75 quartiles of the southern hemisphere distribution. (Abbreviations:* nh/sh*: northern/southern hemisphere,* SC*: single centers,* Wkf*: W_k-features,* L*: lows,* H*: highs)*

6.8.3.3 Circulations

The median circulations of all vortex structures (SC, Wkf, highs, lows) at all levels show a clear dependence on the chosen W_k threshold with exponentially decreasing means for increasing thresholds (a linear decrease in the linear-logarithmic plot of Fig. 44).

- ***Dependence on height level:*** The lowest median circulations with values between about $1.5 \cdot 10^6\,\mathrm{m}^2/\mathrm{s}$ (for $W_k = 2$) and $6 \cdot 10^6\,\mathrm{m}^2/\mathrm{s}$ (for $W_k = 0.8$) occur at the 1000 hPa level and the highest median circulations are observed at the 300

hPa level ($7 \cdot 10^6\,\mathrm{m}^2/\mathrm{s}$ for $W_k = 2$ and $4 \cdot 10^7\,\mathrm{m}^2/\mathrm{s}$ for $W_k = 0.8$).

- ***Comparison of SC/Wkf circulations:*** While all systems (SC, Wkf, lows, highs) have almost equal medians at the 1000 hPa level, the SC have smaller circulations than the W_k features for lower W_k thresholds ($W_k \leq 1.2$) at upper levels.

- ***Comparison of lows/highs:*** The main difference between the circulations of highs (Fig. 44b,d) and lows (Fig. 44a,c) occurs at the 600 hPa level for all W_k thresholds where the lows (either SC or Wkf) have considerably higher median circulations than the highs. The same is valid at the 300 hPa level, but the difference between lows and highs is much smaller and only occurs for smaller W_k thresholds ($W_k \leq 1.2$).

- ***Comparison of southern/northern hemisphere:*** On the southern hemisphere, the circulations of the upper levels are of comparable order to the northern hemisphere. At the 300 hPa level, the southern hemispheric median circulations are even a bit smaller. However, the circulations at the 1000 hPa level are considerably larger on the southern hemisphere. Although, the smallest circulations are still observed at the 1000 hPa level and the highest at the 300 hPa level, respectively, the difference between the median circulations of the different levels is noticeably smaller.

- ***Variability:*** The upper and lower quartiles (0.25 and 0.75) occur symmetric around the median circulations although the axes are scaled in a linear-logarithmic manner in Fig. 44. This indicates that the circulations are rather lognormally than normally distributed. Therefore, the variability of the detected circulations is much larger compared to the variability of normally distributed parameters such as the numbers or the radii. The interquartile range which includes 50% of the systems is very broad: e.g. for a W_k threshold of $W_k = 1$ the range is between 10^6-$10^8\,\mathrm{m}^2/\mathrm{s}$.

6.8.4 Summary and Discussion of Results

In summary, we observe a strong dependence of the numbers, radii and circulations of single centers and W_k features on the W_k thresholds with a decreasing tendency for increasing W_k thresholds. While the mean radii and median circulations are smallest at the 1000 hPa level, the numbers are largest at the 1000 hPa level.
The most surprising result concerning the number of identified vortices might be that the number of the single centers becomes smaller than the number of the W_k features with increasing W_k threshold. At first, one would expect them to be at least equal. However, this result originates in the different definitions of single centers and W_k features. While single centers are defined as local vorticity extrema surrounded by at least 8 grid points

with vorticity values smaller or equal (or larger or equal for vorticity minima) than the center point, W_k features are determined as simply connected regions of W_k values larger than a certain threshold. For the identification of simply connected regions, we only need to evaluate the 4 direct neighbors around a local point. This can lead in some cases (e.g. diagonal neighbors fulfilling the threshold criterion) to the detection of two W_k features and only one single center at the same time. An example is given in Figure 45(b,c) for a W_k threshold of $|W_k| = 1.5$. Furthermore, we can see in Figure 45(a) how complex the reduction of vortex sizes with increasing W_k thresholds is. In general, the areas that include multiple vorticity centers become considerably smaller with increasing threshold (see for example the area that includes storm Anatol). Meanwhile, for systems that include only one single vorticity center, the reduction of their sizes is only minor (see e.g. the system located at 45°N, 60°W). Furthermore, it should be noted that the W_k extrema do not necessarily coincide with the vorticity extrema (see again storm Anatol, Fig.45a).

It is maybe impossible to decide which approach is "more correct", i.e. how many neighboring points need to be considered. On the one hand, the comparison to the eight surrounding points is a common method successfully used in the identification of local extrema (e.g. used by Blender et al., 1997; Schneidereit et al., 2010) and we can see in Fig.45c that there is no second extremum in the vorticity field. On the other hand, in the example given in Figure 45b we observe a second local extremum in the W_k^* field. Furthermore, there are values of $\|W_k^*\|$ below the threshold along the diagonal line between the smaller W_k feature (for a threshold of $W_k^* < -1.5$) and its northwesterly neighbor. This can be supported by a bilinear interpolation between these points (indicated by the green numbers in Fig. 45c).

The best way to deal with these opposed results is to bear in mind that the definitions are based on different fields and that therefore it cannot be said which definition is better. While the vorticity describes the amount of rotation, the W_k number relates the value of the rotation to the deformation at the same points. On the one hand, we have a pure value of the rotation, on the other hand we have a relational value that only tells us how much larger, smaller or equal the rotation is in direct comparison to the deformation.

Moreover, we have seen that the mean radii and mean circulations of the identified systems in general decrease with increasing W_k threshold. In Fig. 46 we plotted these mean values against each other. We observe a nearly linear dependence on this synoptic-scale data. That means that with increasing W_k threshold the mean circulation seems to depend linearly on the radius. Further, from the definition of the circulation as closed path integral (107), we can expect the velocity to be constant inside the vortex:

$$\Gamma = \oint_S \mathbf{u} \cdot d\mathbf{r} \approx 2\pi U R \qquad \text{with } U \approx const. \text{ on the synoptic scale} \tag{243}$$

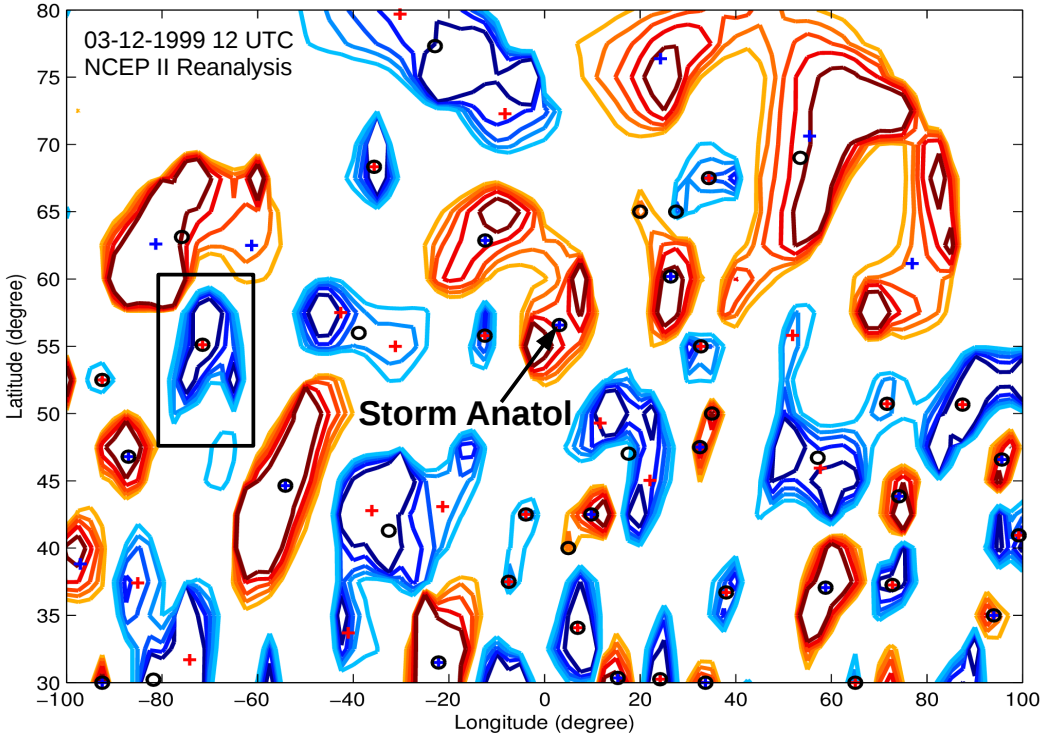

(a) Extended W_k number; contours for $|W_k|$=0.8,1.0,1.2,1.5,2.0 (increasing from light to dark colors)

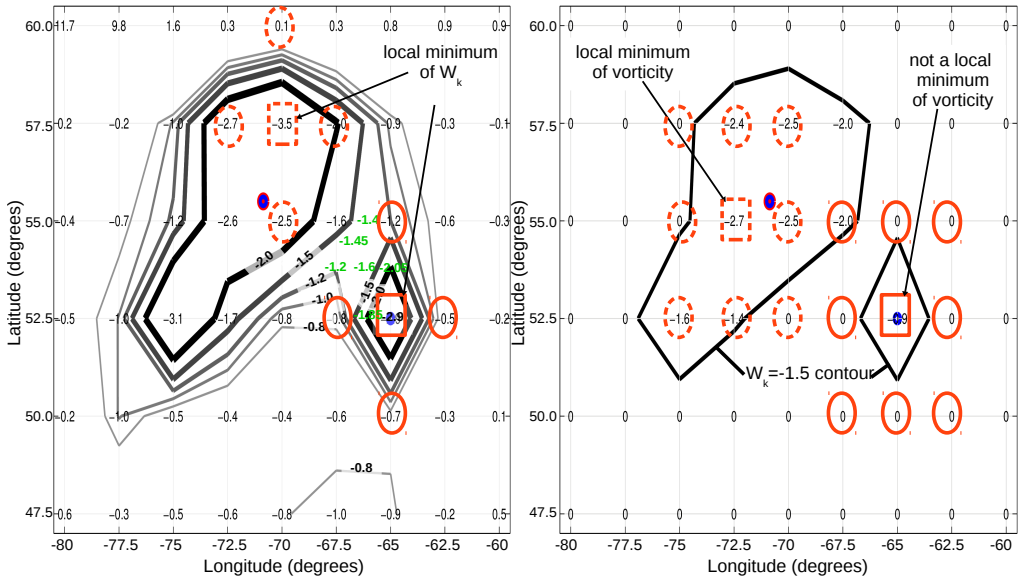

(b) Extended W_k number; contours for W_k =-0.8,-1,-1.2,-1.5,-2

(c) Vorticity ($10^{-5}s^{-1}$) in the field of W_k<-1.5

Figure 45: *Example of extended W_k contours for an arbitrarily chosen date (here 03-12-1999 12UTC, 6 hours before storm Anatol reached its maximum intensity). (a) Positive (red) and negative (blue) W_k contours used in the systematic analysis (with $|W_k| = (0.8, 1.0, 1.2, 1.5, 2.0)$; lighter colors equal smaller absolute values of W_k; black box indcates the example system analysed in (b,c); crosses/black circles indicate the locations of single centers/W_k features identified at a W_k threshold of 1.0; (b) W_k contours for example system (high) and W_k-feature definition basd on the four direct neighbors around each point; green numbers are derived by bilinear interpolation of the W_k field; (c) Vorticity (in $10^{-5}s^{-1}$) in the field of $W_k < -1.5$ and single centers (SC) definition taking into account all 8 neighbors around each point. Orange boxes indicate the local points of interest (local minima), and their corresponding neighbors (orange circles).*

where U is the wind speed and R is the radius of the system. This was also assumed in Müller et al. (2015) and the result shown here further supports their assumptions. The linear dependence might not hold at smaller scales. Otherwise, systems that are smaller than about 160-180 km would be missing. This value is about the value of the intercept of the linear fits applied to the curves in Fig. 46 for the assumption of zero circulation[69]. A better fit that allows for $\Gamma(R = 0) = 0$ is a polynomial fit including

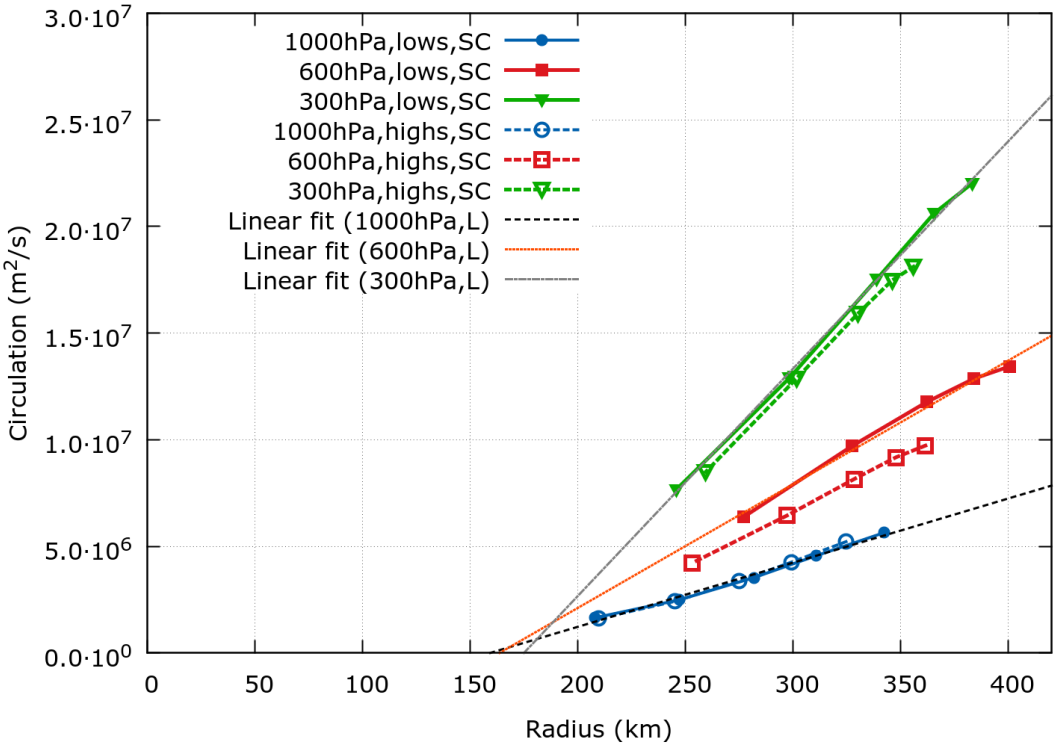

Figure 46: *Mean circulation (m^2/s) vs. mean radius (km) in dependence of the chosen W_k threshold. The symbols with the highest radius correspond to a threshold value of $W_k = 0.8$. Mean radii (and mean circulations) decrease with increasing W_k thresholds. Smallest mean radii correspond to $W_k = 2.0$. The explicit thresholds are $W_k = (0.8, 1.0, 1.2, 1.5, 2.0)$.*

a quadratic and a linear term. A quadratic term alone would coincide with a constant vorticity inside the vortex[70] while the linear term alone coincides with constant velocity inside the vortex.

We also compared the computing time for different W_k thresholds. Exemplarily, we calculated the mean computing times that were necessary for the simultaneous identification of W_k-features and single centers in the NCEP data (northern hemisphere, 1000 hPa level, only cyclonic systems) for the 40 timesteps of the first 10 days of December 1999 (see Table 8). In general, we observe that the mean times approximately divide with respect to the W_k thresholds. However, variations of the computing times can be

[69] However, this is also the boundary of the size which is determined by the resolution of the data set that is 2.5 degrees in this case (NCEP data).

[70] This follows from the definition of the circulation as area integral over the vorticity (see equations (107) and (108)): $\Gamma = \oint_S \mathbf{u} \cdot d\mathbf{r} = \int_{A_0} \zeta dA$ where A_0 is the area enclosed by the closed path S.

Table 8: *Mean computing time (s) and quartiles (s) needed for the identification of cyclonic W_k-features and single centers per timestep for different W_k-thresholds (NCEP II Reanalysis, northern hemisphere, 1000 hPa level, 01/12/1999 00 UTC–10/12/1999 18 UTC). Only the identification part of the program code is taken into account. Total computing time is for the whole program is estimated in the last row of the table.*

W_k-threshold	0.8	1.0	1.2	1.5	2.0
mean computing time (s)	4.73	2.39	1.33	0.67	0.30
0.25 quantile (s)	2.84	1.37	0.78	0.34	0.04
0.75 quantile (s)	6.57	3.35	1.91	0.94	0.44
approximate total computing time (min) per month for the whole program	≈ 90	≈ 60	≈ 45	≈ 30	≈ 20

quite large from one timestep to another (see interquantile ranges in Table 8). Note, that the explicit computing times futhermore depend on the season and on the height level (not shown). The most interesting reduction might be the one between $W_k = 1.0$ and $W_k = 1.2$ since it is so close to the original vortex definition ($W_k = 1.0$ threshold). It should be noted that the total program takes more computing time than the values given here. For these values we only considered the part of the program that identifies the W_k-features/single centers and determines their properties (center of circulation, area). On average, the identification of cyclones in the NCEP data took about 1 hour for a whole month, i.e. about 30 seconds per timestep, at the 1000 hPa level for a $W_k = 1.0$ threshold. This higher computing time is mainly caused by the import and export of the data, the calculation of the relevant fields, and so forth. Furthermore, the time of the export (saving procedure) of the identified systems depends on the total number of the systems and it takes longer the more systems are detected.

The question arises in which cases and if we might benefit from a larger or smaller W_k threshold. In Schielicke et al. (2016), we proposed that a smaller threshold could be used in order to detect early circulations and that a larger threshold can be used in order to find stronger systems. Therefore, we plotted some timesteps during the development of storm Anatol in Figure 47. On the one hand, we can detect the development of storm Anatol earlier in case of a smaller threshold of $W_k = 0.8$ (Fig. 47a,b: two timesteps earlier than published, see Fig. 34). Anatol seems to develop from a stretched filament of a quasi-stationary cyclonic circulation that is located over the Atlantic ocean at about 60°W,42.5°N. Anatol cuts off from its "*mother circulation*" at 02-12-1999 06UTC (Fig. 47c) where it is first detected as a single center system. On the other hand, we seem to be able to longer follow the decay of cyclones with the threshold of $W_k = 0.8$ (Fig. 47e,f). However, the large computing time that is needed for the identification of W_k

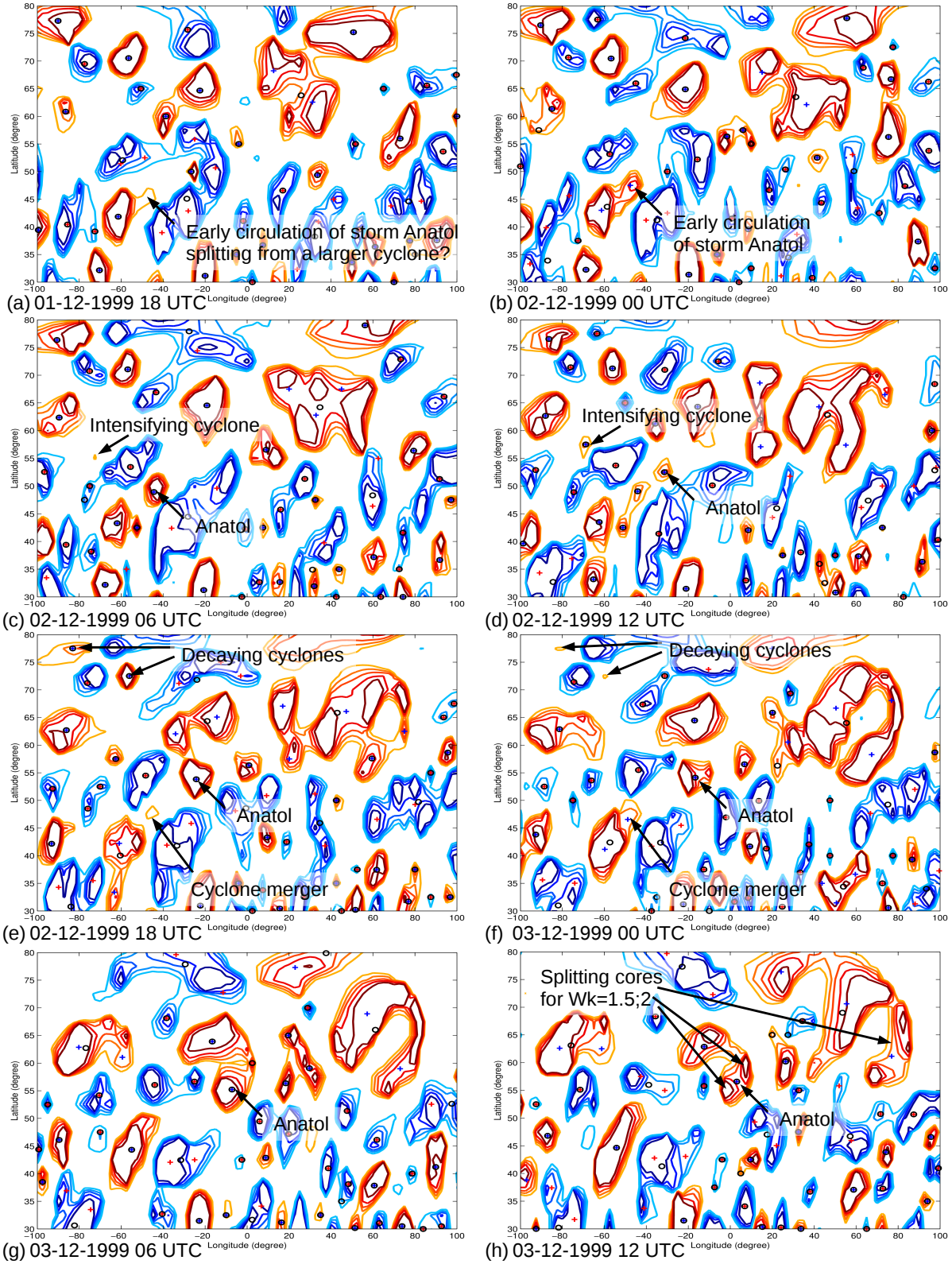

Figure 47: *Extended W_k contours during the development of storm Anatol. Positive (red) and negative (blue) W_k contours (with $|W_k| = (0.8, 1.0, 1.2, 1.5, 2.0)$; lighter colors equal smaller absolute values of W_k. Crosses/black circles indicate the locations of single centers/W_k features identified at a W_k threshold of 1.0.*

features for a threshold of $W_k = 0.8$ is a disadvantage (see Tab. 8). The best application of this small W_k- threshold might be in the analysis of single (extreme) cases. In these cases, we might benefit from an earlier detection of the systems that allows a deeper insight into the generation processes. This might especially be interesting in the early detection of tropical cyclone circulations. For the analysis of large data sets a higher W_k-threshold should be chosen.

For higher W_k-thresholds the computing time is considerably reduced (Tab. 8). We observe that most of the multiple center systems split into smaller cores with respect to the increasing W_k number (e.g. Fig. 47h). However, the W_k features detected with a higher W_k-threshold ($W_k = 1.5, 2.0$) do not always coincide with the local vorticity extrema or even miss the extrema (Fig. 47h). Thereby, a threshold of $W_k = 2.0$ means that inside the detected region all points have a rotation rate that is at least twice as high as the deformation rate.

In conclusion, it can not be satisfactorily answered which threshold one should choose because it also depends on the investigated problem. The best option might be to stick to the original $W_k = 1.0$ threshold following the definition of Truesdell (1953). Then, we can interpret the W_k features as a larger scale circulation area that can contain smaller systems. This is similar to the observation of a cyclone family where multiple systems are embedded in a large-scale cyclonic circulation. In the following chapter we will analyze vortex structures in differently resolved data sets ranging from large-scale, synoptic to small-scale, convective vortices with help of the W_k-method that we have introduced in this chapter. Thereby, we will use the $W_k = 1.0$ threshold. We will see that the W_k-method represents a consistent method of vortex identification across the scales.

7 Statistical Analysis of Vortices on different Scales

Finally, we will analyze and compare the properties of vortex structures in differently-resolved data sets. For the analysis of the data sets we will use the (extended) W_k-method with the vortex identification criterion $\|W_k^*\| > 1$ and the tracking method based on the W_k-method that we have introduced in chapter 6. The analysis in this chapter also serves as a testbed for the new methods.

7.1 Data

We will analyze three different data sets. The main difference between the data sets is the difference in their spatio-temporal resolutions. The horizontal resolutions range from synoptic-scale resolving, horizontal resolutions of 2.5° (≈ 280 km) of the NCEP reanalysis data set to meso-scale resolving 0.5° (≈ 55 km) of the CFSR (reanalysis) data set to convective-scale resolving simulated data of different idealized supercell set-ups carried out with the WRF model with a horizontal resolution of 1 km. It is very important to bear in mind that differently-resolved data captures processes on different scales. In finer resolutions small-scale processes might dominate the appearances of the vortex structures and therefore the vortex type observed. In the following, we will introduce the data sets in more detail.

7.1.1 NCEP II reanalysis data

The NCEP-DOE AMIP-II[71] global reanalysis dataset is an updated version of the NCEP-NCAR[72] reanalysis data (Kanamitsu et al., 2002). It is available for the years starting from 1979 to the present (satellite-data era) with a horizontal resolution of 2.5°×2.5° on a latitude-longitude grid. This resolution is equal to a horizontal distance of about 280 km at the equator. While the latitudinal grid spacing remains constant the longitudinal grid spacing narrows approaching the poles and becomes exactly zero at the poles. Among other parameters, the horizontal wind fields (u, v) are given on 17 pressure levels (1000, 925, 850, 700, 600, 500, 400, 300, 250, 200, 150, 100, 70, 50, 30, 20, 10 hPa) every 6 hours (00, 06, 12, 18 UTC). For the analysis we will use the horizontal wind field data at the 1000, 600 and 300 hPa levels for the complete year 1999.

7.1.2 CFSR reanalysis data

The Climate Forecast System Reanalysis (CFSR) data was also conducted at the National Center for Environmental Prediction (NCEP). It was calculated by a global, coupled atmosphere-ocean-land surface-sea-ice model with a high resolution (T382L64,

[71] National Center for Environmental Prediction (NCEP)–Department of Energy (DOE) Atmospheric Model Intercomparison Project (AMIP) II
[72] National Center for Atmospheric Research (NCAR)

$\approx$ 38 km, Saha et al., 2010)[73]. The data is available as gridded, global data set with a spatial resolution of $0.5° \times 0.5°$ ($0.5° \approx 55$ km at the equator) on a regular latitude-longitude grid and a temporal resolution of 1 hour. Thereby, an analysis with assimilation of satellite data and conventional data (atmospheric model) and an analysis of the sea ice and ocean is made at 00, 06, 12 and 18 UTC. From these standard analysis times a 9 hour coupled guess forecast is started with hourly coupling to the ocean model. Furthermore, the data is available on 37 pressure levels from 1000 hPa to 1 hPa[74]. We restricted the analysis to the 1000, 600 and 300 hPa level. In our analysis, we used the standard analysis times (00, 06, 12, 18 UTC) as well as the hourly forecast data for the hours between two analysis steps. Because of the higher computational capacity required for the analysis of vortices in the higher spatio-temporally resolved data, we restricted the analysis to the northern hemisphere and to two months: June 1999 as a summer month and December 1999 representing a winter month. Furthermore, we used the data of January 1999 for the analysis of the vortex tracks.
The most important point concerning our analysis of vortex structures on different scales is the higher spatio-temporal resolution compared to the NCEP II reanalysis data. With the higher resolution, we are able to investigate not only vortices on the synoptic scale, but also resolve mesoscale vortices. Furthermore, the higher resolution additionally gives a higher resolved orography (see Figure 48 in comparison to the NCEP orography) that can induce more, finer scale disturbances and vortices.

7.1.3 WRF simulated data

In order to obtain data on even finer scales, i.e. the convective scale, we needed to simulate the data since there is no higher resolved global reanalysis data set freely available so far. Furthermore, we are specifically interested in data that represents vortex structures. Therefore, we decided to simulate supercells that consist of rotating updrafts with a convection-permitting, high resolution model: the *Weather Research and Forecasting model*, abbreviated as WRF. WRF solves the fully-compressible, nonhydrostatic Euler equations. It is a very flexible model that can be run on high-performance computer clusters as well as on a single laptop.
We did the simulation with WRF model version 3.6.1 installed on a laptop. We initialized the model in three runs with the originally implemented idealized supercell test case of a predefined quarter-circle sounding after Weisman and Klemp (1982) (called *original* run) and two modifications of this original sounding (called *linear shear*/*doubled-speed* runs). Denoting the wind vector as $\mathbf{u} = (u, v, w)$, we can summarize the difference

[73] T382 stands for a spectral model resolution with truncation T382 with a resolution at the equator of about 38 km or 0.313°; and L64 stands for 64 vertical (sigma) levels(NCAR/UCAR ClimateDataGuide: National Center for Atmospheric Research Staff (Eds), 2013).

[74] The CFSR data is available on the following atmospheric pressure levels (hPa): 1000, 975, 950, 925, 900, 875, 850, 825, 800, 775, 750, 700, 650, 600, 550, 500, 450, 400, 350, 300, 250, 225, 200, 175, 150, 125, 100, 70, 50, 30, 20, 10, 7, 5, 3, 2, 1.

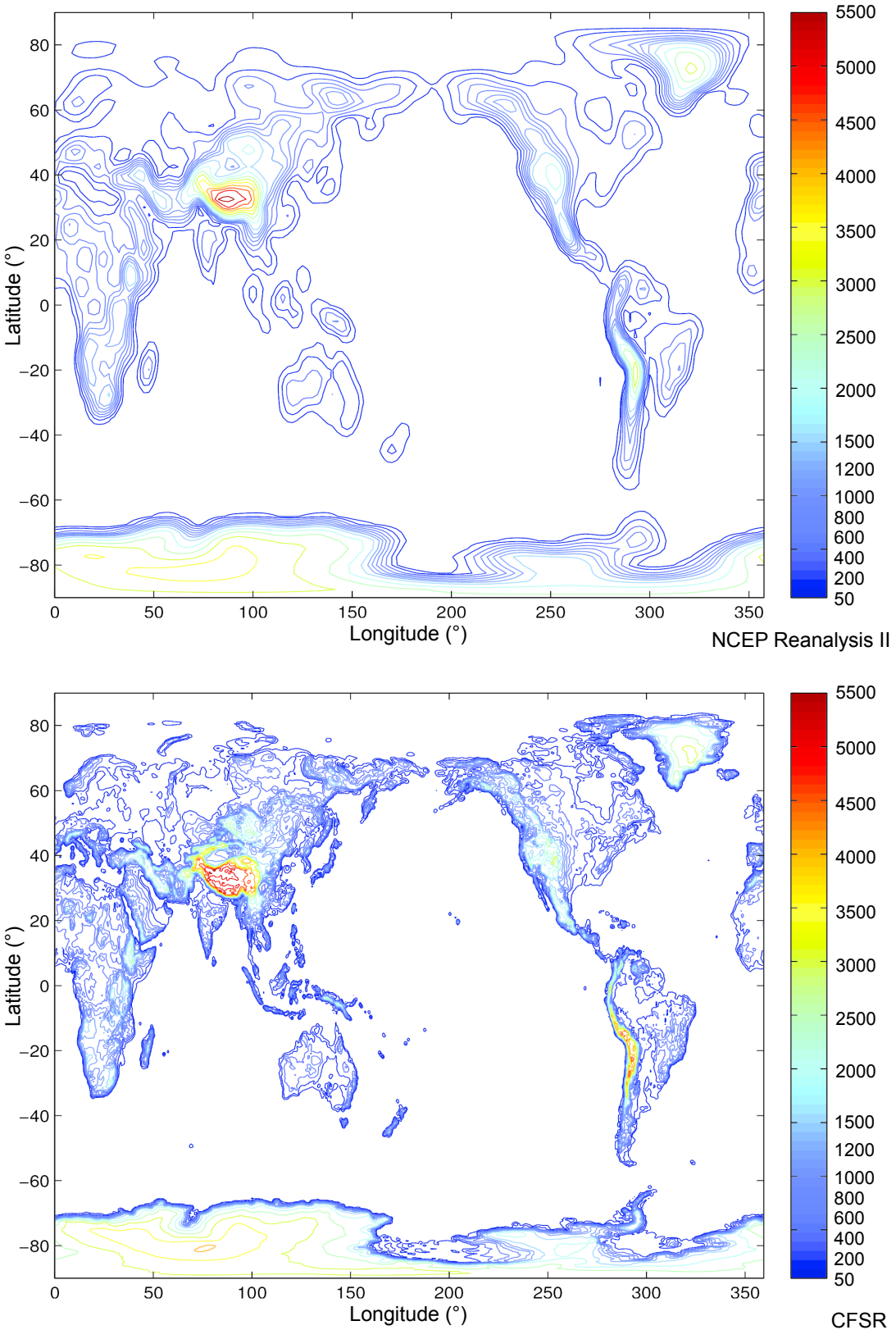

Figure 48: *Orography fields: (top) NCEP II reanalysis data, (bottom) CFSR data. Labels on the colorbar correspond to the contours plotted; the lowest level is 50 m.*

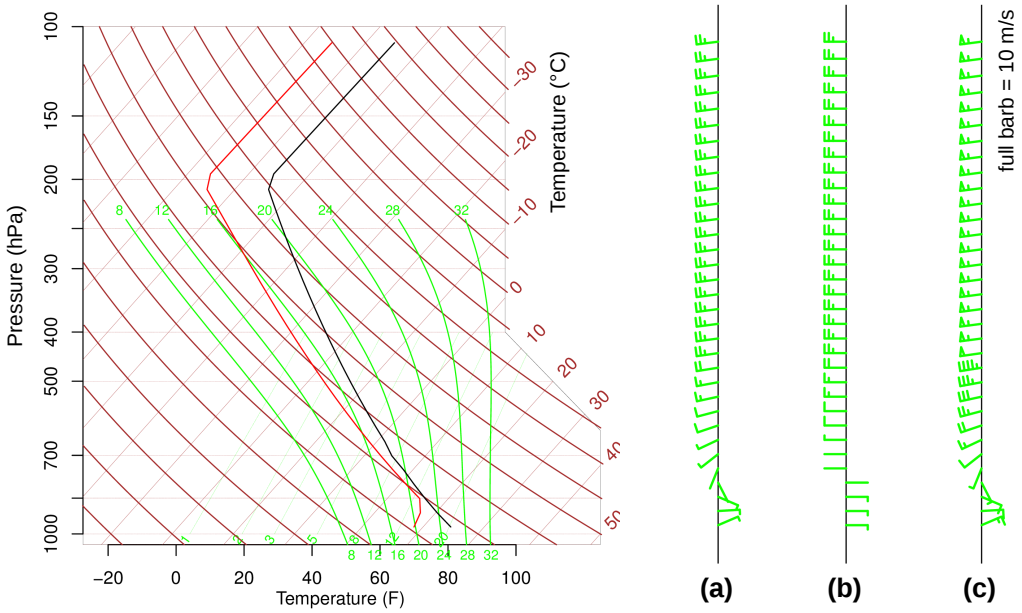

Figure 49: *Input sounding for WRF simulation of idealized supercell: (Left) Log p-skew T diagram with vertical profiles of temperature (black) and dew point (red); thin red diagonals are isotherms, thick red curves are dry adiabats, green thin parallel lines are the isolines of the water vapor mixing ratios (g/kg), green thick lines are moist adiabats and the isobars are horizontal. (Right) Vertical wind profiles: (a) Original wind profile implemented in WRF after Weisman and Klemp (1982); (b) Zero-v-wind profile: u-component (east-west) is equal to that in (a), but the v-component (north-south) is set to zero; (c) Doubled-speed profile: The magnitudes of the u- and v-components of the original wind profile (a) are doubled, the direction of the wind vectors stay the same as in (a). Heights correspond to the pressure axis on the (left).*

between the input soundings of the simulations as follows:

- **Original**: The original sounding and wind profile after Weisman and Klemp (1982) are taken for the simulation.
- **Linear shear**: The v-component of the original vertical wind profile is set to zero at every height level, while the u-component is equal to that of the original wind profile. The other input parameters (temperature, dew point) are taken from the original sounding.
- **Doubled-speed**: The magnitudes of the two wind-components u,v of the original wind profile are doubled. The directions of the wind vectors remain unchanged. The other parameters are taken from the original sounding.

We will refer to the different set-ups by these names: *original, linear shear, doubled-speed* set-ups (or runs). See Fig. 49 for the initial input sounding and the different initial wind profiles.
The model domain has a size of 250 km×200 km (x-,y-direction) with a horizontal resolution of 1 km. A warm bubble of air is placed at the center of the domain at a height

of 1.5 km triggering the convection. The shape of the bubble is a flattened sphere with a vertical diameter of 3 km and a horizontal diameter of 10 km. At its center point the potential temperature perturbation has a maximum of 3 K that decreases as the square of the cosine function to the bubble boundary where it falls to zero.
We used open boundary conditions (to hinder interactions of the vortex structures with each other from boundary effects).

7.2 Identification of vortex structures with help of W_k-method

The data will be analyzed in two steps. At first, we need to extract the vortices from the fields. Next, we will analyze the frequency distributions of the vortex properties (starting with radius and circulation, later energy of displacement and atmospheric moment) concerning exponential or power law behavior. The W_k-method will be used in order to identified vortex regions in the data fields. Thereby, a vortex region is identified in a simply-connected region of $\|W_k^*\| > 1$. We have introduced this definition as W_k feature earlier in chapter 6.4.2. Since we concentrate on the northern hemisphere, positive vorticity is associated with cyclonic motion and negative vorticity with anticyclonic motion. We will analyze W_k features only, because the computational effort, especially for the higher-resolved data sets, stays manageable[75] (see chapter 6.8 and discussion in chapter 6.8.4). Moreover, we restricted the analysis of the reanalysis data sets to the northern hemisphere and to the midlatitudes (30°N–80°N).
We will first analyze the number, radius (size) and circulation (intensity) of the vortices with help of probability density distribution and complementary cumulative distributions as will be described in the following chapter 7.3 for every data set. Thereby, the temporal evolution of the systems is not taken into account, i.e. the systems are analyzed for every single time step as if they are independent of each other.

7.3 Probability density functions: Exponential vs. power laws

Many phenomena are observed to cluster around a typical value: the mean value. This mean value of the distribution characterizes the phenomenon and deviations from that mean are usually observed to be small(examples are the mean height of adult man of a country, mean surface pressure or sea level heights Clauset et al., 2009). Those distributions are called normal or Gaussian distributions and it is sufficient to describe such a distribution by its mean value and its standard deviation.

[75] Although the single center definition introduced in chapter 6.4.2 might represent a better description of large-scale low pressure systems, the W_k features represent the large-scale environment in which single centers are embedded, e.g. cyclone families. Since the identification of single centers needs the contouring function, the computational effort is too large: simple tests showed that the computation time for the identification of single centers in case of the CFSR data was about 40 times larger than needed for the identification of W_k features. However, a comparison of single center and W_k features in the different data sets as well as an optimization of the identification via contours is a relevant topic of future work.

However, there are also many phenomena which do not follow a normal distribution but show rather large deviations from a calculated mean value. In some cases, the calculation of the mean value makes no sense since it does not in the slightest describes the distribution: Clauset et al. (2009) gives as an example the mean number of citizens in a U.S. city that is only about 8000. This number seems absurdly small compared to the millions of people living in big cities such as New York or Los Angeles. Hence, the mean value has no meaning in this case and describes in no way the distribution. These phenomena are better described by heavy-tailed distributions such as power law, lognormal or stretched-exponential distributions. Those heavy-tailed distributions allow for large deviations from the calculated average value of the data set.
In this work, we will focus on analyzing the distributions of the vortex properties regarding exponential and power law behavior, respectively. These two models constitute two extremes: While on the one hand, exponential functions describe distributions that are determined by characteristic scales, power laws on the other hand describe scale-invariant behavior. We will first introduce general equations followed by a comparison of different explicit probability density distributions.

7.3.1 General definitions

The probability of a continuous random variable X of being inside the finite interval $[a, b]$ is expressed with help of the ***probability density function*** $p(t)$ (called PDF) as (Bronstein et al., 2005, chapter 16.2.2.2)

$$Pr(a \leq X \leq b) = \int_a^b p(t)dt \qquad \text{with} \quad p(t) = Cf(t) \tag{244}$$

where C is a normalization constant and $f(t)$ is a function. The corresponding ***cumulative distribution function*** $P(X)$ of a continuous random variable X (called CDF) describes the probability of X being smaller than a threshold x. It is defined as

$$P(X) = Pr(X \leq x) = \int_{-\infty}^{x} p(t)dt \ . \tag{245}$$

In this thesis, we will rather use the ***complementary cumulative distribution function*** $\bar{P}(X)$ of a continuous random variable X (called $CCDF$) that gives the probability of X being larger than a threshold x and is defined as

$$\bar{P}(X) = Pr(x > X) = \int_{x}^{+\infty} p(t)dt \ . \tag{246}$$

If the total probability is normalized to one, we can also write

$$\bar{P}(X) = 1 - P(X) \ . \tag{247}$$

Many distributions with different numbers of tunable parameters exist. The higher the number of the parameters is, the better probably is the fit of the function to the observed data. Nonetheless, a distribution that has only few free parameter such as the exponential or the power-law distributions has the advantage to be much easier to be interpreted than those characterized by more parameters. In the following we will introduce some distributions in more detail.

7.3.2 Exponential distribution

Besides a minimum value $x_{min} \geq 0$, an exponential distribution is determined by only one parameter $\lambda > 0$ that describes the typical decay of the distribution. A random variable x is exponentially distributed if its probability density function $p(x) = Cf(x)$ behaves as

$$p(x) \sim e^{-\lambda x} \qquad \text{(PDF)} \tag{248}$$

The normalization constant C depends on the value of x_{min} and on λ and can be determined by $\int_{x_{min}}^{\infty} Ce^{-\lambda x'} dx' = 1$. It follows that $C = \lambda e^{\lambda x_{min}}$ (see Table 9).
The complementary cumulative distribution function $\bar{P}(x) = C\bar{F}(x)$ with $\bar{F}(x) = \int f(x')dx'$ is also an exponential distribution with the same decay rate λ

$$\bar{P}(x) \sim e^{-\lambda x} \qquad \text{(CCDF)} \tag{249}$$

The specialty about the parameter λ of an exponential distribution is that it has a unit if x has a unit. More precisely, λ needs to have the reciprocal unit of x and therefore, the reciprocal $1/\lambda$ has a special meaning: it is equal to the expected value of the distribution or in other words the mean of the distribution. Furthermore, $1/\lambda$ describes a typical scale of the distribution. The mean μ and variance σ^2 of an exponential distribution are given as

$$\mu = \frac{1}{\lambda} \quad , \quad \sigma^2 = \frac{1}{\lambda^2} \tag{250}$$

If we scale x by a constant factor c as $x \to c\tilde{x}$, then the exponential distribution behaves as follows

$$p(c\tilde{x}) \sim e^{-\lambda c\tilde{x}} = e^{-\tilde{\lambda}\tilde{x}} \qquad \text{with } \tilde{\lambda} = \lambda c \tag{251}$$

We see that in this case the characteristic parameter is scaled by a factor of c, too, but the exponential behavior remains.
A known example of exponential distributions is the distribution of radioactive decay where λ is called the radioactive half-life. Another example was already given in section 5.2 as the distribution of atmospheric vortex (extratropical and tropical lows, tornadoes)

intensities with respect to their energy of displacement.

7.3.3 Power-law distribution

Likewise to the exponential distribution, a power law distribution is described wholly – besides a minimum value $x_{min} > 0$ – by a parameter α called the power law exponent or scaling parameter. A random variable x is power law distributed if its probability density function $p(x) = Cf(x)$ obeys a law proportional to

$$p(x) \sim x^{-\alpha} \qquad \text{(PDF)} \tag{252}$$

where $f(x) = x^{-\alpha}$. It is obvious that this would grow infinitely large for $x \to 0$. Hence, we need the lower bound x_{min} to be different from zero. The normalization constant is then calculated from

$$1 = \int_{x_{min}}^{\infty} Cx^{-\alpha} dx' = \left[\frac{C}{1-\alpha} x^{-\alpha+1} \right]_{x_{min}}^{\infty} \tag{253}$$

This is only possible for $\alpha > 1$ since the term $x^{-\alpha+1} \to \infty$ for $\alpha < 1$. Then the normalization constant C reads (see Table 9)

$$C = (\alpha - 1) x_{min}^{\alpha-1} \qquad \text{for } \alpha > 1 \tag{254}$$

The complementary cumulative distribution function (CCDF) of the power law distribution is also proportional to a power law but the scaling parameter is different by one:

$$\bar{P}(x) \sim x^{-\alpha+1} \qquad \text{(CCDF)} \tag{255}$$

A calculation of the moments of the power law distributions further shows that the power law distribution has no finite mean for $\alpha < 2$ and no finite variance for $\alpha < 3$ (Newman, 2005). Most power laws of empirical data are observed to have values of α in the range of $2 \leq \alpha \leq 3$ (e.g Newman, 2005). However, the Gutenberg-Richter law which describes the relation of earthquake numbers and magnitudes has an empirically determined value of $\alpha \approx 1.6$-1.8 which is smaller than 2 and therefore the distribution of earthquake magnitudes has no finite mean. Furthermore, the distribution of tornado magnitudes (atmospheric moments) also showed power law behavior over a large range of moments with a value $\alpha \approx 1.2$ (see chapter 5.3 , Figure 20; and Schielicke and Névir, 2011, 2013).

A special property of power laws is their scale-invariance. This means that by scaling the range of the distribution by a constant factor c, we do not change the shape of the

distribution only the outcome range is multiplied by the constant factor $c^{-\alpha}$

$$f(cx) = (cx)^{-\alpha} = c^{-\alpha} f(x) \sim f(x) \ . \tag{256}$$

This property is unique to power laws (e.g. see chapter III.E in Newman, 2005, where this statement is proved). Therefore, power laws seem to be connected to scale-free or scale-invariant behavior.

7.3.4 Other distributions with at least two parameters: Normal, lognormal and stretched-exponential distribution

Among the most common probability density functions $p(x) = Cf(x)$ beside the exponential and the power law distributions are the normal, the lognormal and the stretched-exponential distributions. We listed their functions $f(x)$ and normalization constants C in Table 9.

7.3.4.1 Normal distribution

The normal or Gaussian distribution is probably the most famous among these distributions. It is defined over the whole range of $-\infty < x < +\infty$ and it is symmetric around its mean value μ with a standard deviation σ (or variance σ^2). A random variable is normally distributed if its probability density function is proportional to

$$p(x) \sim e^{-\left(\frac{x-\mu}{\sqrt{2}\sigma}\right)^2} \qquad \text{(PDF, normal distribution)} \tag{257}$$

which has its maximum at μ (also equal to the mean and median of the distribution) and inflection points at $\mu \pm \sigma$. An important property of the normal distribution is the following: The sum $X = c_1 X_1 + c_2 X_2$ with constants $c_1, c_2 \in \mathbb{R}$ of two random variables X_1, X_2 that are independent and normally distributed with the parameters μ_1, σ_1 and μ_2, σ_2, is also normally distributed with parameters $\mu = c_1\mu_1 + c_2\mu_2$ and $\sigma = \sqrt{c_1^2\sigma_1^2 + c_2^2\sigma_2^2}$ (Bronstein et al., 2005, chapter 16.2.4). This shows the connection of the normal distribution to additive processes.

7.3.4.2 Stretched-exponential distribution

While data that is normally- or exponentially-distributed shows no large deviations from their observed mean, we observe for some empirical data rather strong deviations. This data is better described by heavy-tailed distributions such as the power law, lognormal or stretched-exponential distributions. Distributions with a heavy tail are usually investigated in a double-logarithmic plot. In general, the empirical data is often observed to occur (slightly) curved in that plots and a power law behavior often appears only over a small range of the whole data set (see Avnir et al., 1998, who point out that in physical systems the scaling range of the applied power laws covers on average only

1.3 orders in magnitude.). This observed curvature can come from finite-size effects. E.g. Laherrere and Sornette (1998) gives the example of earthquake sizes: there cannot be an earthquake of infinitely large magnitude (on finite-sized Earth) since this would imply infinitely high energy release.
Laherrere and Sornette (1998) propose alternatively to use the stretched-exponential in order to describe the whole range of the data with help of one model. A random variable x obeys a stretched-exponential distribution if its probability density function $p(x) = Cf(x)$ behaves as

$$p(x) \sim x^{\beta-1} \exp\left(-\widetilde{\lambda} x^{\beta}\right) \qquad \text{(PDF, stretched-exponential distribution)} \tag{258}$$

The smaller the exponent β, the heavier is the tail of the distribution. For $\beta > 1$, the stretched-exponential distribution decays faster than the exponential. If the exponent $\beta < 1$, the stretched-exponential falls off slower than the exponential function, that is retrieved for $\beta = 1$. Moreover, if the exponent approaches zero ($\beta \to 0$), Sornette (2009) showed that the stretched-exponential pdf above a certain threshold converges to a Pareto distribution. We can write $\widetilde{\lambda} = 1/(\lambda\beta)$. Laherrere and Sornette (1998) write the cumulative distribution function (CDF) of the stretched-exponential in the following form

$$P_{cum}(x) \sim \exp\left[-\frac{x^{\beta}}{\lambda\beta}\right] \qquad \text{(CDF : stretched-exponential distribution)} \tag{259}$$

where we have (after Laherrere and Sornette, 1998)

β: exponent that controls the behavior of the tail

λ: a typical multiplicative factor

$\lambda\beta$: a reference scale from which all moments of the distribution can be determined

Note, that the reference scale $\lambda\beta$ has the same unit as x but to the power of β. In general, the term $\lambda\beta$ is not the mean of the distribution. Frisch and Sornette (1997) showed that the stretched-exponential distribution follows from multiplicative processes and Laherrere and Sornette (1998) interpret the reciprocal of the exponent $1/\beta$ as the number of generations in the multiplicative process.

7.3.4.3 Lognormal distribution

Another heavy-tail distribution is the lognormal distribution. A continuous random variable X is lognormally distributed if the random variable $Y = \log X$ is normally-distributed with parameters μ_L, σ_L^2. The probability density function of the lognormally

distributed random variable X obeys

$$p(x) \sim \frac{1}{x} \exp\left(-\left(\frac{\ln x - \mu}{\sqrt{2}\sigma}\right)^2\right) \qquad \text{(PDF : lognormal)} \tag{260}$$

for $x > 0$. The lognormal distribution is skewed and its mean μ and variance σ^2 are

$$\mu = \exp\left(\mu_L + \frac{\sigma_L^2}{2}\right) \quad , \quad \sigma^2 = \left(\exp(\sigma_L^2) - 1\right) \exp\left(2\mu_L + \sigma_L^2\right) \tag{261}$$

Mitzenmacher (2004) pointed out that the lognormal distribution can appear as a straight line over several orders of magnitude in a log-log plot. This can be seen by calculating the logarithm of (260)

$$\ln p(x) \sim -\ln x - \left(\frac{\ln x - \mu}{\sqrt{2}\sigma}\right)^2 = -\frac{1}{2\sigma^2}(\ln x)^2 + \left(\frac{\mu}{\sigma^2} - 1\right)\ln x - \frac{\mu^2}{2\sigma^2}$$

If the variance σ^2 is very large then the $(\ln x)^2$ (first term on the right) becomes small compared to the linear term $\ln x$ (second term on the right). We have already mentioned that the sum of two independent, normally distributed random variables is also normally distributed. From the relationship of lognormal and normal distribution[76] it then follows that the product of two lognormally distributed independent random variables is also lognormally distributed[77]. This shows the connection of lognormal distributions and multiplicative processes which stands in contrast to the connection of normal distributions and additive processes. Interestingly, Mitzenmacher (2004) showed that a multiplicative model leads to a lognormal distribution if no lower bound is given and the lowest classes of an income model can come close to zero. However, the same model can lead to a power law distribution if there is a lower bound or a lowest class of minimum income (called the Champernowne, 1953, model). The question of what processes generate and which conditions lead to a specific distribution is an interesting, but unfortunately too extensive topic at this point. The interested reader is referred to the work of Mitzenmacher (2004) as a detailed introduction to the generative mechanisms producing power law and lognormal distributions and multiplicative models. Finally, we give a summary of some probability density functions in Table 9.

[76] We mentioned earlier that a continuous random variable X is lognormally distributed if the random variable $Y = \log X$ is normally-distributed.

[77] Two lognormally distributed random variables $X_1 = 10^{Y_1}$ and $X_2 = 10^{Y_2}$ have the product: $X_1 X_2 = 10^{Y_1} 10^{Y_2} = 10^{Y_1+Y_2} \Leftrightarrow Y_1 + Y_2 = \log(X_1 X_2)$. Since the sum of two normal distributions $Y = Y_1 + Y_2$ is also normally distributed, we conclude that the product of the two lognormally distributed random variables $X_1 X_2$ is also lognormally distributed.

7.3.5 How to determine the appropriate probability density of complementary cumulative distributions?

Alstott et al. (2014) published a python package "*powerlaw*" that allows to analyze and visualize the probability density functions o different data sets (empirical and theoretical). They summarize three steps to determine possible power law behavior in a very concise manner as: **visualizing**, **fitting** and **comparing**. Clauset et al. (2009) elaborate on the problems of identifying a power law in empirical data: often the slope is approximated by a least-squares linear regression fit to the probability density distribution in a double logarithmic plot. However, this can lead to significant systematic errors as Clauset et al. (2009) point out. They also point out that it is better to use the complementary cumulative distribution function (CCDF) in order to find the correct power law exponent since no binning is needed for the CCDF.

Therefore, we will apply fits to the complementary cumulative distribution functions and proof for either exponential or power law behavior by using a small part of the distribution and push that small range piecewise through the whole range, calculating for each part the parameters of the distributions. If the parameters stay constant over a decent part of the distribution, this will give more evidence that we have found a good fit to the distribution. The fits will be mainly produced with help of gnuplot. Only in some cases we will use the python "*powerlaw*" package of Alstott et al. (2014) that offers the possibility to compare a pure power law with other distributions such as the stretched-exponential or the lognormal distribution.

Table 9: *Summary of the probability density functions $p(x) = Cf(x)$ of a continuous random variable x with normalization constant C; C was derived such that $\int_{x_{min}}^{\infty} Cf(x) = 1$; $\mathrm{erfc}(x)$ is the complementary Gaussian error function that is defined as $\mathrm{erfc}(x) = 1 - \mathrm{erf}(x) = (2/\sqrt{\pi}) \int_{x_{min}}^{\infty} \exp(-t^2)dt$. This table is adopted from Clauset et al. (2009) (their Table 2.1) with slight modifications. Note, that $\widetilde{\lambda} = 1/(\lambda\beta)$.*

Name of distribution	function $f(x)$	Normalization constant C
exponential	$e^{-\lambda x}$	$\lambda e^{\lambda x_{min}}$
power law	$x^{-\alpha}$	$(\alpha - 1)x_{min}^{\alpha-1}$
power law with cut-off	$x^{-\alpha}e^{-\lambda x}$	$\frac{\lambda^{1-\alpha}}{\Gamma(1-\alpha,\lambda x_{min})}$
stretched-exponential	$x^{\beta-1}e^{-\widetilde{\lambda}x^{\beta}}$	$\beta\widetilde{\lambda}e^{\widetilde{\lambda}x_{min}^{\beta}}$
lognormal	$\frac{1}{x}\exp\left(-\frac{(\ln x-\mu)^2}{2\sigma^2}\right)$	$\sqrt{\frac{2}{\pi\sigma^2}}\left[\mathrm{erfc}\left(\frac{\ln x_{min}-\mu}{\sqrt{2}\sigma}\right)\right]^{-1}$
normal	$\exp\left(-\frac{(x-\mu)^2}{2\sigma^2}\right)$	$\sqrt{\frac{2}{\pi\sigma^2}}\left[\mathrm{erfc}\left(\frac{x_{min}-\mu}{\sqrt{2}\sigma}\right)\right]^{-1}$

7.4 Synoptic-scale vortices in NCEP reanalysis data (2.5° res.)

In this chapter, we will focus on the analysis of the number, the geometric properties as well as the intensity (circulation) of the large-scale vortex structures (W_k features) identified in the NCEP II data set.

7.4.1 Number of W_k features (NCEP)

Figure 50 shows the monthly means of the identified numbers of cyclonic and anticyclonic W_k features per time step for the year 1999. Thereby, the temporal resolution of the data is 6 hours. The means were calculated from a 3-days running mean (=12 time steps) over the time series of the identified numbers per time step. The standard deviations of these smoothed time series are in the order of ±2 systems. The three main observations are (cf. Figure 50):

(1) The number of cyclonic W_k features compared to anticyclonic W_k features is of comparable order at every level.

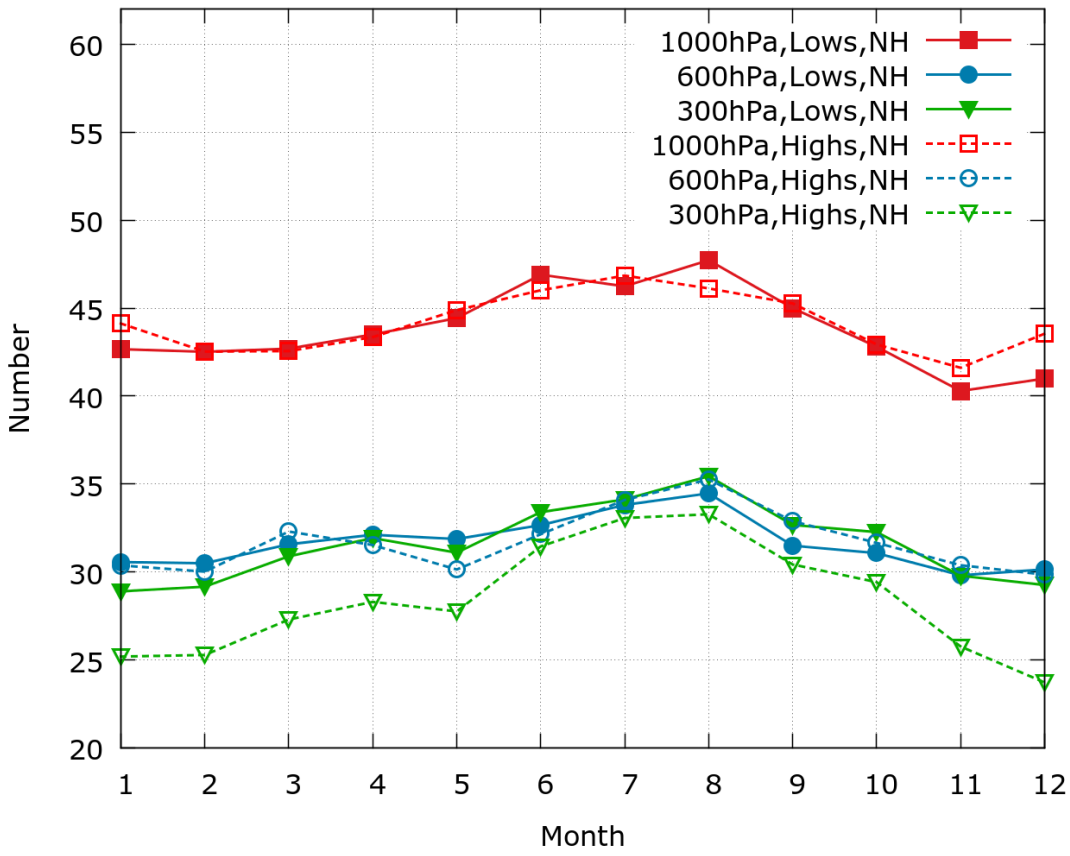

Figure 50: *Monthly mean number of identified W_k features per time step for the year 1999 (NCEP II reanalysis, 30° N–80° N). The standard deviation of each curve is in the order of ±2. Lows denote cyclonic, highs denote anticyclonic systems.*

(2) The number of systems at the 1000 hPa level is significantly larger (≈ 44) than the number at the other two levels (≈ 28 at 300 hPa, Highs and ≈ 32 at the other levels, see Figure 50).

(3) The curves reveal a seasonal behavior with a maximum number observed in the summer months June to August and a minimum in the winter seasons from January to March and November to December.

The largest interseasonal variability is observed for the 300 hPa, Highs ($\Delta N = 9.6$) and for the 1000 hPa, Lows ($\Delta N = 7.4$). Furthermore, the increase of the curves is relatively weak up to the maximum in July and August, while the mean numbers fall off faster afterwards (see especially 1000 hPa, Lows, Figure 50).

7.4.2 Radius of W_k features (NCEP)

We can make some general observations concerning the radii distributions of highs and lows (see Fig. 51):

- ***Number:*** We have already observed that the number of W_k features (Wkf highs and lows) is larger near the ground than at the upper levels. We can now see, that this high number is mainly caused by small systems with radii smaller than 300 km.
- ***Dependence on height:*** In general, larger systems are more frequent in the upper levels.
- ***Dependence on season:*** In winter (December) the systems can become much larger than the systems in summer (June).
- ***Comparison of highs and lows:*** In the NCEP data, the Wkf highs can reach radii considerably larger than the lows.

We applied exponential and power law fits piecewise to the data (Fig. 52). Both models do not fit over the whole data range, but rather in small parts mostly between 500 and 1000 km (Fig. 52). Thereby, the highs better fit the exponential model than the lows. The same applies for the power law model: only over a small range the power law exponent is relatively stable especially in case of the winter highs (Fig. 52d). Although less rapidly between 500 and 1000 km, the power law exponent fitting the lows increase over the whole range which indicates that the power law model is not the best fit to the data (Fig. 52c).
The black lines in Fig. 52 indicate the ranges over which the characteristic parameters of the fits appears to be relatively stable. We observe that the mean radii determined by the exponential fits are subsynoptic ($R < 1000$ km) for both highs and lows, but in general the radii increase with height in most cases (see Fig. 52a,b). The mean radii

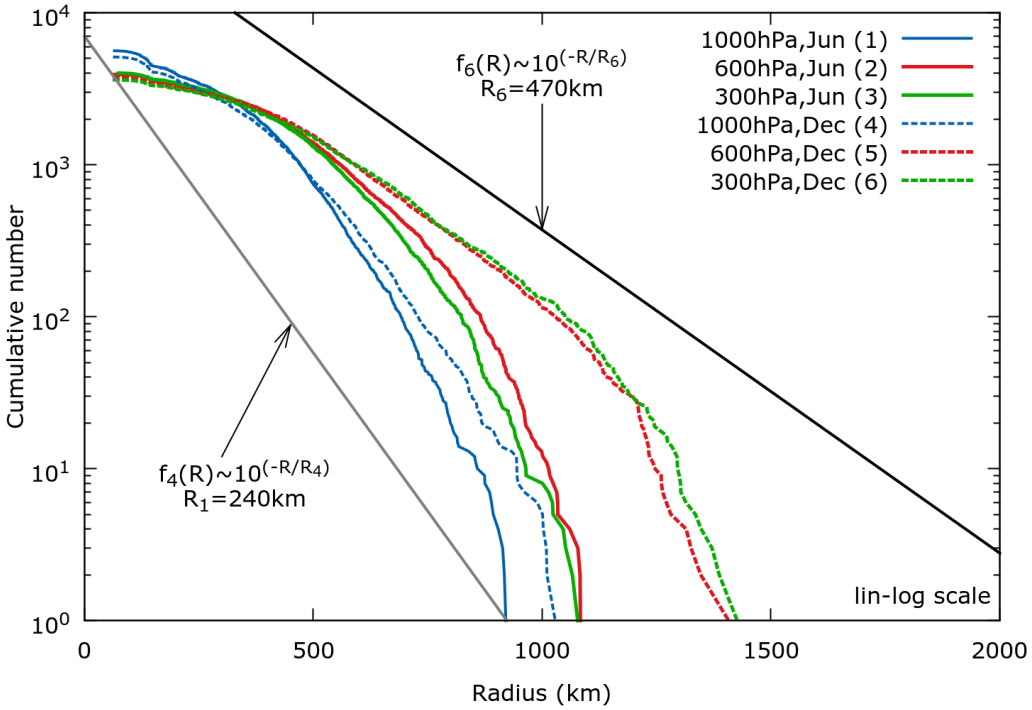

(a) CCD of lows radii, NCEP

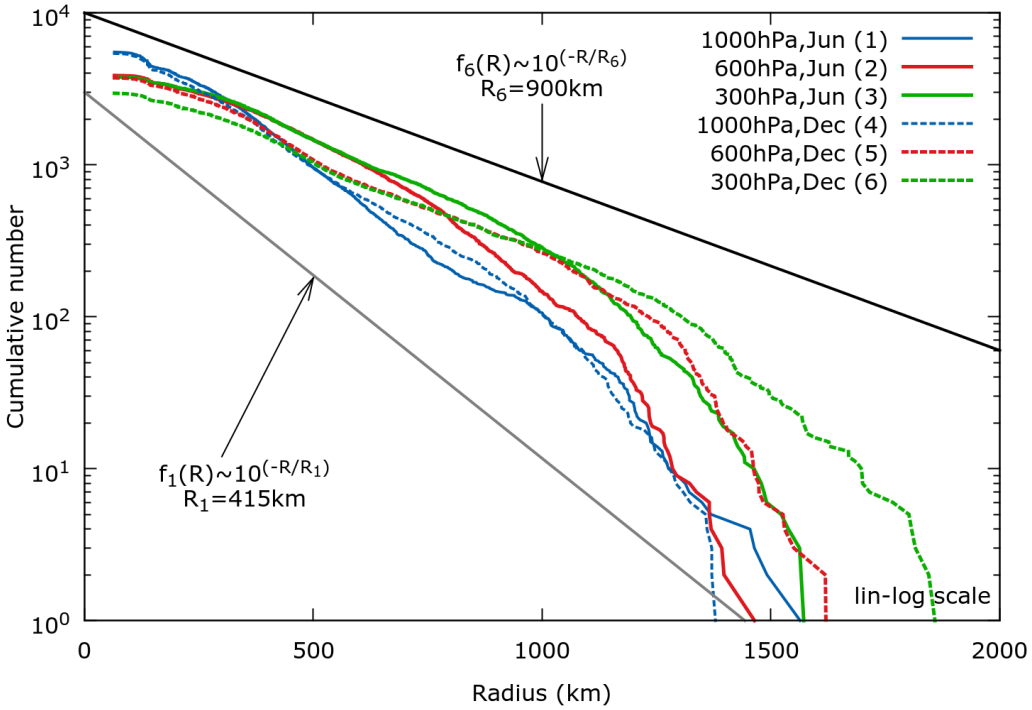

(b) CCD of highs radii, NCEP

Figure 51: *(a),(b): Complementary cumulative distribution (CCD) of the radii of (a) cyclonic ("lows") and (c) anticyclonic ("highs") W_k features identified in the NCEP II data (2.5° resolution): June/December 1999 at the 1000/600/300 hPa levels. The CCDs are not normalized.*

of the lows are considerably smaller than the highs by a factor of about 1.5-2. Since we extract vortex cores, the radii sizes are expected to be subsynoptic and the small mean radii of the lows at the 1000 hPa level (about 200-250 km) are in line with the earlier results (see chapter 6.7.4) as well as with the literature (e.g. Schneidereit et al., 2010, who observed cyclone radii between 300 and 500 km at the 1000 hPa level). We furthermore observe, that the characteristic radii of the summer lows at the 300 hPa level (green solid line in Fig. 52a) are smaller than the radii of the summer lows at the 600 hPa level (red solid line in Fig. 52a). This implies that the depressions in summer are shallower than in winter. In contrast, the mean radii of the winter lows at the 600 and 300 hPa levels (green and red dashed line in Fig. 52a) are approximately

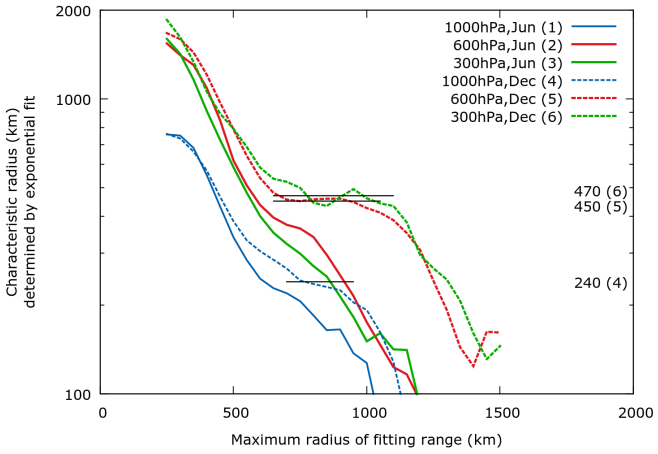

(a) Exponential fit: Characteristic radii of lows

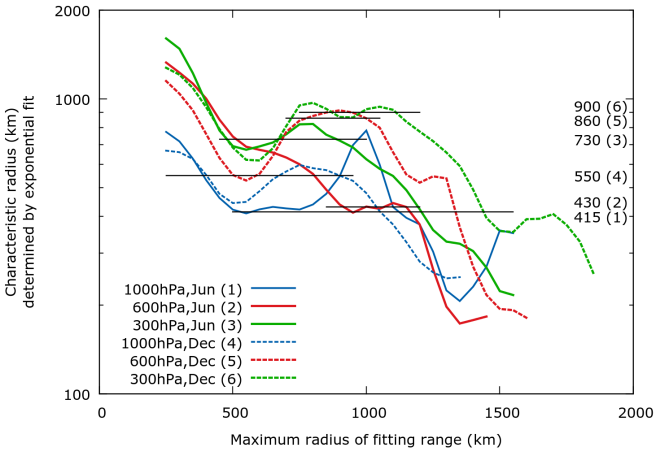

(b) Exponential fit: Characteristic radii of highs

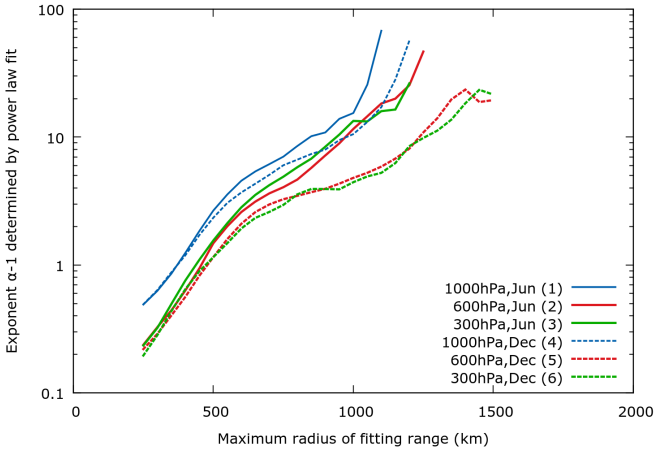

(c) Power law fit: Exponent of lows

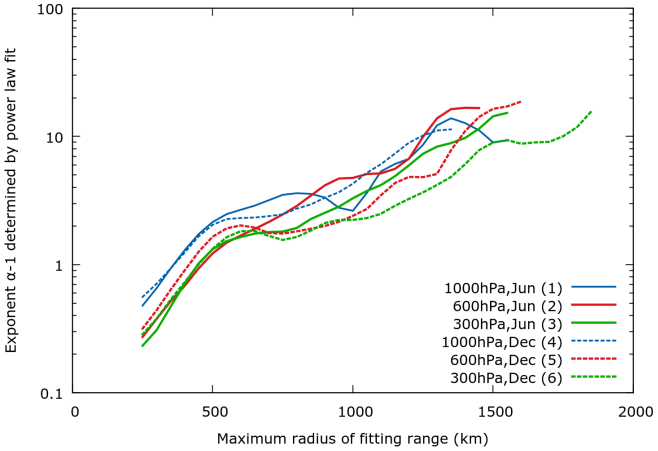

(d) Power law fit: Exponent of highs

Figure 52: *(a),(b): Characteristic parameters (radii) of exponential fits piecewise applied to the CCDs plotted in Fig. 51; (c),(d): Power law exponent of power law fits piecewise applied to the data in Fig. 51. The piecewise fits cover a range of 200 km starting every 50 km. Axis of abscissae gives the maximum radius of the particular fitting ranges. Black lines and corresponding labels indicate a range over which the characteristic parameters determined by the fit are relatively stable.*

Table 10: ***Stretched-exponential fits (radius, NCEP):*** *Characteristic parameters λ, β of the stretched-exponential fits CCDF $\sim \exp(-\widetilde{\lambda} x^{\beta})$ with $\widetilde{\lambda} = 1/(\lambda\beta)$ applied to the NCEP radius data plotted in Fig. 51 with a starting value of 200 km.*

		June				December		
System, Level	N_{tot}	N/N_{tot}	β	$\lambda\beta$ (km$^{\beta}$)	N^*_{tot}	N^*/N_{tot}	β^*	$\lambda^*\beta^*$ (km$^{\beta^*}$)
H,1000	5521	0.71	1.39	240	5398	0.67	1.29	250
H, 600	3873	0.83	1.81	290	3733	0.82	1.24	320
H, 300	3780	0.86	1.59	330	2955	0.83	1.27	360
L,1000	5639	0.70	2.46	160	5118	0.71	2.11	180
L, 600	3930	0.86	2.48	200	3750	0.86	2.12	250
L, 300	4011	0.86	2.60	190	3626	0.87	2.00	270

equal which might indicate that the systems are vertically well-organized throughout the whole troposphere.

In case of the power law fit, the exponent is only relatively stable in case of the highs and in ranges between 500 and 1000 km. This is less than one order in magnitude. The exponent is smaller in the upper levels (green and red lines in Fig. 52d) compared to the 1000 hPa level (blue lines). Furthermore, the exponents are slightly smaller in winter compared to the summer. This is in accordance with the earlier observation that the systems in the upper levels and in winter show larger radii than near the ground or in summer. However, both models — exponential as well as power law model — fail in describing the whole data set. Therefore, we also applied several other models to the data by applying the python powerlaw package of Alstott et al. (2014). We decided to compare the results obtained by the stretched-exponential model since it seems to fit well in most of the data sets and parameters we aim to analyze. Since we want to compare different data sets and conditions, we decided to use a fixed starting value that covers the majority of the data and compare the obtained results rather than searching for the best fit[78]. The results are summarized in Table 10. In all cases, the exponents β are larger than 1. Hence, the distributions decay faster than an ordinary exponential distribution. Except of the highs in June whose β ranges between 1.4 to 1.8, the β are nearly equal over height with about 1.3 (highs, December); 2.5 (lows, June) and 2.1 (lows, December). The variation of the exponents with respect to the height levels is about 0.1 and therefore only slight. The interseasonal difference of the exponents is larger (about 0.3 to 0.4) with faster decay rates in June.

[78]The powerlaw package by Alstott et al. (2014) offers parameters such as the Kolmogorov-Smirnov distance to quantify the goodness of fit. The Kolmogorov-Smirnov distance is equal to the largest vertical distance between to sets of data, e.g. between the applied model and the observational data.

7.4.3 Circulation of W_k features (NCEP)

Likewise to the radius distributions, the circulation distributions depend on the height level as well as on the season (see Fig 53a,b). Thereby, the circulation magnitudes increase with height and can reach higher values in December compared to June. The characteristic (mean) circulation magnitudes of the highs determined by an exponential fit to the data are on average twice the magnitudes of the lows at the respective levels (see Fig. 54a,b). Furthermore, we observe that the exponential fit applies well to the tail of the distribution. Thereby, the cyclonic systems with magnitudes larger than $10^7\,\mathrm{m}^2/\mathrm{s}$ cover more than one order in magnitude, while the exponential fit applied to the circulation magnitudes of the highs fits not so well (Fig. 54a,b). Interestingly, the power law model seems to fit for lower circulation magnitudes around $10^6\,\mathrm{m}^2/\mathrm{s}$ especially for the low pressure systems which can be seen by the relatively stable values for the exponents in Fig. 54c,d.
The stretched-exponential fits reveal exponents that lie between 0.6 and 0.9 in all cases with smaller β at the 1000 hPa level ($\beta \approx$ 0.6-0.7) and higher values at the upper levels ($\beta \approx$ 0.8-0.9, see Table 11). Only the December highs have smaller $\beta \approx 0.6$ at all levels. While the exponents are almost equal for the systems at the upper levels, the reference scales $\lambda\beta$ grow by a factor of about 2.5 from the 1000 hPa level to the 600 hPa level and further almost double from the 600 hPa level to the 300 hPa level where the reference scales are the largest.

Table 11: ***Stretched-exponential fits (circulation, NCEP):*** *Characteristic parameters λ, β of the stretched-exponential fits CCDF $\sim \exp(-\widetilde{\lambda}x^{\beta})$ with $\widetilde{\lambda} = 1/(\lambda\beta)$ applied to the circulation magnitudes data plotted in Fig. 53 with a starting value of $5 \cdot 10^5\ m^2/s$.*

		June				December		
System, Level	N_{tot}	N/N_{tot}	β	$\lambda\beta$ $(\mathrm{m}^2/\mathrm{s})^{\beta}$	N^*_{tot}	N^*/N_{tot}	β^*	$\lambda^*\beta^*$ $(\mathrm{m}^2/\mathrm{s})^{\beta^*}$
H,1000	5521	0.86	0.67	$0.98{\cdot}10^7$	5398	0.87	0.58	$1.03{\cdot}10^7$
H, 600	3873	0.95	0.78	$2.67{\cdot}10^7$	3733	0.95	0.63	$2.78{\cdot}10^7$
H, 300	3780	0.98	0.76	$5.46{\cdot}10^7$	2955	0.97	0.60	$6.36{\cdot}10^7$
L,1000	5639	0.86	0.73	$0.96{\cdot}10^7$	5118	0.87	0.63	$1.25{\cdot}10^7$
L, 600	3930	0.95	0.85	$2.60{\cdot}10^7$	3750	0.95	0.81	$3.52{\cdot}10^7$
L, 300	4011	0.98	0.88	$4.22{\cdot}10^7$	3626	0.98	0.83	$5.83{\cdot}10^7$

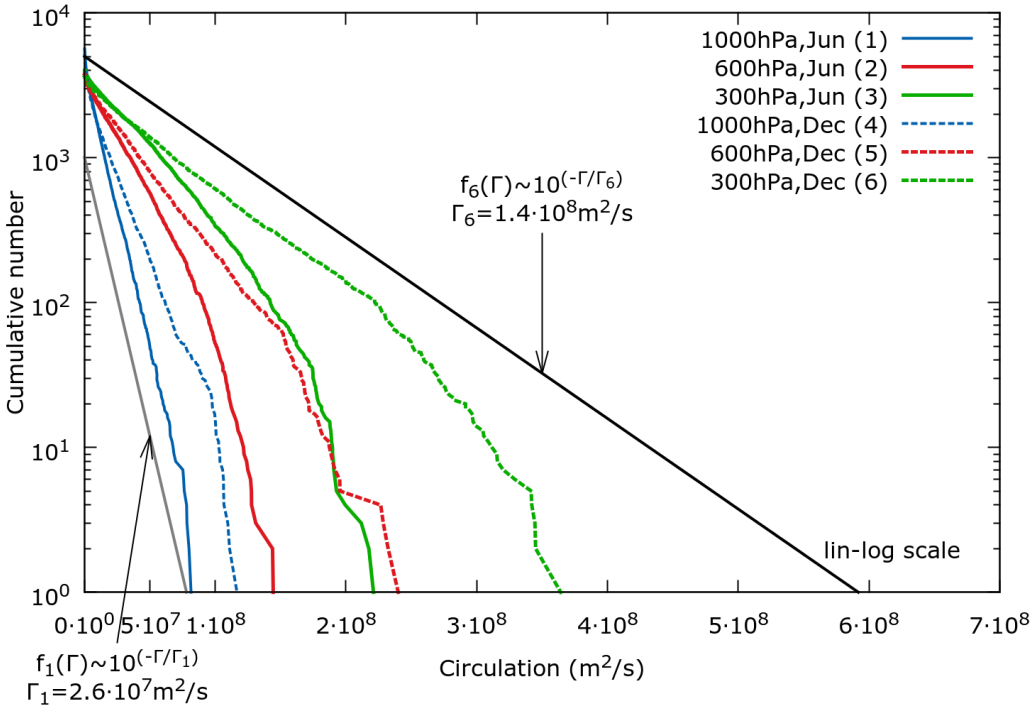

(a) CCD of circulation of lows, NCEP

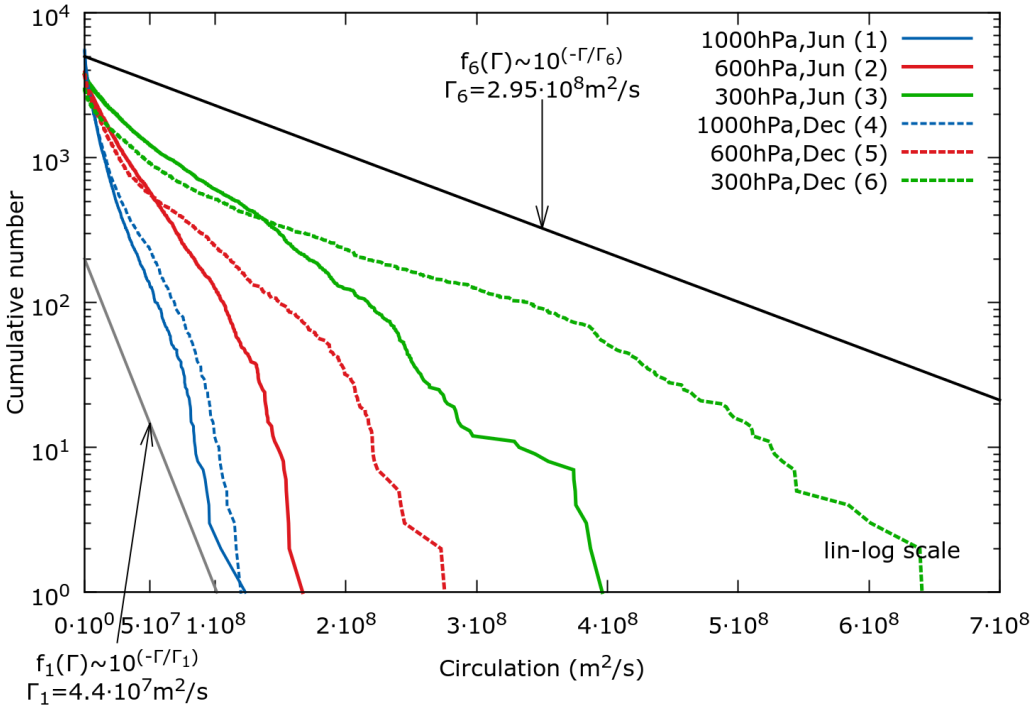

(b) CCD of circulation magnitudes of highs, NCEP

Figure 53: *(a),(b): Complementary cumulative distribution (CCD) of the circulation magnitudes (absolute values) of (a) cyclonic ("lows") and (c) anticyclonic ("highs") W_k features identified in the NCEP II data (2.5° resolution): June/December 1999 at the 1000/600/300 hPa levels.*

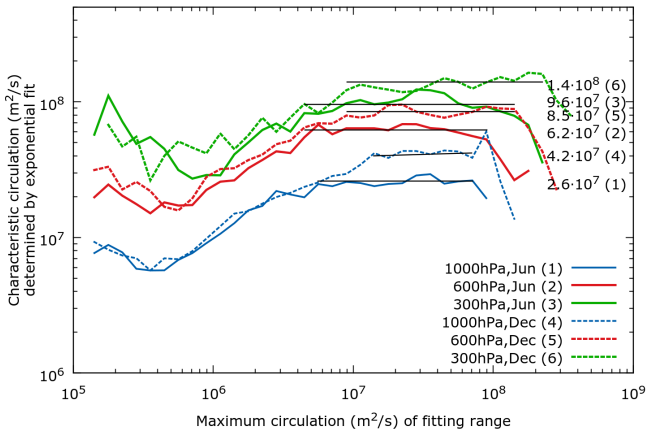

(a) Characteristic circulation of lows

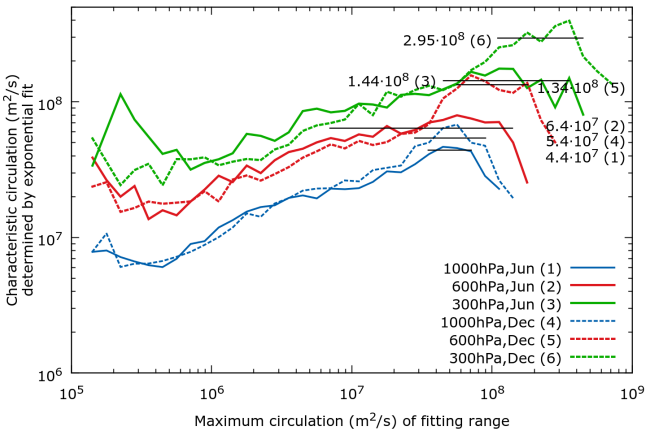

(b) Characteristic |circulation| of highs

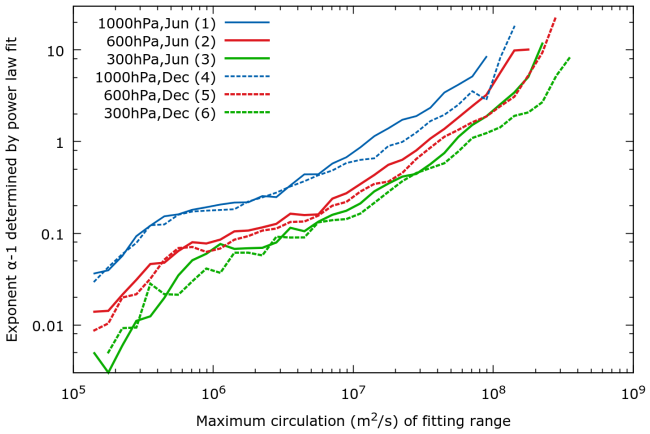

(c) Power law exponent of lows circulation

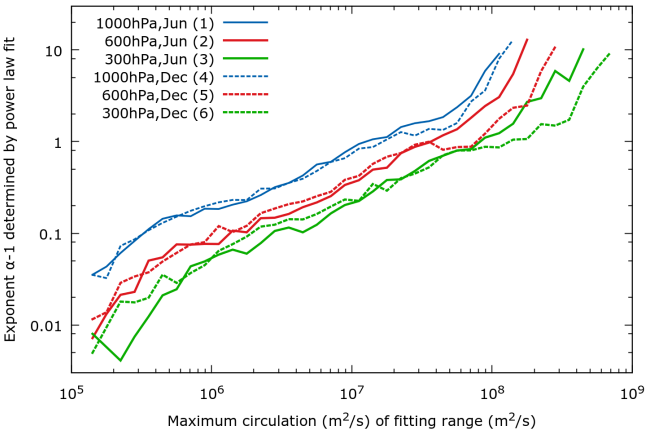

(d) Power law exponent of highs |circulation|

Figure 54: *Circulations of cyclonic ("lows") and anticyclonic ("highs") W_k features identified in the NCEP II data (2.5° resolution): June/December 1999 at the 1000/600/300 hPa levels. (a),(b): Characteristic parameters (circulation magnitudes) of exponential fits and (c),(d): power law exponents of the power law fits applied to the CCDs plotted in 53a,b, respectively. The (nonlinear) fitting range is given by* $[10^{5+0.1\cdot t} : 10^{5.15+0.1\cdot t}]$ *m^2/s for t=0,1,2,...; axis of abscissae gives the maximum circulation magnitudes of the particular fitting ranges. Black lines and corresponding labels indicate a range over which the parameters determined by the fit are relatively stable.*

7.5 Meso-scale vortices in CFSR reanalysis data (0.5° res.)

In the following, we will analyze the vortices identified in the CFSR data in the same manner as the NCEP data concerning their numbers, radii and circulations.

7.5.1 Number of W_k features (CFSR)

The number of the W_k features identified in the CFSR data strongly decreases with height (Table 12). There is also a seasonal dependence: The number of W_k features at the 1000 hPa level is higher in December compared to June while the identified W_k features (highs and lows) are more numerous in June at the 600 and 300 hPa level. The high number of W_k features near the ground is caused by a high number of small-scale systems (see chapter 7.5.2). With height the areas of the W_k features increase significantly (see the example in Fig. 55). Note, that a W_k feature in contrast to the single center definition can include several vorticity centers and the areas grow together due to smoother gradients.

7.5.2 Radius of W_k features (CFSR)

We plotted the complementary cumulative distributions functions of the radii of highs and lows in Fig. 56. Since there are so many small systems, we decided to plot the range up to 200 km (lows)/300 km(highs) with double-logarithmic axes. The data in this range definitely not follows an exponential distribution but rather a distribution with a fatter tail. Note, how the black and gray curves that describe exponential distributions cut through the data in Figure 56. Similar to the NCEP data, there is a clear dependence on the height level with more numerous small systems ($R < 100$ km) at the 1000 hPa level. The number of large systems with radii $R > 200$ km increase with height. There is no seasonal dependence at the 1000 and 600 hPa levels: the distributions are almost equal (see Fig. 56a,b). Only the systems, highs as well as lows, at the 300 hPa level show a clear seasonal dependence at the tail of the distributions with larger systems

Table 12: *Average number of identified W_k features in the CFSR data per timestep (per hour) in different height levels for June and December 1999.*

	Highs		Lows	
Level	June	December	June	December
1000 hPa	920	1000	780	830
600 hPa	590	510	500	430
300 hPa	320	220	230	180

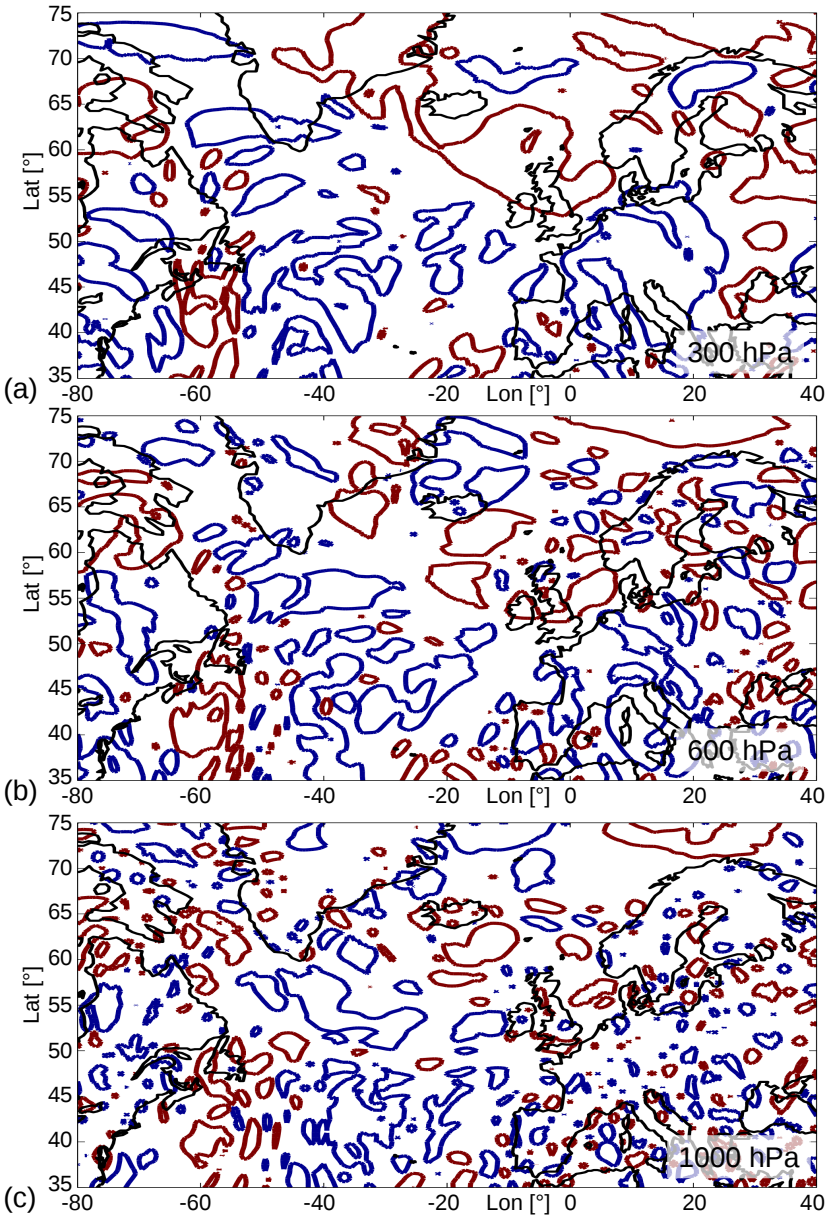

Figure 55: *W_k features identified in different levels in the CFSR data at 3 December 1999 12 UTC (Anatol case): (a) 300 hPa; (b) 600 hPa; (c) 1000 hPa levels. Red/blue lines indicate the $W_k = +1/W_k = -1$ contour and W_k features are enclosed by these contours.*

occurring in December.

We observe that the radii distributions of highs and lows are well described with the exponential model over the (sub)synoptic range between about 200 and 600 km (Fig. 57a,b). In particular, the 300 hPa December lows and highs even fit well the exponential model up to radii of about 1000 km (lows) and 1200 km (highs), respectively. However, the exponential model seems not to fit so well in the lowest radii ranges and in the upper tails as can be seen by the strong increase and decrease, respectively, of the characteristic parameter of the exponential fits (Fig. 57a,b). The power law model does not fit well in

the upper tails either, however, in the lowest radii ranges the exponents of the piecewise applied power law fits show a slighter increase and even a constant behavior up to about 400 km for the highs in 1000 hPa in June and December (Fig. 57c,d).
For comparison reasons, we applied the stretched-exponential model to the data that is larger than $R \geq 60$ km which is about the range where the distributions in Fig. 56a,b approximately start to decay. This range covers about 50% of the upper level data of the highs and lows, but only about 25% at the 1000 hPa level indicating that there are much more smaller systems than in the upper levels (see Table 13). We observe that the exponents β as well as the reference scale $\lambda\beta$ of the stretched-exponential fits increase with height from $\beta \approx 0.25$ at the 1000 hPa level to $\beta \approx 0.6$-0.8 at the 300 hPa level. Only the lows show a slight variation of the exponents depending on the season while there is no seasonal dependence in case of the highs. The closer the exponents are to zero the fatter is the tail of the distribution. As we have already noted, this applies especially to the systems at the 1000 hPa level, in particular to the highs (Fig. 57d). Otherwise, the closer the exponent is to one, the distribution is rather described by en exponential distribution which better fits at the 300 hPa level (especially for the lows, see Table 13 and Fig. 57a).

7.5.3 Circulation of W_k features (CFSR)

The circulations identified in the CFSR data cover several orders in magnitude starting with about $10^4\,\mathrm{m}^2/\mathrm{s}$ up to about $10^8\,\mathrm{m}^2/\mathrm{s}$ (Fig. 58). The observation concerning the *numbers* of small circulations (more numerous at the 1000 hPa level), concerning the *height dependence* (increasing circulations with height), with respect to the *seasonal dependence* (only occurs at the 300 hPa level with larger circulations in December

Table 13: ***Stretched-exponential fits (radius, CFSR):*** *Characteristic parameters λ, β of the stretched-exponential fits CCDF $\sim \exp(-\widetilde{\lambda} x^{\beta})$ with $\widetilde{\lambda} = 1/(\lambda\beta)$ applied to the CFSR radius data plotted in Fig. 56 with a starting value of 60 km.*

	June 1999				December 1999			
System, Level	N_{tot}	N/N_{tot}	β	$\lambda\beta$ [km$^{\beta}$]	N^*_{tot}	N^*/N^*_{tot}	β^*	$\lambda^*\beta^*$ [km$^{\beta^*}$]
H,1000	658816	0.26	0.21	0.015	743080	0.23	0.21	0.011
H, 600	424028	0.43	0.49	22	375716	0.41	0.52	31
H, 300	232577	0.54	0.62	74	165884	0.49	0.55	77
L,1000	559808	0.28	0.42	3.4	620005	0.25	0.53	10
L, 600	357286	0.43	0.54	27	322361	0.44	0.66	54
L, 300	167098	0.55	0.79	95	137239	0.52	0.74	127

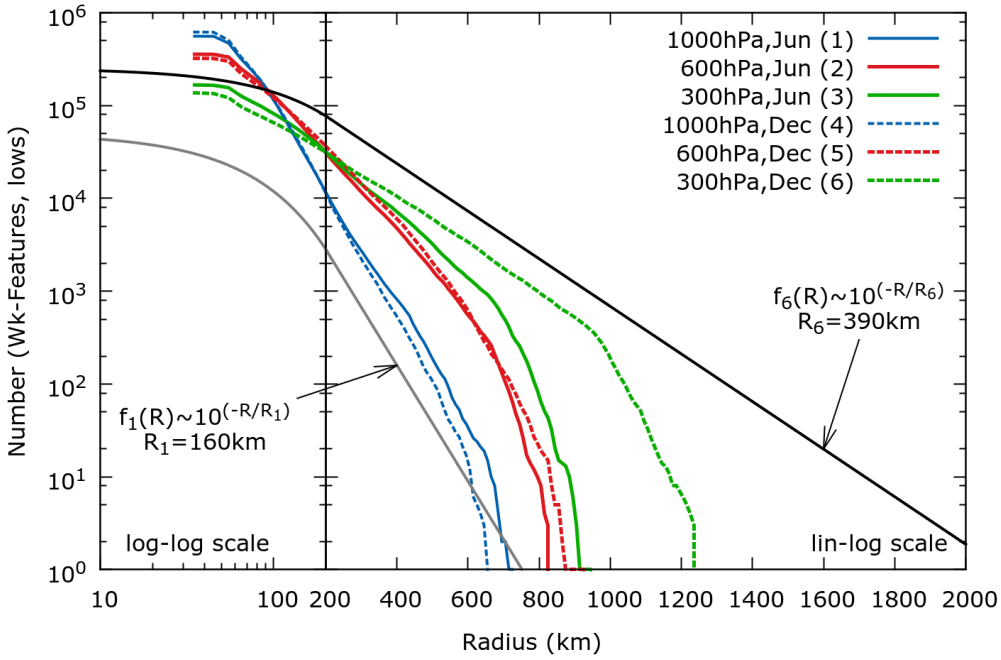

(a) CCD of radius of lows, CFSR

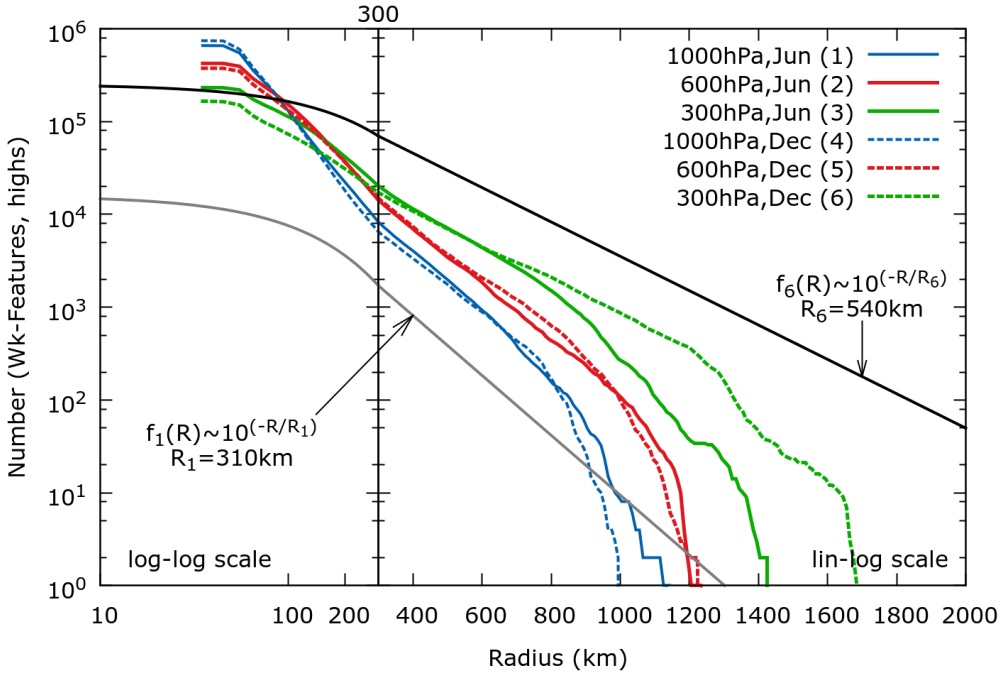

(b) CCD of radius of highs, CFSR

Figure 56: *(a),(b): Complementary cumulative distribution (CCD) of the radii of (a) cyclonic ("lows") and (c) anticyclonic ("highs") W_k features identified in the CFSR data (0.5° resolution): June/December 1999 at the 1000/600/300 hPa levels.*

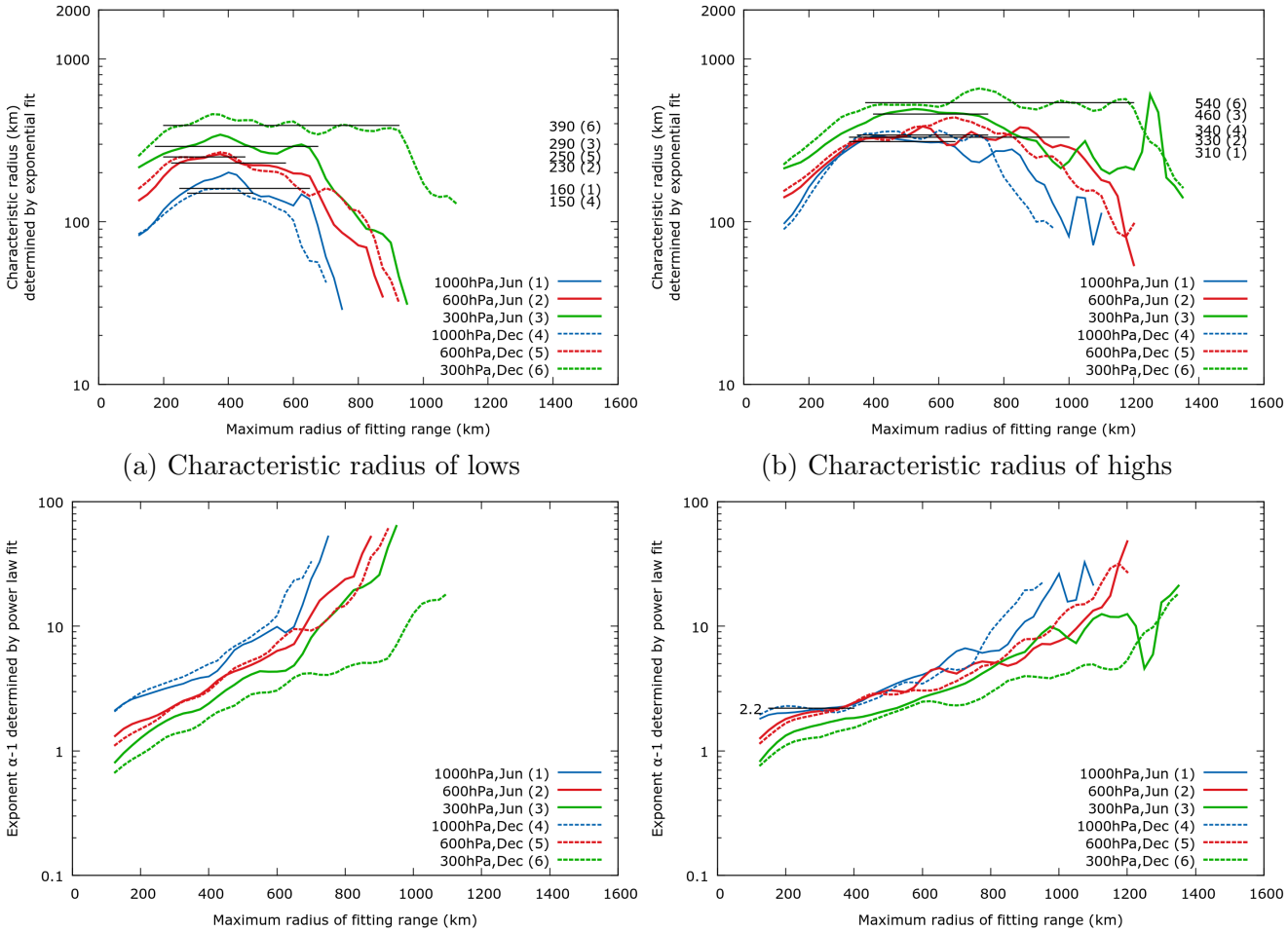

(a) Characteristic radius of lows

(b) Characteristic radius of highs

(c) Power law exponent of lows radius

(d) Power law exponent of highs radius

Figure 57: *Analysis of radii of cyclonic ("lows") and anticyclonic ("highs") W_k features identified in the CFSR data (0.5° resolution): June/December 1999 at the 1000/600/300 hPa levels. (a),(b): Characteristic parameters (radii) of exponential fits and (c),(d) power law exponents of power law fits, applied to the CCDs plotted in 56a,b, respectively. The fitting range is given by* $[25 \cdot t : 100 + 25 \cdot t]$ *m for t=1,2,...; axis of abscissae gives the maximum radius of the particular fitting ranges. Black lines and corresponding labels indicate a range over which the characteristic parameters determined by the fits are relatively stable.*

compared to June) and concerning a *comparison of highs and lows* (highs tend to have higher circulations in the tail of the distribution than the lows) are similar to the results observed for the CFSR radii.

The piecewise exponential fits show that the exponential model can only be applied to the tail of the distributions of highs and lows (Fig. 59 a,b). The exponential model might fit for the smallest circulations as well, however the identification at this small range might fail in identifying all systems. The piecewise power law fits of highs and lows at all heights lead to nearly constant exponents in the range of about $10^5 - 10^6\,\mathrm{m}^2/\mathrm{s}$. Additionally, except for the 300 hPa lows, the power law exponents are relatively stable in the range of about $10^6 - 10^7\,\mathrm{m}^2/\mathrm{s}$ with a different, larger value of the exponents (see

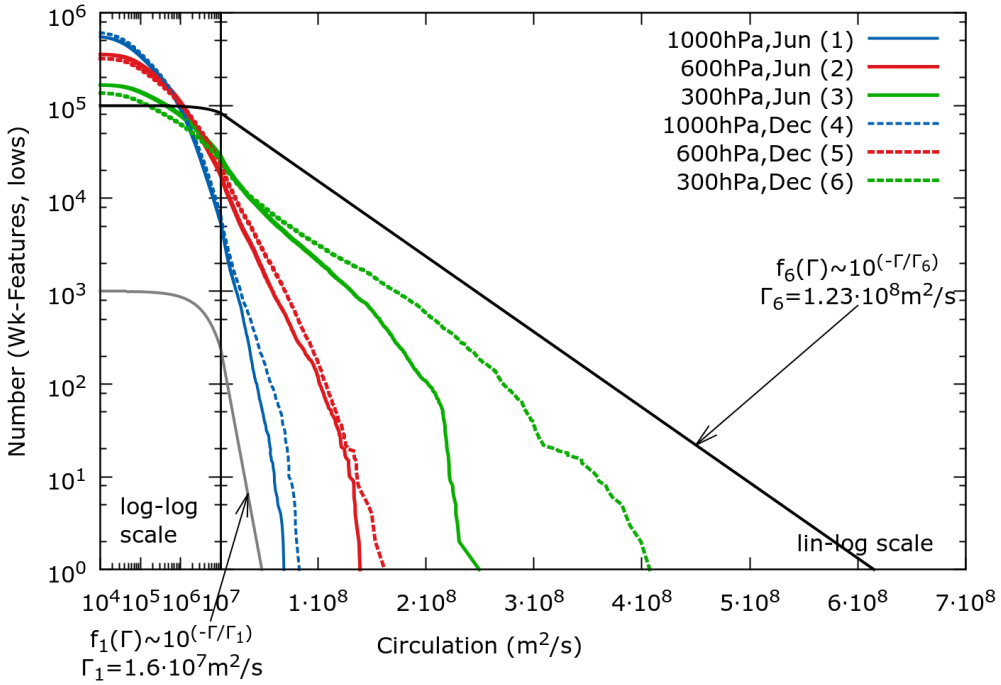

(a) CCD of circulation of lows, CFSR

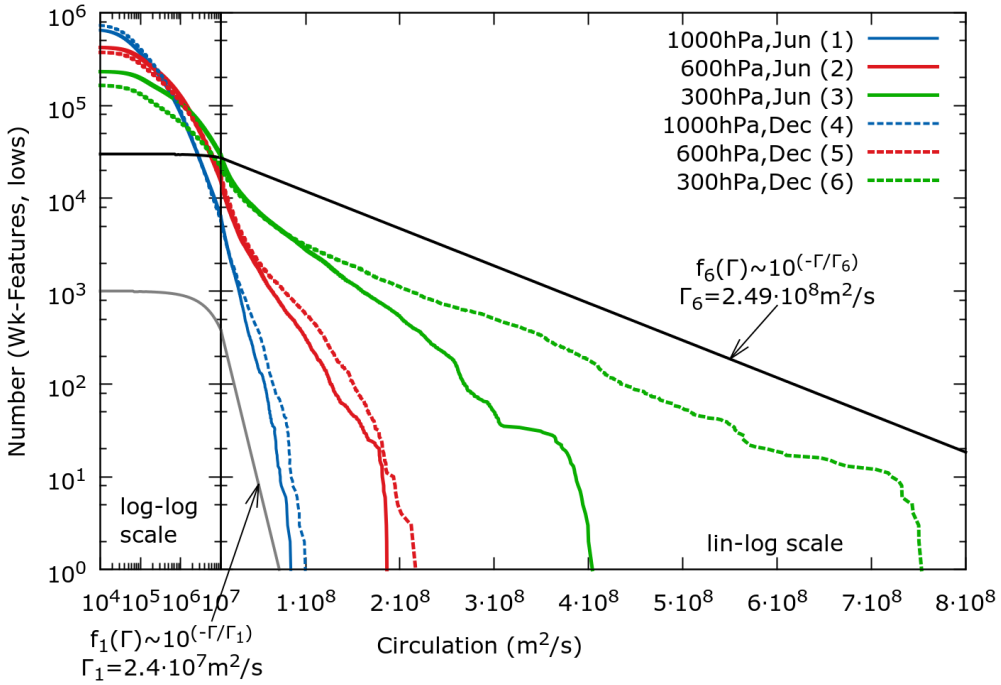

(b) CCD of |circulation| of highs, CFSR

Figure 58: *(a),(b): Complementary cumulative distribution (CCD) of the circulation magnitudes of (a) cyclonic ("lows") and (c) anticyclonic ("highs") W_k features identified in the CFSR data (0.5° resolution): June/December 1999 at the 1000/600/300 hPa levels.*

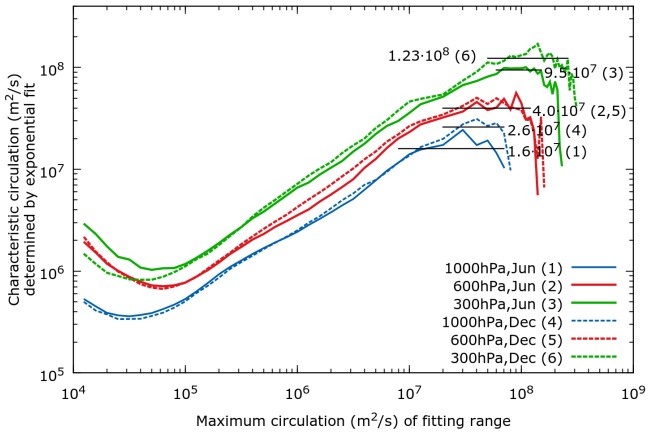

(a) Characteristic circulation of lows

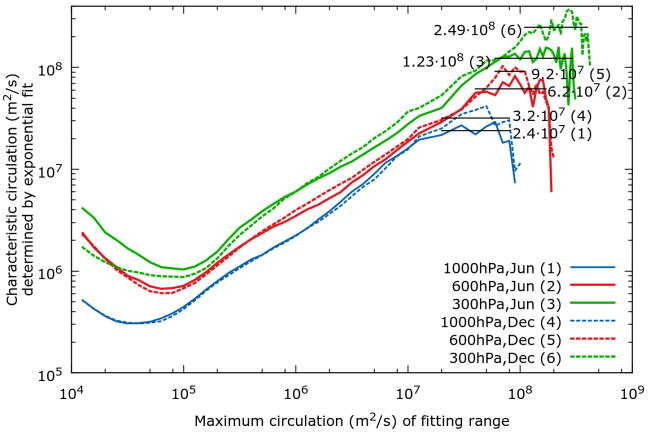

(b) Characteristic |circulation| of highs

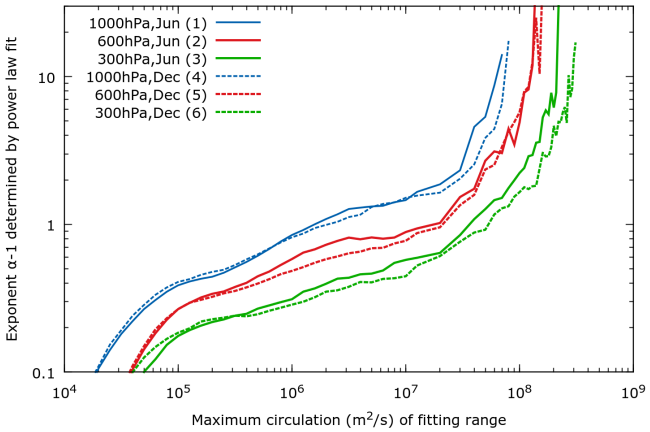

(c) Power law exponent of lows circulation

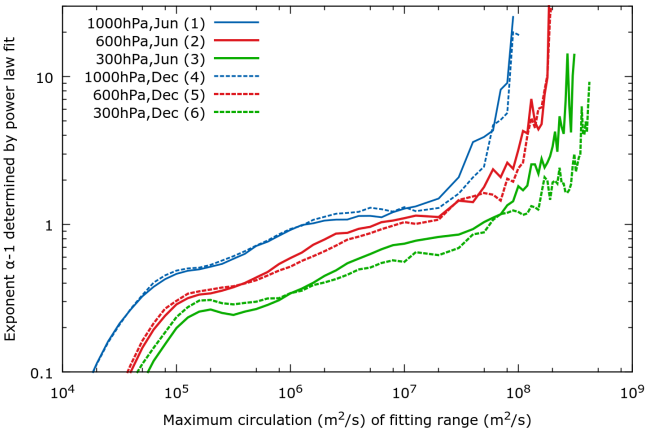

(d) Power law exponent of highs |circulation|

Figure 59: *Analysis of circulation magnitudes of cyclonic ("lows") and anticyclonic ("highs") W_k features identified in the CFSR data (0.5° resolution): June/December 1999 at the 1000/600/300 hPa levels. (a),(b): Characteristic parameters (circulation magnitudes) of exponential fits and (c),(d) power law exponents of power law fits, applied to the CCDs plotted in 58a,b, respectively. The (nonlinear) fitting range is given by $[10^{4+0.1\cdot t} : 10^{4.1+0.1\cdot t}]$ m for t=0,1,2,...; axis of abscissae gives the maximum radius of the particular fitting ranges. Black lines and corresponding labels indicate a range over which the characteristic parameters determined by the fits are relatively stable.*

Figure 59 c,d).

For comparison reasons, we also applied stretched-exponential fits to the data (see Table 14). These fits show for all distributions independent of season, height and vortex type approximately the same (stretched-exponential) exponent with a value of about $\beta \approx 0.3$ which is close to zero. Hence, the distributions have rather fat tails. However, the reference scales $\lambda\beta$ that characterize the stretched-exponential distributions show a clear dependence on height where the largest values occur at the 300 hPa level. These reference scales of circulation increase with height. The $\lambda\beta$ values are in general smaller in December compared to June while the exponents β are slightly smaller in December compared to June, too.

Table 14: ***Stretched-exponential fits (circulation, CFSR):*** *Characteristic parameters λ, β of the stretched-exponential fits $CCDF \sim \exp(-\widetilde{\lambda} x^{\beta})$ with $\widetilde{\lambda} = 1/(\lambda\beta)$ applied to the circulation magnitudes of the CFSR data plotted in Fig. 58 with a starting value of $5 \cdot 10^4\ m^2/s$.*

		June				December		
System, Level	N_{tot}	N/N_{tot}	β	$\lambda\beta$ $(m^2/s)^{\beta}$	N^*_{tot}	N^*/N_{tot}	β^*	$\lambda^*\beta^*$ $(m^2/s)^{\beta^*}$
H,1000	658816	0.75	0.27	$0.05 \cdot 10^6$	743080	0.75	0.27	$0.04 \cdot 10^6$
H, 600	424028	0.90	0.33	$0.49 \cdot 10^6$	375716	0.90	0.28	$0.30 \cdot 10^6$
H, 300	232577	0.95	0.30	$1.57 \cdot 10^6$	165884	0.91	0.22	$0.45 \cdot 10^6$
L,1000	559808	0.78	0.34	$0.21 \cdot 10^6$	620005	0.76	0.30	$0.13 \cdot 10^6$
L, 600	357286	0.90	0.31	$0.50 \cdot 10^6$	322361	0.90	0.28	$0.43 \cdot 10^6$
L, 300	167098	0.93	0.30	$2.30 \cdot 10^6$	137239	0,90	0.27	$1.97 \cdot 10^6$

The small values of β (close to zero) furthermore imply that the distributions rather resemble power law distribution than exponential ones. This is in accordance with the relatively stable exponents that were observed in the piecewise power law fits as we have already mentioned (see Figure 59c,d). Subsequently, we want to find out what happens if we further increase the horizontal resolutions. However, since there is no finer-resolved reanalysis data set available, we will study simulated data in the following section.

7.6 Convective-scale vortices in WRF's simulated supercells (1 km res.)

The case of convective scale vortices is of special interest not only with respect to the statistical properties of the vortices. It is rather a testbed for the ability of the W_k-method to identify the vortex structures. So far to our knowledge, no publication exists that deals with the identification of vortices on different scales with help of a uniform method. Vorticity for example has a different magnitude on the convective scale compared to the synoptic scale. Furthermore, pressure perturbations are small on the convective scale and might be blurred by a larger-scale background gradient. Therefore, we will first present some results for different time steps and height levels.
In general, convective storms are categorized in three storm types: short-living, isolated single cells; multicells composed of several single cells; and supercells that are characterized by a persisting (>60 min), rotating updraft moving to the right or left of the mean wind (Weisman and Klemp, 1984). Studies showed that the storm type depends on the environmental conditions. While supercells prefer environments with moderate to high buoyancy and high vertical wind shear, multicells rather prefer high buoyancy and low to moderate shear (see Weisman and Klemp, 1984, and references therein). Vertical shear influences the storm organization in two ways (Markowski and Richardson, 2011): (1) On the one hand, the vertical shear controls the interference of the updraft with the downdraft, outflow and precipitation. In low-shear environments the rain-cooled outflow can cut off the relatively warm airflow into the supercell that feeds the convection while this cut-off process is hindered in high-shearing environments; (2) On the other hand, the shear has influence on dynamic vertical pressure gradients that control the lifting of air along the gust front. In weak-shear environments the lifting is weak too, the initiation of new cells fails. As a result, only isolated, short-lived single cells occur.
From the literature we know what to expect from the simulations: Weisman and Klemp (1982, 1984) analysed the appearance of deep moist convection in purely linear shear and in directional shear environments for several shear and buoyancy magnitudes. Their results for purely linear or unidirectional shear cases showed that weak shear leads to short-lived single cells, low to moderate shear to multicells and moderate to high shear leads to splitting storms and supercells (Weisman and Klemp, 1982). Furthermore, the modelled convection in these purely linear shear cases is symmetric with respect to the shear axis. In the case of clockwise curved hodographs, i.e. in directional shear environments, the supercell convection develops on the right flank and multicellular convection is favoured on the left flank of the developing storm systems (Weisman and Klemp, 1984). The higher the mean shear is, the larger is the deviation of the right-moving supercell from the mean motion of the storm system. Furthermore, the results found in Weisman and Klemp (1982) concerning the low to high shear environments are also confirmed for directionally varying shear environments. However, in directional shear,

the symmetry observed in the unidirectional shear cases is broken and the supercellular structures occur on the right flank while multicells preferably occur on the left flank. This observation is reversed for counterclockwise hodographs.

The motion of a supercell is mainly caused by linear and nonlinear dynamic pressure perturbations. This can be seen from the calculation of the divergence of the equation of motion neglecting the Coriolis force terms. Thereby, the velocity gradient tensor enters the equations and the contributions of the stain-rate tensor and the rotation tensor become important. An explicit derivation can be found in e.g. Markowski and Richardson (2011, chapter 8.4.5). Following Markowski and Richardson (2011) we will give a short explanation in the following. The nonlinear dynamic forcing stems from the fact that a vertical vorticity extremum is associated with a low pressure perturbation. As a horizontal vortex line is tilted to the vertical due to the updraft, the vertical vorticity extrema will be arranged on the flanks of that updraft in a linear shear environment (characterized by a straight hodograph). Hence, low pressure perturbations occur collocated with the vorticity extrema. This induces a (symmetric) split of the storm system. Thereby, the cyclonic system moves to the right and the anticyclonic system to the left. This especially applies to the early stages of the supercell's life cycle. The linear contribution to the dynamic pressure perturbation stems from the interaction of the supercell with the environmental shear. It can be shown that in an environment characterized by a clockwise curved hodograph an upward-directed vertical pressure gradient exists on the right flank of the updraft and a downward-directed vertical pressure gradient exists on its left flank. As a result, the right-moving storm is enhanced while the left-moving system is suppressed. If the hodograph is curved counterclockwise, the opposite is true and the left-mover becomes stronger. The stronger the curvature of the hodograph is, the stronger are the enhancement and the suppression, respectively.

The evolution of the convective cells of the doubled-speed simulation is plotted in Fig. 60 for different times ($t = 45, 90, 120$ min) and height levels ($z \approx 0.5, 3.5, 7.5$ km). We observe that most of the cells move with the background stream (e.g. near the ground, the cells move predominantly to the southwest as in Fig. 60g-i while they move to the northeast in the upper levels as in Fig. 60a-f) The cells trigger the initiation of more cells during their development along an outflow boundary. The convective cells are connected to vortices of positive and negative circulations probably because the initially horizontal vorticity is tilted into vertical vorticity along with the uplifting and descending air in the cells.

The cell with the highest intensity (i.e. the highest circulation) forms as one of the first cells. It is a right-moving supercell that persist until the end of the simulation (see black boxes in Fig. 60, the supercell can be observed in the upper levels, but not near the ground). The thin red and blue lines indicate the tracks of the cells. These tracks were formed by connecting appropriate cells in successive time steps (see chapter 6.5). In the beginning of the simulation the supercell is not tracked properly. A reason

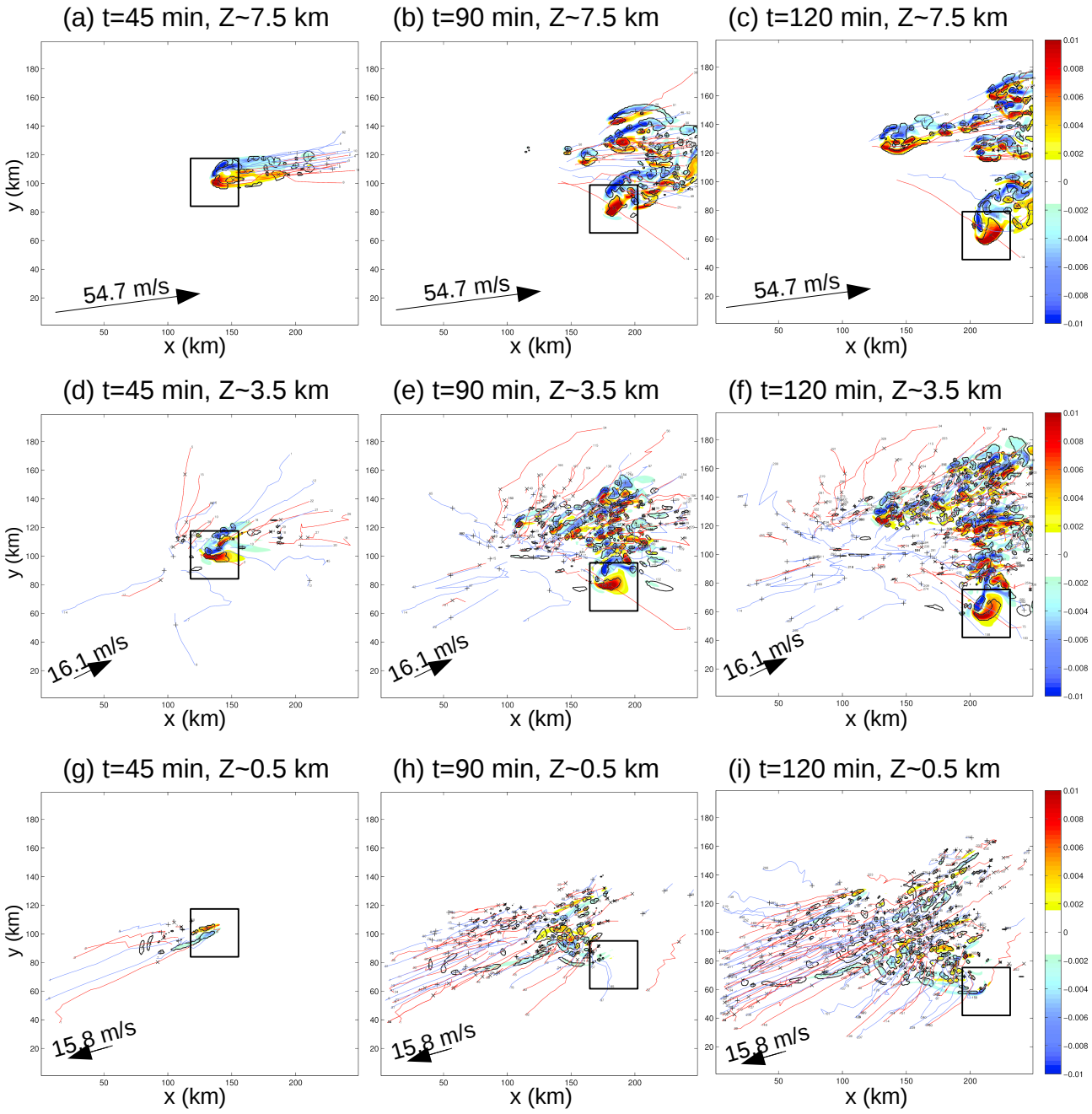

Figure 60: *Vorticity (in 1/s, color shaded) and vortex structures (black closed contours and the centers of circulation are indicated by crosses) identified with help of the W_k-method for several time steps and height levels of the doubled wind speed simulation done with WRF. Thin red and blue lines indicate the tracks of the cells with small numbers (the track numbers) plotted at the endpoints of the tracks and crosses indicating the actual positions of the cells in that time step. Black arrows indicate the background velocity vector and its magnitude that is based on the initial hodograph.*

might be that in the first time steps the cells especially grow in height before they start moving (cf. also Fig. 26 in chapter 6.5). However, some time steps after initiation of the supercell, the cells are tracked correctly and the tracks show nicely the deviation from the mean direction of all cells (in the upper levels: see Fig. 60b,c,e,f).
We additionally plotted the evolution of the vertical structure of the supercell vortex whose positive circulation core is accompanied by a negative core (see Fig. 61). We think, that these two vortex structures in fact belong to the same vortex tube corresponding with the up- and downdraft of the supercell as indicated by the black dashed lines in Figure 61(d). However, the W_k-method used here is defined such that we can analyze the vortex structures in a plane, i.e. vortex patches where the vertical vorticity is larger than the deformation. In order to see the missing part of the vortex tube at the top of the troposphere, we would need to use the three-dimensional version of the W_k-method. This is of course possible, however we are highly interested in the information of the sign of the circulation in a plane which is more easily to obtain with help of the two-dimensional W_k-method. Although we will see that there is not much difference in the statistics of convective-scale vortices with positive and negative circulations, there is a large difference in the synoptic scale between lows (positive circulations) and highs (negative circulations).
Nonetheless, it is astonishing that the W_k-method seems to work so nicely in the convective scale, too. The advantage of the W_k-method over other vortex identification methods in meteorology is that we do not need to change any threshold values when changing the horizontal scale. Therefore, we will be able to compare the statistics of vortices identified on different scales. First, we will analyze the convective scale vortices in the following and then go on to a synopsis chapter comparing the results of the vortices identified in all three data sets.

7.6.1 Radius of W_k features (WRF)

The radii distributions of the W_k features identified in the original and in the linear-shear WRF runs follow over nearly the whole data range the same distribution (see Fig. 62, blue and red curves). Only the cyclonic vortices of the original run have some larger systems, which can be attributed to the long-lasting, right-moving supercell that forms in this run. This is confirmed by the piecewise applied exponential fits that show a relatively stable behavior over nearly the whole data range revealing approximately the same characteristic (mean) radii with $R_{1,4} = 1.9\,\text{km}$ (original) and $R_{2,5} = 1.7\,\text{km}$ (linear-shear) for these runs (Fig. 63a). Note, that the piecewise fits are only applied up to radii of about $R \approx 6\,\text{km}$ in the original and linear-shear case since we did not want to apply the fits to less than 4 data points. The doubled-wind speed cases are better described by power laws than by exponential laws (see Fig. 63b). Thereby, the averaged power-law exponent of the cyclonic systems is slightly smaller than the exponent of the anticyclonic systems. The detected anticyclonic W_k features can even have larger sizes

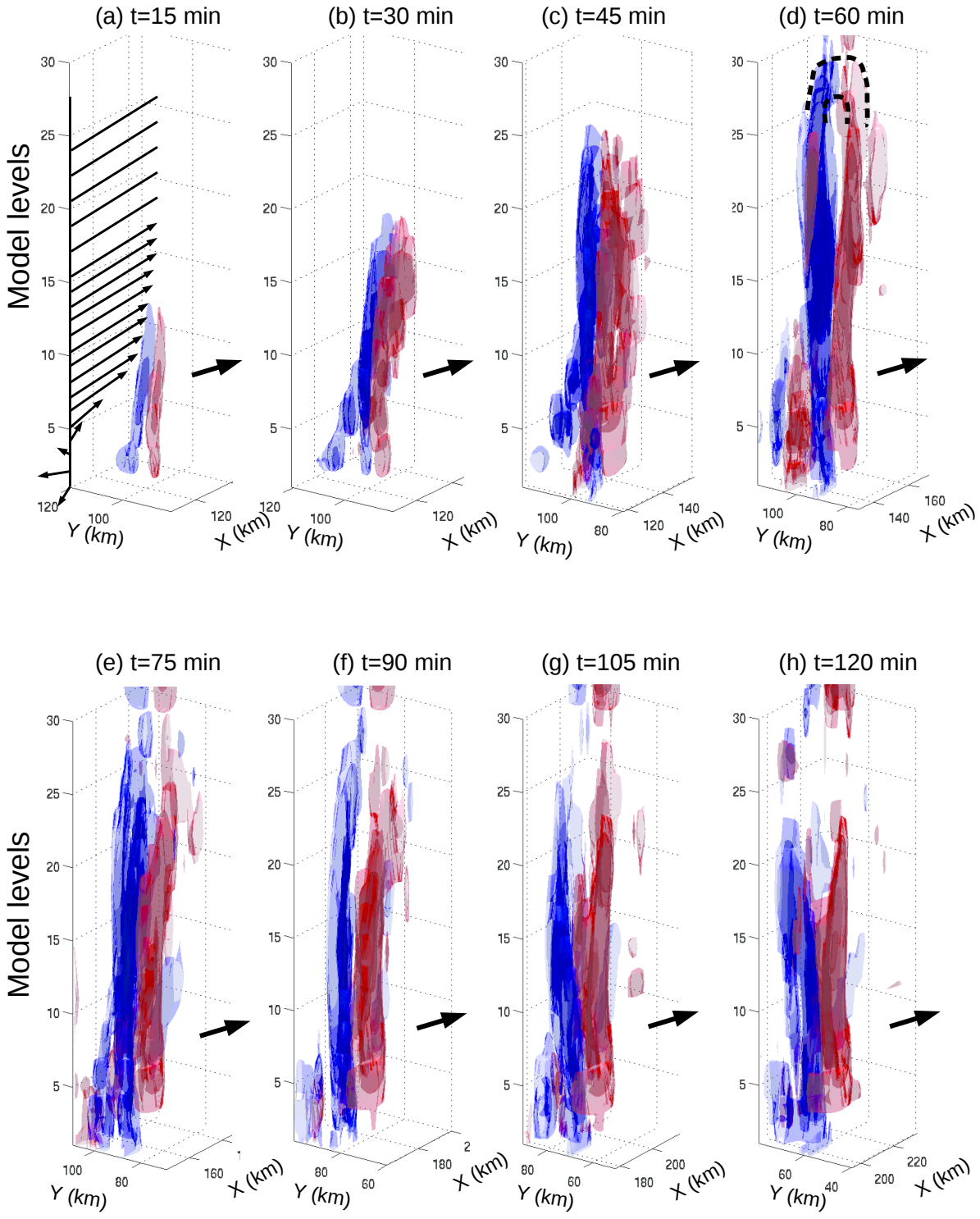

Figure 61: *Vertical development of a supercell: Isosurfaces of (smoothed) vorticity* $[(\pm 1, \pm 5) \cdot 10^{-3}\ s^{-1}]$ *of the right-moving supercell in the field of* $W_k > 1$ *(lighter colors are equal to low vorticity magnitudes) for different time steps of the doubled wind speed WRF simulation. Positive vorticity surfaces are plotted in red and negative in blue. Cells are viewed from the back (cell motion indicated by the thick black arrow). The sector plotted is cut from the large field given in Fig. 60 where its approximate position is given by the black box. Black dashed lines in (d) indicate the possible connection of the vorticity tubes.*

than the cyclonic ones (see the fatter tail of the dashed green line compared to the solid green line in Fig. 62). Looking at the example figures (Fig. 60f) of the vorticity fields and identified W_k features reveals that the large anticyclonic systems might not be very intense (see the low vorticity magnitudes of the large anticyclonic system located at the top right corner ($x \approx 240; y \approx 170$), in Fig. 60f). We also applied stretched-exponential fits to the distributions of the WRF runs in order to compare the results with that of the NCEP and CFSR data (Table 15). However, the parameters — the exponent β and the reference scaling parameter $\lambda\beta$ — strongly depend on the starting value (see Table 15). Therefore, it is not easy to interpret the results. In the beginning of the distributions, the radii are discrete coinciding with one, two, three, and so forth grid points of $1 \times 1\,\mathrm{km}^2$ area[79]. While the application of the stretched-exponential distributions to the majority of the data set (about 70-80%) with a starting radius of $R = 780\,\mathrm{m}$[80] shows that the exponents β increase with increasing curved shear, however a larger starting radius of $R = 1260\,\mathrm{m}$ (original and linear-shear case) and $R = 1780\,\mathrm{m}$ (doubled-wind speed case), respectively, leads to exponents that are almost equal in the order of $\beta \approx 0.3$-0.4. The latter cases cover about 30% of the data. The reference scale $\lambda\beta$ for the different starting values also increase with increasing curved shear although the values of the scales are

[79] Since the grid point areas A of the vortices are multiples of $1\,\mathrm{km}^2$, the radii $R = \sqrt{A/\pi}$ have uneven values.

[80] A radius of 780 m corresponds to two grid points.

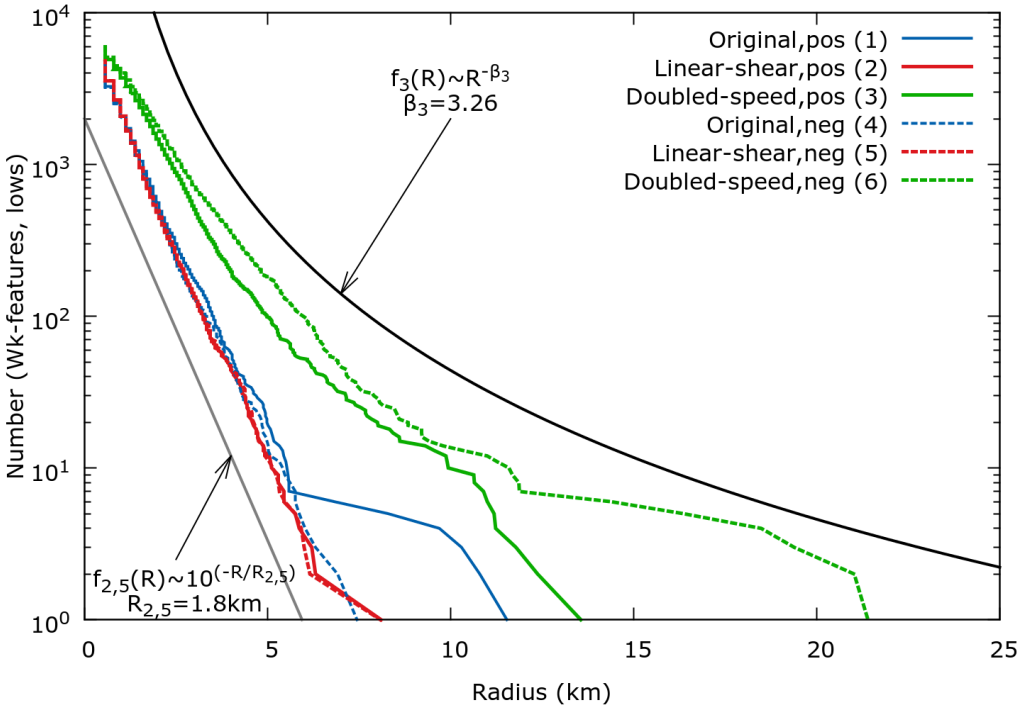

Figure 62: *Complementary cumulative distribution (CCD) of the radii of cyclonic and anticyclonic W_k features identified in three different WRF supercell simulations (1 km resolution) at a height of approximately 3.5 km.*

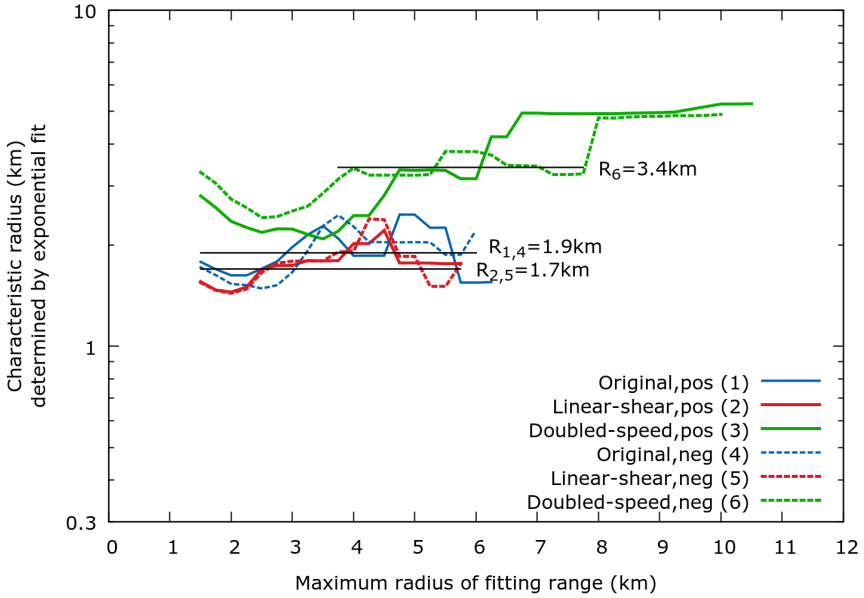

(a) Characteristic radii determined by exponential fits

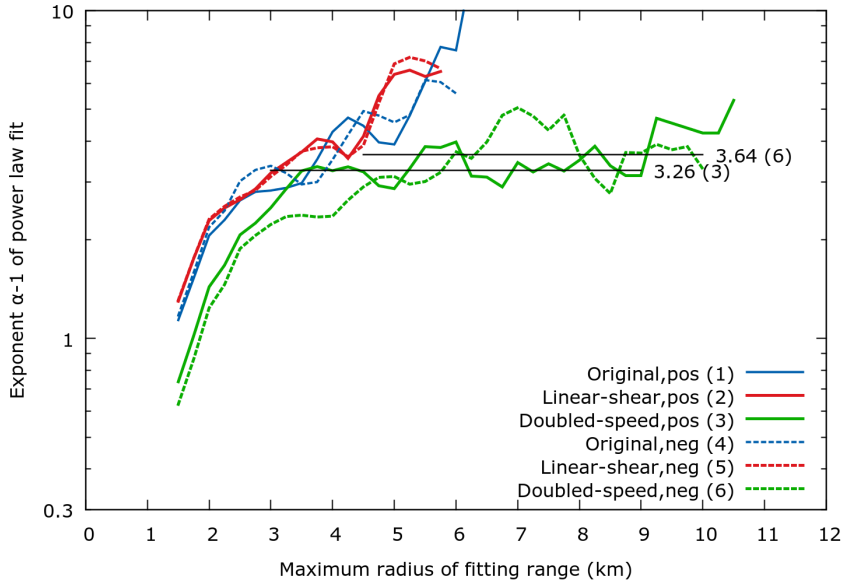

(b) Exponents determined by power law fit

Figure 63: *Results of fits applied to the complementary cumulative distribution plotted in Fig. 62: (a) Characteristic parameters (radii) of exponential fits applied to the CCDs in Fig. 62; (b) Exponents of power law fits applied to the CCDs in Fig. 62. The fits were applied piecewise to the data (in 250 m steps starting with 500 m) with a fitting range of 1000 m.*

considerably different (Table 15). Interestingly, most of these values are smaller (for the larger radii starting values even significantly smaller) than the resolution of the WRF data.

Table 15: ***Stretched-exponential fits (radius, WRF):*** *Characteristic parameters λ, β of the stretched-exponential fits CCDF $\sim \exp(-\widetilde{\lambda} x^{\beta})$ with $\widetilde{\lambda} = 1/(\lambda\beta)$ applied to the radii of different WRF set-ups plotted in Fig. 62 with a starting value of 780 m.*

		Cyclonic systems				Anticyclonic systems			
System, Level	R_{start} (m)	N_{tot}	N/N_{tot}	β	$\lambda\beta$ $(\mathrm{m})^{\beta}$	N^*_{tot}	N^*/N^*_{tot}	β^*	$\lambda^*\beta^*$ $(\mathrm{m})^{\beta^*}$
Linear-shear	780	4969	0.72	0.46	94	4968	0.72	0.42	63
Original	780	4470	0.73	0.56	251	4487	0.72	0.65	347
Doubled-speed	780	5920	0.83	0.84	905	5956	0.85	0.83	1080
Linear-shear	1260	4969	0.34	0.31	4.3	4968	0.34	0.28	1.6
Original	1260	4470	0.39	0.29	3.3	4487	0.37	0.34	11
Doubled-speed	1780	5920	0.33	0.39	48	5956	0.39	0.36	40

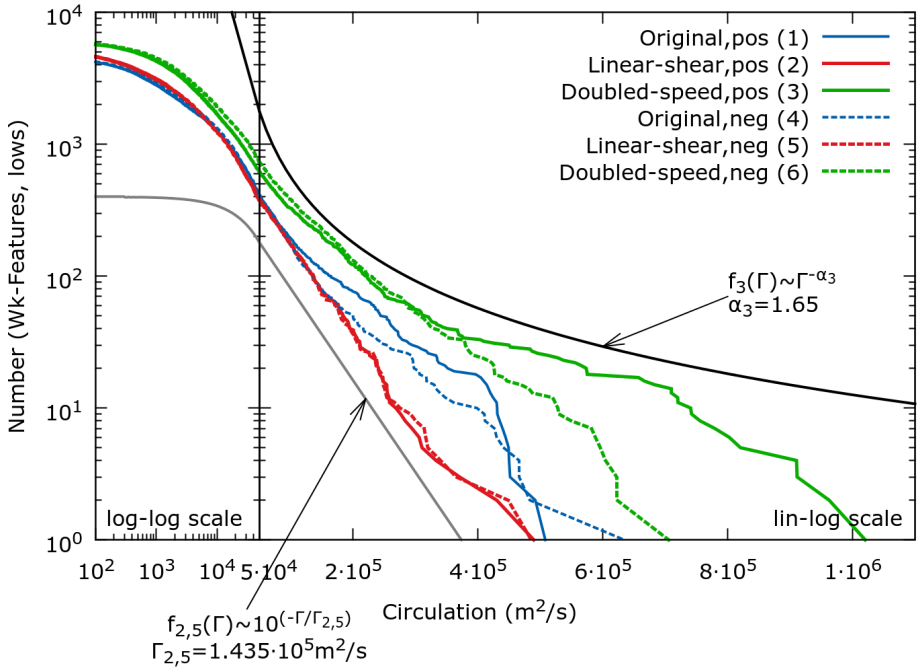

Figure 64: *Complementary cumulative distribution (CCD) of the circulations of cyclonic and anticyclonic W_k features identified in three different WRF supercell simulations (1 km resolution) at a height of approximately 3.5 km.*

7.6.2 Circulation of W_k features (WRF)

The complementary cumulative distributions of the positive and negative circulations of the identified W_k features in the WRF data are shown in Figure 64. We plotted the lower circulation magnitudes ($\|\Gamma\| < 5 \cdot 10^4\,\mathrm{m}^2/\mathrm{s}$) in a double-logarithmic manner

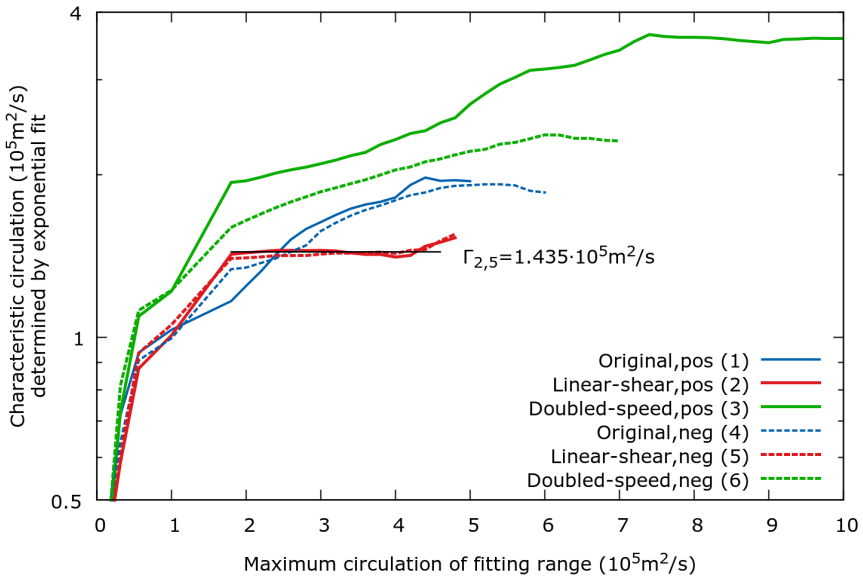

(a) Characteristic radii determined by exponential fits

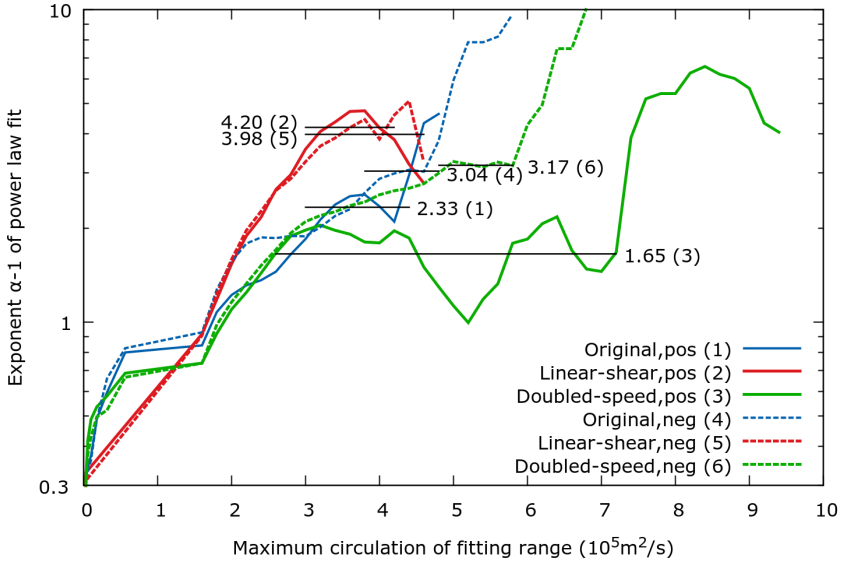

(b) Exponents determined by power law fit

Figure 65: *Results of fits applied to the complementary cumulative distribution plotted in Fig. 64: (a) Characteristic parameters (circulations) of exponential fits applied to the CCDs in Fig. 64; (b) Exponents of power law fits applied to the CCDs in Fig. 64. The fits were applied piecewise to the data. Thereby for circulations smaller than* $10^4 m^2/s$*, the fitting ranges increased gradually as* $[10^{(2+0.25\cdot t)} : 10^{(2.5+0.25\cdot t)}]$ *where t is a natural number between 0 and 10. For circulations larger than* $10^4 m^2/s$*, the fitting range had a constant length of* $1.5 \cdot 10^5 m^2/s$ *and the steps were* $2 \cdot 10^4 m^2/s$*.*

and the higher circulations ($\|\Gamma\| \geq 5 \cdot 10^4\,\mathrm{m}^2/\mathrm{s}$) in a single-logarithmic plot. While the lower circulation magnitudes neither follow an exponential distribution nor a power law distribution, we find evidence for both models in the tails of the distributions. Thereby, the exponential law fits well in the linear-shear case and the power law fits well in the

Table 16: ***Stretched-exponential fits (circulation, WRF):*** *Characteristic parameters λ, β of the stretched-exponential fits $CCDF \sim \exp(-\widetilde{\lambda} x^{\beta})$ with $\widetilde{\lambda} = 1/(\lambda\beta)$ applied to the circulations of different WRF set-ups plotted in Fig. 62 with a starting value of $5 \cdot 10^2\ m^2 s^{-1}$.*

	Cyclonic systems				Anticyclonic systems			
System, Level	N_{tot}	N/N_{tot}	β	$\lambda\beta$ $(\mathrm{m}^2/\mathrm{s})^{\beta}$	N^*_{tot}	N^*/N_{tot}	β^*	$\lambda^*\beta^*$ $(\mathrm{m}^2/\mathrm{s})^{\beta^*}$
Linear-shear	4969	0.73	0.37	$0.76{\cdot}10^4$	4968	0.73	0.36	$0.75{\cdot}10^4$
Original	4470	0.75	0.32	$0.66{\cdot}10^4$	4487	0.76	0.36	$0.90{\cdot}10^4$
Doubled-speed	5920	0.83	0.33	$0.75{\cdot}10^4$	5956	0.85	0.36	$1.14{\cdot}10^4$

doubled-speed run (especially for the cyclonic circulations) as can be seen by the piecewise applications of the laws and their relatively stable parameters over a wide range of the distributions (see Fig. 65a,b). Furthermore, it should be noted that the distributions of positive and negative circulations in the linear-shear case are approximately equal and the differences between the distributions of positive and negative W_k features increase with increasing directional and speed shear.

We also applied the stretched-exponential model of the python powerlaw package (Alstott et al., 2014) to the data (summarized in Table 16). The stretched-exponentials fit well in all cases and, interestingly, in all cases the exponent β of the distributions are similar with values between 0.32 and 0.37. This result is even stable for starting circulation values covering the majority of the data (covering at least about 50% of the data, not explicitly shown here). The reference scales (circulation magnitudes) $\lambda\beta$of the distributions are in the order of 10^3 to 10^4. While these reference scales are almost equal ($\approx 7 \cdot 10^3\,(\mathrm{m}^2/\mathrm{s})^{\beta}$) for the cyclonic systems in all runs, the typical scales of the anticyclonic systems increase slightly with increasing intensity of the initial shear magnitude (directional and speed shear). Note, how similar the values of all parameters (including the total numbers) are in the case of the linear-shear run. Furthermore, we observe the highest number of W_k features in the doubled-speed run while the smallest number of W_k features is detected in the original run. The highest background speed, i.e. the fastest motion of the convective cells, occurs in the doubled-speed run. Since the systems can move outside the domain (non-periodic boundary conditions), this also implies that a higher number of systems is triggered in case of the doubled-speed run compared to the other two runs.

7.7 Summary and discussion of results of NCEP, CFSR and WRF data concerning circulation and radius distributions

In summary, we tested the distributions of circulation and radius of the W_k features in the NCEP, CFSR and WRF data sets for exponential and power law behavior. The results are summarized in Table 17 below. In short, we can conclude that the subsynoptic W_k features are rather power law distributed with respect to radius and circulation while the synoptic systems are rather exponentially distributed. Since power law and exponential distributions only have one tunable parameter, the models only fit in small ranges of the data. Therefore we additionally investigated the distributions with help of other functions that are characterized by at least two tunable parameters. Thereby, we used the python powerlaw package of Alstott et al. (2014) which allows to test for multiple functions. We found, that the best fit in nearly all cases — especially for the circulation magnitudes — is the stretched-exponential distribution (CCDF $\sim \exp(-\widetilde{\lambda}x^{\beta})$ with $\widetilde{\lambda} = 1/(\lambda\beta)$). Interestingly, the exponents β of the CCDF concerning the circulation

Table 17: *Summary of the results concerning radius and circulation. Here, the synoptic range is defined for radii larger than 500 km and circulations larger than* $10^7\ m^2/s$.

	Data set	Subsynoptic range	Synoptic range
RADIUS	NCEP		· exponentially distributed over a large range (Dec. lows, highs) · decays faster than exponential (June lows)
	CFSR	· rather power law distributed	· rather exponentially distributed
	WRF	Depends on the simulation: · exponential (linear shear run) · power law (doubled-speed run)	
CIRCULATION	NCEP	· rather power-law distributed for magnitudes of order 10^6	· exponentially distributed for magnitudes of order 10^7-10^8
	CFSR	· rather power-law distributed for magnitudes of order 10^5 and 10^6, albeit with different exponents	· exponentially distributed for magnitudes of order 10^7-10^8
	WRF	Depends on the simulation: · exponential (linear shear run) · power law (doubled-speed run)	

magnitudes are approximately equal for all systems in the CFSR data set (lows/highs in summer/winter) with values between 0.2 and 0.3. In the WRF data set we observe slightly larger exponents β of about 0.35 in all runs (cyclonic/anticyclonic systems). These low β values indicate that the distributions have a heavy tail (heavier than exponential). In the NCEP data set, the β values are higher and lie between 0.6 and 0.9 indicating that these distributions are closer to an exponential distribution.

Laherrere and Sornette (1998) point out that stretched-exponential distributions are connected to multiplicative processes and that the inverse of β can be interpreted as the number of levels (or generations) in the multiplicative process. For β equal to 0.2 or 0.3 (CFSR/WRF data), we derive a number of $1/\beta = 1/0.2 = 5$ or $1/\beta = 1/0.3 \approx 3$ generations. In addition, we observed that the reference scales of the stretched-exponentials are 1-2 orders in magnitude smaller than the expected circulation magnitudes of the resolved systems in the data set (see Table 1)[81]. We can hypothesize that 3-5 of the systems with reference scale $\lambda\beta$ generate the observed systems in a multiplicative manner. In contrast to an additive generation process, the multiplicative process implies that the interaction of the involved systems might be nonlinear which would lead to a stronger intensification than expected from a linear model. How this multiplicative model really applies to the atmosphere is not clear, but further future investigations of this topic would be interesting. Especially since we observe the same exponent, i.e. the same generation process, across different scales. Speculating, this could mean that a convective-scale system that was generated by a number of smaller-scale systems is again involved as one of the systems that generate a larger scale (mesoscale) system, and so forth. It should be noted that we only studied the behavior of W_k features. This might influence the distributions, especially in the higher ranges of the distributions. Hence, the results should be tested and compared in a future study for single centers, too.

Concerning the radius, the stretched-exponential distributions show different results. The NCEP data shows exponents β much larger than 1 and even larger than 2 in case of the lows. This means that the distributions fall off much faster than an ordinary exponential distribution. The stretched-exponential fits applied to the CFSR data indicate a clear dependence on height and a dependence on the season with the smallest values of β at the lowest level (resembling power law distributions with heavy tails) and increasing values of β at the upper levels of the troposphere (resembling exponential distributions with typical scales). These interesting results might be related to the more small-scale turbulent structures caused by orographic effects and friction in the lowest levels while the flow is more smooth in the upper levels. The results in case of the

[81] We observe reference scales of about $\Gamma_{ref,CFSR} = \lambda\beta = 10^5\text{-}10^6\,\mathrm{m^2/s}$ in the CFSR data set and $\Gamma_{ref,WRF} = \lambda\beta = 10^3\text{-}10^4\,\mathrm{m^2/s}$ while we expected typical circulations of $10^7\,\mathrm{m^2/s}$ for intense tropical cyclones (hurricanes) and $10^6\,\mathrm{m^2/s}$ for supercells. Probably, the less-intense mesoscale and convective-scale systems are one order in magnitude smaller.

WRF data are not consistent over the whole range of the data set. For the systems with radii larger than about 1.2 km (or > 1.7 km in the doubled-speed run) the β values of the stretched-exponential distributions are approximately equal for all runs with values around 0.35. This is similar to the β values of the circulation distributions.

Moreover, we want to compare our results to the existing literature. Usually, the publications concerning the distributions of cyclone radii or intensity do not discuss the form of the statistical model. Hence, we will only compare the typical values observed in other studies. The cyclone radius is a parameter that was studied by some authors and the result found here that the typical scale of the radii is subsynoptic is also confirmed in other publications such as in Schneidereit et al. (2010) (see also our discussion in chapter 6.7.4). It is not easy to compare the circulation results with existing publication since the circulation is a parameter that is only rarely used in the atmospheric sciences. An exception is the publication of Sinclair (1997) who found that the circulation magnitudes of cyclones in NCEP data are in the order of $10^7\,\mathrm{m^2/s}$ and larger. This is in accordance with our results. Moreover, a theoretical estimation yields for typical wind magnitudes of $U \approx 10\,\mathrm{m/s}$ and synoptic radii of $R \approx 1000\,\mathrm{km}$ circulation magnitudes of $\Gamma \approx 2\pi RU \approx 6 \cdot 10^7\,\mathrm{m^2/s}$ in the synoptic range which is in accordance with our observations. Furthermore, highs are usually observed to be larger than lows which fits with our findings in terms of the radii of W_k features. Since the circulation magnitude depends on the size of the systems, the larger circulations observed in the high pressure systems can be dedicated to this size effect although the wind speeds observed in cyclones can be much higher than the speeds occurring in highs.

Finally, we want to point out that we only considered circulation and radius so far. These properties followed from idealized vortex models which were observed in an inertial, nonrotating reference frame (chapter 4). However, we have seen that it is possible to derive vortex intensity measures in a noninertial, rotating reference frame that additionally considers the rotation rate of the Earth, i.e. the Coriolis force term. The introduced parameters, energy of displacement and atmospheric moment, could be interpreted as energy that was necessary to generate the vortex. While the energy of displacement is mass-specific, the atmospheric moment involves the total volume that was covered during the life cycle of the vortex. We have studied the three data sets with respect to these two intensity measures, too (see Appendix C for preliminary results). In short, we observe that the distributions concerning the energy of displacement behave similar to the circulation distributions. The distributions of the atmospheric moments (considering the vortex life time volumes) hint to a power law behavior that envelops all scales (see Figure C83).

8 Final summary of this work

The main objective of this thesis was the identification of vortex structures and their properties in atmospheric flows of different resolutions. Motivated by the lack of a consistent identification procedure across the scales as well as a clear definition of vortex size and intensity we decided to tackle the problem from two sides. On the one hand we studied the kinematic properties of the flow in order to determine the geometric properties of a vortex; on the other hand we investigated the vortices concerning their dynamic aspects.

Thereby, the kinematics proved to be a treasure chest revealing useful methods in order to define the size of a vortex as well as to determine the deformation of identified contour lines and areas over time (chapter 2). Moreover, with the help of the kinematic approaches we can differentiate between the deformation and rotation of the flow field. This led to the introduction of the kinematic vorticity number method (W_k-method) that locally compares the rates of rotation and deformation (see chapter 6 and published in Schielicke et al., 2016). A vortex core region is then defined in regions where the rotation rate prevails over the strain rate. Due to the dimensionless definition as a ratio, the main advantage of the novel method is its successful application in different flow situations, different height levels and different grid resolutions giving consistent results. Additionally, we were able to introduce a tracking method based on the W_k-method. Overall, the W_k-method proved a useful tool in the identification and study of vortices and it has been applied in various ways (see Table 18 for an overview over applications of the W_k-method).

On the other hand, the dynamic equations can be used in order to identify typical balances of forces depending on the scale of the vortex (chapter 3). Furthermore, the dynamics reveal the importance of the circulation in the study of vortices and their interactions. Circulation can be interpreted as a measure of the intensity of a vortex due to its integral definition. Under idealized conditions, vortex models based on the dynamic equations lead to the recognition of characteristic vortex properties that determine the flow field around the vortex (chapter 4). These important properties are i.a. the circulation and the radius of the vortex core. However, these vortex models are highly idealized. They are studied in an inertial, non-rotating coordinate system and the equations resemble the cyclostophicly-balanced horizontal equations of motion. But we observe, that larger-scale real atmospheric vortices are influenced by the rotation of the Earth. Hence, the Coriolis force term in the equations of motion becomes significant. In order to account for the Coriolis term in larger-scale flow, we introduced two scale-dependent intensity measures: called the energy of displacement and the atmospheric moment. While the energy of displacement can be interpreted as the mass-specific en-

Table 18: *Overview over applications of the W_k-method*

Topic	Applications of W_k-method	Reference
3D analysis of vortices	Storm system Anatol	Schielicke et al. (2016), chapter 6.7
	Simulated supercell	Schielicke et al. (2015), chapter 7.6
Idealized vortices	Test of differen set-ups	Schielicke et al. (2016), chapter 6.6
Point vortex dynamics:	Analysis of blocking situations	Sonntag (2012, bachelor's thesis)
		Isernhagen (2015, diploma thesis)
		Hirt (2016, master's thesis)
	Trapezoid method	Müller et al. (2015)
Statistics	Vortex size and circulation	chapter 7
	Estimating the vortex energy	chapter C
	Study vortices on different scales	chapter 7
	First climatologies	chapter 6.7
Vortex tracking	Improvement due to additional information on size, intensity, deformation of areas	chapter 6.5

ergy that was necessary to generate the vortex, the atmospheric moment represents its mass-related counterpart that takes into account the volume that was affected during the vortex life time (chapter 5 and published in Schielicke and Névir, 2009, 2011, 2013). We were able to improve the derivation of the energy of displacement by using a modified Rankine ansatz. This enables a consistent derivation of the energies for vortices on different scales. Furthermore, we could express the energy of displacement in terms of the circulation and the vortex area (see chapter 5.2.5 and 5.5).

Afterward, we studied the properties (circulation and radius) of vortex structures in three data sets of different resolutions with respect to exponential and power-law behavior. The main finding is that we found power law behavior for small-scale, less-intense vortices concerning their radius and their circulations and exponential behavior in the tails (chapter 7). We obtained a similar result for the mass-specific energy of displacement. In addition we found that two-parameter distributions such as the stretched-exponential distribution better fit the complete data set. Especially in case of the circulation, the exponents that characterize the stretched-exponential distributions are of comparable order for different data sets. This might be a hint that the vortices on different scales probably stem from (the same) multiplicative processes. Moreover, we

were able to reproduce the results of Schielicke and Névir (2009) who found a unified exponential behavior with an exponential decay rate of about 1000 J/kg for the tails of the distributions (see Appendix C). With respect to the mass-related atmospheric moments we found hints to unified power law behavior that envelops all distributions with an exponent of about 0.6 which is in the same order as the exponent of the Gutenberg-Richter law of earthquakes (see chapter C.2.2). However, further investigations are necessary.

In conclusion, we want to point out that we were able to define and implement a method that is able to extract vortex structures from differently resolved data sets. The method can be and has been applied successfully in various manners. Moreover, we introduced intensity measures based on the horizontal equations of motion. Although the results need to be further investigated, these intensity measures seem to hint to a unified behavior of vortices on different scales.

Appendix A Application of the W_k-method in the identification of point vortices in reanalysis data and their application to blockings

We have already introduced the concept of point vortices in chapter 3.4.5 and the reader is referred to this chapter for refreshing the basic concept. It is important to remember that the equations of motion of N point vortices were derived under inviscid, barotropic and incompressible conditions. Here, we will first present the equations of motion in different representations and introduce their invariants followed by explicit mathematical details on specific motions of $N \leq 3$ point vortices.

A.1 Mathematical representations and invariants of the point vortex equations

Summarized, the dynamics of a set of N point vortices with circulations Γ_i that are located at z_i with $i = 1, .., N$ is given in complex coordinates as (see eq. 133)

$$\frac{dz_\alpha}{dt} = \frac{i}{2\pi} \sum_{\substack{\beta=1 \\ \alpha \neq \beta}}^{N} \frac{\Gamma_\beta}{\ell_{\alpha\beta}^2} (z_\alpha - z_\beta)$$

$$\alpha = 1, .., N$$

where $\ell_{\alpha\beta} = ||z_\alpha - z_\beta||$ denotes the distance between the two vortices denoted by α, β. The corresponding two-dimensional equations of motion of N point vortices located at (x_α, y_α) in cartesian coordinates are given by the following 2N non-linear ordinary differential equations (cf. e.g. Aref, 2007):

$$\frac{dx_\alpha}{dt} = -\frac{1}{2\pi} \sum_{\substack{\beta=1 \\ \alpha \neq \beta}}^{N} \frac{\Gamma_\beta (y_\alpha - y_\beta)}{\ell_{\alpha\beta}^2} \tag{262a}$$

$$\frac{dy_\alpha}{dt} = +\frac{1}{2\pi} \sum_{\substack{\beta=1 \\ \alpha \neq \beta}}^{N} \frac{\Gamma_\beta (x_\alpha - x_\beta)}{\ell_{\alpha\beta}^2} \tag{262b}$$

$$\text{for } \alpha = 1, .., N$$

The point vortex equations can also be expressed in terms of the intervortical distances.

Then for $N \geq 3$ equations (262) read (after Newton, 2001, chapter 2.1, equation (2.1.5))

$$\frac{d\ell_{\alpha\beta}^2}{dt} = \frac{2}{\pi} \sum_{\substack{\gamma=1 \\ \gamma\neq\alpha\neq\beta}}^{N} \Gamma_\gamma \sigma_{\alpha\beta\gamma} A_{\alpha\beta\gamma} \left(\frac{1}{\ell_{\beta\gamma}^2} - \frac{1}{\ell_{\gamma\alpha}^2} \right) \tag{263}$$

where $A_{\alpha\beta\gamma}$ is the area of the triangle spanned by the three vortices and $\sigma_{\alpha\beta\gamma} = \pm 1$ is equal to $+1$ in case of a counter-clockwise arrangement of the vortices denoted by α, β, γ and -1 in case of a clockwise arrangement. The area $A_{\alpha\beta\gamma}$ of the triangle can be expressed in terms of the intervortical distances with help of Heron's formula as

$$A_{\alpha\beta\gamma} = \sqrt{s(s-\ell_{\alpha\beta})(s-\ell_{\beta\gamma})(s-\ell_{\alpha\gamma})} \tag{264}$$

$$\text{where} \qquad s = \frac{1}{2}(\ell_{\alpha\beta} + \ell_{\beta\gamma} + \ell_{\alpha\gamma}) \tag{265}$$

It should be remembered that these point vortex equations stem from the inviscid, incompressible equations of motion. They are a rather good model for large-scale atmospheric dynamics as was shown in e.g. Müller et al. (2015).

The study of the dynamics of point vortices go back to Helmholtz (1858). Helmholtz not only introduced the important concepts of vortex lines and filaments and the relation to vorticity dynamics already mentioned in chapter 3.4.2, he also introduced the equations of the motion of straight parallel vortex filaments and discussed the special case of one and two of such vortices (Helmholtz, 1858, §5). Assume that the vortex filaments are straight and parallel to the z-axis. A plane perpendicular to that axis intersects all vortex filaments and the equations simplify to the two-dimensional point vortex equations. About 20 years later, Kirchhoff (1876) in his lectures on mathematical physics, discussed the equations for N interacting point vortices and presented the Hamiltonian structure of the equations (Aref, 2007; Kirchhoff, 1876, chapter 20, §3, equations (14))[82]:

$$\Gamma_\alpha \frac{dx_\alpha}{dt} = \frac{\partial H}{\partial y_\alpha} \quad , \quad \Gamma_\alpha \frac{dy_\alpha}{dt} = -\frac{\partial H}{\partial x_\alpha} \qquad \text{for } \alpha = 1,..,N \tag{266}$$

where

$$H = -\frac{1}{4\pi} \sum_{\substack{\alpha,\beta=1 \\ \alpha\neq\beta}}^{N} \Gamma_\alpha \Gamma_\beta \ln \ell_{\alpha\beta} = const. \tag{267}$$

is conserved during the motion of the N point vortices. Note, that H depends on the intervortical distances. Kirchhoff (1876, chapter 20, equations (15),(18)) showed that

[82] We follow the nomenclature of Aref (2007) here which is different from the one published in Kirchhoff (1876) original one: e.g. m instead of Γ for the circulations, P instead of H for the Hamiltonian. The structure of the equations is similar of course.

there are three further conserved quantities which are called "the ***zonal momentum*** P_x, the ***meridional momentum*** P_y and the vertical component of the ***angular momentum*** L_z" (cf. Müller et al., 2015, their equations (5)-(7)). These momentums read

$$P_x = \sum_{\alpha=1}^{N} \Gamma_\alpha y_\alpha = const. \tag{268}$$

$$P_y = -\sum_{\alpha=1}^{N} \Gamma_\alpha x_\alpha = const. \tag{269}$$

$$L_z = -\frac{1}{2}\sum_{\alpha=1}^{N} \Gamma_\alpha (x_\alpha^2 + y_\alpha^2) = const. \tag{270}$$

With help of these conserved quantities, we can find another quantity that can be written in terms of the intervortical distances $\ell_{\alpha\beta}$ (Müller and Névir, 2014, their equation (1.10)):

$$M := -\Gamma_{total} L_z - \frac{1}{2}(P_x^2 + P_y^2) = \frac{1}{4}\sum_{\substack{\alpha.\beta=1 \\ \alpha\neq\beta}}^{N} \Gamma_\alpha \Gamma_\beta \ell_{\alpha\beta}^2 = const. \tag{271}$$

where

$$\Gamma_{total} := \sum_{\alpha=1}^{N} \Gamma_\alpha = const.$$

is the total circulation which is conserved, too (see also eq. 138). Another important conserved quantity is the quadratic sum of the circulations (e.g. Müller et al., 2015)

$$V := \frac{1}{2}\sum_{\substack{\alpha,\beta=1 \\ \alpha\neq\beta}}^{N} \Gamma_\alpha \Gamma_\beta = const. \tag{272}$$

We have furthermore already introduced the center of circulation $\mathbf{C}$ (see eq. 139)

$$\mathbf{C} = \frac{\sum_{\alpha=1}^{N} \Gamma_\alpha \mathbf{x}_\alpha}{\Gamma_{total}} = const.$$

and we have seen that it is a conserved quantity, too. In addition, we have mentioned in section 3.4.5 that the motion of N point vortices depends on the total circulation and their circulation center. If Γ_{total} is different from zero ($\Gamma_{total} \neq 0$), the N point vortices move around their center of circulation $\mathbf{C}$. If the total circulation is zero ($\Gamma_{total} = 0$) all vortices translate along parallel paths with the same speed. In the following, we will give a short overview over these types of motion for systems of $N \leq 3$ point vortices.

A.2 On the motion of $N \leq 3$ point vortices

At first, we assume that the fluid is initially at rest (before adding the point vortices to the fluid) and that the motion occurs under inviscid, barotropic conditions. The equations of motion then reduce to the two-dimensional point vortex equations (133).

A.2.1 Point vortex systems of $N = 1$ and $N = 2$

Helmholtz (1858) and Kirchhoff (1876) already discussed the motion of one and two point vortices. The motion of a single ($N = 1$) point vortex is trivial. Since the center of circulation lies inside the point vortex itself and the vortex moves around its center of circulation, its position remains unchanged. Nevertheless, the vortex induces a velocity according to the Biot-Savart formula (see chapter 3.4.4).
The equations of motion of $N = 2$ point vortices with non-zero circulations $\Gamma_1 \neq 0$, $\Gamma_2 \neq 0$ read (in complex formulation):

$$\frac{d\mathbf{z}_1}{dt} = i\frac{\Gamma_2}{2\pi\ell_{12}^2}(\mathbf{z}_1 - \mathbf{z}_2) \tag{273a}$$

$$\frac{d\mathbf{z}_2}{dt} = i\frac{\Gamma_1}{2\pi\ell_{12}^2}(\mathbf{z}_2 - \mathbf{z}_1) \tag{273b}$$

where $\ell_{12} = |\mathbf{z}_1 - \mathbf{z}_2|$ is the distance between the two vortices. We will first assume that $\Gamma_{total} = \Gamma_1 + \Gamma_2 \neq 0$. Further, we assume w.l.o.g. that the center of circulation $\mathbf{C}$ coincides with the origin ($\mathbf{C} = \mathbf{0} = (0,0)$)

$$\mathbf{C} = \frac{\Gamma_1\mathbf{z}_1 + \Gamma_2\mathbf{z}_2}{\Gamma_{total}} = \mathbf{0} \tag{274}$$

Then it follows ($\Gamma_{total} \neq 0$)

$$\mathbf{z}_1 = -\frac{\Gamma_2}{\Gamma_1}\mathbf{z}_2 \tag{275}$$

This means that the two vortices lie on a straight line that connects $\mathbf{z}_1$, $\mathbf{z}_2$ and $\mathbf{C}$. If the vortices have circulations of the same sign (i.e. both positive or both negative), we can conclude from (275) that $\mathbf{C}$ lies between the two vortices while $\mathbf{C}$ lies outside in case of different signs. When transforming the system to polar coordinates $(x, y) \rightarrow (\rho, \phi)$ with

$$x_\alpha = \rho_\alpha \sin\phi_\alpha \quad , \quad y_\alpha = \rho_\alpha \cos\phi_\alpha \tag{276}$$

where $\alpha = (1,2)$ denotes the index of the vortices and ρ_1, ρ_2 is the distance between $\mathbf{C}$ and the vortex positions. It follows from (275) that the angles between the vortices are either identical ($\theta_1 = \theta_2$ for different signs of circulations) or different by one π ($\theta_1 = \theta_2 + \pi$ for same signs of circulations). We further know that H is a conserved

quantity (see eq.(267))

$$H = -\frac{\Gamma_1\Gamma_2}{2\pi}\ln(\ell_{12}) = const. \tag{277}$$

$$\frac{dH}{dt} \propto \frac{d\ell_{12}}{dt} = 0 \tag{278}$$

$$\text{i.e. } \ell_{12} = const. \tag{279}$$

This means that the intervortical distance does not change with time. With some basic calculations, we can show that the distances ρ_1, ρ_2 remain constant in time[83]. Therefore, only the angles ϕ_i change in time with the same rate: Since $d\mathbf{C}/dt = 0$ we can conclude that

$$\widetilde{\omega} = \frac{d\phi_1}{dt} = \frac{d\phi_2}{dt} \ . \tag{280}$$

The equations of motion (273) decouple when using (275) in either (273a) and (273b), respectively. We derive for $\alpha = (1,2)$

$$\frac{d\mathbf{z}_\alpha}{dt} = i\frac{(\Gamma_1+\Gamma_2)}{2\pi\ell_{12}^2}\mathbf{z}_\alpha \tag{281}$$

This is a periodic motion. We can solve these equations with the ansatz $\mathbf{z}_\alpha = A_\alpha \exp(i\widetilde{\omega}t)$ where A_α is a constant that is proportional to the distances ρ_α between the vortices and the center of circulation and $\widetilde{\omega}$ is the angular velocity. From $d\mathbf{z}_\alpha/dt = i\widetilde{\omega}\mathbf{z}_\alpha$ we obtain

$$\widetilde{\omega} = \frac{\Gamma_1+\Gamma_2}{2\pi\ell_{12}^2} = \frac{\Gamma_{total}}{2\pi\ell_{12}^2} \tag{282}$$

Hence, it follows that the two vortices rotate at circles around their common center of circulation with a constant angular velocity $\widetilde{\omega}$ and a period of $T = 2\pi/\widetilde{\omega}$, respectively. Thereby, the orientation of the rotation (clockwise or anticlockwise around the center of circulation) depends on the vortex with the largest absolute circulation. Note, that in case of $\Gamma_1 = \Gamma_2$, both vortices rotate on the same circle around $\mathbf{C}$. The explicit velocity of each vortex can be calculated by (273).

A special case occurs when the total circulation vanishes. Assume that $\Gamma_{total} \to 0$ and w.l.o.g. $\Gamma_1 > 0$. Then the center of circulation approaches infinity $\mathbf{C} \to \infty$ as well as the distances between the vortex locations $\mathbf{z}_\alpha$ and $\mathbf{C}$. However, the intervortical distance

[83] It is easy to see that in the case of vortices with circulations of the same sign (here $\mathbf{C}$ lies between the vortices), the distances between the vortices and $\mathbf{C}$ remains constant. Otherwise, we would violate either $d\mathbf{C}/dt = 0$ or $d\ell_{12}/dt = 0$. If both vortices lie on one side of $\mathbf{C}$ (circulations of different signs, both vortices could move away from $\mathbf{C}$ with the same rate (or by the same distance $\mathbf{c}$) such that $d\ell_{12}/dt = 0$ is still fulfilled. However from $d\mathbf{C}/dt = 0$ and $\mathbf{C} = \mathbf{0}$, we can conclude for some arbitrary $\mathbf{c}$: $\mathbf{C} = (\Gamma_1\mathbf{z}_1 + \Gamma_2\mathbf{z}_2)/\Gamma_{total} = (\Gamma_1(\mathbf{z}_1+\mathbf{c}) + \Gamma_2(\mathbf{z}_2+\mathbf{c}))/\Gamma_{total}$ and therefore $\Leftrightarrow \mathbf{0} = (\Gamma_1+\Gamma_2)\mathbf{c}$. Since in general $\Gamma_1 + \Gamma_2 \neq 0$, $\mathbf{c}$ must be zero and the distances ρ_1, ρ_2 remain constant.

still remains constant ($\ell_{12} = ||\mathbf{z}_1 - \mathbf{z}_2|| = const.$). The motion still is periodic, but the circle diameters increase until approaching a straight line as radius $\rho \to \infty$. We can differentiate between two cases:

(1) $\Gamma_1 \to -\Gamma_2$ with $|\Gamma_1| > |\Gamma_2|$
From (275) it follows then that vortex 1 with positive circulation Γ_1 and position $\mathbf{z}_1$ is closer to $\mathbf{C}$. Applied to atmospheric sciences this means in other words that the vortex of positive circulation is south of the vortex of negative circulation. This situation is also called a "high-over-low" configuration. From (282) we can conclude:

$$\widetilde{\omega} \to 0 \text{ with } \widetilde{\omega} > 0$$

which is identical to a vortex motion to the west.

(2) $\Gamma_1 \to -\Gamma_2$ with $|\Gamma_1| < |\Gamma_2|$
This case is reverse to case (1) with the vortex with negative circulation being south of the one with positive circulation ("low-over-high" — the typical configuration of the midlatitudes on the northern hemisphere). From (282) it follows:

$$\widetilde{\omega} \to 0 \text{ with } \widetilde{\omega} < 0$$

which is identical to a vortex motion to the east (the prevailing westerlies).

In case of $\Gamma_1 = -\Gamma_2$ both vortices move with the same speed (absolute value) v that is given by

$$v = \frac{|\Gamma_1|}{2\pi\ell_{12}} \tag{283}$$

The direction of the motion can be determined by the considerations above or directly by evaluating the equations of motion (273). An overview over the possible motions of different N=2 point vortex configurations is given in Figure A66.

A.2.2 Point vortex systems of $N = 3$: Relative equilibria

A special type of motion of a N point vortex system is called relative equilibrium. Relative equilibria are characterized by constant intervortical distances. Using the equations of motion with respect to the intervortical distances (equations 263), this leads to the following conditions for the distances ℓ_{12}, ℓ_{13}, ℓ_{23} between the vortices indexed 1,2 and

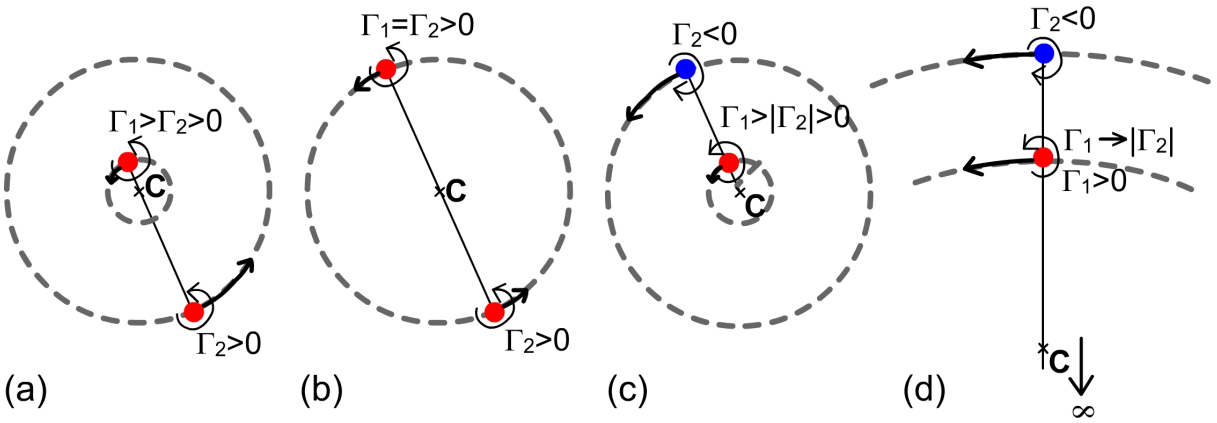

Figure A66: *Overview over the possible motions of a N=2 point vortex system, in general both vortices move on circles around their center of circulation: (a) Vortices with circulations of the same sign, here* $\Gamma_1 > \Gamma_2 > 0$ ("satellite storm")*; (b) same situation as in (a), but the circulations have the same magnitude* $\Gamma_1 = \Gamma_2$ *and the storms move on the same circle; (c) the vortices have circulations of different signs and different magnitudes* $|\Gamma_1| > |\Gamma_2|, \Gamma_1 > 0$*, (d) same situation as in (c) but the circulation magnitudes approach each other, then the center of circulation moves to infinity and the trajectories approach straight lines.*

3:

$$\frac{d\ell_{12}^2}{dt} = \frac{2}{\pi}\Gamma_3 \sigma A \left(\frac{1}{\ell_{23}^2} - \frac{1}{\ell_{31}^2}\right) = 0 \tag{284}$$

$$\frac{d\ell_{23}^2}{dt} = \frac{2}{\pi}\Gamma_1 \sigma A \left(\frac{1}{\ell_{31}^2} - \frac{1}{\ell_{12}^2}\right) = 0 \tag{285}$$

$$\frac{d\ell_{31}^2}{dt} = \frac{2}{\pi}\Gamma_2 \sigma A \left(\frac{1}{\ell_{12}^2} - \frac{1}{\ell_{23}^2}\right) = 0 \tag{286}$$

where A is the area of the triangle spanned by the three vortices and $\sigma = \pm 1$ for counter-clockwise ($\sigma = +1$) and clockwise ($\sigma = -1$), respectively, arrangement of the vortices 1, 2, and 3. From this set of equations we can conclude that in the nontrivial case of $\Gamma_i \neq 0$ either the area A must be zero or the triangle needs to be equilateral to fulfil the above conditions

$$A = 0 \quad \text{or} \tag{287}$$

$$\ell_{12} = \ell_{23} = \ell_{13} \tag{288}$$

If $A = 0$, the vortices are collinear. For collinear vortices to form a relative equilibrium, the temporal change of the area must be zero ($dA/dt = 0$), too. The explicit condition can be expressed by Heron's formula in terms of the intervortical distances. We will not discuss this case further, but more details can be found in Newton (2001, chapter 2.2). The properties of the motion of the relative equilibrium of $N = 3$ point vortices forming an equilateral triangle of side length ℓ can be derived in an analogous manner to the case of $N = 2$ vortices. The three point vortices move around their common center of

circulation **C** with angular velocity $\widetilde{\omega}$ where (cf. Newton, 2001, chapter 2.2.1)

$$\widetilde{\omega} = \frac{\Gamma_{total}}{2\pi\ell^2} \tag{289}$$

For vanishing total circulation $\Gamma_{total} = 0$ the center of circulation lies in infinity and the vortices translate on parallel lines with the same speed v given by (e.g. Müller et al., 2015, their equation (13))

$$v = |\mathbf{v}| = \frac{\sqrt{2(\Gamma_1^2 + \Gamma_2^2 + \Gamma_3^2)}}{4\pi\ell} \tag{290}$$

Assume the following arrangement of the vortices: Vortex 1 and 3 have circulations of the same sign (either positive or negative) and the straight line connecting vortex 1 and 3 lies on the x-axis. The location of vortex 1 coincides with the origin. Then the translational vector at the origin reads (Müller and Névir, 2014)

$$\mathbf{v} = \frac{1}{4\pi\ell} \begin{pmatrix} \sqrt{3}\Gamma_2 \\ \Gamma_1 - \Gamma_3 \end{pmatrix} \tag{291}$$

If the circulation $\Gamma_1 \neq \Gamma_3$ the velocity vector has a non-zero y-component and the triangle translates by an angle with respect to the x-axis. This translation angle α between velocity vector and x-axis is given by (see also Müller and Névir, 2014, their equation (3.9))

$$\alpha = \arctan\left(\frac{\Gamma_1 - \Gamma_3}{\sqrt{3}\Gamma_2}\right) \tag{292}$$

The motion of 2 and 3 point vortices in relative equilibrium with vanishing total circulation has a nice application in the atmospheric sciences even though there are surprisingly few publications on this topic (see Kuhlbrodt and Névir, 2000; Müller et al., 2015, and references therein). The arrangements of certain 2 and 3 point vortex systems resemble atmospheric large-scale weather patterns that are known as high-over-low or omega blocking (see Fig. A67). Those blocking events are long-living, quasi-stationary weather patterns that can have a high impact on society due to caused droughts and floods. Some examples are the heat wave in western Europe in summer 2003 that simultaneously led to heavy precipitation in eastern Europe; the heat wave over eastern Europe and western Russia in summer 2010 that was accompanied by an anomalously high number of wildfires causing smoke and smog in the Russian capital Moscow; at the same time heavy rain events causing floods occurred in Pakistan (e.g. Witte et al., 2011; Lau and Kim, 2012; Müller et al., 2015).

The idea is that the N=2 or N=3 point vortex system of zero total circulation ($\Gamma_{total} = 0$) is arranged in the following manner: The vortex of negative circulation lies north of the

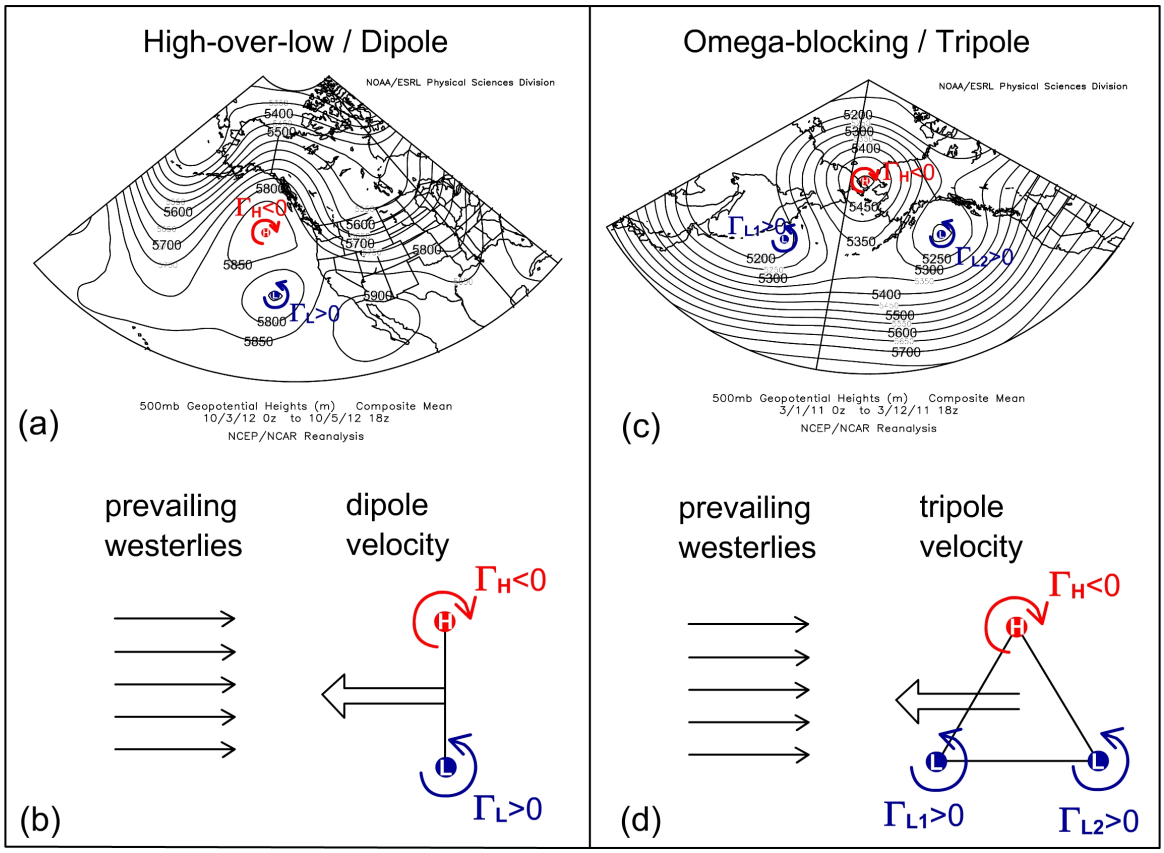

Figure A67: *Examples of (a) high-over-low and (c) omega blocking weather patterns and their (b) dipole and (d) tripole point vortex counterparts. Images of the 500 hPa geopotential height means in (a),(c) are provided by the NOAA/ESRL Physical Sciences Division, Boulder Colorado from their Web site at* `http://www.esrl.noaa.gov/psd/` *based on NCEP/NCAR reanalysis data (Kalnay et al., 1996). Plots are given in polar stereographic projection for the following regions in the North Pacific/dates: (a) 20°-80° N, 180°-280° longitude for 3-5 October 2012; (b) 30°-90° N, 130°-250° longitude for 1-12 March 2011. This figure is adopted and modified from Müller et al. (2015, their Figure 2 which treats the omega/tripole case). Note, that the triangle in (d) is equilateral.*

vortex with positive circulation in case of N=2, and north-east, north-west in case of N=3, respectively (see Figure A67). If in the latter case the positive circulations of the two southern vortices denoted by 1 and 3 are equal ($\Gamma_1 = \Gamma_3$), such a configuration translates with tripole velocity (291) to the west while the typical westerly flow of the midlatitudes points in the opposite direction (i.e. to the east). Likewise, the N=2 point vortex system translates to the west with the dipole velocity given in (283). Therefore, the N=2, N=3 point vortex system can become stationary if the dipole/tripole velocity and the westerly flow are of the same magnitude (see Figure A67). An explicit application of a $N = 3$ point vortex relative equilibrium with respect to Omega blocking situations will be given in section A.3 (published recently in Müller et al., 2015).

A.2.3 Self-similar collapsing/expanding motion of $N = 3$ point vortices

Under certain conditions another interesting solution of a $N = 3$ point vortex system occurs: the self-similar collapse. We have already introduced the equations of motion with respect to the intervortical distances (263). In case of three point vortices, these equations read

$$\frac{d\ell_{12}^2}{dt} = \frac{2\Gamma_3}{\pi}\sigma A\left(\frac{1}{\ell_{23}^2} - \frac{1}{\ell_{13}^2}\right) \tag{293a}$$

$$\frac{d\ell_{23}^2}{dt} = \frac{2\Gamma_1}{\pi}\sigma A\left(\frac{1}{\ell_{31}^2} - \frac{1}{\ell_{21}^2}\right) \tag{293b}$$

$$\frac{d\ell_{31}^2}{dt} = \frac{2\Gamma_2}{\pi}\sigma A\left(\frac{1}{\ell_{12}^2} - \frac{1}{\ell_{23}^2}\right) \tag{293c}$$

where A is the area of the triangle spanned by the three vortices denoted by 123; $\sigma = +1$ for counterclockwise arrangement of the vortices and $\sigma = -1$ for a clockwise arrangement. A self-similar motion requires that the intervortical distances change in the same manner, i.e. the distances then satisfy (e.g. Aref, 2010)

$$\ell_{\alpha\beta}(t) = f(t)\ell_{\alpha\beta}(0) \tag{294}$$

where $f(t)$ is the same function for all distances $\ell_{\alpha\beta} \in [\ell_{12}, \ell_{23}, \ell_{31}]$ and it follows that (Aref, 2010)[84]

$$f(t) = \sqrt{1 - \frac{t}{t_c}} \tag{295}$$

where t_c is the collapse time if $t_c > 0$.
Furthermore, we can conclude:

$$\frac{l_{23}(t)}{l_{31}(t)} = \frac{l_{23}(0)}{l_{31}(0)} = \lambda_1 = const. \tag{296}$$

$$\frac{l_{12}(t)}{l_{31}(t)} = \frac{l_{12}(0)}{l_{31}(0)} = \lambda_2 = const. \tag{297}$$

This means that the shape of the triangle remains invariant while the area can change (Aref, 2010). Relative equilibria discussed in the previous section are therefore a special case of self-similar motions where both the area and the shape of the triangle remain constant. Here, we are interested in the collapse of vortices. This implies that after a finite time t_c the three vortices meet in their center of circulation $\mathbf{C}$ (eq. 139).

[84] Using ansatz (294) in (293) leads to

$$\frac{d\ell_{12}^2(t)}{dt} = \frac{df^2(t)}{dt}\ell_{12}^2(0) = \frac{2\Gamma_3}{\pi}\sigma A\left(\frac{\ell_{13}^2(0) - \ell_{23}^2(0)}{\ell_{13}^2(0)\ell_{23}^2(0)}\right) = const.$$

which means that f^2 is linear in time. Hence, $f(t) = \sqrt{1 - t/t_c}$ with collapse time t_c.

This further means that at time t_c the intervortical distances are zero. Therefore, the conserved quantity M (eq. 271) that depends on the intervortical distances needs to be zero:

Collapse condition 1 :

$$M = \frac{1}{4} \sum_{\substack{\alpha,\beta=1 \\ \alpha \neq \beta}}^{3} \Gamma_\alpha \Gamma_\beta \ell_{\alpha\beta}^2 = 0 \tag{298}$$

We have already mentioned that the other conserved quantity that depends on the intervortical distances is the Hamiltonian H (eq. 267). Using ansatz (294) in (267) gives (e.g. Aref, 2010)

$$H(t) \propto \log\left[f(t)\right]^{3h} \quad \text{with} \quad h := \frac{1}{3}\left(\frac{1}{\Gamma_1} + \frac{1}{\Gamma_2} + \frac{1}{\Gamma_3}\right) \tag{299}$$

Since $H(t) = const.$ is a conserved quantity, this leads to the second condition of collapsing motions (Müller and Névir, 2014):

Collapse condition 2 :

$$h = \frac{1}{3}\left(\frac{1}{\Gamma_1} + \frac{1}{\Gamma_2} + \frac{1}{\Gamma_3}\right) = 0 \quad \Leftrightarrow \quad V = \frac{1}{2} \sum_{\substack{\alpha,\beta=1 \\ \alpha \neq \beta}}^{3} \Gamma_\alpha \Gamma_\beta = 0 \tag{300}$$

where h is the harmonic mean of the three vortex circulations and V was already introduced as conserved quantity in (272) as quadratic sum of the circulations. A zero harmonic mean leads to the conclusion, that the circulations cannot be of the same sign. Then the total circulation is nonzero ($\Gamma_{total} = \Gamma_1 + \Gamma_2 + \Gamma_3 \neq 0$) and the origin can be moved to the center of circulation **C** and the motion can be described in polar coordinates $(\rho_\alpha, \phi_\alpha)$ for $\alpha = 1, 2, 3$[85]. Aref (2010) showed that the shape of the vortex trajectories is given by the equation of a logarithmic spiral in polar coordinates

$$\rho_\alpha = \rho_\alpha(0) \exp\left(-\frac{\phi_\alpha}{2\Omega t_c}\right) \tag{301}$$

where Ω is a real parameter. Aref et al. (1992) and Aref (2010) give a geometric way to find the initial positions that lead to the collapsing/expanding motion of three point vortices (see Fig. A68). An explicit example of a collapsing motion of three point vortices in comparison to a real large-scale low pressure system was already given in section 3.4.5 (see Fig. 14).

[85] A detailed derivation can be found in e.g. Gröbli (1877); Aref (2010).

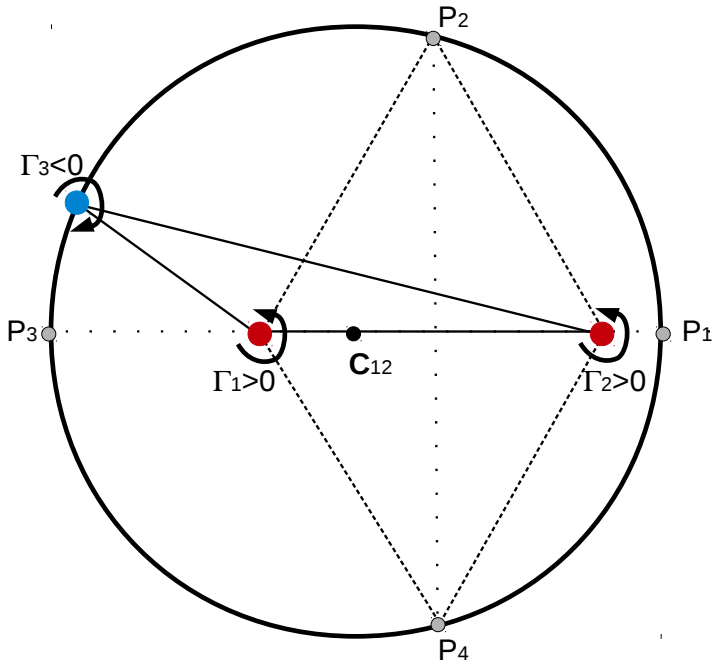

Figure A68: *Geometric way to find the initial positions of the three point vortices leading to self-similar motion. The two vortices 1 and 2 with circulations of the same sign* $\Gamma_1 = 2\,m^2/s$, $\Gamma_2 = 2\,m^2/s$ *(i.e. here positive) are used to construct an equilateral triangle whose one side is equal to the connecting line between the two vortices. The equilateral triangle's tip builds point* P_2 *(or* P_4*). A circle around the center of circulation* $\mathbf{C}_{12}$ *of the two vortices 1 and 2 with a radius that is equal to the distance between the points* P_2 *and* $\mathbf{C}_{12}$ *is constructed. The motion of the three point vortices is self-similar if vortex 3 with circulation* $\Gamma_3 = -1\,m^2/s$ *(i.e. here negative) lies on that circle. Relative equilibria occur if vortex 3 is located at the positions denoted as* P_i *with* $i = (1,2,3,4)$*. Collapsing/Expanding motion occurs for a counterclockwise/clockwise arrangement of the vortices 123. The figure is plotted in the style of Aref et al. (1992) (their Fig. 3).*

A.3 On the problem of point vortex identification in real data and application on atmospheric blocking situations

The point vortex equations were derived under inviscid, incompressible and barotropic conditions. These conditions are approximately observed in atmospheric large-scale motions, too. Therefore, it seems to be reasonable, that the point vortex concept can be applied to the large-scale motions as well.

However, there is obviously a difference between the mathematical concept of a point vortex and a real vortex. Mathematically, point vortices are defined as vortices without spatial extent, i.e. their radius is equal to zero, but their circulation is nonzero and the location of the vortex is assigned to a point in the field. In contrast, real vortices are observed to have a certain extent and we have already discussed the problem of detecting either their size or their intensity in the body of this thesis (see sections 5 and

6). The question is, how can we turn vortices observed in real data to point vortices in order to apply the point vortex equations?

We will use here the W_k-method in order to calculate the circulations of the identified vortices of the reanalysis fields (horizontal wind fields (u, v) and the 500 hPa geopotential height fields NCEP II reanalysis data with a spatial resolution of $2.5° \times 2.5°$ and 6-hourly temporal resolution NCEP, 2000; Kanamitsu et al., 2002). The vortex center will be placed at the center of circulation of each identified vortex, i.e. of a certain area of either positive or negative vorticity and the strength of the vortex will be defined as the corresponding circulation. We will apply the W_k-method in an atmospheric blocking situation. Atmospheric blocking situations are long-lasting, stationary weather periods that are characterized by an anomalous, more meridionally-organized flow in the midtroposphere (e.g. Rex, 1950, who defined explicit criteria for the identification of blockings). Atmospheric blockings are of high relevance to society due to their possible serious impacts caused by drought periods on the one hand and heavy rainfalls on the other. A famous example is the blocking event in summer 2010 in eastern Europe and Russia that caused extremely high temperatures over a period of weeks accompanied by a high number of wildfires in Russia and that at the same time was accompanied by floods and heavy rainfalls in Pakistan (e.g. Lau and Kim, 2012; Witte et al., 2011).

In Fig. A69, some time steps (about 7 days) of an omega blocking situation that determined the weather over the eastern part of Europe and West-Russia in the summer months in 2010 are shown. We denoted the circulation centers of the identified vortices with numbers and tracked them in time with the tracking method introduced in chapter 6.5. In the beginning of the displayed period, the omega pattern is build by the vortices of positive circulations numbered 237, 189, 73 and of negative circulation called 186 (see Fig. A69a). The overall pattern changes in the following days: the vortex numbered 237 intensifies and moves farther south while the vortex numbered 189 weakens while moving northward (Fig. A69b,c) and finally dissipates (Fig. A69d). At the same time, the vortex of negative circulation (numbered 186) starts to weaken while a new negative circulation (number 229) enters the old pattern from the east (Fig. A69d-f). For a short period, the pattern of a high-over-low arrangement composed of the vortices called 229 and 237 is taken (Fig. A69d-f). While being stationary over such a long period, the vortex of positive circulation with number 73 is also exchanged by a new positive circulation (number 319, Fig. A69g). Finally, the old omega pattern is re-established by new vortices of positive circulation called 302, 301 southeast and 319 southwest and negative circulation called 229 north of these two lows (Fig. A69g,h). As a result, the overall large-scale pattern remains stationary, but we have seen that the smaller-scale vortices that form the pattern undergo a much more variable dynamic.

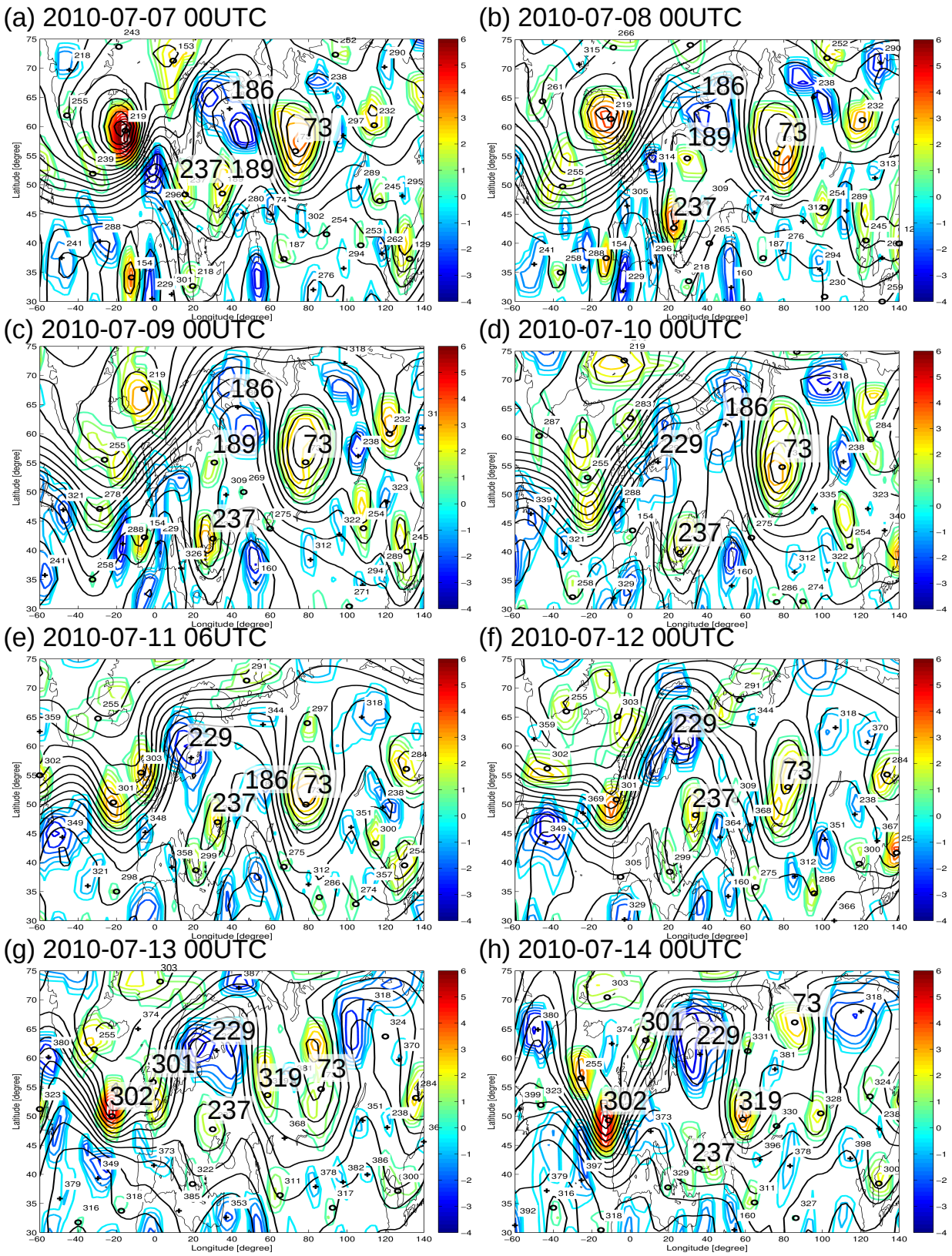

Figure A69: *Some time steps of an omega blocking situation over East-Europe/West-Russia in the period from 7–14 July 2010. Colors: Vorticity* $(10^{-5}s^{-1})$ *plotted in the field of* $W_k > 1$*; black circles/crosses: center of circulation of the identified vortices of positive/negative circulation; numbers above the black circles/crosses: track number.*

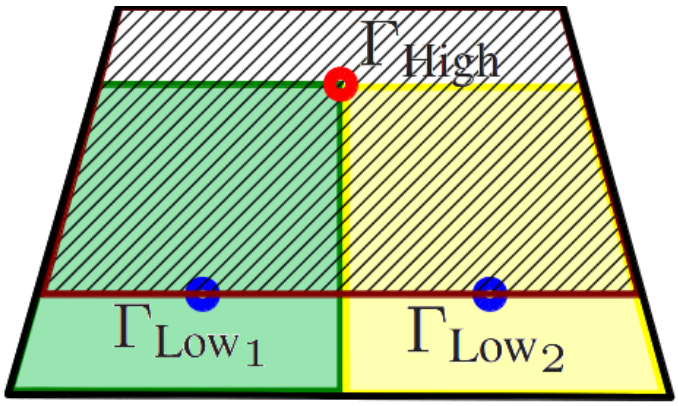

Figure A70: *Trapezoid approximating the region of the omega block. In the green area, the total cyclonic circulation Γ_{Low1} is calculated, and in the yellow area, the total cyclonic circulation Γ_{Low2} is determined. The total anticyclonic circulation Γ_{High} is calculated in the striped area. Figure adopted from Müller et al. (2015) (their Fig. 3).*

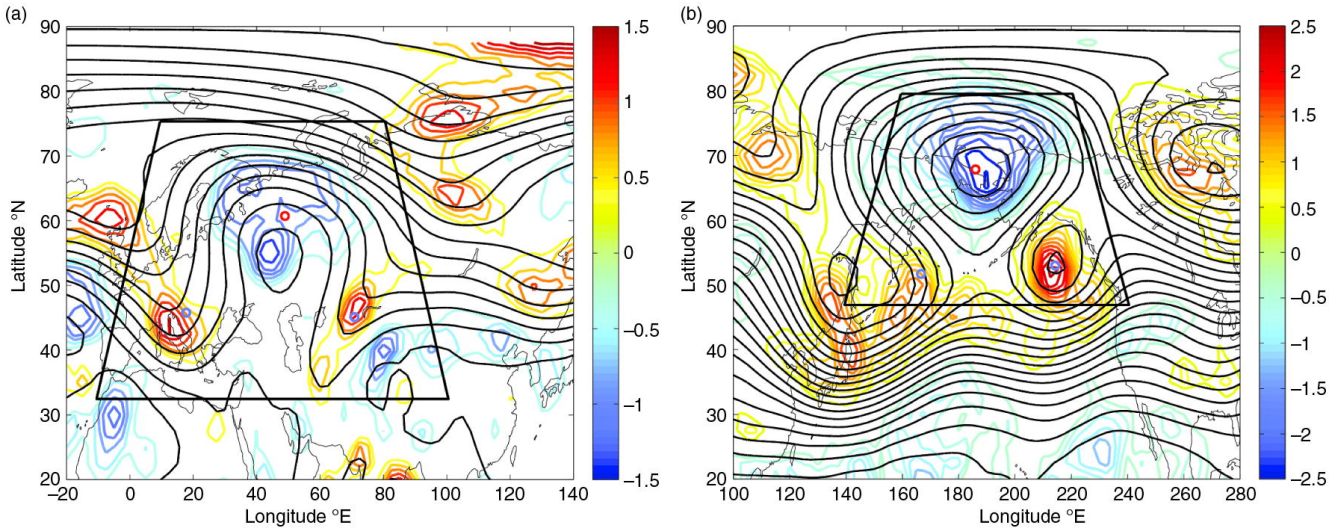

Figure A71: *Temporal averages [(a) 24 July 2010, 00 UTC to 7 August 2010, 18 UTC and (b) 1 March 2011, 00 UTC to 11 March 2011, 12 UTC] of geopotential height (black contours) and relative vorticity (in $10^{-5}\,s^{-1}$, coloured contours). The vorticity is shown in the field of kinematic vorticity number $W_k > 1$. The trapezoids encircle the area of zero total circulation, and the blue and red circles mark centers of the low- and high-pressure areas, respectively. Note the different ranges of vorticity in the plots. Figure adopted from Müller et al. (2015) (their Fig. 4).*

The stationarity of the larger-scale omega pattern led to the idea to approximate the general omega pattern as an isosceles trapezoid composed of a northerly high and two southerly lows that was published in Müller et al. (2015). Instead of using single tracked vortices, all vortex structures — or more precisely every grid point that fulfills $W_k \geq 1$ — inside specified areas of the trapezoid were used to determine the circulations of the three vortices and their circulation centers (see Fig. A70). We have seen (Figure A67) that a configuration likewise to that plotted in Fig. A70 of the three point vortices

with circulations $\Gamma_{Low1}, \Gamma_{Low2}, \Gamma_{High}$ on an equilateral triangle of side length ℓ with total circulation equal to zero ($\Gamma_{total} = \Gamma_{Low1} + \Gamma_{Low2} + \Gamma_{High} = 0$) will move to the west with velocity $v_\Delta = \sqrt{\Gamma_{Low1}^2 + \Gamma_{Low2}^2 + \Gamma_{High}^2}/(4\pi\ell)$. Therefore, the tripole configuration will move in the opposite direction of the typical westerly flow of the midlatitudes. Hence, if the translational speed of the point vortex triangle is of the same magnitude as the westerlies the vortex tripole will remain stationary. Therefore, one requirement to the trapezoid is that the total circulation calculated inside the trapezoid is approximately zero. We derived this by calculating the total circulation of a number of different trapezoidal shapes seperately for every time step in order to find the shape with the minimum absolute value of the total circulation within the shape. We applied this method of pattern recognition successfully to two example omega blockings and could confirm that the average motion of the triangle point vortex arrangement v_Δ is in the order of the averaged westerly flow with only minor deviations of less than 1 m/s (see Fig. A71 for an overview over the mean shapes and fields). Thereby, we could explain the stationarity of the general pattern (explicit details on the method and the results can be found in our publication: Müller et al., 2015).

A.4 Discussion and Conclusion

On the one hand, we have seen in the two examples that the W_k-method used here in order to identify the intensities and locations of vortices seems to give plausible results. Furthermore, the point vortex concept seems to be a useful concept even for atmospheric flows and the dynamics of relative equilibria can explain the stationarity of atmospheric blocks. Müller et al. (2015) and in more detail Hirt (2016) studied the stability of the tripole with respect to perturbations of the vortex positions as well as deviations of the total circulation from zero. Especially, the first analysis is interesting since we observe that the intervortical distance between the two low pressure systems is much larger than the distance between the lows and the high (these distances to the high are in fact approximately equal for both lows). Hirt (2016) sowed that the perturbation of one of the lows position in northern direction has much more dramatic influence on the vortex dynamics than a perturbation in eastern direction. In both cases after some time, the three vortices will move to a collinear state and both lows exchange their positions (the low that was initially southwest of the high will move southeast to it after being in the collinear state and vice versa). However, while in case of the northward perturbation one of the lows turns north of the high, in the other rather observed case of an eastward perturbation both lows stay southward of the high (see Fig. A72 originally published in Hirt, 2016, her Fig. 41). Indeed, we observe in the real cases that the dynamics of the low pressure systems is much more variable than the motion of the high. Sometimes we even observe the transformation of the tripole omega pattern to a dipole structure or the exchange of the lows by "new" ones while the "old" vortices move away with the

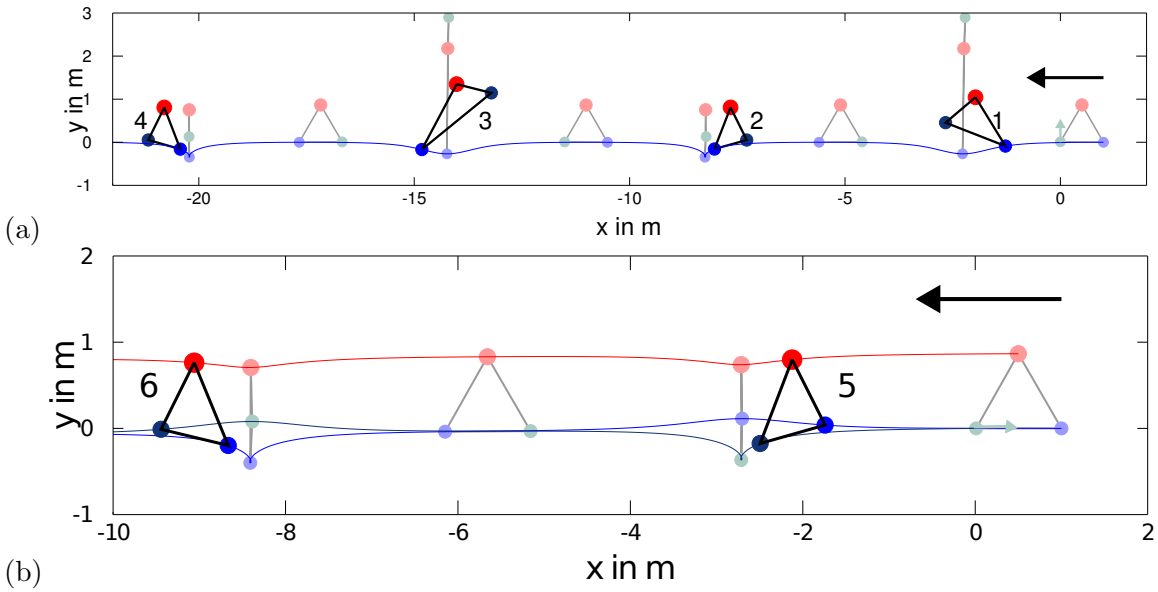

Figure A72: *Perturbations of the relative equilibria states (equilateral triangles) of two N=3 point vortex systems. The initial configurations of the vortices are shown on the right of the figures and the perturbation of the vortex position is indicated by the green arrow (only one vortex position is perturbed). Trajectories of the point vortices are plotted as colored lines. Vortex positions are given as red and blue circles. Examples of the triangle vortex configurations for some time steps are marked by numbers 1 to 6 and in lighter colors. Black arrow on the top right indicates the general direction of motion to the west. The vortex position of the southwesterly low is perturbed (a) in the northern direction and (b) in the eastern direction. Adopted with permission from Hirt (2016) (her Fig. 41). More details can be found in Hirt (2016).*

westerly flow.

However, on average the vortex patterns and configurations seem to be persistent and the point vortex dynamics give realistic results. Hence, the mathematical concept of point vortices offers additional new insights in the real geophysical vortex dynamics also with respect to the stability of weather patterns. However, further analysis in this direction will be necessary but seems to hold promising results.

Appendix B Climatology of kinematic properties in reanalysis data

In this section we will study the climatology of the kinematic properties, i.a. the rates of deformation, divergence and rotation, of the atmospheric flow fields. We will deal with the whole fields. No distinction is made between vortex areas and strain-dominated regions. First, kinematic properties — with emphasis on the kinematic vorticity number — are considered at every point in the field before further analysis.

B.1 Data

For the analysis, we used the global NCEP-DOE AMIP II reanalysis data that has a regular grid resolution of $2.5° \times 2.5°$ and a temporal resolution of 6 hours. For the climatologies we considered geopotential height and wind fields for the period from 1 January 1980 to 31 December 2001 at the following pressure levels (in hPa): 1000, 925, 850, 700, 600, 500, 400, 300, 250, 200, 150, 100, 70, 30, 10.

B.2 Methods: Areal average of W_k and vertical means

For the climatology in section B.3, area-averaged $\overline{W_k}$ values with $\overline{W_k} = \int W_k dA / \int dA$ were calculated for every time step (6-hourly) at each pressure level from 1000 up to 10 hPa for a period from 1 January 1980 to 31 December 2001. Therefore, W_k was computed at every grid point with help of equation (214). Area-averages of W_k were calculated for northern and southern hemisphere separately. An example histogram of the extended W_k^* numbers observed at every grid point of the northern hemisphere for an arbitrary day shows that the W_k number behaves in general well and clusters axisym-

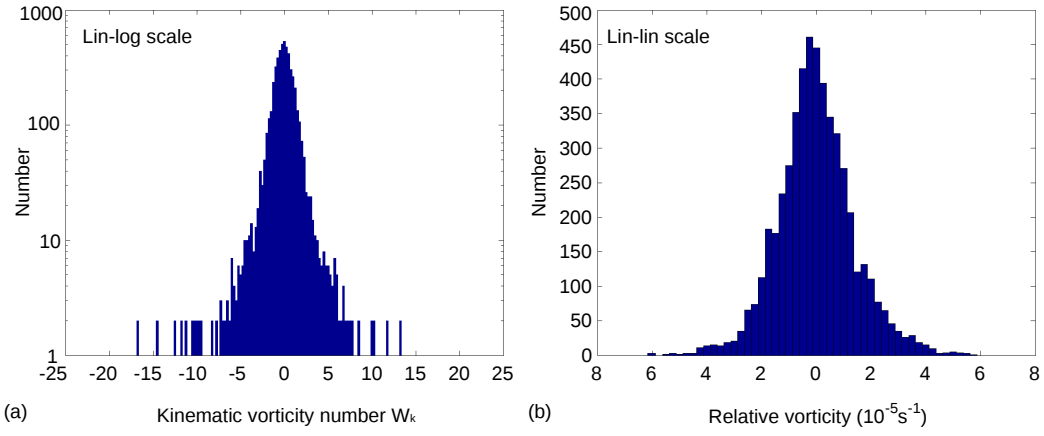

Figure B73: *Histogram of (a) the W_k number and (b) the relative vorticity for an arbitrary date (2011-03-01 00 UTC) evaluated at every grid point of the northern hemisphere.*

metric around $W_k = 0$ just as the relative vorticity (see Fig. B73). However, sometimes we observe values of $W_k = \infty$. Such local singularities ($W_k \to \infty$ when deformation $\|\mathbf{S}\| \to 0$) were excluded prior to averaging. The resulting time series was split into monthly series for further analysis. The monthly temporal means were calculated as trimmed means in order to reduce the influence of outliers: the 10% largest and lowest values were excluded from the calculation of the mean.

The vertical mean of a variable X was calculated by:

$$< X >:= \frac{\int_P^{P_0} X dp}{P_0 - P} \tag{302}$$

where P_0 and P are the lower and upper pressure levels. For a vertical mean over the whole atmosphere $P_0 = 1000$ hPa and $P = 0$ hPa.

B.3 Results: Vertical monthly distribution of area-averaged W_k fields

Figures B74 and B75 show the vertical distribution of monthly mean values of W_k for selected heights for the northern (NH) and the southern hemisphere (SH). While the levels close to the boundaries of the NCEP data - at the atmospheric boundary layer close to the surface (<850 hPa) and at the lower to middle stratosphere near the top of the data (>100 hPa) - have averages smaller than 1 ($\overline{W_k}|_{Bound} < 1$), the middle troposphere has values larger than, but close to 1 ($\overline{W_k}|_{MidAtm} > 1$, here $\overline{W_k} < 1.15$). The distributions show a seasonal dependence with a maximum (minimum) in the hemispheric summer (winter) season at the atmospheric boundary layer and reversed behavior at the stratospheric levels. The stratospheric extrema preceed the inversed extrema in the lower levels by about 1 to 2 months: e.g. the minimum in NH occurs in June/ July at the stratosphere, while the maximum at the atmospheric boundary layer occurs in August. The seasonal variation is less pronounced in the middle troposphere and the reversed behavior between lower and upper levels commence above the 500 hPa level. Furthermore, in the northern hemisphere the monthly $\overline{W_k}$-values up to about 200 hPa are smaller than in the southern hemisphere. The vertical mean $< \overline{W_k} >$ is relatively stable with

$$\begin{aligned} \frac{1}{12}\sum_{i=1}^{12} < \overline{W_k} >|_{SH} &= 1.0342 \pm 0.0018 \\ \frac{1}{12}\sum_{i=1}^{12} < \overline{W_k} >|_{NH} &= 1.0105 \pm 0.0057 \end{aligned}$$

where the standard deviation is added. The standard deviation is larger in the NH where the seasonal variation of $< \overline{W_k} >$ is larger compared to the SH.

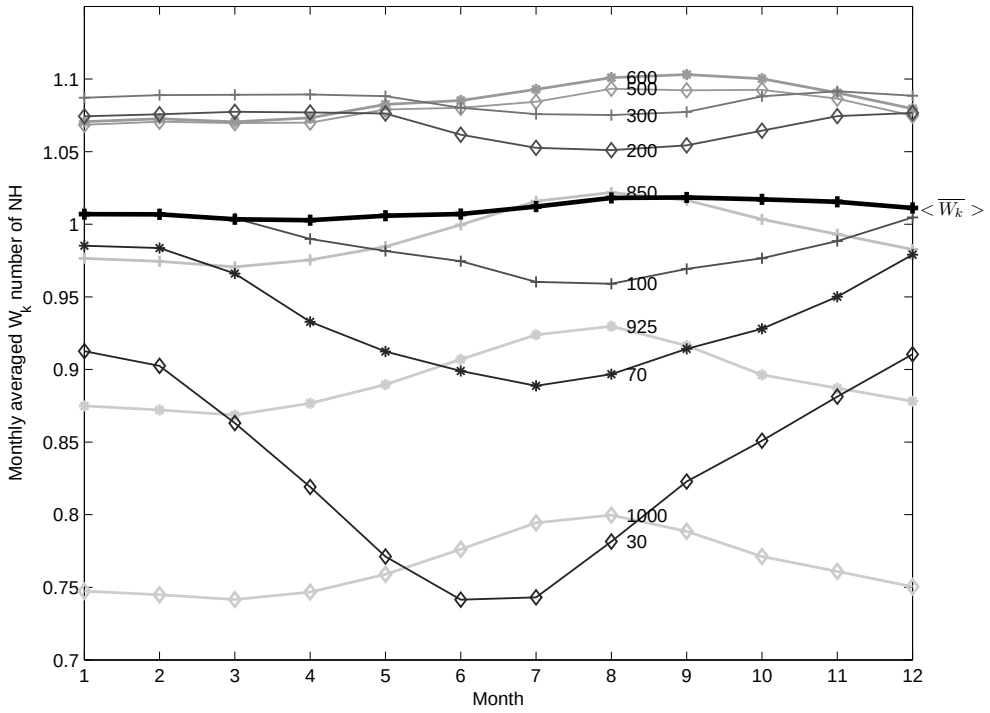

Figure B74: *Vertical distribution of the monthly trimmed means of area averaged* $\overline{W_k}$ *for the* ***northern hemisphere****. Period for calculation of monthly means is 1980-2001.* $< \overline{W_k} >$ *denotes the vertically averages of* $\overline{W_k}$*.*

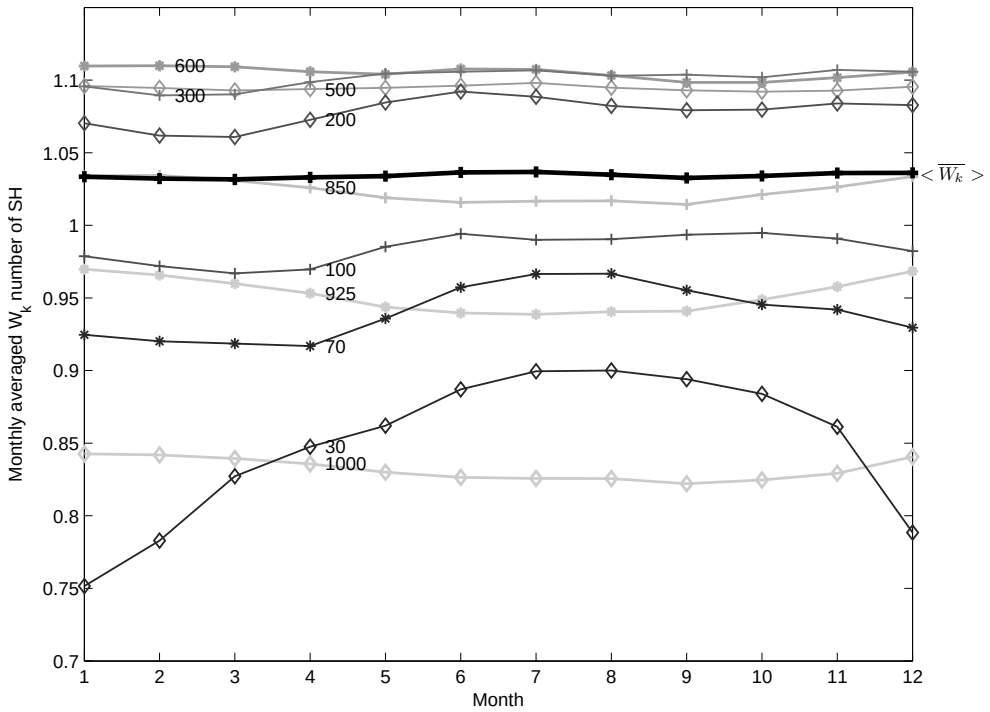

Figure B75: *Vertical distribution of the monthly trimmed means of area averaged* $\overline{W_k}$ *for the* ***southern hemisphere****. Same notation, period as in Fig. B74.*

In order to determine if the monthly values are distinctly different, we plotted the vertical distributions and the corresponding standard deviations of the NH monthly averaged $\overline{W_k}$ values of February and August in Figure B76a. The monthly averages are

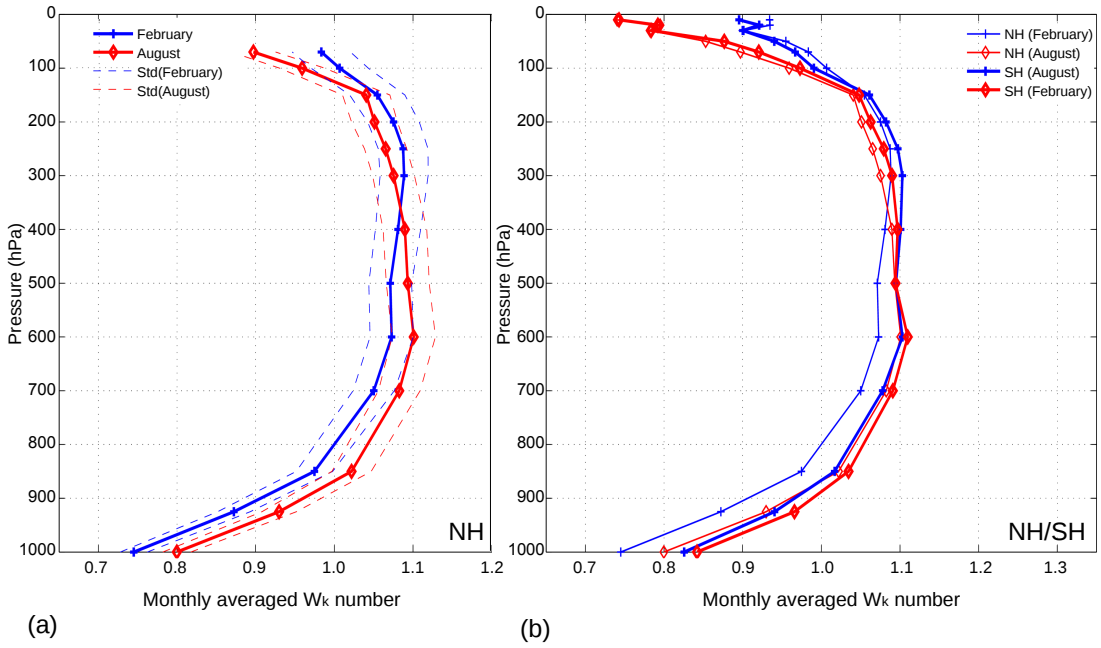

Figure B76: *Vertical distribution of the monthly trimmed means of area averaged $\overline{W_k}$: (a) means for two months (February/August, solid) on the northern hemisphere with standard deviation (dashed); (b) means for two hemispheric summer and winter months (February: NH winter/SH summer and August: NH summer/SH winter) for the northern (NH, thin lines) and southern hemisphere (SH, bold lines) for two hemispheric summer and winter months. Period for calculation of monthly means is 1980-2001.*

different by at least one standard deviation for the 1000 up to the 850 hPa level and above the 100 hPa level. In February, the $\overline{W_k}$-value at the ground is lower than in the stratosphere ($\approx$0.75 compared to $\approx$0.94). This behavior is reversed in August: $\approx$0.8 near the surface compared to $\approx$0.77 above 50 hPa. Although the values in the middle atmosphere (between about 700 and 150 hPa) are not clearly different, the vertical tendency is different: while the curve increases up to a broad maximum around 300 to 250 hPa in February (NH winter), the vertical maximum is already reached in 600 hPa in August (NH summer) slightly decreasing up to 150 hPa before rapidly decreasing above.

The vertical profiles allow a determination of vortex- or rotation-dominated flow levels compared to deformation- and divergence-dominated layers by dividing the vertical distributions into levels of $\overline{W_k} > 1$ and $\overline{W_k} < 1$, respectively. Therefore, the midlevels between about 850 and 150 hPa are vortex-dominated regions and the two boundary-layers (lower than 850 hPa and above 100 hPa) are dominated by divergent and deformational flow. Equation ... showed that the sum of the squares of divergence and vorticity equal the sum of the squares of shearing and stretching deformation and that the sum of the

ratios of divergence/vorticity and deformation equals 1. The influence of divergence on the flow field in the different layers can therefore be seen by the differences of the curves in Figures B77a,b to 1: Near the surface, the dominance of divergence on the flow is

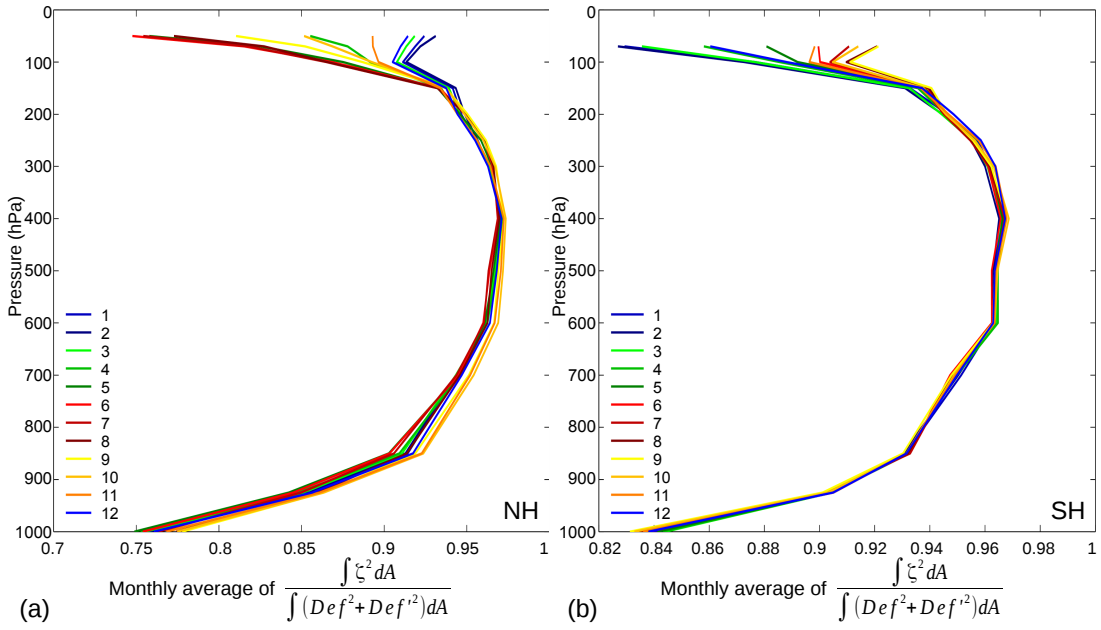

Figure B77: *Vertical distribution of the ratio of area-averaged vorticity squared and sum of deformations squared (without divergence) for (a) the northern hemisphere and (b) the southern hemisphere from 1980 to 2001.*

relatively large (e.g. ≈24% in the NH and ≈16% in the SH for all month); in the middle levels divergence only contributes by about 5% and in the upper levels, the influence of divergence depends on the season. While it is low in the winter seasons (5−10%), it increases in the summer months up to about 35% in both hemispheres (see Fig. B77a,b). On the other hand, this statement can be formulated as: in the hemispheric winter months, the influence of the polar vortex is dominating in the stratosphere compared to the summer flow.

Furthermore we have calculated how much vorticity is concentrated in the vortices identified by the W_k-method. In general, about 60 % of the vorticity (positive and negative) is concentrated in the identified vortex regions on both hemispheres. Thereby, the lows occupy about 15 % (NH and SH) and the highs about 20.6 % (NH) to 22 % (SH) of the total area on the hemispheres. This behavior is stable throughout the year and through all levels except of the 1000 hPa level, which has smaller values compared to the other levels: 49 %/ 46 % (53 %/ 53 %) of the positive/ negative vorticity is concentrated in about 12 %/ 14 % (13 %/ 17 %) of the area on the NH (SH).

B.4 Conclusions

The most important findings are:

- The vertically integrated W_k number is approximately 1 independent of the season. Thereby, this reveals an approximate global three-dimensional balance between the deformations (i.e. the symmetric parts of the motion) and the rotations (i.e. the antisymmetric parts).
- We identified divergence-reduced levels between about 700 and 300 hPa and levels that are stronger influenced by the divergence (near the ground at in the stratosphere during the hemispheric summers).
- Furthermore, we found that about 15% of the total area on each hemisphere are covered by cyclonicly-rotating vortices and about 21-22% are covered by anticyclonicly-rotating vortices.

Appendix C Comparison of the W_k features in NCEP, CFSR and WRF data on basis of the energy of displacement and the atmospheric moment

This chapter ties in with the study of the W_k features in the three differently resolved NCEP, CFSR and WRF data sets which was presented in chapter 7. So far, we have only analyzed the vortex structures (W_K features) identified in differently-scaled data sets with help of the vortex properties circulation and radius. These properties stem from theoretical vortex models such as the Rankine vortex model that revealed the significance of circulation and size (vortex radius) on the wind field around an axisymmetric vortex in an inertial, non-rotating reference frame (see chapter 4). These equations are similar in structure to the horizontal equations of motion that describe a vortex that is in cyclostrophic balance in a noninertial, rotating reference frame (see chapter 3.2.1.3). On a rotating planet however, the cyclostrophic balance does not hold for the larger scales that are also influenced by the planet's rotation rate. More appropriate parameters characterizing such large-scale vortices might be the energy of displacement and the atmospheric moment, respectively. We introduced these parameters earlier in this thesis in chapter 5 as the mass-specific/mass-related energy that was necessary to produce the vortex (see also Schielicke and Névir, 2009, 2011, 2013). We will use the energy of displacement and the atmospheric moment in the following in order to compare the data sets.

C.1 Data and Methods

In chapter 5.5 we showed that the energy of displacement e can be expressed in terms of circulation Γ and vortex area A (see Table 7 for more details). These parameters were already determined with help of the W_k-method for W_k features in the different data sets (see previous sections) and this data will be the basis for the calculation of the energy of displacement e and the atmospheric moment M_a. However, we additionally require knowledge over the whole life cycle of the W_k features, especially in case of the atmospheric moment. More precisely, we need to find the moment of maximum intensity as well as the mean size and track length in order to estimate the volume covered by each vortex over its life time. Therefore, it is necessary to track the W_k features, i.e. to connect the features in time. We used a simple tracking method based on the calculation of vortex area overlaps. These overlaps were found by moving the $W-k$ features identified at time step t a half time step Δt forward and the W_k features identified at the following time step $t+\Delta t$ a half time step backward. The forward/backward motion is calculated separately for each vortex by the mean wind inside the area covered by the

vortex (more details on the tracking method are given in chapter 6.5).

Due to the high computational costs, we only concentrated on cyclonic systems at the 1000 hPa level in the NCEP data (January to December 1999) and in the CFSR data (only January 1999). Note, that tropical cyclones are not included since we restricted the analysis to tracks that lie within a latitudinal band between 30°N and 80°N. In case of the simulated WRF data, we used one of the midlevels (level 7 at about 3.5 km height) to form the tracks of cyclonic W_k features due to the high activity of the convective cells at these levels.

We only considered systems that lived at least 3 time steps (=12 hours in the NCEP data) and 5 time steps (=4 hours in the CFSR data), respectively. No such restrictions on the lifetimes were done for the different WRF runs. In total, we found 6743 tracks (NCEP) and 26386 tracks (CFSR) that were non-stationary. In the WRF data. the number of tracks depend on the set-up: 991 (linear-shear run), 845 (original run), and 1217 (doubled-speed run).

For comparison reasons, we will additionally use the USA tornado data set of the Service Storm Prediction Center (SPC) of the National Oceanic and Atmospheric Administration (NOAA) (see Storm prediction warning center, 2016) as we have used in Schielicke and Névir (2011). We analyzed the tornado data in the period from 1950 to 2006 (the Fujita scale era). The data sets consists of the following parameters: i.a. the tornado location, time of occurrence, the tornado path length, the width of the path and the Fujita intensity class which follows from an estimate with help of a damage analysis. Each Fujita intensity class (F-class) is connected to a theoretical wind speed via: $v(F) = 6.30ms^{-1}(F+2)^{3/2}$. Per definition, the velocity range of a F-class starts with integer values of F ($F = [0,1,..,5]$) and the average value of the velocity class as $< v(F) >= 6.30ms^{-1}(F+2.5)^{3/2}$. We will consider only data with non-zero values of path length, width and with an assigned Fujita classification. This applies to 46866 cases.

C.1.1 Estimating the energy of displacement on basis of the modified Rankine ansatz

For the reanalysis data (NCEP/CFSR), we will calculate the energy of displacement based on the modified Rankine ansatz under the assumption of gradient wind balance as (see Table 7)

$$\widetilde{e}_{tc} = \left(\frac{1}{2\pi}\right) \cdot \left(\frac{1}{2}\frac{\Gamma^2}{A} + \frac{2}{3}f\Gamma\right) \qquad \text{(gradient wind balance)} \tag{303}$$

since the radii observed for the W_k features are mostly subsynoptic, the choice of the gradient wind balance seems to be an appropriate choice — even in case of the coarsely-scaled NCEP data. Based on the modified Rankine ansatz the energy of displacement of the WRF data will be calculated with help of the expression derived for convectively-scaled data as (see Table 7)

$$\widetilde{e}_t = \left(\frac{1}{2\pi}\right) \cdot \frac{1}{2}\frac{\Gamma^2}{A} \qquad \text{(cyclostrophic balance)} \tag{304}$$

In both cases, we will use the maximum value of the circulation that was detected over the vortex lifetime. We will take mean values of the Coriolis parameter $f = 2\Omega \sin\phi$ with mean latitude ϕ and Earth's rotation rate $\Omega = 2\pi/day \approx 7.27 \cdot 10^{-5}\,\mathrm{s}^{-1}$. The vortex area A will be determined at the moment of maximum circulation, too.

Moreover, we would like to estimate the *total energy of displacement* that additionally takes into account the "*far-field*" influence of the vortex on its surrounding. Thereby, we need to integrate the horizontal equations of motion not only from the center to the vortex core radius (which gives the energy of displacement) but also farther outside the vortex core. We have seen in chapter 5.2.5.1 that this outer-core influence is of equal size as $\widetilde{e}_t$ in case of the cyclostrophic balance (equation 181). Hence, the total energy of displacement would be twice $\widetilde{e}_t$ in this case:

$$e_{conv} = 2 \cdot \widetilde{e}_t \tag{305}$$

where e_{conv} denotes the total energy of displacement of a cyclostrophicly-balanced vortex. In case of the geostrophic balance that only considers the Coriolis acceleration term, the outer-core integral over the horizontal equations of motion increases however with increasing distance from the vortex core radius (see chapter 5.2.5.2). This increase further depends on the value of the exponent α in the modified Rankine ansatz (see Table 6). For the sake of convenience, we will assume that the total energy of displacement is equal to twice the energy of displacement derived for the inner core ($\widetilde{e}_{tc}$) in case of the gradient wind balance, too:

$$e_{cycl} = 2 \cdot \widetilde{e}_{tc} \tag{306}$$

For an exponent of $\alpha = 1/2$ this would be approximately equal to take into account a region around the vortex with a radius of approximately twice the vortex core radius.

For an isolated low pressure system as depicted in Figure C78 the doubling of the vortex core radius would nearly capture the total depression. Hence, this resembles a pressure-based ansatz of vortex size determination. However, it should be remembered that common pressure-based method can give inconsistent results especially in th case of

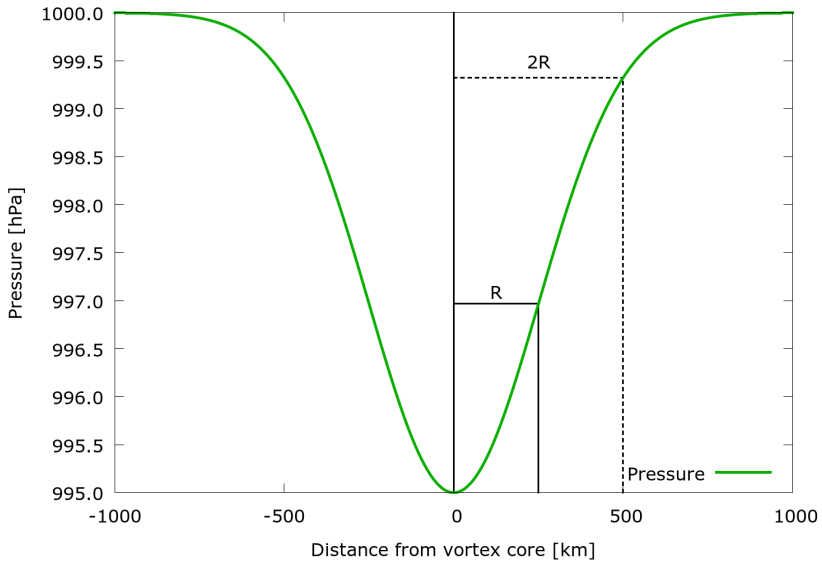

Figure C78: *Illustration of how the doubling of the vortex core radius captures a significant part of the total depression on the example of the radial pressure profile of a Gaussian vortex as defined in chapter 6.6 (for details on the set-up see 6.6.2).*

strong background flows (see e.g. chapters 6.2 and 6.6). The ansatz here is still based on the kinematic W_k-method which seems to give more consistent results in such flows (see e.g. chapter 6.6).

C.1.2 Estimating vortex volumes and atmospheric moments

For the calculation of the atmospheric moments, we need to estimate the whole volume V of the vortices. The total atmospheric moments are estimated by

$$M_{a,cycl} = Ve_{cycl} \quad \text{(NCEP/CFSR)} \tag{307}$$

$$M_{a,conv} = Ve_{conv} \quad \text{(WRF)} \tag{308}$$

where we will use the energy of displacement expressions derived by the modified Rankine ansatz (see section C.1.1). Similar to Schielicke and Névir (2011), we can write $V = L \cdot H \cdot L_{track}$ where $L = 2R$ is the mean vortex width, H is the height and L_{track} is the length of the track. According to Kurgansky (2000) the vortex height is proportional to the vortex width for convective vortices ($H \sim L$ or $H/L = const.$). We will consider this assumption also for larger-scale (pancake-like) vortices here although the constant factor is different from that of the convective (tube-like) vortices[86] We then

[86]Due to the relatively fixed height of the troposphere, the assumption of the proportionality of vortex height and width might not hold anymore. It is an interesting question at what point this assumption breaks since it seems to be reasonable that smaller systems are shallower than larger systems (which is also confirmed by Lim and Simmonds, 2007, who found that the mean radius of shallow cyclones is smaller than that of vertically well-organized systems). However at this point, this is beyond the scope

Table C19: *Aspect ratios H/L of different vortex types or scales from Table 1 and from the results derived in the previous chapters 7.4 (NCEP),7.5 (CFSR) and 7.6 (WRF). The height of the convective cells was estimated from Figure 61 where the supercell reaches up to a height of 30 model levels which is equal to about 15 km.*

Vortex type/scale	H/L from Table 1	H/L from results in chapters 7.4-7.6
Tornadoes:	2000m/100m = 20	2000m/100m = 20
Convective cells (WRF)	10 km/1 km = 10	15 km/1.8 km = 8.3
Mesoscale (CFSR):	10 km/100 km = 0.1	10 km/160 km = 0.0625
Synoptic scale (NCEP):	10 km/1000 km = 0.01	10 km/240 km = 0.042

can estimate the lifetime volume by

$$V = H \cdot L \cdot L_{track} = \frac{H}{L} \cdot L^2 \cdot L_{track} = \frac{4}{\pi} \frac{H}{L} \underbrace{\pi R^2}_{=A} \cdot L_{track} \tag{309}$$

where A is the vortex area which is one of the parameters that was already determined with help of the W_k-method. For the differently-scaled data, we will assume different aspect ratios H/L (summarized in Table C19, right hand side). We also observe that the rough estimations made at the beginning (Table 1) fit relatively well with our observations in Table C19.

Furthermore, we need to consider that the differently-resolved data sets have a lower boundary under which smaller or less-intense systems are missing. These systems would add to the total number of detected systems. In general, a complementary cumulative distribution function starts with a value of 1 since it displays the number larger than a certain threshold divided by the total number of systems. In order to account for the different resolutions of the data, we will additionally divide these numbers by an appropriate factor F. Let us assume that the WRF data has a factor of $F_{WRF} = 1$ and is therefore the reference data whose CCDF starts with one. The resolution of the WRF data is 1 km. Furthermore, we will assume that the tornado data has an approximate resolution of 100 m and therefore is different from the WRF data by a factor of $F_t = 0.1$. Likewise, we will estimate the difference between the WRF data and the CFSR data by a factor of $F_{CFSR} = 50$ which is also approximately the difference in the resolutions of the two data sets. Although the resolutions of the CFSR and the NCEP data differ only by a factor of 5, we will use another approach in order to estimate the factor F_{NCEP}: We found 6743 non-stationary tracks in the NCEP data in 12 months and 26386 tracks in the CFSR data in 1 month in the same region (northern hemisphere between 30°N and 80°N). This means that we detected about 47 times more tracks in the CFSR data.

of this thesis.

Therefore, we estimate $F_{NCEP} = 47 \cdot F_{CFSR} = 2350$. This factor is about ten times larger than the factor of increase in resolution and accounts for the nonlinear dependence of identified vortices on the grid and temporal resolution. Summarized the factors are

Tornadoes:	$F_t = 0.1$
Convective cells (WRF):	$F_{WRF} = 1$
Mesoscale (CFSR):	$F_{CFSR} = 50$
Synoptic scale (NCEP):	$F_{NCEP} = 2350$

We will divide the cumulative numbers of the CCDF by these factors in order to account for the underestimation of W_k features in coarser resolved data sets.

C.2 Results and Comparison to Schielicke and Névir (2009,2011)

An overview over the complementary cumulative distributions (CCDF) of all data sets (WRF, CFSR, NCEP) concerning the energy of displacement (abbreviated as *eod* in the following) is given in Figure C79. Besides the energy of displacement expressions based on the modified Rankine ansatz, we also plotted the US Tornado data (as published in Schielicke and Névir, 2011).

Applying exponential fits to the synoptic range[87] of the data confirms the nearly identity of the typical decay rates of the tornado and the CFSR data, at least over a certain range of energy of displacement values (see Figure C80). However, we also observe that the less-intense systems — especially the CFSR data — do not decay like an exponential distribution but rather seem to follow a power law decay.

While the reanalysis data and the tornado data are characerized by almost similar decay rated, the simulated WRF data decays significantly faster for values larger than about 500 J/kg and its range is considerably smaller than that of the other data sets. Possible reasons for this stronger decay of the WRF simulated data might be the following:

- The simulations mostly produce small-scale convective cells. In the runs characterized by a curved hodograph (orginal, doubled-speed) probably only one of the cells is long-lived and deviates from the mean wind fitting the general definition of supercells. Hence, we might have to few data at higher intensity range.
- We investigated the WRF cells at one of the midlevels at about 3.5 km height while the other data sets are investigated at or near the ground.

[87] We estimate the synoptic range concerning the energy of displacements e for magnitudes approximately larger than $e > 200\,\mathrm{J/kg}$. This is equal to wind speeds in the order of 10 m/s: for $v = 10\,\mathrm{m/s}$, we estimate $eod = v^2 + fvR \approx 200\,\mathrm{J/kg}$ where $R = 10^6$ km and $f = 10^{-5}\mathrm{s}^{-1}$).

- Although the simulations produce realistic features, the set-ups are still highly idealized (e.g. single initial warm bubble that triggers the convection).

We are not able to explain the different behavior of the simulated data in the framework of this thesis. For this purpose further investigations, simulations with various initial set-ups and a comparison to real observational data are necessary. This would be an interesting topic for future studies. However, it should be noted that the tail of the WRF distribution is regardless exponential. As we have seen in chapter 7.3.2 the characteristic decay rate changes by a constant factor if the variable is multiplied by the same factor, but the exponential structure is conserved. The same holds for the tails of the energy of displacement distributions of the other data sets.

Furthermore, we observe a different behavior for the less-intense energy of displacement ranges, Here, the curves rather show a power law behavior, at least over certain ranges of the data (see Figure C79). In the following we would like to take a closer look at the single contributions of the Coriolis and centrifugal force terms in comparison to the calculated energy of displacement.

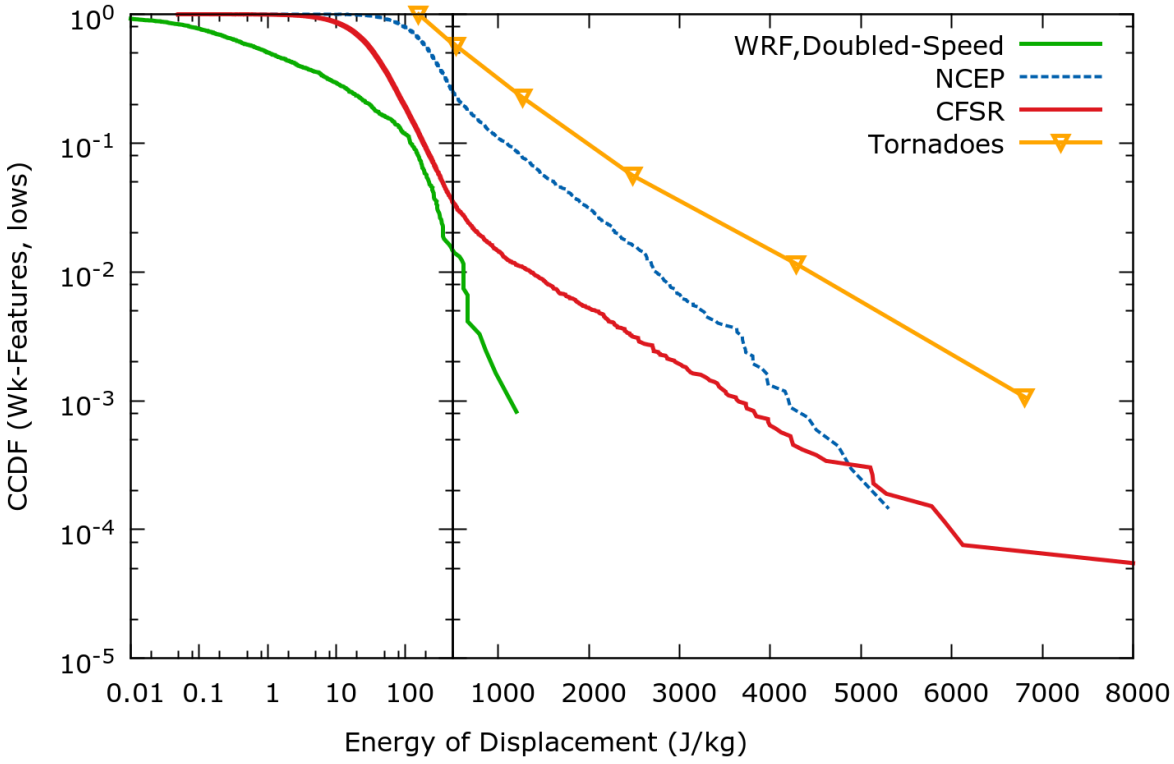

Figure C79: *Normalized complementary cumulative distributions (CCDF) of the energy of displacements e for different data sets. US-Tornado data (1950-2006) was added as published in Schielicke and Névir (2011) for comparison reasons.*

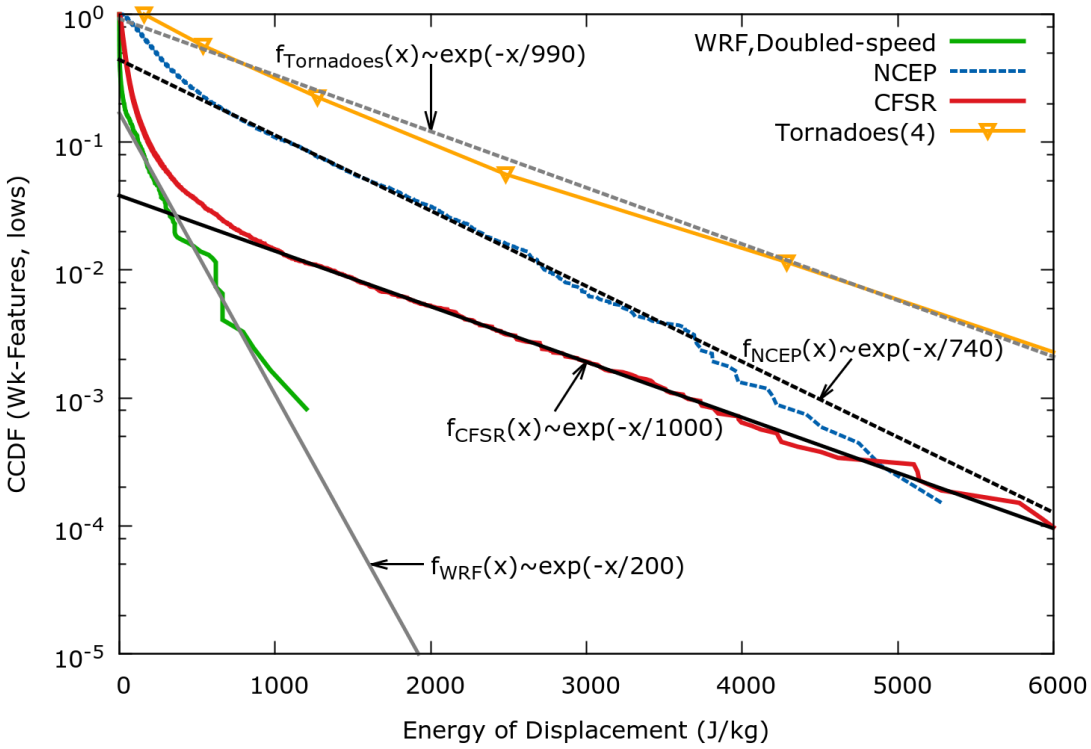

Figure C80: *Exponential fits applied to a subset of the synoptic range plotted in Figure C79: Normalized complementary cumulative distributions (CCDF) of the energy of displacements e for data sets of different resolutions. Exponential fits were applied to the energy of displacement calculated with help of the modified Rankine ansatz. Fitting ranges in J/kg are: WRF* $[100:1000]$*; NCEP* $[600:4000]$*; CFSR* $[1000:4000]$*; the tornado data was fitted for all Fujita-scales (F0-F5, energy of displacement range* $[10:7000]$*).*

C.2.1 Coriolis and centrifugal force contributions

In order to study the influence of the Coriolis and centrifugal terms we plotted the energy contributions in four different ways (see Figure C81):

(1)	Modified Rankine ansatz (chapter 5.2.5)	$e_1 = 2 \cdot \frac{1}{2\pi}\left(\frac{\Gamma^2}{2A} + \frac{2}{3}f\Gamma\right)$
(2)	Coriolis term	$e_2 = 2 \cdot \frac{1}{2\pi} \cdot \frac{2}{3}f\Gamma$
(2b)	Geostrophic balance (Schielicke and Névir, 2009)	$e_{2b} = 2 \cdot \frac{1}{2\pi}f\Gamma$
(3)	Centrifugal term	$e_3 = 2 \cdot \frac{1}{2\pi}\left(\frac{\Gamma^2}{2A}\right)$

Note that the geostrophic balance term in (2b) is equal to 3/2·Coriolis term.

In case of the NCEP data, calculations (1) and (2b) give almost identical distributions (see Figure C81a, blue solid and green dashed line). This means that the centrifugal

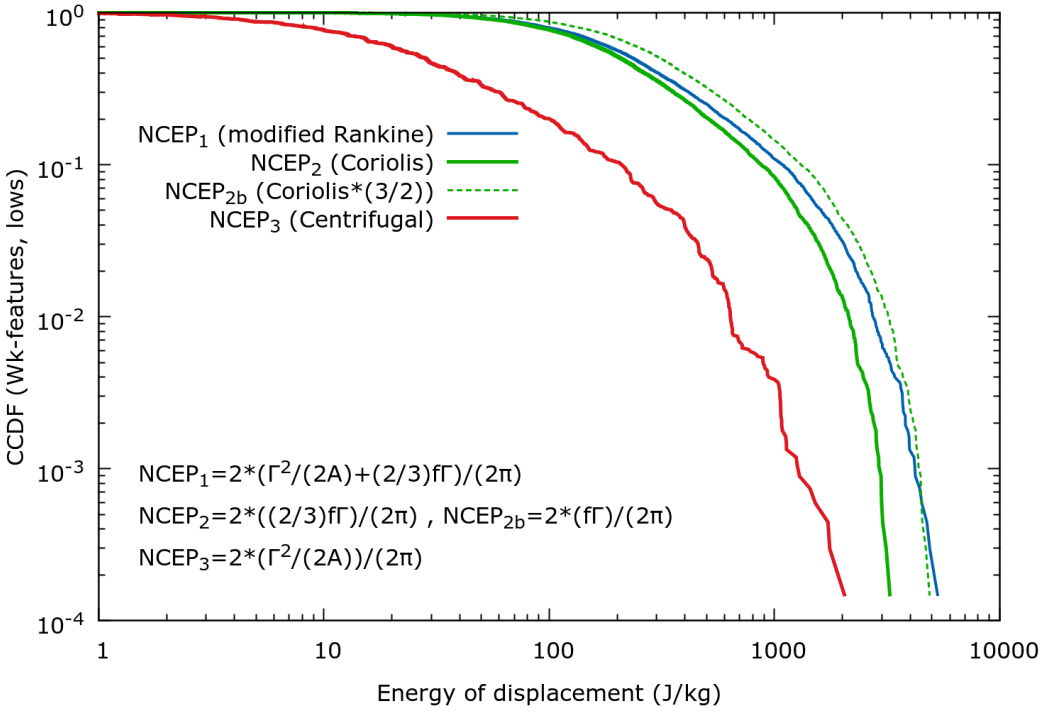

(a) NCEP data

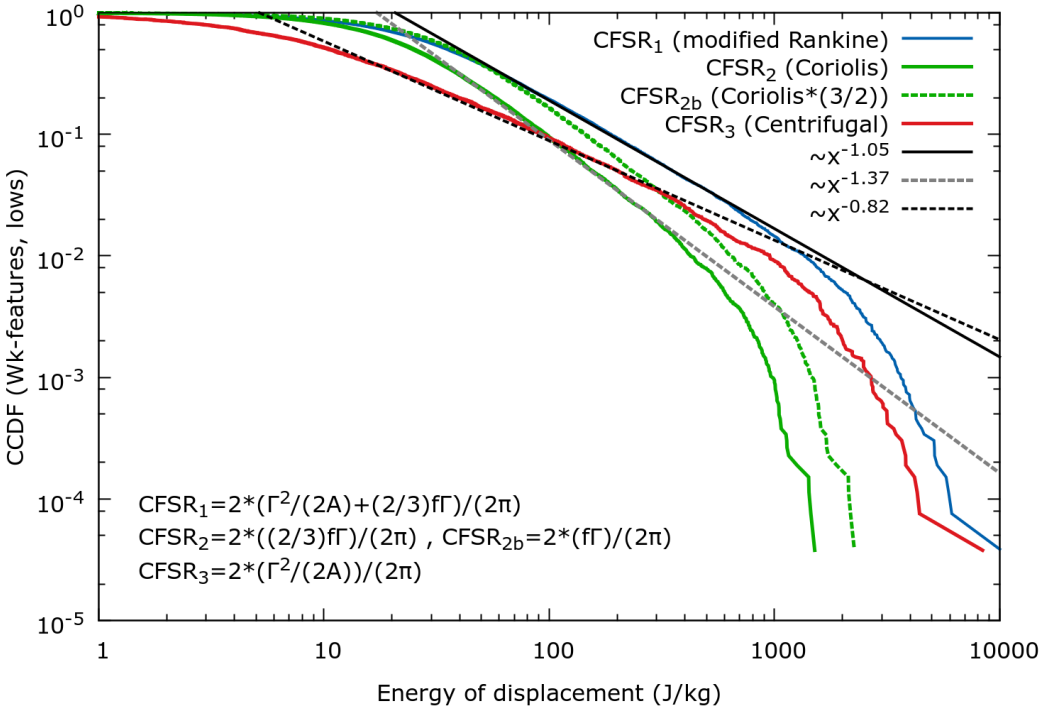

(b) CFSR data

Figure C81: *Comparison of the complementary cumulative distributions (CCDF) with respect to different energy of displacement calculations for (a) NCEP and (b) CFSR data. Indices indicate the way of calculation: Index 1:* $e_1 = 2 \cdot (\Gamma^2/(2A) + (2/3)f\Gamma)/(2\pi)$ *(modified Rankine ansatz); index 2:* $e_2 = 2 \cdot ((2/3) \cdot (f\Gamma))/(2\pi)$ *(Coriolis term); index 2b:* $e_2b = 2 \cdot (f\Gamma)/(2\pi)$ *(Coriolis term multiplied by 3/2); index 3:* $e_3 = 2 \cdot (\Gamma^2/(2A))/(2\pi)$ *(centrifugal term). Fitting ranges in (b): CFSR*$_1$ *(modified Rankine)* $[50 : 1000]$ *J/kg; CFSR*$_2$ *(Coriolis)* $[30 : 1000]$ *J/kg; CFSR*$_3$ *(Centrifugal)* $[10 : 1000]$ *J/kg.*

term $\Gamma^2/(2A)$ is only approximately one third of the Coriolis term:

$$\frac{\Gamma^2}{2a} \approx \frac{1}{3} f\Gamma$$

Hence, the centrifugal term has only minor impact on the total magnitude of the energy of displacement (compare red and blue solid lines in Figure C81a). Only for the tail the influence of the centrifugal term (3) increases, however, it is still smaller than the contribution of the Coriolis term (2).

The CFSR data behaves differently (see Figure C81b): The influence of the centrifugal force is significantly larger for energy of displacement magnitudes of $e > 100\,\mathrm{J/kg}$ and increases with increasing e. However, the energy of displacement e calculated by the modified Rankine ansatz experience a stronger influence by the Coriolis term in the range of small e. A multiplication of the Coriolis term by a constant factor leads to a shift of the boundaries of these ranges. In the case presented here, this shift is only minor. Hence the high magnitudes of e are still dominated by the centrifugal term. Moreover, we observe a power law decay over a range of about two orders in magnitude for each of the presented terms.

In case of the different WRF runs we observe that the energy of displacement distributions shows analogously behavior with power law decay for lower values of e and an exponential decay in the tails (see Figure C82). The parameters are nearly equal for all runs. Additionally, we calculated the associated Coriolis terms. It is obvious that the Coriolis term has insignificant influence in comparison to the centrifugal term.

C.2.2 Atmospheric moments

Finally, we plotted the atmospheric moment distributions of all data sets in Figure C83. The atmospheric moments and the complementary cumulative distributions were derived as is described in section C.1.2. The atmospheric moments are the mass-related equivalent to the mass-specific energies of displacement and can be interpreted as vortex magnitudes. Likewise to the seismic moments of earthquakes, the atmospheric moments describe the total magnitude of the vortex or the total energy released during the vortex life time. Atmospheric vortices cover a broad range of atmospheric moments (see Figure C83).

The CFSR data seems to approximately follow a power law over a range of five orders for of atmospheric moments between 10^{17} J and 10^{22} J. Although the other data sets show no clear power law behavior, the data sets seem to compound the CFSR power law in other ranges of the atmospheric moments. Thereby, the smaller the systems the smaller are the values of the atmospheric moments. The power law exponent has a value of about

≈ 0.6 which is of comparable order to the published power law exponents of the famous Gutenberg-Richter law of earthquake magnitudes (seismic moments). The exponents of the Gutenberg-Richter law are close to $2/3 \approx 0.67$ (Ben-Zion, 2003) depending on the region with smaller exponents in subduction zones compared to mid-ocean ridges (e.g. Bayrak et al., 2002). E.g. for the southern California region, we observed an exponent of about 0.8 (see Figure 20). For comparison reasons, we also added the fit to the low values of the tornado moments that leads to an exponent of about 0.2 as in Figure 20 and published in Schielicke and Névir (2013). This should show the possible range of the power law exponents. We will conclude this analysis with two observations:

(1) The atmospheric moments of the W_k features in the CFSR data set are power-law distributed over a large range of moments with an exponent comparable to that of the Gutenberg-Richter law of earthquake magnitudes;

(2) All other data sets of vortices on different scales are nicely enveloped by the power law fitted to the CFSR data.

However, these results need to be further proved carefully. This could be done in different ways. One possibility would be to resolve the finer scales in the CFSR data set

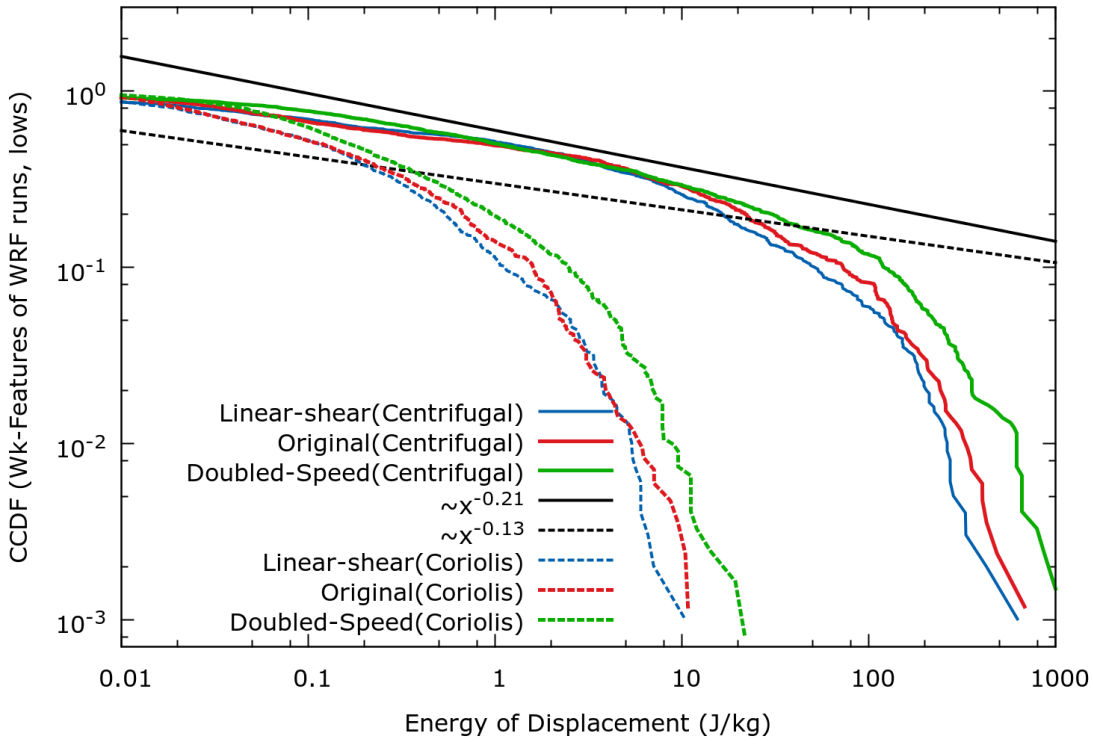

Figure C82: *Complementary cumulative distributions (CCDF) concerning the energy of displacement e and its contributions for different WRF runs. The centrifugal term is calculated as* $2 \cdot \frac{1}{2\pi}\left(\frac{\Gamma^2}{2A}\right)$ *and the Coriolis term as* $2 \cdot \frac{1}{2\pi} \cdot \frac{2}{3} f\Gamma$ *with* $f = 10^{-4} s^{-1}$. *The power law exponents were estimated in the ranges* $[0.03 : 0.5]$ *J/kg (Original run) and* $[0.1 : 10]$ *J/kg (Doubled-speed run).*

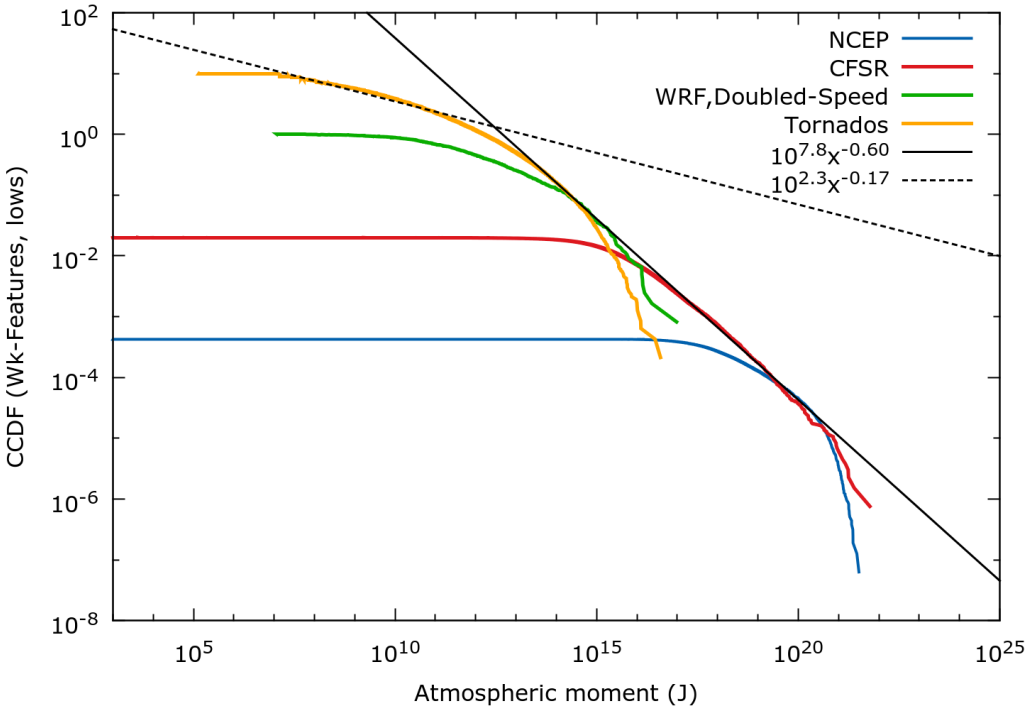

Figure C83: *Modified complementary cumulative distributions (CCDF) of the atmospheric moments for different data sets. Atmospheric moments of the US-Tornado data series (1950-2006) as published in Schielicke and Névir (2011, 2013) were added for comparison reasons. Fit ranges: CFSR data* $[10^{17} : 10^{22}]$ *J; Tornado data* $[10^{7} : 10^{12}]$ *J.*

by dynamical downscaling the data with the help of a convection-resolving model. On the other hand, a study of Doppler radar measurements of supercells would be helpful in order to further investigate the convective scale. Finally, it would be interesting to find a physical explanation for the power law behavior, for the value of the exponent and to set up an appropriate model of multiplicative generation processes that possibly causes the observed behavior.

References

Adrian, R., Christensen, K., and Liu, Z.-C. (2000). Analysis and interpretation of instantaneous turbulent velocity fields. *Experiments in fluids*, 29(3):275–290.

Alstott, J., Bullmore, E., and Plenz, D. (2014). powerlaw: a python package for analysis of heavy-tailed distributions. *PloS one*, 9(1):e85777.

American Meteorological Society (2012). Particle. Glossary of meteorology. [Available online at http://glossary.ametsoc.org/wiki/particle] Last modified: 20 Feb 2012; Last accessed: 22 Jun 2015.

Aref, H. (2007). Point vortex dynamics: a classical mathematics playground. *Journal of Mathematical Physics*, 48(6):065401.

Aref, H. (2010). Self-similar motion of three point vortices. *Physics of Fluids (1994-present)*, 22(5):057104.

Aref, H., Rott, N., and Thomann, H. (1992). Gröbli's solution of the three-vortex problem. *Annual Review of Fluid Mechanics*, 24(1):1–21.

Avnir, D., Biham, O., Lidar, D., and Malcai, O. (1998). Is the geometry of nature fractal? *Science*, 279(5347):39–40.

Batchelor, G. K. (2000). *An introduction to fluid dynamics*. Cambridge Mathematical Library. Cambridge university press, 14th edition.

Bayrak, Y., Yılmaztürk, A., and Öztürk, S. (2002). Lateral variations of the modal (a/b) values for the different regions of the world. *Journal of Geodynamics*, 34(5):653–666.

Ben-Zion, Y. (2003). Key formulas in earthquake seismology. *International handbook of earthquake and engineering seismology*, 81:1857–1875. online available at http://citeseerx.ist.psu.edu/viewdoc/download?doi=10.1.1.475.478&rep=rep1&type=pdf Last accessed: 4 Jan 2016).

Ben-Zion, Y. and Ampuero, J.-P. (2009). Seismic radiation from regions sustaining material damage. *Geophysical Journal International*, 178(3):1351–1356.

Blender, R., Fraedrich, K., and Lunkeit, F. (1997). Identification of cyclone-track regimes in the north atlantic. *Quarterly Journal of the Royal Meteorological Society*, 123(539):727–742.

Bronstein, I. N., Semendjajew, K. A., Musiol, G., and Mühlig, H. (2005). *Taschenbuch der Mathematik*. Verlag Harri Deutsch, Frankfurt am Main, 6. edition.

Bryan, G. (2015). Confronting the effects of surface drag on severe storms using numerical simulations. Conference talk at the European Conference on Severe Storms (ECSS) in Wiener Neustadt, Austria, 14.-18. September 2015.

Camargo, S. J. and Sobel, A. H. (2005). Western north pacific tropical cyclone intensity and enso. *Journal of Climate*, 18(15):2996–3006.

Campa, J. and Wernli, H. (2012). A pv perspective on the vertical structure of mature midlatitude cyclones in the northern hemisphere. *Journal of the Atmospheric Sciences*, 69(2):725–740.

Chakraborty, P., Balachandar, S., and Adrian, R. J. (2005). On the relationships between local vortex identification schemes. *Journal of Fluid Mechanics*, 535:189–214.

Champernowne, D. G. (1953). A model of income distribution. *The Economic Journal*, 63(250):318–351.

Chavas, D. R., Lin, N., and Emanuel, K. (2015). A model for the complete radial structure of the tropical cyclone wind field. part i: Comparison with observed structure*. *Journal of the Atmospheric Sciences*, 72(9):3647–3662.

Chong, M., Perry, A. E., and Cantwell, B. (1990). A general classification of three-dimensional flow fields. *Physics of Fluids A: Fluid Dynamics (1989-1993)*, 2(5):765–777.

Clauset, A., Shalizi, C. R., and Newman, M. E. (2009). Power-law distributions in empirical data. *SIAM review*, 51(4):661–703.

Cushman-Roisin, B. and Beckers, J.-M. (2011). *Introduction to geophysical fluid dynamics: physical and numerical aspects*, volume 101. Academic Press.

Dahl, J. M., Parker, M. D., and Wicker, L. J. (2014). Imported and storm-generated near-ground vertical vorticity in a simulated supercell. *Journal of the Atmospheric Sciences*, 71(8):3027–3051.

Dotzek, N. (2009). Derivation of physically motivated wind speed scales. *Atmospheric Research*, 93(1):564–574.

Dotzek, N., Kurgansky, M. V., Grieser, J., Feuerstein, B., and Névir, P. (2005). Observational evidence for exponential tornado intensity distributions over specific kinetic energy. *Geophysical Research Letters*, 32(24).

Dunkerton, T., Montgomery, M., and Wang, Z. (2009). Tropical cyclogenesis in a tropical wave critical layer: Easterly waves. *Atmospheric Chemistry and Physics*, 9:5587–5646.

Flaounas, E., Kotroni, V., Lagouvardos, K., and Flaounas, I. (2014). Cyclotrack (v1.0) – tracking winter extratropical cyclones based on relative vorticity: sensitivity to data filtering and other relevant parameters. *Geoscientific Model Development*, 7(4):1841–1853.

Fortak, H. (1967). *Vorlesungen über Theoretische Meteorologie - Kinematik der Atmosphäre*. Institut für Theoretische Meteorologie der Freien Universität Berlin, Berlin, Germany.

Frisch, U. and Sornette, D. (1997). Extreme deviations and applications. *Journal de Physique I*, 7(9):1155–1171.

Fujita, T. T. (1971). Proposed characterization of tornadoes and hurricanes by area and intensity. 42 p.

Golitsyn, G., Mokhov, I., Akperov, M., and Bardin, M. Y. (2007). Distribution functions of probabilities of cyclones and anticyclones from 1952 to 2000: An instrument for the determination of global climate variations. In *Doklady Earth Sciences*, volume 413(1), pages 324–326. Springer.

Gray, S. L. and Dacre, H. F. (2006). Classifying dynamical forcing mechanisms using a climatology of extratropical cyclones. *Quarterly Journal of the Royal Meteorological Society*, 132(617):1119–1137.

Gray, W. M. and Shea, D. J. (1973). The hurricane's inner core region. ii. thermal stability and dynamic characteristics. *Journal of the Atmospheric Sciences*, 30(8):1565–1576.

Gröbli, W. (1877). *Specielle Probleme über die Bewegung geradliniger paralleler Wirbelfäden*. PhD thesis, Druck von Zürcher und Furrer, Zürich. 86 pp. Also published in *Vierteljahresschrift der Naturforschenden Gesellschaft in Zürich*, 22, 37–81, 129–165. In German language online available under http://www.ngzh.ch/archiv/1877_22/22_1/22_4.pdf and http://www.ngzh.ch/archiv/1877_22/22_2/22_11.pdf.

Grotjahn, R. and Castello, C. (2000). A Study of Frontal Cyclone Surface and 300-hPa Geostrophic Kinetic Energy Distribution and Scale Change. *Monthly Weather Review*, 128:2865–2874.

Grotjahn, R., Hodyss, D., and Castello, C. (1999). Do Frontal Cyclones Change Size? Observed Widths of North Pacific Lows. *Monthly Weather Review*, 127:1089–1095.

Haak, U. and Ulbrich, U. (1996). Verification of an objective cyclone climatology for the north atlantic. *METEOROLOGISCHE ZEITSCHRIFT*, 5:24–30.

Haimes, R. and Kenwright, D. (1999). On the velocity gradient tensor and fluid feature extraction. *AIAA paper*, 3288.

Hanley, J. and Caballero, R. (2012). Objective identification and tracking of multicentre cyclones in the era-interim reanalysis dataset. *Quarterly Journal of the Royal Meteorological Society*, 138(664):612–625.

Hanson, C., Palutikof, J., and Davies, T. (2004). Objective cyclone climatologies of the north atlantic–a comparison between the ecmwf and ncep reanalyses. *Climate Dynamics*, 22(6-7):757–769.

Helmholtz, H. (1858). Über Integrale der hydrodynamischen Gleichungen, welche den Wirbelbewegungen entsprechen. *Journal für die reine und angewandte Mathematik*, 55:25–55.

Hewson, T. D. and Titley, H. A. (2010). Objective identification, typing and tracking of the complete life-cycles of cyclonic features at high spatial resolution. *Meteorological Applications*, 17(3):355–381.

Hirt, M. (2016). Statistical and dynamical analyses of atmospheric blockings with an idealized point vortex model. Master's thesis, Freie Universität Berlin.

Hodges, K. et al. (1994). A general-method for tracking analysis and its application to meteorological data. *Monthly Weather Review*, 122(11):2573–2586.

Hodges, K. I., Hoskins, B. J., Boyle, J., and Thorncroft, C. (2003). A comparison of recent reanalysis datasets using objective feature tracking: Storm tracks and tropical easterly waves. *Monthly Weather Review*, 131(9):2012–2037.

Holton, J. R. (2004). *An introduction to dynamic meteorology*, volume 88. Elsevier Academic press.

Hunt, J. C. (1998). Lewis fry richardson and his contributions to mathematics, meteorology, and models of conflict. *Annual Review of Fluid Mechanics*, 30(1):xiii–xxxvi.

Hunt, J. C., Wray, A., and Moin, P. (1988). Eddies, streams, and convergence zones in turbulent flows. In *Studying Turbulence Using Numerical Simulation Databases, 2*, volume 1, pages 193–208.

Isernhagen, C. (2015). Blockierende Wetterlagen aus Sicht der atmosphärischen Wirbeldy- namik: Theorie und Anwendung. Diploma thesis, Freie Universität Berlin.

Jeong, J. and Hussain, F. (1995). On the identification of a vortex. *Journal of Fluid Mechanics*, 285:69–94.

Kalnay, E., Kanamitsu, M., Kistler, R., Collins, W., Deaven, D., Gandin, L., Iredell, M., Saha, S., White, G., Woollen, J., et al. (1996). The ncep/ncar 40-year reanalysis project. *Bulletin of the American Meteorological Society*, 77(3):437–471.

Kanamitsu, M., Ebisuzaki, W., Woollen, J., Yang, S.-K., Hnilo, J., Fiorino, M., and Potter, G. (2002). NCEP-DOE AMIP-II reanalysis (R-2). *Bulletin of the American Meteorological Society*, 83(11):1631–1643.

Kanamori, H. and Anderson, D. L. (1975). Theoretical basis of some empirical relations in seismology. *Bulletin of the Seismological Society of America*, 65(5):1073–1095.

Kew, S. F., Sprenger, M., and Davies, H. C. (2010). Potential vorticity anomalies of the lowermost stratosphere: a 10-yr winter climatology. *Monthly Weather Review*, 138(4):1234–1249.

Kirchhoff, G. (1876). *Vorlesungen über Mathematische Physik: Mechanik Vol. 1.* Teubner Verlag, Leipzig.

Kirk, P. J. (2014). An updated tornado climatology for the uk: 1981–2010. *Weather*, 69(7):171–175.

Klein, R. (2008). An unified approach to meteorological modelling based on multiple-scales asymptotics. *Advances in Geosciences*, 15(15):23–33.

Kolmogorov, A. N. (1941). The local structure of turbulence in incompressible viscous fluid for very large reynolds numbers. In *Dokl. Akad. Nauk SSSR*, volume 30(4), pages 299–303.

Kosiba, K. and Wurman, J. (2010). The three-dimensional axisymmetric wind field structure of the spencer, south dakota, 1998 tornado. *Journal of the Atmospheric Sciences*, 67(9):3074–3083.

Kosiba, K. A., Trapp, R. J., and Wurman, J. (2008). An analysis of the axisymmetric three-dimensional low level wind field in a tornado using mobile radar observations. *Geophysical Research Letters*, 35(5).

Kudela, H. (2014). Self-similar collapse of n point vortices. *Journal of Nonlinear Science*, 24(5):913–933.

Kuhlbrodt, T. and Névir, P. (2000). Low-order point vortex models of atmospheric blocking. *Meteorology and Atmospheric Physics*, 73(3):127–138.

Kunnen, R., Clercx, H., and Geurts, B. (2010). Vortex statistics in turbulent rotating convection. *Physical Review E*, 82(3):036306.

Kurgansky, M. (2000). The statistical distribution of intense moist-convective spiral vortices in the atmosphere. In *Doklady Earth Sciences c/c of Doklady-Akademiia Nauk*, volume 371, pages 408–410. Interperiodica Publishing.

Lackmann, G. (2011). *Midlatitude synoptic meteorology: Dynamics, Analysis and Forecasting.* American Meteorological Society, Boston, Massachusetts.

Laherrere, J. and Sornette, D. (1998). Stretched exponential distributions in nature and economy:"fat tails" with characteristic scales. *The European Physical Journal B-Condensed Matter and Complex Systems*, 2(4):525–539.

Lambeck, K. (2005). *The Earth's variable rotation: geophysical causes and consequences*. Cambridge University Press.

Lau, W. K. and Kim, K.-M. (2012). The 2010 Pakistan flood and Russian heat wave: Teleconnection of hydrometeorological extremes. *Journal of Hydrometeorology*, 13(1):392–403.

Lee, J. J., Samaras, T., and Young, C. (2004). Pressure measurements at the ground in an f-4 tornado. In *Preprints, 22d Conf. on Severe Local Storms, Hyannis, MA, Amer. Meteor. Soc., CD-ROM*, volume 15.

Lim, E.-P. and Simmonds, I. (2007). Southern hemisphere winter extratropical cyclone characteristics and vertical organization observed with the era-40 data in 1979–2001. *Journal of Climate*, 20(11):2675–2690.

Lionello, P., Dalan, F., and Elvini, E. (2002). Cyclones in the mediterranean region: the present and the doubled co2 climate scenarios. *Climate Research*, 22(2):147–159.

Mallen, K. J., Montgomery, M. T., and Wang, B. (2005). Reexamining the near-core radial structure of the tropical cyclone primary circulation: Implications for vortex resiliency. *Journal of the Atmospheric Sciences*, 62(2):408–425.

Markowski, P. and Richardson, Y. (2011). *Mesoscale meteorology in midlatitudes*, volume 2. John Wiley & Sons.

Markowski, P. and Richardson, Y. (2015). How does surface drag affect the development of near-surface vertical vorticity in supercell thunderstorms? Conference talk at the European Conference on Severe Storms (ECSS) in Wiener Neustadt, Austria, 14.-18. September 2015; http://meetingorganizer.copernicus.org/ECSS2015/ECSS2015-95.pdf (abstract) and http://presentations.copernicus.org/ECSS2015-95_presentation.pdf (presentation with co-author George Bryan).

Mikusky, E. (2007). *On the structure of concentrated atmospheric vortices in a gradient wind regime and its motion on synoptic scales*. PhD thesis, Universität Hamburg, Fachbereich Geowissenschaften.

Mitzenmacher, M. (2004). A brief history of generative models for power law and lognormal distributions. *Internet Mathematics*, 1(2):226–251.

Müller, A. and Névir, P. (2014). A geometric application of nambu mechanics: the motion of three point vortices in the plane. *Journal of Physics A: Mathematical and Theoretical*, 47(10):105201.

Müller, A., Névir, P., Schielicke, L., Hirt, M., Pueltz, J., and Sonntag, I. (2015). Applications of point vortex equilibria: blocking events and the stability of the polar vortex.

Tellus A, 67. 29184, http://dx.doi.org/10.3402/tellusa.v67.29184 Published as an Open Access article distributed under the terms of the Creative Commons Attribution 4.0 International License (http://creativecommons.org/licenses/by/4.0/).

Müller, G. (1979). Probleme der Umrechnung von Windstärkeangaben nach der Beaufortskala und Windgeschwindigkeitswerten (Procedures for the conversion of wind force data based on the beaufort-scale into values of wind velocity). *Meteorologische Rundschau*, 32:7–12.

Munich Re (2014). Significant natural disasters since 1980 - costliest winter storms in europe (overall losses). http://www.munichre.com/en/reinsurance/business/non-life/natcatservice/significant-natural-catastrophes Accessed: 21 May 2015.

Murray, R. J. and Simmonds, I. (1991). A numerical scheme for tracking cyclone centres from digital data. *Australian Meteorological Magazine*, 39(3).

National Centers for Environmental Prediction National Weather Service NOAA US Department of Commerce (1994). Ncep/ncar global reanalysis products, 1948-continuing. http://rda.ucar.edu/datasets/ds090.0 Accessed: 28 Sep 2012.

NCAR/UCAR ClimateDataGuide: National Center for Atmospheric Research Staff (Eds) (2013). The climate data guide: Common spectral model grid resolutions. [Retrieved from https://climatedataguide.ucar.edu/climate-model-evaluation/common-spectral-model-grid-resolutions] Last modified: 23 Jul 2013; Last accessed: 18 Jan 2016.

NCEP (2000). National Centers for Environmental Prediction/National Weather Service/NOAA/U.S. Department of Commerce, NCEP/DOE Reanalysis 2 (R2). Research Data Archive at the National Center for Atmospheric Research, Computational and Information Systems Laboratory. NCEP, Silver Spring.

Neu, U., Akperov, M. G., Bellenbaum, N., Benestad, R., Blender, R., Caballero, R., Cocozza, A., Dacre, H. F., Feng, Y., Fraedrich, K., et al. (2013). Imilast: A community effort to intercompare extratropical cyclone detection and tracking algorithms. *Bulletin of the American Meteorological Society*, 94(4):529–547.

Newman, M. E. (2005). Power laws, pareto distributions and zipf's law. *Contemporary Physics*, 46(5):323–351.

Newton, P. K. (2001). *The N-Vortex Problem: Analytical Techniques*, volume 145. Springer-Verlag, New York.

Nielsen, J. W. and Dole, R. M. (1992). A Survey of Extratropical Cyclone Characteristics during GALE. *Monthly Weather Review*, 120:1156–1168.

Novikov, E. and Sedov, I. B. (1979). Vortex collapse. *Zhurnal Eksperimentalnoi i Teoreticheskoi Fiziki*, 77:588–597. English translation available under http://www.jetp.ac.ru/cgi-bin/dn/e_050_02_0297.pdf.

Päschke, E., Marschalik, P., Owinoh, A. Z., and Klein, R. (2012). Motion and structure of atmospheric mesoscale baroclinic vortices: dry air and weak environmental shear. *Journal of Fluid Mechanics*, 701:137–170.

Pinto, J. G., Spangehl, T., Ulbrich, U., and Speth, P. (2005). Sensitivities of a cyclone detection and tracking algorithm: individual tracks and climatology. *Meteorologische Zeitschrift*, 14(6):823–838.

Pisarenko, V. and Sornette, D. (2004). Statistical detection and characterization of a deviation from the gutenberg-richter distribution above magnitude 8. *Pure and Applied Geophysics*, 161(4):839–864.

Pültz, J. (2014). Blockierende Wetterlagen und ihre Beschreibung mit der Punktwirbeldynamik in der Ebene und auf der Kugel. Bachelor's thesis, Freie Universität Berlin.

Rex, D. F. (1950). Blocking action in the middle troposphere and its effect upon regional climate. *Tellus*, 2(4):275–301.

Riehl, H. (1963). Some relations between wind and thermal structure of steady state hurricanes. *Journal of the Atmospheric Sciences*, 20(4):276–287.

Rudeva, I. A. (2008). On the relation of the number of extratropical cyclones to their sizes. *Izvestiya Atmospheric and Oceanic Physics*, 44:273–278.

Rudeva, I. A. and Gulev, S. K. (2007). Climatology of cyclone size characteristics and their changes during the cyclone life cycle. *Monthly Weather Review*, 135:2568–2587.

Saha, S., Moorthi, S., Pan, H.-L., Wu, X., Wang, J., Nadiga, S., Tripp, P., Kistler, R., Woollen, J., Behringer, D., Liu, H., Stokes, D., Grumbine, R., Gayno, G., Wang, J., Hou, Y.-T., Chuang, H.-Y., Juang, H.-M. H., Sela, J., Iredell, M., Treadon, R., Kleist, D., Van Delst, P., Keyser, D., Derber, J., Ek, M., Meng, J., Wei, H., Yang, R., Lord, S., Van Den Dool, H., Kumar, A., Wang, W., Long, C., Chelliah, M., Xue, Y., Huang, B., Schemm, J.-K., Ebisuzaki, W., Lin, R., Xie, P., Chen, M., Zhou, S., Higgins, W., Zou, C.-Z., Liu, Q., Chen, Y., Han, Y., Cucurull, L., Reynolds, R. W., Rutledge, G., and Goldberg, M. (2010). The ncep climate forecast system reanalysis. *Bulletin of the American Meteorological Society*, 91(8):1015–1057.

Schielicke, L. and Névir, P. (2009). On the theory of intensity distributions of tornadoes and other low pressure systems. *Atmospheric Research*, 93(1):11–20. https://doi.org/10.1016/j.atmosres.2008.09.021.

Schielicke, L. and Névir, P. (2011). Introduction of an atmospheric moment combining eulerian and lagrangian aspects of vortices: Application to tornadoes. *Atmospheric Research*, 100(4):357–365. https://doi.org/10.1016/j.atmosres.2010.08.027.

Schielicke, L. and Névir, P. (2013). Comprehensive analysis of tornado statistics in comparison to earthquakes: intensity and temporal behaviour. *Nonlinear Processes in Geophysics*, 20(1):47–57. https://doi.org/10.5194/npg-20-47-2013.

Schielicke, L., Névir, P., and Ulbrich, U. (2015). Size and intensity of vortex structures in a simulated idealized supercell as seen from the kinematic vorticity number. Poster presentation at the European Conference on Severe Storms (ECSS) in Wiener Neustadt, Austria, 14.-18. September 2015; http://meetingorganizer.copernicus.org/ECSS2015/ECSS2015-152.pdf (abstract) and http://presentations.copernicus.org/ECSS2015-152_presentation.pdf (poster).

Schielicke, L., Névir, P., and Ulbrich, U. (2016). Kinematic vorticity number - a tool for estimating vortex sizes and circulations. *Tellus A*, 68. 29464, http://dx.doi.org/10.3402/tellusa.v68.29464 Published as an Open Access article distributed under the terms of the Creative Commons Attribution 4.0 International License (http://creativecommons.org/licenses/by/4.0/).

Schinke, H. (1993). On the occurrence of deep cyclones over europe and the north atlantic in the period 1930-1991. *Contributions to atmospheric physics*, 66(3):223–237.

Schneidereit, A., Blender, R., and Fraedrich, K. (2010). A radius-depth model for midlatitude cyclones in reanalysis data and simulations. *Quarterly Journal of the Royal Meteorological Society*, 136:50–60.

Schuh, H., Dill, R., Greiner-Mai, H., Kutterer, H., Müller, J., Nothnagel, A., Richter, B., Rothacher, M., Schreiber, U., and Soffel, M. (2003). Erdrotation und globale dynamische Prozesse: Stand und Ziele der Modellbildung, der Mess- und der Auswerteverfahren. *Mitteilungen des Bundesamtes für Kartographie und Geodäsie*, Band 32.

Shaughnessy, E. J., Katz, I. M., and Schaffer, J. P. (2005). *Introduction to fluid mechanics*, volume 8. Oxford University Press New York.

Simmonds, I. (2000). Size changes over the life of sea level cyclones in the ncep reanalysis. *Monthly Weather Review*, 128(12):4118–4125.

Simmonds, I. and Keay, K. (2000). Mean southern hemisphere extratropical cyclone behavior in the 40-year ncep-ncar reanalysis. *Journal of Climate*, 13(5):873–885.

Simmonds, I., Murray, R. J., and Leighton, R. (1999). A refinement of cyclone tracking methods with data from frost. *Aust Meteor Antarctic Mag Special Issue*, pages 35–49.

Sinclair, M. R. (1994). An objective cyclone climatology for the southern hemisphere. *Monthly Weather Review*, 122(10):2239–2256.

Sinclair, M. R. (1997). Objective identification of cyclones and their circulation intensity, and climatology. *Weather and forecasting*, 12(3):595–612.

Smagorinsky, J. (1974). Global atmospheric modelling and the numerical simulation of climate. In Hess, W. N., editor, *Weather and climate modification*, pages 633–686. Wiley, New York.

Sonntag, I. (2012). Die Punktwirbeldynamik und ihre Anwendung in der großskaligen Dy- namik der Atmosphäre. Bachelor's thesis, Freie Universität Berlin.

Sornette, D. (2009). Probability distributions in complex systems. In *Encyclopedia of Complexity and Systems Science*, pages 7009–7024. Springer. online available at https://arxiv.org/pdf/0707.2194.pdf.

Storm prediction warning center (2016). Severe weather database files (1950-2015). [Available online at http://www.spc.noaa.gov/wcm/#data] Last annual updates occurred on 9 Mar 2016; Last accessed: 20 Oct 2016.

Thompson, R. L., Bacchi, R. D. A., and J, M. F. (2009). What is a vortex? *Procedings of COBEM 2009*. 20th International Congress of Mechanical Engineering, November 15-20, 2009, Gramado, RS, Brazil.

Tipler, P. A. (2000). *Physik*. 3. korrigierter Nachdruck. Spektrum Akademischer Verlag Heidelberg – Berlin – Oxford.

Tory, K. J., Dare, R., Davidson, N., McBride, J., and Chand, S. (2013). The importance of low-deformation vorticity in tropical cyclone formation. *Atmospheric Chemistry and Physics*, 13(4):2115–2132.

Trigo, I. F. (2006). Climatology and interannual variability of storm-tracks in the euro-atlantic sector: a comparison between era-40 and ncep/ncar reanalyses. *Climate Dynamics*, 26(2-3):127–143.

Truesdell, C. (1953). Two measures of vorticity. *Indiana Univ. Math. J.*, 2:173–217.

Truesdell, C. (1954). *The Kinematics of Vorticity*. Indiana University Press, Bloomington.

Ulbrich, U., Fink, A., Klawa, M., and Pinto, J. (2001). Three extreme storms over europe in december 1999. *Weather*, 56(3):70–80.

Ulbrich, U., Leckebusch, G., and Pinto, J. (2009). Extra-tropical cyclones in the present and future climate: a review. *Theoretical and Applied Climatology*, 96(1-2):117–131.

van Bebber, W. (1891). Die zugstrassen barometrischer minima nach den bahnenkarten der deutschen seewarte für den zeitraum 1875-1890. *Meteorologische Zeitschrift*, 8:361–366.

Weisman, M. L. and Klemp, J. B. (1982). The dependence of numerically simulated convective storms on vertical wind shear and buoyancy. *Monthly Weather Review*, 110(6):504–520.

Weisman, M. L. and Klemp, J. B. (1984). The structure and classification of numerically simulated convective stormsin directionally varying wind shears. *Monthly Weather Review*, 112(12):2479–2498.

Wernli, H. and Schwierz, C. (2006). Surface Cyclones in the ERA-40 Dataset (1958–2001). Part I: Novel Identification Method and Global Climatology. *Journal of the Atmospheric Sciences*, 63:2486–2507.

Witte, J., Douglass, A., Silva, A. d., Torres, O., Levy, R., and Duncan, B. (2011). Nasa A-Train and Terra observations of the 2010 Russian wildfires. *Atmospheric Chemistry and Physics*, 11(17):9287–9301.

WSCE (2006). *A recommendation for an Enhanced Fujita scale (EF-Scale).* [Wind Science and Engineering Center, Texas Tech University.

Wu, J.-Z., Ma, H.-Y., and Zhou, M.-D. (2007). *Vorticity and vortex dynamics*. Springer Science & Business Media.

Nomenclature

Acronyms

Symbol	Description	Units
CDF	Cumulative distribution function	
CCDF	Complementary cumulative distribution function	
cf.	Abbreviation of confer	
CFSR	Climate Forecast System Reanalysis	
coord.	Coordinates	
distr.	Distribution	
E	East	
e.g.	Abbreviation of *exempli gratia* (for example)	
eq.	Abbreviation of equation	
Fig.	Abbreviation of figure	
i.a.	Abbreviation of *inter alia*	
N	North	
NCEP	National Center for Environmental Prediction	
NH	Northern hemisphere	
PDF	Probability density function	
S	South	
SC	Single centers	
SH	Southern hemisphere	
Tab.	Abbreviation of table	
W	West	
Wkf	W_k feature	
WRF	Weather Research and Forecasting (model)	

Greek Symbols

Symbol	Description	Units
α	Angle between unit vectors $\mathbf{i}$ and $\boldsymbol{t}$	(°)
α	Angle between translation vector $\mathbf{v}$ and x-axis (of N=3 point vortex system)	(°)
α	Eigenvalues of $\nabla\mathbf{u}$	
α	Exponent in modified Rankine ansatz	1
α	Exponent of power law	1
$\alpha = \rho^{-1}$	Specific volume	$\mathrm{m^3\,kg^{-1}}$
β	Exponent of stretched-exponential distr.	1
β	Power law exponent	1
$\gamma = \gamma(t)$	Time-dependent stretching factor (Burgers vortex)	
Γ	Circulation $\Gamma = \oint_{c(A')} \mathbf{u} \cdot d\mathbf{s} = \int_{A'} 2\boldsymbol{\omega} \cdot d\mathbf{A}$	$\mathrm{m^2\,s^{-1}}$
Γ_a	Absolute circulation $\Gamma_a = \Gamma + \int_{A'} 2\boldsymbol{\Omega}_E \cdot d\mathbf{A}$	$\mathrm{m^2\,s^{-1}}$
Γ_{total}	Total circulation	$\mathrm{m^2\,s^{-1}}$
$\lambda_1, \lambda_2, \lambda_3$	Eigenvalues of a 3×3 tensor	
λ	Decay rate in exponential function	
λ	Multiplicative factor (stretched exponential distr.)	
λ	Scaling factor	
$\lambda\beta$	Reference scale (stretched-exponential distr.)	
$\widetilde{\lambda} = 1/\lambda\beta$	Reciprocal of reference scale (stretched-exponential distr.)	
μ	Bulk viscosity	$\mathrm{kg\,s\,m^{-1}}$
μ	Mean	
$\nu = \rho/\mu$	Kinematic viscosity ($\nu = \rho/\mu$)	$\mathrm{m^2\,s^{-1}}$
φ	Latitude (in radians or degree)	Rad or (°)
ϕ	Angular component of polar coordinates	Rad

$\Phi(\mathbf{r}, t)$	Field depending on space and time	
Φ_z	Centrifugal potential	$\mathrm{m}^3\,\mathrm{s}^{-2}$
Φ_g	Potential of gravity	$\mathrm{m}^3\,\mathrm{s}^{-2}$
Φ	Total geopotential	$\mathrm{m}^3\,\mathrm{s}^{-2}$
ρ	Density	$\mathrm{kg\,m}^{-3}$
ρ, ϕ	Polar coordinates (2d)	
ρ	Radial component of polar coordinates	m
ρ_c	Density at the center of the vortex at the moment of maximum intensitx	$\mathrm{kg\,m}^{-3}$
$\bar{\rho}$	Averaged density inside the life time volume of the vortex	$\mathrm{kg\,m}^{-3}$
$\Delta\sigma = \sigma^0 - \sigma^f$	Stress drop	Pa
σ^0	Initial stress before earthquake	Pa
σ^f	Final stress after earthquake	Pa
σ^2	Variance	
θ	Potential temperature	K
$\zeta = \mathbf{k} \cdot \nabla \times \mathbf{u}$	Vertical component of relative vorticity vector	s^{-1}
$\zeta = v_x - u_y$	Vertical component of vorticity vector in cartesian coordinates	s^{-1}
$\zeta_{mean} = \frac{\Gamma}{A}$	Mean vorticity in area A	s^{-1}
$\zeta_g = \frac{1}{\rho f}\nabla^2 p$	Geostrophic vorticity	s^{-1}
$\zeta_a = \mathbf{k} \cdot \nabla \times \mathbf{u}_a$	Vertical component of absolute vorticity vector $\zeta_a = \zeta + f$	s^{-1}
$\overline{\zeta^2}$	Areal average of squared vorticity	s^{-2}
$\widetilde{\omega}$	Angular velocity (magnitude): $\widetilde{\omega} = \frac{d\phi}{dt}$	$\mathrm{Rad\,s}^{-1}$
$\|\mathbf{\Omega}\|$	Local rotation rate $\|\mathbf{\Omega}\| = \frac{1}{\sqrt{2}}\sqrt{\overline{\zeta^2}}$	s^{-1}
$\|\mathbf{\Omega}_E\|$	Rotation rate of Earth (magnitude) $\|\mathbf{\Omega}_E\| = 2\pi/day = 7.27 \cdot 10^{-5}\,\mathrm{s}^{-1}$	s^{-1}

Roman Symbols

Symbol	Description	Units
A	Area	m^2
A	Rupture surface	m^2
a	Acceleration	$\mathrm{m\,s}^{-2}$
AW^2	Term similar to W_k but components are averaged over area (2d): $AW^2 = \frac{\overline{\zeta^2}}{D_h^2+Def^2+Def'^2}$	1
B	Beaufort-scale (class)	1
B	Bernoulli-streamfunction $B = \frac{1}{2}\mathbf{u}^2 + h + \Phi_g$	$\mathrm{m}^2\,\mathrm{s}^{-2}$
b	b-values of earthquakes	m^2
$C = fv_h$	Coriolis acceleration	$\mathrm{m\,s}^{-1}$
$C' = lw\sin\alpha$	Coriolis acceleration II	$\mathrm{m\,s}^{-1}$
C	Normalization constant of PDF	
$C^{HV} = \frac{L}{H}$	Reciprocal of aspect ratio	1
$C^{LE} = \frac{\bar{\rho}}{\rho_c}$	Ratio of averaged density and density at vortex core	1
$\widetilde{C}$	Dimensionless shape factor	1
c	Constant factor	
c_g	Group velocity	$\mathrm{m\,s}^{-1}$
c_p	Specific heat at constant pressure ($c_p = R + c_v = 1004\,\mathrm{J\,kg}^{-1}\,\mathrm{K}$ for dry air)	$\mathrm{J\,kg}^{-1}\,\mathrm{K}$
c_v	Specific heat at constant volume ($c_v = 717\,\mathrm{J\,kg}^{-1}\,\mathrm{K}$ for dry air)	$\mathrm{J\,kg}^{-1}\,\mathrm{K}$
D	Depth	Pa
D_h	Divergence (2d) ($D_h = u_x + v_y$)	s^{-1}
$\overline{D_h^2}$	Areal average of squared divergence	s^{-2}
Def	Stretching deformation (2d) ($Def = u_x - v_y$)	s^{-1}
$\overline{Def^2}$	Areal average of squared stretching deformation	s^{-2}

Def'	Shearing deformation (2d) ($Def' = u_y + v_x$)	s^{-1}
$\overline{Def'^2}$	Areal average of squared shearing deformation	s^{-2}
$dv = dxdydz$	Volume element	m^3
$e = c_v T$	Internal energy (mass-specific)	$\mathrm{m}^2\,\mathrm{s}^{-2}$
e	Energy of displacement	$\mathrm{m}^2\,\mathrm{s}^{-2}$
$e_{ec}, \widetilde{e}_{ec}$	Energy of displacement under geostrophic balance	$\mathrm{m}^2\,\mathrm{s}^{-2}$
$e_t, \widetilde{e}_t$	Energy of displacement under cyclostrophic balance	$\mathrm{m}^2\,\mathrm{s}^{-2}$
$e_{tc}, \widetilde{e}_{tc}$	Energy of displacement under gradient wind balance	$\mathrm{m}^2\,\mathrm{s}^{-2}$
$erf(x)$	Gaussian error function of x	
$erfc(x) = 1 - erf(x)$	Complementary Gaussian error function of x	
$\exp(x), e^x$	Exponential function of x	
F	Fujita-scale (class)	1
f	Coriolis parameter ($f = \mathbf{k} \cdot \boldsymbol{\Omega}_E = 2 \lVert \boldsymbol{\Omega}_E \rVert \sin\phi$)	s^{-1}
$f(t)$	Probability density function (unnormalized)	
G	Green's function (distribution)	
g	Acceleration of gravity (magnitude) $g \approx 10\,\mathrm{m\,s}^{-2}$	$\mathrm{m\,s}^{-2}$
H	Height scale	m
H	Hamiltonian (point vortex model)	
H/L	Aspect ratio	1
$h = e + p\alpha$	Enthalpy (mass-specific)	$\mathrm{m}^2\,\mathrm{s}^{-2}$
I, II, III	Invariants of a 3×3 tensor	
$J(u,v) = det(\nabla \mathbf{v})$	Jacobi determinant of horizontal velocity components (2d)	s^{-2}
L	Length scale (horizontal)	m
$\widetilde{L}$	Characteristic length of fault	m
L_{Track}	Path length	m

L_z	Angular momentum (point vortex model)	
l	Coriolis parameter ($l = \mathbf{j} \cdot \mathbf{\Omega}_E = 2 \lVert \mathbf{\Omega}_E \rVert \cos\phi$)	s^{-1}
$\ell_{\alpha,\beta}$	Intervortical distance between two point vortices α, β	m
$l = \lVert \mathbf{r} \rVert$	Length of line element	m
$\ln(x)$	Natural logarithm of x	
$\log(x)$	Decadic (common) logarithm of x with base 10	
$M_* = V_* \bar{\rho}$	Total mass	kg
$M_a = M_* e$	Atmospheric moment	J
M_o	Seismic moment (earthquake magnitude)	J
N	Number	
N_{tot}	Total number	
n	Normal direction in natural coordinates	
P, Q, R	Invariants of $\nabla \mathbf{u}$	
$P = \nabla \cdot \mathbf{u}$	First invariant of $\nabla \mathbf{u}$	s^{-1}
$P = \frac{1}{\rho} \frac{\partial p}{\partial n}$	Pressure gradient acceleration	$\mathrm{m\,s}^{-1}$
ΔP	Pressure difference between vortex core pressure and environmental pressure	Pa
$\Delta_h P$	Horizontal pressure difference	Pa
$\Delta_z P$	Vertical pressure difference	Pa
P_x	Zonal momentum (point vortex model)	
P_y	Meridional momentum (point vortex model)	
$P(X)$	Cumulative distribution function (CDF) below threshold x: $P(X) = Pr(X \leq x)$	
$\bar{P}(X)$	Complementary cumulative distribution function (CCDF) above threshold x: $\bar{P}(X) = Pr(X > x)$	
$Pr(X)$	Probability of random variable X	
p	Pressure	Pa
p_s	Standard pressure (usually $p_s = 1000\,\mathrm{Pa}$)	Pa

$p(t)$	Probability density function (PDF)	
$Q = \frac{1}{2}(\|\mathbf{\Omega}\|^2 - \|\mathbf{S}\|^2)$	Second invariant of $\nabla\mathbf{u}$	s^{-2}
$R = det(\nabla\mathbf{u})$	Third invariant of $\nabla\mathbf{u}$ (3d)	s^{-3}
R	Gas constant ($R = 287\,\mathrm{J\,kg^{-1}\,K}$ for dry air)	$\mathrm{J\,kg^{-1}\,K}$
R	Radius of curvature in natural coord. system	m
R	Vortex (core) radius	m
$Re = \frac{UL}{\nu}$	Reynolds number	1
$Ro = \frac{U}{fL}$	Rossby number	1
r, θ, z	Coordinates of cylindrical coordinate system	
s	Entropy (mass-specific)	$\mathrm{J\,kg^{-1}\,K}$
s	Streamwise direction in natural coordinates	
$\|\mathbf{S}\|$	Local strain rate (2d) $\|\mathbf{S}\| = \frac{1}{\sqrt{2}}\sqrt{D_h^2 + Def^2 + Def'^2}$	s^{-1}
T	Temperature	K
T	Torro-scale (class)	1
T	Time scale	s
ΔT	Dissipative time scale $\Delta T = 10 \cdot L^{2/3}\,\mathrm{m}^{3/2}\,\mathrm{s}$	s
t	Time	s
Δt	Time step	s
U	Magnitude of horizontal wind components	$\mathrm{m\,s^{-1}}$
u	Velocity component in x-direction (cartesian)	$\mathrm{m\,s^{-1}}$
u_{max}	Maximum velocity at vortex core radius	$\mathrm{m\,s^{-1}}$
u_r	Velocity component in radial direction (cylindrical)	$\mathrm{m\,s^{-1}}$
u_θ	Velocity component in azimuthal direction (cylindrical)	$\mathrm{m\,s^{-1}}$
$u_x = \frac{\partial u}{\partial x}$	Partial derivative of u with respect to x	s^{-1}

$u_y = \frac{\partial u}{\partial y}$	Partial derivative of u with respect to y	s^{-1}
u_z	Velocity component in vertical direction (cylindrical)	$\mathrm{m\,s}^{-1}$
V_*	Total during life time affected volume	m^3
v	Velocity component in y-direction (cartesian)	$\mathrm{m\,s}^{-1}$
v	Translational speed (magnitude) of point vortices	
v_h	Magnitude of horizontal velocity	$\mathrm{m\,s}^{-1}$
$v_x = \frac{\partial v}{\partial x}$	Partial derivative of v with respect to x	s^{-1}
$v_y = \frac{\partial v}{\partial y}$	Partial derivative of v with respect to y	s^{-1}
W	Magnitude of vertical wind component	$\mathrm{m\,s}^{-1}$
$W_k = \frac{\|\mathbf{\Omega}\|}{\|\mathbf{S}\|}$	Kinematic vorticity number	1
$\overline{W}_k = \frac{\int W_k dA}{\int dA}$	Areal-averaged kinematic vorticity number	1
$W_k = \frac{\sqrt{\zeta^2}}{\sqrt{D_h^2+Def^2+Def'^2}}$	Kinematic vorticity number (2d)	1
$W_k^* = \frac{\zeta}{\sqrt{D_h^2+Def^2+Def'^2}}$	Extended kinematic vorticity number (2d)	1
w	Velocity component in z-direction (cartesian)	$\mathrm{m\,s}^{-1}$
X	Random variable	
x	Threshold in CDF and CCDF	
x_{min}	Lower bound in e.g. power law distr.	
$Z = \frac{v_h^2}{R}$	Centrifugal acceleration	$\mathrm{m\,s}^{-1}$
$z = x + iy$	Complex variable	

Tensors

Symbol	**Description**	**Units**
$\mathbf{F}_{N.S.}$	Navier-Stokes tensor	Pa
$\mathbf{I}$	Unit tensor	1

$\nabla \mathbf{u}$	Velocity gradient tensor	s^{-1}
$\mathbf{T}$	Stress tensor ($\mathbf{T} = -p\mathbf{I} + \mathbf{F}_{N.S.}$)	Pa
$\mathbf{S}$	Strain-rate tensor/deformation tensor $\mathbf{S} = \frac{1}{2}\left(\nabla \mathbf{u} + (\nabla \mathbf{u})^T\right)$	s^{-1}
$\mathbf{S}'$	Deviator of strain-rate tensor (3d) ($\mathbf{S}' = \mathbf{S}' - \frac{1}{3}(\nabla \cdot \mathbf{u})\mathbf{I}$)	s^{-1}
$\mathbf{\Omega}$	Vorticity/rotation tensor $\mathbf{\Omega} = \frac{1}{2}\left(\nabla \mathbf{u} - (\nabla \mathbf{u})^T\right)$	s^{-1}

Vectors

Symbol	Description	Units
$\mathbf{C}$	Center of circulation	m
$d\mathbf{A}$	Material area element	m^2
$d\mathbf{x}$	Material line element	m
$\mathbf{e}_r, \mathbf{e}_\theta, \mathbf{e}_z$	Unit vectors of cylindrical coordinate system in x, y, z-direction	1
$\mathbf{F}_R$	Frictional acceleration ($\mathbf{F}_R = \frac{1}{\rho}\nabla \cdot \mathbf{F}_{N.S.} = \nu \nabla^2 \mathbf{u}$)	$\mathrm{m}^2\,\mathrm{s}^{-2}$
$\mathbf{g}$	Acceleration of gravity (vector)	$\mathrm{m}\,\mathrm{s}^{-2}$
$\mathbf{i}, \mathbf{j}, \mathbf{k}$	Unit vectors of cartesian coordinate system in x, y, z-direction	1
$\mathbf{r} = (x, y, z)$	Space coordinate vector (3d) in cartesian coordinates	m
$\boldsymbol{t}, \boldsymbol{n}, \boldsymbol{k}$	Unit vectors of natural coordinate system in *streamwise,normal,*z-direction	1
$\mathbf{u} = (u, v, w)$	Velocity vector (3d) in cartesian coordinates	$\mathrm{m}\,\mathrm{s}^{-1}$
$\mathbf{u} = (u_r, u_\theta, u_z)$	Velocity vector (3d) in cylindrical coordinates	$\mathrm{m}\,\mathrm{s}^{-1}$
$\mathbf{u}_a$	Absolute velocity vector	$\mathrm{m}\,\mathrm{s}^{-1}$
$\mathbf{u}_r$	Relative velocity vector	$\mathrm{m}\,\mathrm{s}^{-1}$
$\mathbf{v} = (u, v)$	Velocity vector (2d) in cartesian coordinates	$\mathrm{m}\,\mathrm{s}^{-1}$

$\mathbf{v}$	Translational velocity (vector) of point vortices	
$\mathbf{v}_g = \frac{1}{\rho f}\mathbf{k} \times \nabla p$	Geostrophic velocity (2d)	$\mathrm{m\,s^{-1}}$
$\mathbf{w} = \frac{1}{2}\boldsymbol{\omega}$	Angular velocity of rigid body	$\mathrm{s^{-1}}$
$\boldsymbol{\Omega_E}$	Rotation rate of Earth	$\mathrm{s^{-1}}$
$\boldsymbol{\omega} = \nabla \times \mathbf{u}$	Relative vorticity vector	$\mathrm{s^{-1}}$
$\boldsymbol{\omega} = (\omega_r, \omega_\theta, \zeta)$	Vorticity vector in cylindrical coordinates	$\mathrm{s^{-1}}$
$\boldsymbol{\omega}_a = \nabla \times \mathbf{u}_a$	Absolute vorticity vector $\boldsymbol{\omega}_a = \boldsymbol{\omega} + 2\boldsymbol{\Omega}_e$	$\mathrm{s^{-1}}$
$\boldsymbol{\omega}_r = \boldsymbol{\omega}$	Relative vorticity vector	$\mathrm{s^{-1}}$

Other Symbols

Symbol	**Description**	**Units**
$\mathbf{A}^T$	Transpose of n×n tensor $\mathbf{A}$	
$\|\mathbf{A}\|$	Euclidean norm of n×n tensor $\mathbf{A}$ with $\|\mathbf{A}\| = \sqrt{tr(\mathbf{A}\mathbf{A}^T}$	
$det(\mathbf{A})$	Determinant of n×n tensor $\mathbf{A}$	
$tr(\mathbf{A})$	Trace of n×n tensor $\mathbf{A}$	
$\frac{D}{Dt} = \frac{\partial}{\partial t} + \mathbf{u} \cdot \nabla$	Material time derivative	$\mathrm{s^{-1}}$
$\frac{\partial}{\partial t}$	Local time derivative	$\mathrm{s^{-1}}$
$\nabla_h = \boldsymbol{t}\frac{\partial}{\partial s} + \boldsymbol{n}\frac{\partial}{\partial n}$	Nabla-operator in natural coordinates (2d)	$\mathrm{m^{-1}}$
$\nabla_h = \mathbf{i}\frac{\partial}{\partial x} + \mathbf{j}\frac{\partial}{\partial y}$	Nabla-operator in cartesian coordinates (2d)	$\mathrm{m^{-1}}$
$\mathbf{u} \cdot \nabla$	Advection	$\mathrm{s^{-1}}$
$< X >= \frac{\int_P^{P_0} X dp}{P_0 - P}$	Vertical average of variable X	Unit of X

List of Figures

List of Tables

Acknowledgments

I would like to thank Prof. Uwe Ulbrich, Prof. Rupert Klein and PD Dr. Peter Névir for giving me the opportunity to work on this thesis in the framework of the Helmholtz graduate research school GEOSIM. I am thankful to the Helmholtz association and the Helmholtz graduate research school GEOSIM who financially supported the work on this topic.

I thank my supervisor Prof. Uwe Ulbrich and all the members of his working group for supporting me with helpful discussions and comments. I am thankful to my supervisor PD Dr. Peter Névir for the numerous insightful discussions on the topic and for the guidance in defining the central theme of this work. Furthermore, I thank Prof. Rupert Klein who immediately helped with substantial comments and hints whenever I asked for.

I would like to thank Christoph Gatzen, Annette Müller and Dr. Martin Göber who carefully read through different stages of the thesis and helped with thoughtful comments, suggestions and discussions on the various topics of the thesis. Furthermore, I am grateful to Prof. Johannes Dahl who — as an expert of the convective scale — helped whenever I had questions on that topic.

Selbstständigkeitserklärung

Hiermit erkläre ich an Eides statt, dass ich die vorliegende Arbeit selbstständig und ohne fremde Hilfe angefertigt, keine anderen als die angegebenen Quellen und Hilfsmittel benutzt und die den benutzten Quellen wörtlich oder inhaltlich entnommenen Stellen als solche kenntlich gemacht habe. Diese Arbeit hat in gleicher oder ähnlicher Form noch keiner Prüfungsbehörde vorgelegen.

Ort, Datum	Unterschrift